Dipl.-Ing. Angelina Orthacker, BSc

Developing Methods for 3D STEM to Reveal Atomic-Scale Spinodal Decomposition

DOCTORAL THESIS

To achieve the university degree of
Doktorin der technischen Wissenschaften

submitted to

Graz University of Technology

Supervisor:
Ao.Univ.-Prof. Dipl.-Ing. Dr.techn. Gerald Kothleitner
Institute of Electron Microscopy and Nanoanalysis

Graz, October 2019

AFFIDAVIT

I declare that I have authored this thesis independently, that I have not used other than the declared sources/resources, and that I have explicitly indicated all material which has been quoted either literally or by content from the sources used. The text document uploaded to TUGRAZonline is identical to the present doctoral thesis.

Date	Signature

This is the page which is usually filled with one wise quote. Weirdly enough I have spent a great amount of time pondering, which quote is worthy of filling this page - this one very special page allowing me to share something personal and meaningful. As I tremendously enjoy a great laugh, part of me wanted to fill this page just with ***"42"*** (**Douglas Adams**). But then again, the number *23,* due to its prominence in my life would be far more worthy of filling this page, but can unfortunately not be quoted.

A quote of ***Friends*** would have been nice, as there seems to be a Friends-quote fitting for almost any situation in life, but apparently not for the beginning of a PhD-thesis. Thought about it, but "***~~Joey~~ Angie does not share food***", doesn't seem ideal…

As a kid I was inspired by a graffiti I came across: "*The only reality is imagination*". But I figured this could give the wrong impression. "***Imagination is more important than knowledge. Knowledge is limited. Imagination encircles the world.***" Would be a more sophisticated version also highlighting the value of imagination, but it seems a little too posh and unimaginative (for a physicist) to quote **Albert Einstein.**

Roald Dahl, J.K. Rowling (also Robert Galbraith) and Sempé & Goscinny, I would have loved to quote, as their imagination, witty observation, and brutally direct to satiric words made me laugh, cry and hope and probably also shaped my character. But then again, neither an instruction on how to spot a real witch, nor a statement like "*Ils sont fous, les adultes!*" seemed quite right at this point.

There are some very wise words I came across in French class as a teenager, when we had to read this book by **Antoine de Saint Exupéry**, which turned out to be pretty inspiring, if you managed to look past the fact, that reading it was a school assignment. I was captured by the snake, who ate the elephant. But I will never forget the words "***on ne voit bien qu'avec le cœur. L'essentiel est invisible pour les yeux.***" for their truth, and my belief that the world would be a better place, if people lived by these words.

I could stop at this point. But if you care to read on, I would also like to share something personal with you. Some quick snapshots of what makes me feel alive:

Putting myself out there, I am thinking of running in the woods: Inhaling air, as fresh as it can be. Letting the sounds of birds and the beauty of the sunlight trickling through the leaves soothe my soul. Feeling strength and also some pride in the victory of having climbed yet another hill in running stride. …But "I" am also rushing down a slope on skis. Carved turns, loving how my body is pressed by forces described by physics, when going through a compression. Another ride in soft fresh snow, my ski tips hanging over the edge, while I slightly push myself forward and gravity's pull makes me feel like I am falling I realize there's no way back, so I'll better make it a good one. Trying to be brave and nimble. Loving the dynamic evolving when the rhythm is just right, and the energy of one curve throws you into the next. …Music flooding through my body, which moves automatically, and the world feels just right, when dancing. …Laughing with friends. …savouring (NOT sharing ;)) gorgeous food. …Hugging a loved one. …Enjoying the company of family. …FEELING. LOVING. LIVING.

Never give up. Life is a series of challenges waiting to be mastered. When a curve balls hits you, priorities might switch. What used to be important may not be relevant, as new challenges await you. And you will master them. …master them millimetre by millimetre or step by step. Because you are lucky enough to live, love and feel. Enjoy every second of it. Appreciate the millions of little pleasures life is made up of. And never forget those wise words the fox told the little prince.

Abstract

To reduce complexity perfection is widely assumed when describing materials. Material systems are tailored as closely as possible to suit a model that can easily be measured, explained and calculated. Nature, however, does not always follow the human understanding of perfection. Neither do real life materials used in industrial applications. The goal of this work was to make use of and to further develop experimental methods to enable the understanding of real life materials - instead of model systems – down to the atomic scale. Therefore method development and improvement in quantitative analytical scanning transmission electron microscopy (STEM), especially concerning analytical tomographic techniques, but also including STEM simulations was performed. These developments were fruitfully applied to an industrially cast AlMg4Sc0.4Zr0.12 aluminium alloy, which was investigated following different heat treatment procedures: Quantitative analytical electron tomography revealed that the composition of the ordered $L1_2$ precipitates exhibited unexpected deviations from prefect stoichiometry. These deviations and the interplay of ordering, Gibbs energies and activation energies acting upon it were found to lead to Al networks within the $Al_3(Sc,Zr)$ precipitate, with widths down to single atomic columns. Thermodynamic calculations and simulations confirmed the atomic-scale spinodal decomposition within the nanoprecipitates and its energetic advantage. Such networks influence the diffusion process within the precipitates and thus are responsible for their final structure and composition. Experimental findings further indicated a self-limiting diffusion process taking place within the nanoprecipitates. Possible other consequences of the discovered atomic scale network, or its counterpart – an agglomerate of nanoprecipitates - and the quantum character of the one dimensional diffusion are yet to be investigated. Beyond that the discovered structures and processes are a prime example of the novel findings enabled by improving experimental methods to allow the investigation of non-idealised material systems in highest detail.

Kurzfassung

Zur Verringerung der Komplexität wird bei der Beschreibung von Materialien häufig Perfektion angenommen. Materialsysteme werden so nahe wie möglich auf ein Model zugeschnitten, welches einfach gemessen, erklärt und berechnet werden kann. Die Natur folgt allerdings nicht immer dem menschlichen Verständnis von Perfektion, genauso wenig, wie Materialien, die in industriellen Applikationen Anwendung finden. Ziel dieser Arbeit war es experimentelle Methoden zu benutzen und weiter zu entwickeln um reale Materialien – statt Modellsysteme – bis zur atomaren Skala zu verstehen. Dafür wurden im Bereich der quantitativen analytischen Rastertransmissions-elektronenmikroskopie (STEM) Methoden entwickelt und verbessert, insbesondere bezüglich analytisch-tomografischer Techniken, aber auch im Bereich der STEM Simulationen. Diese Entwicklungen wurden erfolgreich an einer industriell gegossenen AlMg4Sc0.4Zr0.12 Aluminium-legierung, welche nach unterschiedlichen Wärmebehandlungen untersucht wurde, angewandt: Quantitative analytische Elektronentomografie zeigte unerwartete Abweichungen der Zusammensetzung der geordneten $L1_2$ - Ausscheidung von der perfekten Stöchiometrie. Es wurde entdeckt, dass diese Abweichungen zusammen mit der darauf wirkenden Wechselwirkung von Ordnung, Gibbs-Energien und Aktivierungsenergien zu Al-Netzwerken in den Al_3(Sc,Zr)-Ausscheidungen führen, die bis zu einzelnen Atomsäulen schmal sein können. Thermodynamische Berechnungen und Simulationen bestätigten die spinodale Entmischung auf atomarer Ebene in Nanoausscheidungen und dessen energetischen Vorteil. Solche Netzwerke beeinflussen Diffusionsprozesse in den Ausscheidungen. Experimentelle Ergebnisse deuteten weiters auf einen selbst limitierenden Diffusionsprozess innerhalb der Nanoausscheidungen hin. Mögliche andere Konsequenzen eines Netzwerks auf atomarer Ebene, oder seines Gegenstücks - eines Agglomerates von Nanoausscheidungen, sowie der Quantencharakter der eindimensionalen Diffusion sind noch zu erkunden. Darüber hinaus sind die entdeckten Strukturen und Prozesse ein Paradebeispiel dafür, wie die Weiterentwicklung von experimentellen Methoden, welche die Untersuchung von nicht idealisierten Materialsystemen in höchstem Detail erlauben, neue Erkenntnisse ermöglicht.

Acknowledgements

First of all I would like to thank the **Austrian Cooperative Research (ACR)** for the finicial support of this thesis and my research stay at Monash and Melbourne University.

Next I would like to thank my supervisor, **Prof. Gerald Kothleitner**. I especially appreciated the freedom he gave me within my work to follow my interests and instincts. It was very exciting and fulfilling to be allowed to dig myself into the fascinating discrepancies which came up while investigating the industrially cast AlMgScZr alloy. Being able to discover the atomic scale spinodal decomposition was a highlight of my life, only enabled by these liberties. Thank you very much! I also really want to thank you, for believing in this work the way you did, resulting in its publication in *Nature Materials*.

A great thank you also goes to **Prof. Ferdinand Hofer** – head of the institute, obviously, for allowing and supporting my work at FELMI-ZFE. But I also want to express my happiness, about his initiative and support of my research stay in Australia. Additionally, the support of social activities, like weekly beach volleyball, the trips and parties brought us all together and made the FELMI-ZFE such a nice working environment.

My **colleagues at FELMI-ZFE** earn a double thank you! First of all for being such amazing companions, and friends. You put joy into my life every single day! In the context of work I would like to especially thank **Martina Dienstleder**, **Roland Schmied** and **Georg Haberfehlner** for teaching me how to prepare my tomography-samples at the FIB and basically drying my tears in the process. (Special thanks to Martina in that respect.) A big round of applause should go to Georg, as the FIB-tips were only a small part of the support he gave me. The software package for tomographic alignment and reconstruction (ToReAl) he wrote, was an essential basis for my work. Martina, **Manuel Paller and the lab team** prepared the samples for non-tomographic investigations. Special thanks, Martina, for the sample preparation for in-situ experiments. A big thanks to everybody for a little help here, and a little advice there.

The cooperation with the *Institute of Material Science, Joining and Forming* at TU Graz was not only extremely fruitful, but also extremely pleasant, due to your great personalities. Thank you very much, **Johannes Taendl, Cecilia M. Poletti** and **Bernhard Sonderegger**. Johannes and Cecilia delivered the samples, shard information and knowledge on the system and took part in the discussions, when the first ideas of a spinodal decomposition and a self-limiting diffusion process came up. Bernhard Sonderegger was the expert who then came in for simulations. He programmed the atomisitic 3D diffusion simulation, supported and guided me when programming the 2D diffusion simulation and also programmed the initial Gibbs energy calculation, which I then adapted.

Another great thanks goes to the people from Monash and Melbourne University, where I was allowed to research for 2 wonderful months. Thank you, **Matt Weyland, Joanne Etheridge, Scott Findlay** and **Les Allen,** and many more, not only for the knowledge and time you shared with me, but especially for making me feel so welcome, even at home. Matt, thank you for inviting me over for Christmas. Joanne, thanks for introducing me to surfing (at the Great Ocean Road).

Finally the most enormous THANKS goes to my parents, **Anton** and **Irmgard Orthacker**, and my boyfriend **Michael Pachler** for your love. You guys supported me. No complaints, when I missed birthday parties or trips, because I had to work on my thesis. No complaints, for all those week-ends,

evenings and holidays where I didn't have time for you. No complaints, all those times my thesis came first. You were so understanding. Things are gonna change. Once this is finally done, I'll make so much time for you, you're gonna get annoyed by me. I promise. Michi, thank you also for letting me occupy your computer (for many, many, many hours), when mine didn't do the job. Sorry, my simulations might have killed your graphics card. (I am still denying it. You have no proof. But just in case you are right… …Sorry.)

Table of Contents

Table of Contents

1 Introduction

Creating strong, yet light and shapeable materials has always been an important skill and has not lost significance up to the present day as awareness rises that our energy consumption has an influence on the planet we live on and therefore ultimately also on our quality of life. At the same time we got used to and do not want to give up on certain luxuries for example concerning mobility. How can all those desires be reconciled? One way to reduce fuel or energy consumption is by building airplanes and cars made of lighter materials. For safety reasons the materials nevertheless should not suffer in strength. Therefore, ongoing research on mechanically strengthening light alloys is of major importance. Concerning the class of alloys gaining their strength from nanoprecipitates a clearer understanding of their formation and mode of action has been won in the last decades through the development and improvement of new techniques especially in the field of transmission electron microscopy.

For a thorough understanding of a material, investigations at the nanoscale are often essential. Analytical techniques like electron energy loss spectroscopy (EELS) and energy dispersive X-ray spectroscopy (EDXS) in scanning transmission electron microscopy (STEM) can reveal important chemical information necessary for the development and improvement of high-tech materials. The integrative character of the signal acquired through transmission, however, might hide important structural details of the material, relevant for its properties. Those details can be revealed through electron tomography, where data is acquired at different tilt angles and, after alignment, reconstructed to form a full 3D model of the material under investigation. The combination of both techniques, analytical STEM and tomography, gives full insight into structure and composition of a material.

This thesis consists of three parts, starting with the fundamentals (part I). The basics of the experimental methods and the instrumentation used are treated in chapter 2. Chapter 3 gives a material scientific overview, treating the AlMgScZr alloy, which played a major role in this thesis, and the thermodynamic basis of solid-state diffusion. Part II (chapters 4 to 7) is devoted to the development, improvement and evaluation of methods. Analytical tomography as a quantitative tool was evaluated and improved. A method allowing the utilisation of simulation tools for more general purposes including defects was created. Additionally a method allowing the calculation of atomic column elemental concentrations with minimised influence of channelling conditions was developed. Part III treats the experimental and theoretical investigation of an AlMgScZr alloy in collaboration with the Institute of Material Science, Joining and Forming. This investigation spanning a large methodical range including analytical tomographic scanning transmission electron microscopy, quantum excitation of phonons simulations as well as thermodynamic calculations and simulations lead to the discovery of diffusion defining atomic scale spinodal decomposition.

Part I - Fundamentals

2 Experimental Methods and Instrumentation

2.1 (Scanning) Transmission Electron Microscopy ((S)TEM)

In a quick overview we shall start with the basics of microscopy, advancing via electron microscopy and finally treating transmission electron microscopic techniques (TEM), with a special focus on scanning transmission electron microscopy (STEM) including analytical techniques.

Observation with the visual sense is a very important tool in many fields of science. But many scientific questions cannot be answered by observing only what the human eyes can resolve, which is about 0.1 – 0.2 mm[1]. The first method of choice to overcome that problem is using an optical microscope. If we neglect special techniques which e.g. make use of non-linear optics, this allows us to observe objects down to the size of a few hundred nm. This is ultimately defined by the diffraction limit, which states that the minimum distance *d* of two sources emitting with the wavelength λ can be brought together, while still being perceived as separate equals:

$$d = 0.61 * \frac{\lambda}{n * \sin(\alpha)} \tag{1}$$

α is the convergence half-angle of the light entering the objective lens. *n* is the refractive index of the medium between objects and objective lens. The basis of this is the Huygens-Fresnel principle, stating that every point on a wave front is the source of spherical wavelets, which interfere with each other. The description of interference resulting from diffraction at a circular aperture via Bessel-functions leads to a circular symmetric solution for intensity that gives a central bright disc (Airy disc), which is surrounded by rings of higher and lower intensity. The Rayleigh criterion then defines the minimum distance of two sources to still be resolved as that where the centre of the Airy disc of the one point falls in the first minimum of the other.[1,2] With the radius of the Airy disc being:

$$r = 0.61 * \frac{\lambda}{n * \sin(\alpha)} \tag{2}$$

we receive equation 1.

In a first approximation we want to neglect aberrations, which will be treated in section 2.1.3 Therefore the resolution is ultimately limited by the wavelength of visible light (which equals several hundred nm), unless another radiation source is used, e.g. electrons.

The wave-particle dualism states that particles have wave-like characteristics. The wavelength

$$\lambda = \frac{h}{m * v} \tag{3}$$

with *h* being Planck's constant, *m* the mass of the particle and *v* the particle's velocity can be attributed to the particle. If the electrons are regarded as waves, energy E transfers to wavelength λ via

$$\lambda = \frac{h}{\sqrt{2meE}} \tag{4}$$

Therefore an electron beam made up of electrons with the same energy *E* can be regarded as an electron wave with a certain wavelength λ.

Electrons proved to be an excellent choice for imaging for several reasons: 1) The possibility to control their paths and velocities by using electromagnetic fields. 2) The (via voltage) easily tuneable velocity of electrons allows an easy adjustment of wavelength – even small enough to image single atoms. 3) The small mass of electrons compared to ions keeping the risk of sample damage e.g. through sputtering comparably low.

Therefore electron microscopes of all kinds belong to the most important tools for investigations of phenomena too small to be observed via visible light. Imaging morphology and structure in the nano- and pico-world represents only a small part of the possible investigations that can be performed in and with electron microscopes. Analytical methods, like for example the analysis of emitted X-rays, or the energy-loss of electrons passing through the sample allow conclusions on the chemical composition of the samples. This will be treated in chapter 2.2.

Electrons can be used to investigate sample surfaces, or be used in transmission to investigate very thin samples (ideally below 100nm). The resolution in electron microscopy is limited to a great part by the interaction volume of the electrons in the sample. When the electrons enter the sample they will be scattered through different mechanisms. For very thin samples this interaction volume can be strongly reduced allowing atomic resolution in transmission, whereas the interaction volume will reduce the resolution for bulk samples to several nm, as schematically shown in Figure 1.

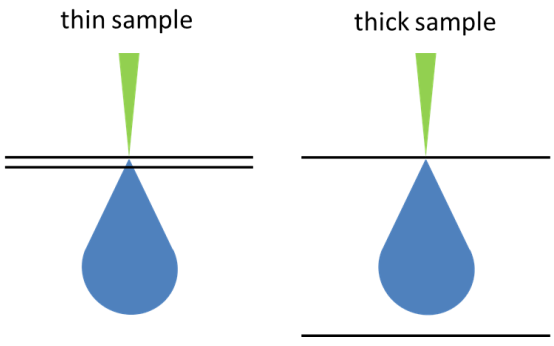

Figure 1: Sketch of the interaction volume of electrons with matter, explaining why the investigation of thin samples in TEM enables a far better resolution than the investigation of thicker samples, as usually investigated in SEM.

This divides electron microscopic techniques into two categories: scanning electron microscopy (SEM) and transmission electron microscopy (TEM). In SEM bulk samples are investigated with an electron beam which is scanned over the sample and the main sources of imaging are secondary electrons and backscattered electrons. As SEM was only minimally used in this thesis as a part of the

dual beam system used for sample preparation (see chapter 2.5.2), it will not be discussed further at this point. In transmission electron microscopy (TEM) very thin samples are investigated and for imaging primarily electrons which passed through the sample – forward scattered electrons - are used. TEM can further be divided into conventional TEM and scanning TEM (STEM). While in STEM a beam is scanned over a sample area - just the way it is in SEM – and at each scanning point signals are detected, which can then be used to form an image, the image formation in TEM can rather be compared to a light microscope, as a sample area is illuminated with a broadened beam and the image that will finally be magnified on a fluorescent viewing screen, is that of the electrons which have passed through the sample. Figure 2 schematically shows the difference between all those techniques described above.

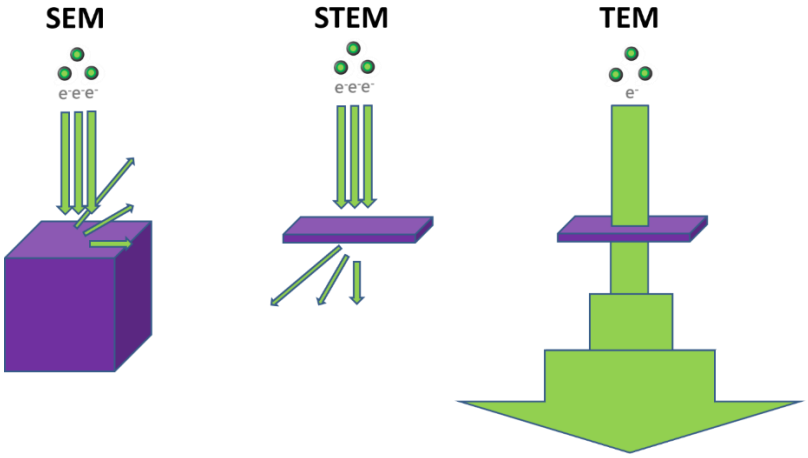

Figure 2: The basic principles of SEM, STEM and TEM imaging.

2.1.1 The Interaction of Electrons and Matter

In order to understand the manifold of signals and imaging techniques used in electron microscopy, the different interaction processes that occur, when an electron passes through matter need to be understood. If electrons are regarded as particles scattering can be divided into two types of processes: elastic and inelastic scattering. Elastic scattering is an interaction process, where the energy of the electron remains constant, thus no energy is exchanged between electron and sample. Merely the direction of the electron trajectory is changed. If inelastic scattering takes place the energy of the electron does not remain constant. Mostly the electron loses energy, which is transferred to an atom within the sample. This now excited atom can again give off the excess energy through various processes.

While an elastic scattering process only enables detection via scattering angle inelastic scattering processes lead to a manifold of signals which can be detected. Signals acquired from elastically scattered electrons are further discussed in sections 2.1.2 and 2.1.3. The manifold of detection mechanisms used for inelastically scattered electrons is discussed in section 2.2.

2.1.2 Transmission Electron Microscopy (TEM)

In conventional TEM whole sample areas are illuminated with a spread – nearly parallel - electron beam, which passes through the sample. The objective lens system forms an image, which is magnified and projected onto the viewing screen or CCD camera. This image, which can even have atomic resolution, is a result of the phase change the electron wave undergoes when passing through the sample. Therefore the image is often not easily interpretable. Contrast can be enhanced

by inserting an objective aperture, which is placed in the back focal plane. This aperture (if correctly centred) will cut off parts of the electron beam which are diffracted into angles higher than those allowed by the aperture, thus limiting the angular range of diffraction. The centred aperture can be used to only allow the non-diffracted central beam to contribute to the image. Imaging in this mode is called bright field (BF) imaging. In contrast the objective aperture can also be used to select a diffracted beam instead. This is then called dark field imaging. Figure 3 shows a bright field image and 8 corresponding dark field images (from a silicon (Si) sample covered in Si and germanium (Ge) domes), each acquired by choosing a different spot with the objective aperture.

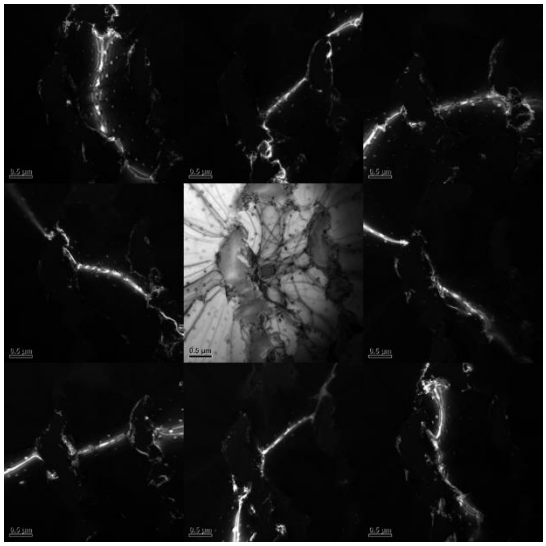

Figure 3: Bright field image (centre) and several dark field images of the same sample region obtained by selecting the nearest surrounding spots, one at a time.

An intermediate lens between the objective lens and the projector lens system enables to choose whether an image or a diffraction pattern is projected on the screen. In conventional TEM mode this lens will project an image onto the focal plane of the projector lens. In diffraction mode the strength of the intermediate lens is changed, so that the diffraction pattern is in the focal plane of the projector lens system and subsequently visible on the viewing screen. The diffraction mode in TEM can be useful to get information on the crystal structure, but as it was not used to collect the findings of this thesis, it will not be discussed further.

2.1.3 Scanning Transmission Electron Microscopy (STEM)

In STEM a finely focussed electron beam is scanned over the sample and just as in SEM a signal is detected for every scanned point. Finally these signals are put together to an image. Figure 4 shows a schematic overview of a STEM with a configuration like the Austrian Scanning Transmission Electron Microscope (ASTEM) – the instrument used for tomographic and analytical (tomographic) STEM investigations in this thesis.

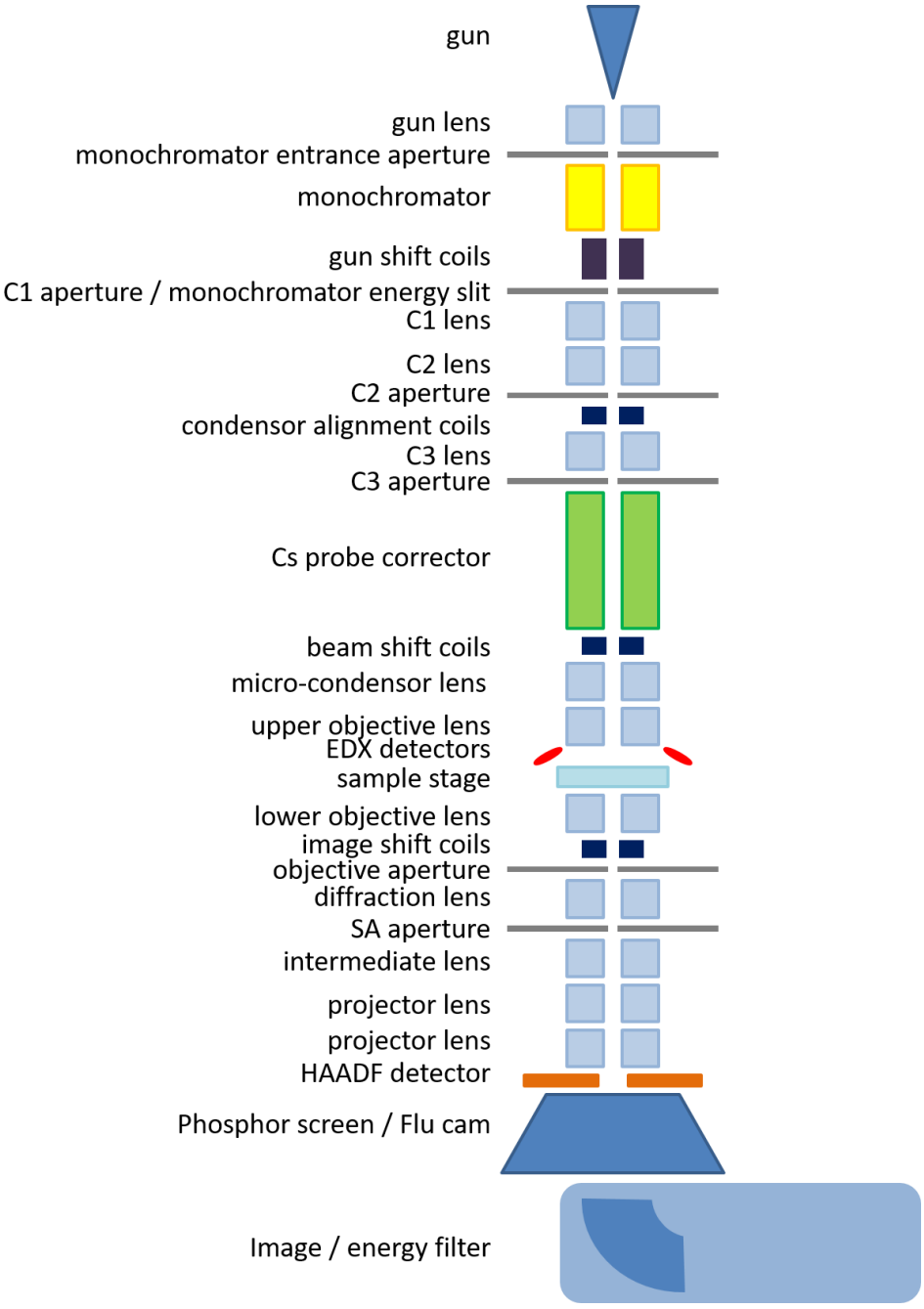

Figure 4: Schematic overview of a scanning transmission electron microscope equipped with a monochromator, a Cs probe corrector an EDX detector system and post column image / energy filter.

The ASTEM is a monochromated, probe corrected FEI Titan^3 (60-300kV) equipped with a Super-X EDX detector and a Gatan Imaging Filter (both will be explained in more detail later), configured to offer ideal conditions for high resolution analytical STEM. Nevertheless, the ASTEM is not a dedicated STEM, but can also be used in TEM mode including energy filtered TEM (see section 2.2.2). During this thesis, however, the (energy filtered) TEM investigations were performed on another instrument: A Tecnai F20 (fomer FEI – now Thermo Fisher), also equipped with a monochromator, an EDX detector (both of which were not used for the work done for this thesis) and a post column energy filter.

The gun in the ASTEM is a Schottky-FEG, which combines high temperature with electric potential for the extraction of electrons. It does not reach the brightness (current density per unit solid angle) and

small energy spread a cold FEG can deliver, but has higher stability and is less sensitive to contamination.[1] The small energy spread is primarily important for a good energy resolution when doing electron energy loss spectroscopy (see section 2.2.1), but also improves STEM image resolution, as the probe is less enlarged by chromatic aberrations. As the system is equipped with a monochromator the energy spread can be reduced right after the source. Even if the monochromator is not used for this purpose, it needs to be adjusted for ideal beam conditions and can be used to adjust the beam intensity. After the gun shift coils, with which the virtual source can be placed on the optical axis, comes the monochromator energy selection slit, or the C1 aperture, depending on whether the monochromator is in use. From the following condenser lenses C2 is not used in STEM mode, as this allows a stronger demagnification of the source on the sample (= a smaller probe → enabling higher resolution). This can easily be explained by the following equations and Figure 5: Not using C2 gives a small ratio v_2/u_2 and thus a greater demagnification (*M* is the magnification) of the source on the sample.

$$M = \frac{v}{u} \tag{5}$$

$$d_1 = d_0 \frac{v_1}{u_1} \tag{6}$$

$$d_{final} = d_1 \frac{v_2}{u_2} = d_0 \frac{v_1}{u_1} \frac{v_2}{u_2} \tag{7}$$

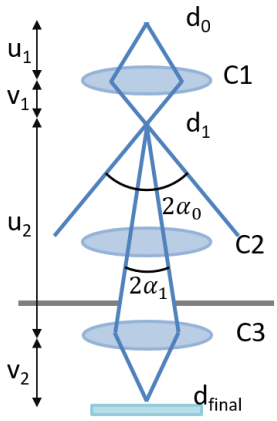

Figure 5: Scheme of demagnification of the source on the sample via the condenser lens system. d_0, d_1 and d_{final} are the diameters of the source and its demagnified images. u_1, v_1, u_2 and v_2 are distances. C1, C2 and C3 are the condenser lenses. α_0 and α_1 are the semi-angles of rays leaving C1 and reaching C3.

For completion it shall be mentioned, that this demagnification (strength of C1 defining α_0) in combination with the condenser aperture (which defines α_1) also leads to a reduced beam intensity:

$$I_{final} = I_0 \left(\frac{\alpha_1}{\alpha_0}\right)^2 \tag{8}$$

The electromagnetic lenses suffer from various aberrations. Astigmatism results from a non-uniform electric field electrons sense when spiralling around the optical axis. It leads to different focus distances for objects orientated in perpendicular directions. This aberration can be corrected by coils

positioned after the lens, called stigmators. Chromatic aberrations (the impact of which can be reduced by having a low spread in beam energy) result from higher energy electrons being focussed at shorter distances than lower energy electrons. Spherical aberrations lead to shorter focus distances for further electrons positioned further from the optical axis.

The problem with electromagnetic lenses is that it is not possible to create lenses without spherical and chromatic aberrations that produce a real image of an object, without charge on the optical axis or temporarily varying fields, which are rotationally symmetric – as shown by Scherzer in 1936.[2] Up to now the condition of non-rotational-symmetry was chosen to correct aberrations. Multipole lens systems are chosen for that purpose. For historical relevance I would like to mention, the two main approaches: A system of two hexapole lenses with two transfer lenses in between was used by Harald Rose and colleagues, who were awarded the Wolf Prize in 2011 for their findings.[3,4] In combination with a Wien type corrector this system allows a simultaneous correction of spherical and chromatic aberrations in images.[4] A combination of quadrupole und octopole lenses are the basis of the Cs corrector which is ascribed to Krivanek.[5]

The probe of the ASTEM is aberration corrected. A hexapole lens system can be tuned with the help of a cross grating (special sample with a well-defined gold pattern, which can be used for calibrations) to reduce astigmatism, coma and higher order aberrations. The best tuning results can be reached, by first reducing the lower order aberrations and adjusting the higher order aberrations only after these deliver constantly good results with no further improvement visible, when only adjusting lower order aberrations. This enables atomic resolution STEM investigations.

High precision movement and tilt of the stage as well as high stability are not only important for high resolution imaging but also especially important for tomographic investigations, to ensure the region of interest stays in the imaged area throughout the tilt series. Analytical investigations, especially EDX spectrum images (see chapters 2.2.3 and 2.2.4) require an extremely high stability to avoid image distortion due to sample drift while collecting sufficient signal. Consequently the combination of analytical methods with tomography raises high demands to the stage. It can be helpful to wait a few minutes between loading the sample and preparing acquisition to allow thermal drift to minimise.

Usually STEM is performed when the microscope is in diffraction mode. As the beam in STEM is not parallel, but spans an angular range (or range of k-vectors) described by the convergence angle, which is determined by the condenser aperture, instead of diffraction spots diffraction discs form. See Figure 6. Either bright field signals (originating from the non-diffracted disc, or dark field signals (originating from diffracted discs) can be detected in the diffraction plane. A variety of detectors exist for that purpose, ranging from bright field (BF) – which collects the intensity of the forward scattered beam - over annular bright field (ABF) and annular dark field (ADF) all the way to high angle annular dark field (HAADF) – collecting signals from increasingly higher scattering angles - schematically shown in Figure 6.

In contrast to TEM images STEM images are made up pixel by pixel, while the beam is scanned over a sample region. The value (or brightness) of each pixel representing the scattered intensity measured by a certain detector, while the beam was on a certain location on the sample, represented by that pixel. Depending on the detector, this stands for the amount of electrons scattered (or diffracted) into a certain angular range. BD and (HA)ADF detectors will basically give complementary

information: Electrons scattered away from the BF detector into higher angles can be detected by a DF detector. Thus regions where a lot of scattering into higher angles occurs will appear dark in an image retrieved from the BF detector and bright in an ADF or HAADF image, depending on the scattering angle. The opposite holds for regions where little scattering into high angles takes place – they will appear bright in the BF images and dark in (HA)ADF images.

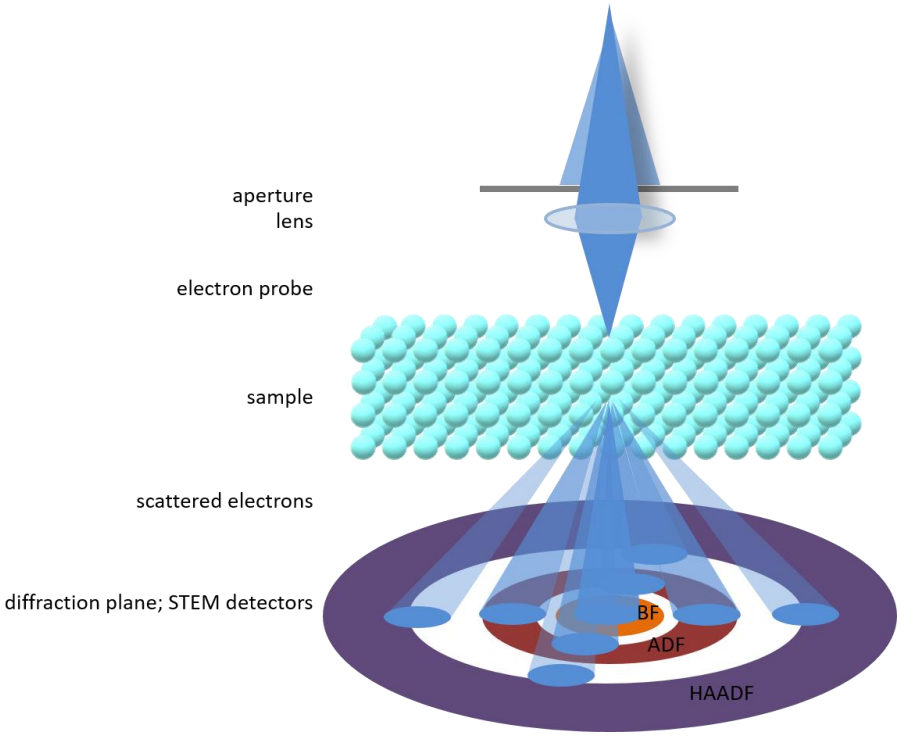

Figure 6: Scheme of scattering of electrons in crystal and STEM detectors. The aperture defines the probe's convergence angle, which determines the size of the discs in the diffraction pattern. The probe is scattered/diffracted in the sample. Dependent on scattering angle range the electrons will be detected by certain detectors.

In detail however BF, ABF and ADF detectors will give signals that are not quite straight forward in interpretation. One reason therefore is phase contrast, resulting from interference of coherently scattered electrons which experience a phase change due to the crystal potential. Another reason ABF and ADF signals can be ambiguous is that they result from "intermediate" scattering angles, which is less intuitive than the signal from the unscattered / forward scatted beam, or very high angle scattering. The probably most intuitive and straight-forwardly interpretable of those signals is the HAADF signal. This is on the one hand due to insensitivity to phase, resulting not only from reduced coherence for high angle scattering, but significantly also from the elimination of phase information due to the signal integration over a large area. On the other hand the HAADF signal is intuitive as it greatly depends on the atomic number (Z) of the material investigated. Scattering to high angles mostly occurs as a result of an electron closely passing a nucleus[6]. This can be described by the Rutherford model, which offers equation 9 for screened (relevant so that $\sigma(\theta)$ does not go to infinity when Θ approaches 0) relativistic differential cross-sections.

$$\frac{d\sigma(\theta)}{d\Omega} = \frac{\lambda_R^4 Z^2}{64\pi^4 a_0^2 \left[sin^2\frac{\theta}{2} + \left(\frac{\theta_0}{2}\right)^2\right]^2} \tag{9}$$

with

$$\theta_0 = \frac{0.117 Z^{\frac{1}{3}}}{E_0^{\frac{1}{3}}} \tag{10}$$

The integration of Ω from Θ to π then delivers equation 11 giving the cross section of electrons elastically scattered into angles > Θ.[1,6,7]

$$\sigma(\theta) = 1.62 * 10^{-24} N_0 \frac{\rho t}{A} \left(\frac{Z}{E_0}\right)^2 cot^2 \frac{\theta}{2} \tag{11}$$

We see that in theory the relation between intensity (I) and Z is $I \sim Z^2$. It can further be seen that in general a high intensity in an HAADF image corresponds to a high Z, or a high sample thickness or density. This model shows good agreeance for high angles Θ, beam energies up to 300 kV and elements with $Z \leq 30$.[1]

For scattering in high angles the electrons have to pass the nucleus very closely, meaning only the sharp parts of the potential are effective. Therefore the atoms scatter independently from each other in this angular range. The intensity in an HAADF image can thus be described via the convolution of the object function O(r), describing the crystal via an array of these sharp scattering cross sections, and the probe intensity profile $|P(\boldsymbol{r})|^2$, as schematically shown in Figure 7.[8]

$$I(\boldsymbol{r}) = O\,(\boldsymbol{r}) * |P(\boldsymbol{r})|^2 \tag{12}$$

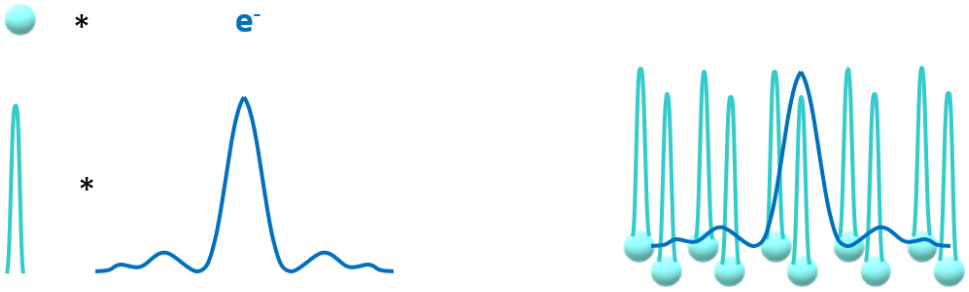

Figure 7: Scheme of convolution of object function and probe intensity profile delivering HAADF image intensity.

An HAADF image therefore is a representation of the object, blurred by the probe. (If the probe were a perfect point, which can be mathematically described by a delta function, the resulting image would be a perfect representation of the object.) Changing the probe's focus will blur or "unblur" the image, but not change the contrast, as it might in coherent imaging.[8] While the phase contrast transfer function (PCTF), which describes the contrast as a function of spatial frequency in conventional TEM has several zeros, the incoherent object transfer function (OTF) – describing the contrast of incoherent signals such as HAADF STEM - decreases monotonically, not exhibiting such an oscillatory behaviour around zero.[2] This enables (easily interpretable) imaging even at high spatial frequencies (distances below 100 pm).

Figure 8 shows examples of HAADF images. In the image on the left an intensity change with thickness (left to centre) and average Z (cluster of spherical precipitates) can be seen. Atomic resolution STEM images as shown in Figure 8 on the right are easily interpretable due to this behaviour of the OTF. Such images are possible as probe corrected systems allow to generate a

probe function fine enough to resolve neighbouring atoms. The Z^2 dependence allows the quick interpretation, that the brightly appearing atomic columns are heavier than those of the matrix.

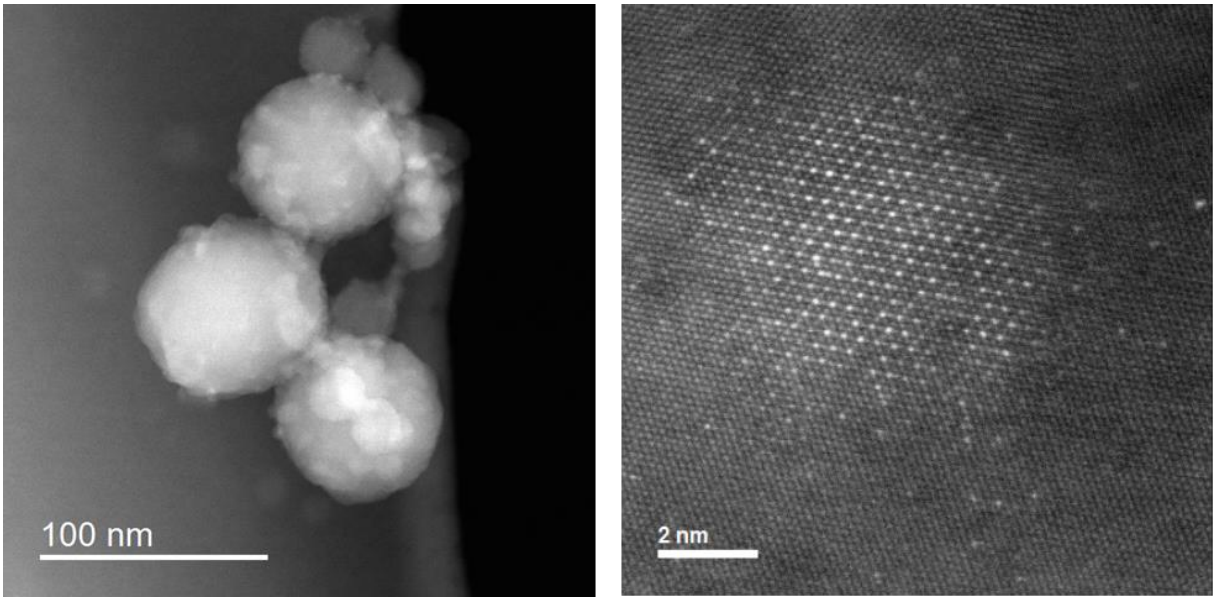

Figure 8: HAADF images; left: Overview image showing spherical precipitates with a higher average Z value than the matrix; right: High resolution image of a precipitate which coherently matches the matrix, with atomic columns of higher average Z value than that of the matrix.

It shall also be mentioned that a further advantage of HAADF signal compared to BF signal is the possibility to simultaneously perform electron energy loss spectroscopy (see chapter 2.2.1) with a post column energy filter. This, together with the possibilities of intuitive interpretation described above, was the reason HAADF was the most used imaging mode during the investigations of this thesis.

The two most common STEM detector types (also used in the tools utilised for this thesis) are the semiconductor detector and the scintillator based detector. A fluorescent material with a quick emission decay (for low detector response times) like e.g. Ce doped yttrium-aluminium-garnet (YAG) is used in a scintillator detector to convert the incoming electron to visible light. After travelling through a light pipe this signal is amplified by a photomultiplier system. In a semiconductor detector electron hole pairs are generated in a doped Si-single crystal by the incoming electron. They are separated either by the internal bias of the p-n junction or by an external reverse bias and finally converted to a current in an external circuit. The scintillator has a higher gain and a better detection quantum efficiency (DQE – see equation 13) for low intensity signals than the semiconductor detector, but is less robust (more prone to radiation damage). It is also more bulky and expensive than a semiconductor detector.[1]

$$DQE = \frac{\left(\frac{S_{out}}{N_{out}}\right)^2}{\left(\frac{S_{in}}{N_{in}}\right)^2} \tag{13}$$

2.2 Analytical Methods of (S)TEM

Instead of using the collection and detection of electrons scattered into different angles to perform imaging, inelastically scattered electrons and products from follow-up processes can be detected. Figure 9 shows a scheme of the different signals that can be obtained during STEM which are relevant for this thesis. Electron energy loss spectroscopy (EELS) and energy dispersive X-ray (EDX) spectroscopy are signals that result from the same initial process, where an incoming electron ionizes an atom and thereby suffers an energy loss. In case of EELS this energy-loss is detected, whereas in case of EDX spectroscopy the X-rays emitted by the atom as it relaxes are detected .[1,9] Both methods offer compositional information, but can act complimentarily, as light elements can be hard to detect with EDX, but are generally unproblematic with EELS, while the situation is reversed for heavy elements.

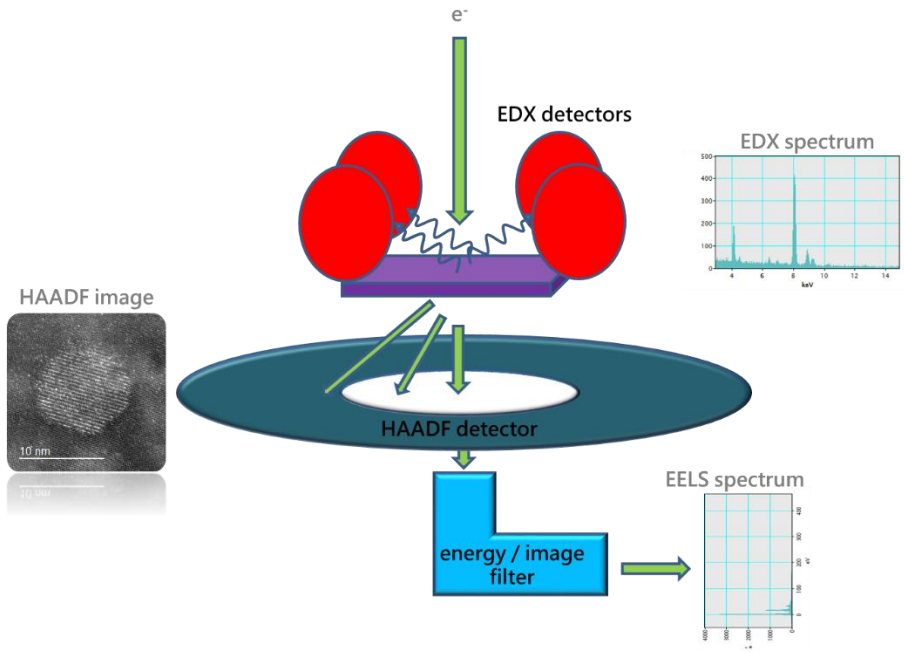

Figure 9: Scheme of signals obtained in STEM mode, which are relevant in this thesis.

2.2.1 Electron Energy Loss Spectroscopy (EELS)

Similar to how a prism can be used to create a spectrum from visible light, a spectrum can also be created from electrons, using electromagnetic lenses, which deflect the electrons according to energy. A charged particle moving in a magnetic field experiences a force perpendicular to its direction of movement and in magnitude directly proportional to its velocity and thus dependent on its energy, the Lorentz force:

$$F = q(E + v \times B) \tag{14}$$

A typical EELS spectrum will have a zero-loss peak, a Gaussian-shaped peak that usually has the highest intensity and represents the electrons that did not suffer a significant[i] energy loss while passing through the sample. The width of this peak depends on the type of source and if a

[i] only very small energy losses e.g. due to phonons, which are collective oscillations of atoms which lead to energy losses < 0.1 eV[1]

monochromator is used or not. A very high and narrow zero-loss peak (implying good energy resolution) is desirable. This region is followed by the low loss region, which is dominated by plasmon interactions, which typically also have a Gaussian characteristic. The characteristic features used for the identification of elements within the sample are ionization edges. While the shapes of those can vary, they do not have a Gaussian appearance, but they start at a specific energy. This marks the minimum energy necessary to eject an electron from its shell into vacuum. Toward the high loss side of each edge the intensity decreases gradually, as the electrons can have any access velocity, when ejected from their shell, allowing an arbitrarily high energy transfer from the incoming electron, thus an arbitrarily high energy loss (but not arbitrarily low). By performing fits for the background and determining the amount of signal at specific edges elemental compositions can be determined.

Not only the summed intensity at an edge carries information, but also the shape of the edge. The fine structure e.g. allows conclusions on the binding of the atoms.[1,9] EELS spectra are mostly acquired in STEM mode, to be site specific.

The ASTEM is equipped with a GIF Quantum. This is an energy filter that allows dual EELS, which is the nearly simultaneous acquisition of two EELS energy ranges with independent exposure control at a rate of up to 1000 spectra per second.[10] This technique is very useful if edges of interest are at very high energy loss, because the zero-loss and low-loss region, which contains information about thickness, valance state and band-gap and is necessary for absolute quantification, can also be acquired. This is technically possible with a very quick shutter, a shift in energy via the drift tube and the horizontal split of the CCD, using top and bottom half for the exposure with one type of spectrum each.[10] Acquisition of the additional low-loss spectrum via dual EELS does not increase the acquisition time noticeably, as the time for exposure of the low-loss is in the range of 1 µs, shutter time around 10 µs compared to the high loss with an exposure in the range of 1 ms.[10] Figure 10 shows an example of a dual EELS spectrum.

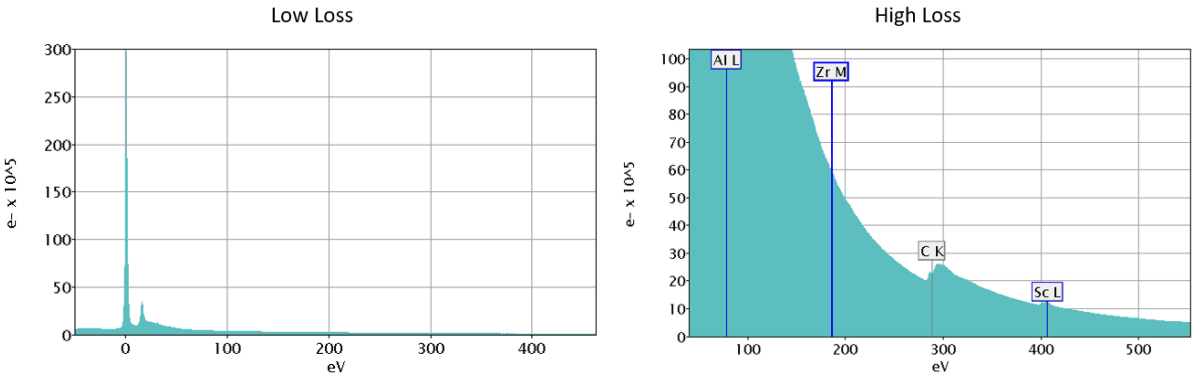

Figure 10: Example of a dual EELS spectrum acquired from an aluminium alloy. The Low-Loss region is shown on the left, the high loss region is shown on the right.

2.2.2 Energy Filtered Transmission Electron Microscopy (EFTEM)

The energy loss electrons suffer during interaction with the sample can also be put to use in TEM imaging mode. In energy filtered TEM (EFTEM) not the spectrum is acquired, but electrons in a certain energy range are selected from the spectrum with a variable slit before forming an image on a camera. This energy choice gives rise to several interesting applications.

TEM zero loss filtering increases contrast by using only elastically scattered electrons for imaging. An image including inelastically scattered electrons suffers from increased blurring through chromatic

aberration, as those electrons vary in energy. The blur results from a displacement d that the electrons may suffer from, which is given by

$$d = C_c \frac{\Delta E}{E} \beta \tag{15}$$

Where C_c is the chromatic aberration constant which is a characteristic of the lens system, ΔE the range of energies of the contributing electrons, E the primary beam energy and β the collection angle of the objective aperture.[1] Consequently the contrast cannot only be improved by choosing a small objective aperture, but also by reducing the range of energies of contributing electrons. If the region of electrons used for imaging is chosen by selecting an energy region of ΔE around the zero loss peak, this technique is called zero-loss filtering.

By acquiring filtered and unfiltered images from the same sample area thickness maps (t/λ) can be created, as the amount of inelastically scattered electrons depends on the thickness t of the sample. The following equation describes the relation:

$$\frac{t}{\lambda} = ln\left(\frac{I_t}{I_0}\right) \tag{16}$$

λ is the inelastic mean free path, I_t and I_0 are the total intensity and the intensity of the zero loss peak only.[11] (This method of thickness determination can also be used in STEM EELS mode.)

Choosing a specific non-zero energy may enhance certain regions of interest in the sample, like e.g. nano-precipitates.

If the distribution of a specific element is to be imaged, filtered images close to an edge in the EELS spectrum corresponding to that element can be used. If a qualitative visualisation of the spatial distribution of a certain element is the goal, jump ratio images are practical. Intensity values cannot quantitatively be related to composition, but jump-ratio images can show higher sensitivity than elemental maps.[12] For this purpose, two images using electrons from certain energy intervals ΔE are acquired, one before the edge I_1, and one after the edge I_2. The division I_2 / I_1 of these images results in an image showing the distribution of the element. If a more quantitative assessment is necessary, the three window method has to be applied. In this case images from not two, but three energy windows are acquired. Two of those three windows are set before the edge, to allow extrapolation of the background to the third window. Subtraction of the background from the post-edge image gives a real intensity estimate of the edge in question.

2.2.3 Energy Dispersive X-Ray Spectroscopy (EDXS)

As described above, in a freshly ionized atom a low energy state is available. This enables an electron to change from a higher energy state to a lower energy state. Thereby energy is set free. One of various possible outlets of energy is the emission of X-rays. These X-rays have specific energies: the difference between the energy of the initial state the electron was in, and the energy of its final state. As the possible energy states, and thus also energy differences are specific for each atom type, an analysis of the energies of the X-rays allows to draw conclusions on the elements present in the material. The correlation between the wavelength of the emitted characteristic X-ray and the atomic number is described by Moseley's law[1,13]:

$$\lambda = \frac{B}{(Z-C)^2} \tag{17}$$

Where λ represents the wavelength of the characteristic X-ray, Z the atomic number of the emitting atom and B and C are constants.

This physical concept is the basis of EDX spectroscopy, where these X-rays are detected, sorted with respect to their energy and counted to gain compositional information. Figure 11 shows an example of an EDX spectrum. The X-axis shows the energy of the detected X-rays, while the y-axis gives the number of X-rays detected in the channel corresponding to that energy.

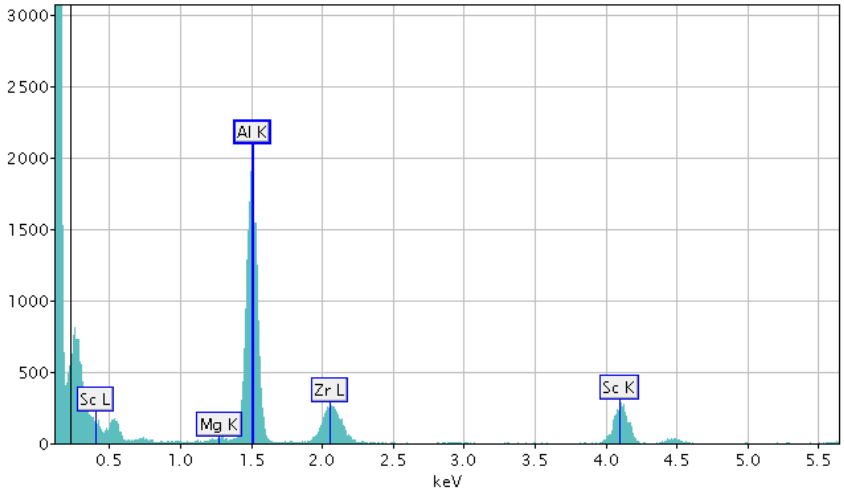

Figure 11: Example of an EDX spectrum acquired from an aluminium alloy.

In the detection lies the first problem of EDX spectroscopy: its inefficiency. X-rays are emitted uniformly in all directions. Therefore most of the X-rays are lost – depending on the solid angle the detector covers (collection angle), only a very small amount of the overall emitted X-rays reaches the detector. Therefore long acquisition times (several minutes) are often necessary for high quality spectra. The thinner the sample, the longer it takes. Long acquisition times however entail the danger of sample damage, especially for thin samples. Inelastic collisions can cause knock-on damage – the displacement of atoms – as well as radiolysis, the breakage of chemical bonds, which is mainly a problem in biological samples of polymers. [1,14–17]

Another difficulty of EDXS is absorption in the sample, which might not only reduce the amount of signal detected, but might even influence elemental concentration quantification. This is not only, due to different distances X-rays from different phases might have to travel through the sample, but also because X-rays with different energies are absorbed to a different extent. This topic is further treated in chapter 5.4.

We encounter a similar difficulty with shadowing, which again in the simplest case means more acquisition time is necessary because less signal reaches the detector as parts of the sample, grid or sample holder literally cast a shadow on (part of) the detector. But also in this case geometric conditions, as well as the difference in absorption for X-rays of different energies might influence elemental quantification. Especially if EDX signals are tomographically reconstructed a different extent of shadowing at different tilt angles might occur and might significantly influence the reconstruction. Therefore shadowing in EDX spectroscopy played a significant role in this work. See chapter 5.1

In EDX spectroscopy artefact peaks may arise from X-rays stemming not from the sample region of interest, but parts of the column, the sample holder or other parts of the sample or grid. Escape peaks may arise, when ionization followed by X-ray emission happens within the detector material. The energy of the escape peak equals the initial X-ray energy minus the energy of the escaped X-ray. Sum peaks can result from the inability of a detector to separate two X-rays which reach the detector within a very short time. This effect is usually avoided through a pile-up rejection system.[1]

EDX analysis was performed at the ASTEM equipped with the Super-X detector system by FEI (now: Thermo Fisher) which consists of 4 Silicon drift detectors, increasing the collection angle compared to systems equipped with one single detector.[18] The effects of the 4-quadrant detector system on absorption of X-rays in the sample (on the path to the detector) is discussed in chapter 5.4. Silicon drift detectors are based on the collection of electron hole pairs which are generated by the incoming X-rays. They are separated by a voltage applied to p- and n-doped regions, which are distributed as rings on the detector surface. These detectors allow a very high throughput of counts, and reduced need for cooling compared to Si(Li) detectors.[19] The Super-X detector system is window-less reducing absorption, and increasing the detectability especially of low Z elements.

2.2.4 Spectrum Images

With the methods described above either one spectrum from a spot or region of the sample can be acquired (EELS or EDXS), or an image containing information of the distribution of one element only (EFTEM). If the distribution of more elements is of interest, it is possible to perform EFTEM at several different edges. One could go even further and perform EFTEM in regular intervals over the whole spectral range of interest, and therefore gain 2D-spatially and energetically resolved information of a certain sample area, as schematically shown in Figure 12 on the left. Another (mostly more easily applicable) method to gain 2D spatial and energy information can be realised in STEM mode, by scanning the beam over a sample area of interest and acquiring a spectrum (EELS[20] and/or EDXS) at each beam position. (Schematically shown in Figure 12 on the right.) The result of such a scan is a spectrum image (SI). In both cases data cubes including spatial and energetic information are retrieved. As a rule of thumb, using EFTEM will allow a larger field of view for a certain spatial resolution while SIs can deliver far better energy resolution. Therefore they are the method of choice if elemental concentration quantification is a goal. As spectrum images are acquired in STEM mode, they also entail the advantage that several signals can be acquired simultaneously. Together with EELS and EDX signals also signals from any annular detectors, which do not disrupt the EELS signal (e.g. HAADF detectors), can be used. If the EELS signal is not acquired, non-annular (e.g. BF) detectors can also be used for simultaneous acquisition. Commercial software packages (e.g. Digital Micrograph by Gatan[21]) allow the easy acquisition of SIs and also easy data processing, including alignment of the energy scale via the zero-loss peak and simultaneous processing of all the spectra as well as the output of elemental maps and the calculation of elemental concentrations.

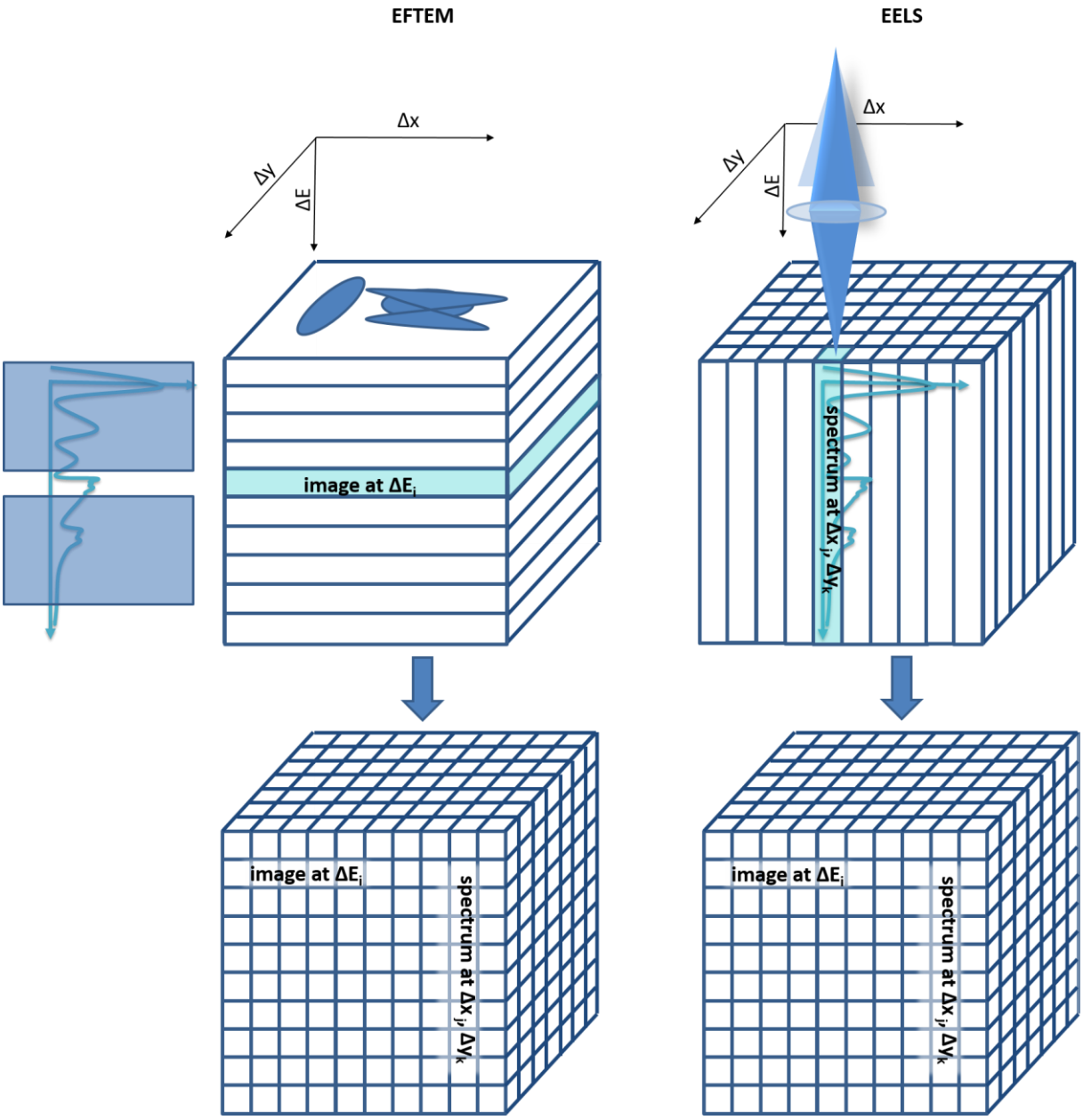

Figure 12: Scheme of datacubes resulting from EFTEM and EELS, both finally containing spatial information (images) in the horizontal planes and energy loss information in the vertical dimension.

2.3 Tomography in TEM

2.3.1 Introduction to Tomography

It is an intrinsic characteristic of transmission electron microscopy that objects are investigated in projection. For interpretation of those projections - to gain information on the original 3D object - additional knowledge is necessary, as the projections exhibit no resolution in beam direction. In order to eliminate the ambiguities of projections without prior knowledge of the sample 2D projections can be acquired at different tilt angles with respect to the incoming beam and reconstructed to give a full 3D model of the object. This process is called tomography.

From a practical point of view this process can be divided into three major steps: Acquisition of the data, alignment of the tilt series, and the reconstruction of the aligned data, as schematically shown in Figure 13.

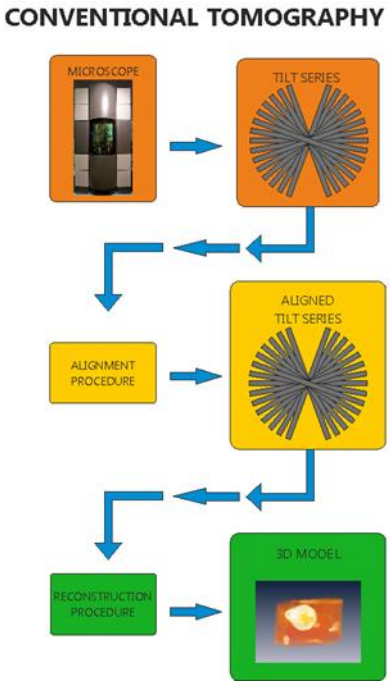

Figure 13: Scheme of major steps in electron tomography.

2.3.2 Principles of Tomography

The mathematical principles of tomography were first outlined by Radon in 1917.[12,22] A Radon transform maps a real space object described by a function *f(x,y)* via projections or line integrals through *f(x,y)* along all possible lines L with unit lengths ds. [12,22]

$$Rf = \int_L f(x,y)ds \tag{18}$$

Parallel rays passing through an object *f(x,y)* at an angle θ to form a projection $P_\theta(t)$, as shown in Figure 14, can be described via[23]

$$x\cos\theta + y\sin\theta = t. \tag{19}$$

Using this relation and a delta function the Radon transform can be written as[23]

$$P_\theta(t) = \int_{-\infty}^{\infty}\int_{-\infty}^{\infty} f(x,y)\,\delta(x\cos\theta + y\sin\theta - t)\,dx\,dy. \tag{20}$$

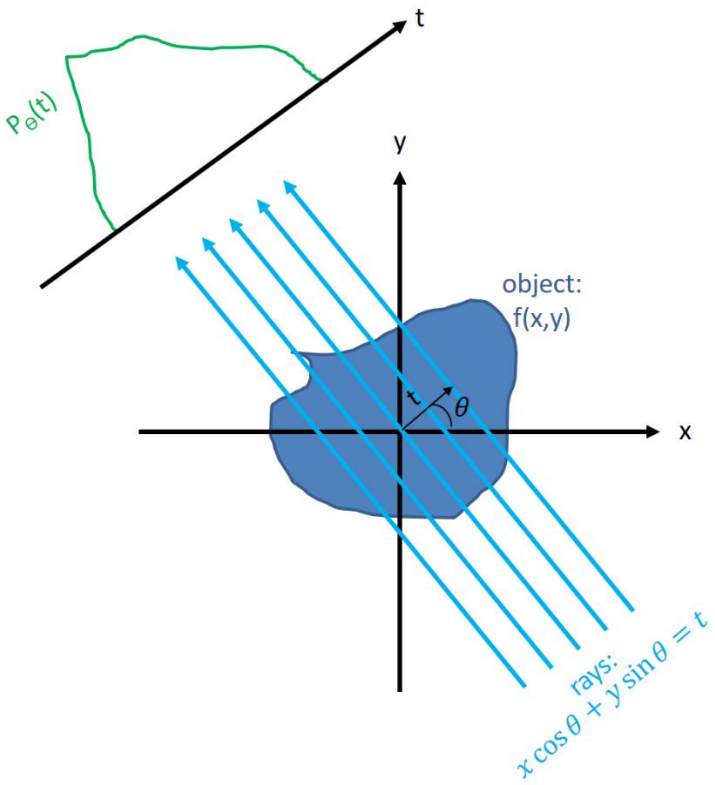

Figure 14: Rays passing through an object f(x,y) to form a projection $P_\Theta(t)$.

Sampling of a real space object through some form of transmitted signal or projection is geometrically equivalent to a discreet sampling of the Radon transform. Therefore the inverse Radon transform is analogous to the reconstruction of an object from its projections. As any experimental sampling will be discreet and thus imperfect the goal in tomography is to achieve the best possible reconstruction. Reconstruction techniques are covered in the next section.

A necessary constraint for tomography is the projection requirement. It states that the function projecting the object needs to vary monotonically as it passes through the object.[12,24] While this condition is fulfilled if incoherent conditions are reached, such as in HAADF STEM, diffraction and Fresnel contrast will be problematic, therefore predominantly coherent signals (BF and signals from low angle annular detectors) need to be handled with care. [7,12,25] If the sample is large in a direction perpendicular to the tilt axis, so that at some tilt angle the sample becomes thick, a contrast reversal might even appear in HAADF STEM, and the projection requirement is not fulfilled.

2.3.3 Reconstruction Techniques

The central slice theorem states that the Fourier transform of a projection of an object at a given angle Θ equals a central section through the Fourier transform of that object at the angle Θ.[12,23,26] Therefore a possible reconstruction of the object can be achieved through inverse Fourier transformation of a superposition of a set of Fourier transformed projections. This method – the direct Fourier reconstruction[12,27]- however is not well suited for practical use due to its computational intensity and the fact that an inverse Fourier transform requires a radial interpolation in Fourier space, (due to sampling - as shown in Figure 15) to a square grid. Due to the reduced sampling at high frequencies, interpolation of those is especially prone to error.[23]

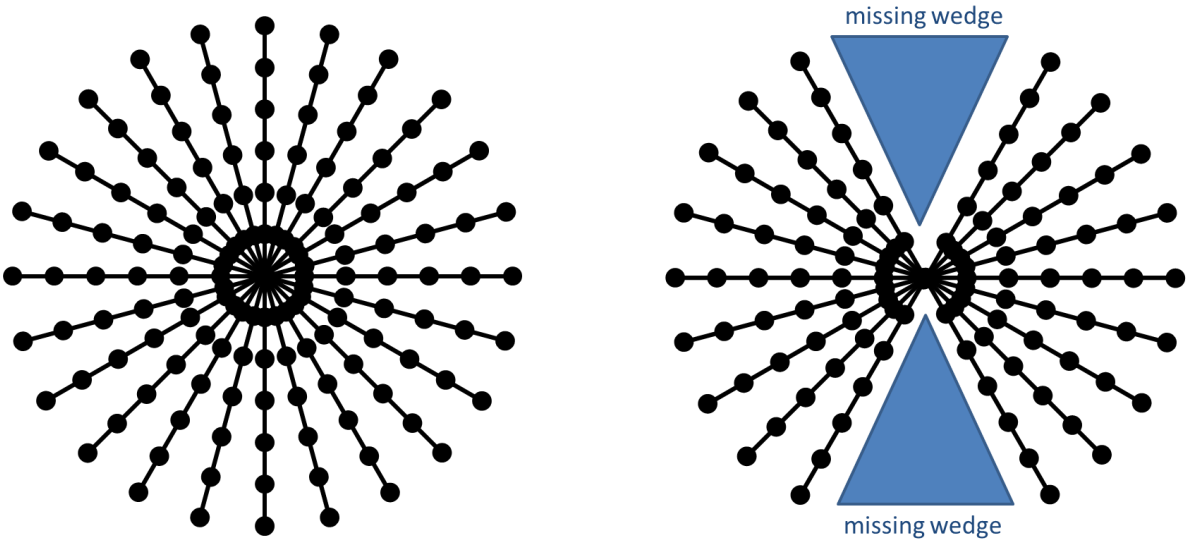

Figure 15: The central slice theorem and the missing wedge. The image on the left shows the unequal sampling at with respect to frequencies in Fourier space. A reduction in sampling at high frequencies can be observed. On the right it is shown that if the tilting angles span an angular range smaller than 180° there is information missing in the z-direction – the missing wedge. This leads to a degradation of resolution in z-direction and is observed as an elongation of the reconstructed object in that direction.

Back-projection methods are based on the theory, that any point in space can be uniquely described by three rays passing through that point. For more complex structures more rays are necessary. By smearing out a projection a bundle of parallel rays can be formed. If a set of projections from different angles is smeared out at the correct angle so that they overlap the object can be reconstructed. This method is known as direct back projection[12,28–30]. The reconstructed object however will be blurred. This is easily understood by regarding the central slice theorem: As the projections represent a central slice through Fourier space, the low frequencies are oversampled compared to the high frequencies, as can be seen in Figure 15. But this can easily be accounted for by multiplying the data in Fourier space with a radially symmetric weighted filter, which equals zero at the centre and reaches a maximum at the edges. This reconstruction technique is called weighted (or filtered) back-projection.

To complement this phenomenological explanation a summary of the derivation of the filtered back-projection (for parallel beam conditions) from the Fourier slice theorem by Kak and Slaney[23] shall also be presented: We start out by describing the object *f(x,y)* as the inverse Fourier transform, of its Fourier transform *F(u,v)*

$$f(x,y) = \int_{-\infty}^{\infty}\int_{-\infty}^{\infty} F(u,v)e^{2\pi j(ux+vy)}\,du\,dv \tag{21}$$

which via polar coordinates,

$$u = w\cos\theta \tag{22}$$
$$v = w\sin\theta \tag{23}$$
$$du\,dv = w\,dw\,d\theta \tag{24}$$

can be rewritten as:

$$f(x,y) = \int_{0}^{2\pi}\int_{0}^{\infty} F(w,\theta)e^{2\pi jw(x\cos\theta+y\sin\theta)}w\,dw\,d\theta \tag{25}$$

By using equation 19 and the relation

$$F(w, \theta + \pi) = F(-w, \theta) \tag{26}$$

we get

$$f(x,y) = \int_0^{\pi} \left[\int_0^{\infty} F(w,\theta)|w| e^{2\pi j w t}\, dw \right] d\theta. \tag{27}$$

Application of the central slice theorem allows us to replace the Fourier transform at the angle θ, with the Fourier transform of the projection taken at the angle θ.

$$f(x,y) = \int_0^{\pi} \left[\int_0^{\infty} \mathcal{F}(P_\theta(w))|w| e^{2\pi j w t}\, dw \right] d\theta \tag{28}$$

The term in the parenthesis represents a filtering operation, where $|w|$ determines the frequency response of the filter. Further equation 28 represents a back-projection of this filtered projection. The term in the parenthesis of equation 28 contributes equally to all (x, y) for which equation 19 holds, which means all point (x, y) along the line where it was originally projected. This operation could therefore be described as smearing back, or backprojecting, over the image plane.[23]

As sampling is always limited reconstructions will never be perfect. The projection, however, will always be a perfect reference. Therefore a possibility of assessing the quality of a reconstruction is always possible by projecting the reconstruction and comparing to the original projections. This can be done with the comparison performed on a system of linear equations:

$$Af = p \tag{29}$$

Where A is the operator forming a projection from the object f, which can be compared to the original projections p.

Going one step further one can get a difference (in terms of "difference between projection and re-projection") reconstruction and use this to modify the original reconstruction. This modification can be performed iteratively, until there is sufficient agreement between projections and re-projections, leading to iterative reconstruction techniques, like e.g. the simultaneous iterative reconstruction technique (SIRT)[31], which was much used on data sets in this thesis. If the difference between projection and re-projection is found via division rather than sum, as described in the flow chart in Figure 16 the technique is called multiplicative SIRT.

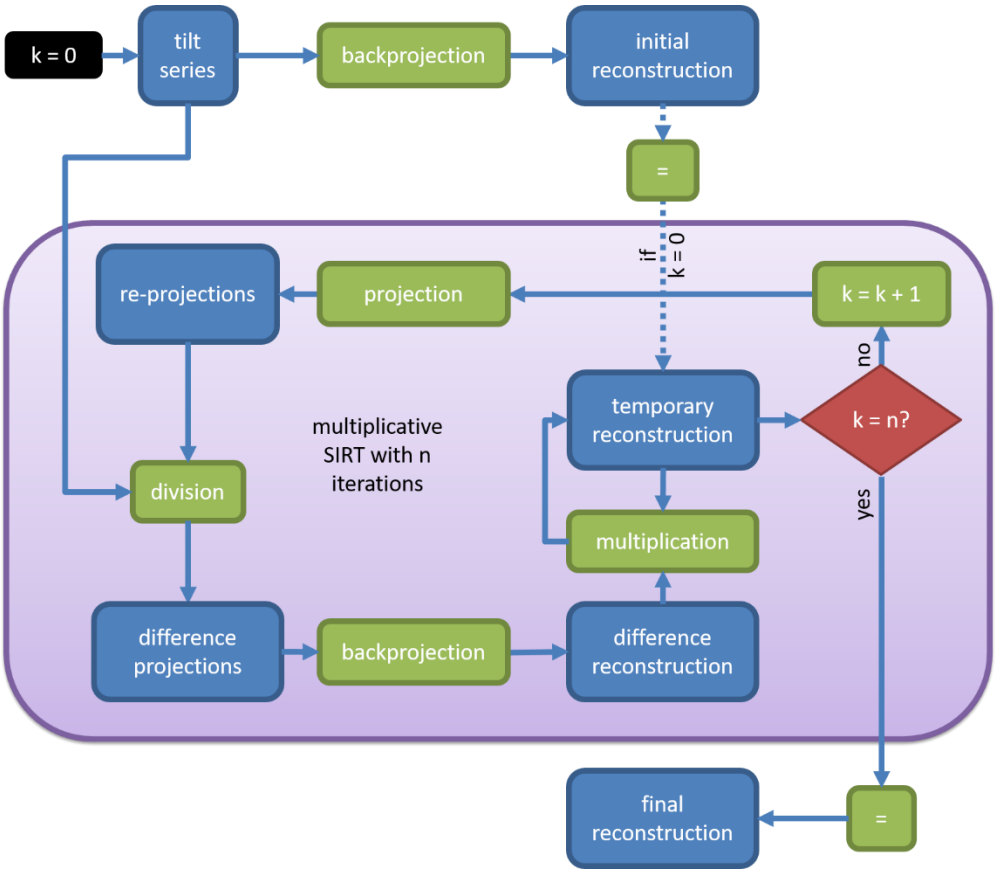

Figure 16: Flow chart describing the principle of the multiplicative SIRT algorithm.

Another source of error that occurs in experiment is noise. Its influence on reconstructions can be reduced, by applying a bandpass filter eliminating high frequencies, like e.g. a Hamming window.[23]

Another possibility to improve reconstructions is given by including prior knowledge of the object in the reconstruction. These methods therefore enable the retrieval of decent reconstruction, even with a limited number of projections. Discrete tomography and compressed sensing algorithms are two prominent examples. In discrete tomography[32] it is assumed, that there is a certain number of discrete grey values. This is very well applicable in case of material samples, which consist of well-defined phases. As the exact grey values are usually not known prior to reconstruction, and their number might also be unknown, it is practical to initially perform non-discrete reconstructions e.g. by using the SIRT algorithm and start discretising after a certain number of iterations, e.g. by using threshold values for different shades of grey. Furthermore border regions can be identified and subjected to further iterations, while non-boarder pixels are kept constant.

Compressed sensing[33–36] assumes a sparse signal. If the relationship between object f and projection p is described as

$$Af = p \tag{30}$$

with the projection matrix A and f is assumed to be sparse, the optimal solution can be found by minimizing the l_1 norm of f.

$$\min\|f\|_1 = \min\sum_i f_i \tag{31}$$

While l1-mimization is only directly applicable in few cases, such as atomic resolution tomography a variation thereof, where the gradient is minimized instead of the signal, is widely applicable. This compressed sensing approach is known as total variation (TV) minimisation and has the following form:

$$\min\|f\|_{TV} = \min\left(\sum_{x,y}\sqrt{\frac{\partial f(x,y)}{\partial x}^2 + \frac{\partial f(x,y)}{\partial y}^2}\right) \tag{32}$$

There are different practical approaches to TV minimization. The one used in this thesis minimizes the following term:

$$\min\|f\|_{TV} + \frac{\mu}{2}\|Af - p\|_2^2 \tag{33}$$

Where μ is a regulation parameter. It weights minimising gradients versus, matching the original projections. While a low μ will suppress noise it might also hide actual high frequency information.

Next to the SIRT algorithm TV minimisation was the most frequently used reconstruction algorithm in this thesis. The advantages and disadvantages of both techniques depending on purpose are discussed in section 5.5.

2.3.4 Acquisition

One very important aspect when choosing acquisition conditions is to consider resolution. For discussing the achievable resolution in tomography we define the x-axis as the tilting axis and assume perfect alignment. (The topic of alignment will be covered below.) Along the x-axis the achievable resolution simply equals the resolution of the original projections. In y and z the achievable resolution depends on the number of projections (N) as well as the diameter of the reconstructed volume. For projections covering ±90° the resolution is described by the Crowther criterion[29]:

$$dy = dz = \frac{\pi D}{N} \tag{34}$$

Therefore a high number of projections is desirable for good resolution. However it must be mentioned that the sample should also not change during acquisition. So in case of beam sensitive samples the number of projections might have to be kept small in order to prevent sample damage. Also contamination can change the sample over time, and thus might degrade reconstructions.

In case ±90° tilt angle cannot be reached the resolution in z direction is further degraded by an elongation factor, which depends on the maximum tilt angle α. So

$$dz = dy * e_{yz} \tag{35}$$

with

$$e_{yz} = \sqrt{\frac{\alpha + \sin\alpha\ \cos\alpha}{\alpha - \sin\alpha\ \cos\alpha}} \tag{36}$$

By regarding the central slice theorem it becomes apparent, that the absence of projections in the range from ±α to 90° entails that there is no information in those directions. In Fourier space this corresponds to a wedge of missing information (see Figure 15) and is therefore referred to as the "missing wedge". This wedge of missing information is to be kept as small as possible. It can be concluded, that a high maximum tilt angle α is desirable. If possible (depending on sample geometry and sample holder) a tilt range of ±90° should be reached.

In case the sample geometry or the sample holder does not allow such high tilts multiple axis tomography might be an alternative - a method to reduce the missing wedge to a missing cone.[37–39] This might still be an option if the full tilt range cannot be reached, but it must be mentioned that this method again leads to more exposition of the sample, if the number of projections for each axis is not reduced. While this method is worth mentioning, it will not be discussed further, as it was not used in this thesis.

In case of STEM tomography it also needs to be considered, that the focus changes with depth. Therefore - depending on sample thickness - the convergence angle must not be chosen to be too large, as this decreases the depth of focus. Especially for thick samples a small convergence angle needs to be chosen. A typical convergence angle chosen for tomographic investigations would be 10mrad.

For a successful acquisition also the projection requirement (described above) needs to be taken into account. It might not be possible to acquire a whole tilt series and fulfil the requirement in every projection. To still be able to retrieve a reconstruction, projections not fulfilling the projection criterion can be eliminated, and reconstructions can be performed with the remaining projections. If applicable compressed sensing algorithms may lead to nearly unaffected reconstructions, as they can make up for a limited number of projections.[33] In any case it might be necessary to preform several reconstructions with different techniques and parameter settings and compare results for reconstruction artefacts to gain the best possible reconstruction.

2.3.5 Alignment Procedures

As mechanical tilting is never perfect with respect to tilt axis stability (which has a visible impact due to the small sample sizes in electron tomography) and also sample drift or a beam shift may occur it is necessary to align the acquired tilt series. Therefore the common tilt axis must be found and the images must be shifted in x and y so that they all back-project to the object at one single position.

A very common alignment technique for biological samples is the tracking of fiducial markers, which are typically gold nano-paricles.[40,41] These need to be sufficiently present near the area of interest. As in the material sciences, the choice in areas to reconstruct is often more limited, this technique is often not easily applicable. The advantage in material science is that usually HAADF contrast is higher than in biological samples. Therefore a cross correlation alignment can usually be carried out quite easily, to find the shifts in x and y, given by the maximum of the cross correlation.[42] It needs to be carried out sequentially to align the whole tilt series. Prior to alignment via cross correlation usually some filtering is performed.

A more accurate alignment of the x- and y- direction is achievable with the projection re-projection comparison alignment[43]. In this iterative approach the cross-correlation procedure is used for primary rough alignment of a tilt series, followed by its reconstruction via weighted back-projection, and its re-projection. Then again the cross-correlation procedure is applied, to find the transition in comparison with the original tilt series.

Another method which can not only be used to find shifts in x-direction (perpendicular to the tilt axis), but also to find the angle of the tilt axis is based on the centre of mass. The movement of sample features is tracked - their path is perpendicular to the tilt direction. Therefore the tilt axis can be discovered by finding the centre of mass of all projections.[44,45] This can be done via finding the 1D centre of mass for each projection in each sinogram (data set of projections over tilt angles arranged in 2D[ii]), which will follow the path of a sine wave around the tilt axis. This method, however, can only be applied if the sample size is limited in y-direction, so that the full sample is always visible in the projections (e.g in case the sample is rod-shaped).

Another way to find the tilt axis is to analyse reconstructions for artefacts. Therefore a quick algorithm – like filtered back-projection – can be used. A wrong shift of the tilt axis will lead to banana shaped distortions of sample features in the reconstruction: The more severe the distortions - the greater the misalignment. A wrong tilt of the tilt axis will lead to a different extent of the distortions in different regions of the reconstruction, as a wrong tilt of the axis will lead to varying differences between the axis used for reconstruction and the actual tilt axis. [46]

2.3.6 Visualisation and Segmentation

As the output of a reconstruction is just a data file it is usually necessary to visualize or even segment the data. Segmentation will be necessary if quantitative information (e.g. how much of a certain phase is present) is to be retrieved. For this thesis the commercial software package “Amira” was used for segmentation.

If rather than an overview, specific, localised information is sought, slices through the reconstruction at the exact location are often most helpful. They may unravel detail, which is either hidden or not as easily extractable from a full 3D representation. Slices may enable the accessibility of more quantitative information, like the size of a feature in x-, y-, or z-direction.

Surface rendering is most useful to show boundaries between distinct phases or regions of a reconstructed sample region in 3D. As a “surface” is defined via a threshold value. Gradual changes cannot be shown via surface rendering.

For the visualisation of properties which exhibit non-discreet or gradual changes within the reconstructed volume, volume rendering can be useful. This is owed to the fact, that volume rendering does not rely on discreet threshold values. It basically works like light passing through a volume. Depending on the density of the volume more or less light will be scattered. The “density” is represented by the intensity values of the voxels in the reconstructed region. Low intensity values will lead to rather transparent regions, high intensity regions, bright or colourful depending on the colour scale used.

[ii] Stacking of projections from a 3D object leads to a stack of sinograms in x-direction, each sinogram being a function of y and Θ.

Segmentation is performed to define discreet regions within a sample. Every voxel of a reconstructed volume is assigned to a certain phase. This can be achieved via various paths: Threshold values are often used. They may be used as a first approximation, or might even be enough for a full segmentation. But due to reconstruction artefacts it is may be necessary to perform manual corrections. Watershed algorithms are also a useful tool. The term “watershed” is quite descriptive of the basic mode of operation of the algorithm: It treats the data like a landscape that is filled with water - the height of the value of a voxel representative of its height in the imaginary landscape. There is a source from which the “water” spreads to connected regions with values low enough.

2.4 Analytical Electron Tomography - Status Quo

Analytical tomography is a term that has developed when referring to electron tomographic reconstructions that not only give morphological information, but also compositional 3D information.

2.4.1 EFTEM, EELS and EDXS Tomography

The first appearance of analytical tomography can be traced to Paul Midgley and Matthew Weyland in 2003 in the form of EFTEM tomography[12]. There it was suggested that tomography of core loss signals of samples of the physical sciences (as opposed to biological samples, which are orders of magnitude more sensitive to beam damage) should be possible. The two possibilities of gaining 3D compositional information from a tilt series of either background subtracted maps of jump ratio maps were considered and compared. While the background subtracted maps, which are created from three images deliver quantitative information, they might not satisfy the projection criterion. Jump ratio maps, created from only two images, will remove additional diffraction contrast, thus fulfilling the projection criterion, but will not deliver quantitative information. The monotonic nature of the signal is given up to 1 to 1.5 t/λ.[12]

As soon as a tilt series of elemental maps is created, it can basically be treated as any other kind of tomographic series and aligned and reconstructed. The main difference are that the number of tilt angles will typically be rather low to acquire the series in a reasonable amount of time and make sure the sample will not suffer any changes throughout the acquisition of the tilt series, and for the same reason the maps might suffer from a lot of noise. Therefore simple reconstruction algorithms like e.g. weighted back-projection are usually not sufficient to retrieve a satisfactory reconstruction and more elaborate methods, like iterative reconstruction techniques[31] or compressed sensing[33,35] algorithms will typically be necessary.

The beginnings and first milestones of EELS tomography can be traced back to Jarausch et al[47] in 2008. In those cases EEL spectrum images were acquired and subsequently maps from different signals of interest were created. These maps did not give compositional information, but in case of Jarausch et al[47] also fine structure maps were used to retrieve 3D maps of variations in Si bonding. But as well as in case of the EFTEM signals, here also maps were created prior to reconstruction.

Naturally also maps can also be drawn from EDX signals and used for reconstruction.[18,48–50]

The reconstruction of EFTEM[51–53], EELS[54,55] and EDX signals gained importance in the years to come. The reconstruction of whole spectra to create 4D data cubes carrying all the information and allowing for compositional analysis after reconstruction, was to be established at this institute years later. [56]

2.4.2 3D-Reconstructions via quantitative STEM

For the sake of completeness it shall also be mentioned that quantitative STEM methods also allow to perform 3D reconstructions including elemental information by distinguishing atom types.[45,57–59] This is a totally different approach, where high resolution STEM (HR STEM) simulations are performed from assumed initial atomic configurations and compared to STEM experimental results. This technique can only be applied to rather small, crystalline samples, like nanoparticles, as exact atomic arrangements need to be assumed and simulated. Consequently this method also needs a great amount of pre-knowledge of the sample and is very time consuming. The combination of quantitative STEM with compressed sensing STEM HAADF tomography was performed on bimetallic nanocrystals[60]. While quantitative STEM including elemental information can also be attributed to analytical tomography, its limitations lead to the inapplicability to the samples of interest in this thesis, and thus to no further considerations.

2.5 Sample Preparation Techniques

Sample preparation is an essential part of scientific research and has a massive influence on the quality of experimental results. In this chapter the standard sample preparation techniques used for (S)TEM investigations and tomography are described. For analytical tomography sample preparation was continuously improved. This optimization process is described in chapter 5.1.

2.5.1 Sample Preparation for 2D Investigations – Ion Milling

The sample preparation of HRSTEM, 2D EDXS and EFTEM investigations was performed as a combination of mechanical methods and Ar-ion milling. The main goal was to reach samples with great amounts of electron transparent areas. For ideal HRSTEM results they should be as thin as possible and show minimum artefacts.

The following procedure was applied to the AlMgScZr samples investigated, which were provided as bulk samples, that were typically about one cm long, half a cm wide and a few mm thick: A plate with a thickness of about 500 µm was cut from the bulk sample using a Well diamond wire saw. To create a disc with a diameter of 3 mm a Gatan ultrasonic disc cutter[61] was utilized. Special care was taken to make sure the region of interest was in the middle of the disc. In the electron beam re-solidified (EBRS) samples (see chapter 3.1), the region of interest was the re-solidified volume, easily identifiable via its appearance of a welding seam. In the sample investigated for the publication[62] the region of interest was additionally marked on the bulk sample. In case of the as cast (AC) samples the whole sample was homogeneous and did not have a volumetrically confined region of interest. The resulting disc was ground to a thickness of 150 µm using a Gatan disc grinder[63], followed by a dimple grinding process using a Gatan dimple grinder[63], Struers 6 µm diamond paste[64] and 0.25 µm diamond felt[65] for polishing until a thickness of 15 µm was reached. The final thinning was performed on a precision ion polishing system (Gatan)[66], where argon ions were accelerated toward the rotating sample with 4 kV and under an angle of 4° at the top and 6° at the bottom. When mounting the sample the region of interest was again taken into consideration to make sure the hole with its electron transparent edge would appear there.

2.5.2 Sample Preparation for Tomography - the Dual Beam Microscope FIB-SEM

The dual beam microscope is a versatile tool and among other applications a very useful TEM sample preparation device. It is unique in allowing a site specific lamella preparation and also ideal for preparing needle shaped samples for tomographic investigations. However, it needs to be kept in

mind that this sample preparation process will always lead to an amorphisation of the sample surface as well as Ga-implantation.

It is made up of a focused ion beam (FIB) column which is mounted at an angle of 52° to the focused electron beam column functioning like a scanning electron microscope (SEM). At the eucentric height both beams meet at the same spot. If this is used as the working height the SEM can be used for watching the working process with the ion beam. The instrument is equipped with a stage that can be rotated and tilted, so that the sample can be milled and viewed from user defined angles. Furthermore an OmniProbe nanomanipulator[67] is installed, which can be used to transfer the lamella from the bulk sample it is cut from to the sample holding grid. The system is also equipped with gas injection systems (GIS), which e.g. allows the deposition of platinum, the release of a Pt- complex as a precursor gas, which is dissolved into a volatile part and a non-volatile Pt-C mixture by the electron or ion beam. The Pt-rich non-volatile part can be used as a protective layer or function as a glue, to attach the lamella to the OmniProbe needle or grid, when used for TEM lamella preparation.

2.5.2.1 Sample Preparation for Tomography

The electron beam can be used to find a position from which the sample is taken. With focused electron beam induced deposition (FEBID)[68] a protective platinum layer can be deposited where the sample will later be cut out. After depositing a first layer with the electron beam, the ion beam can be used for platinum deposition, to increase the growth rate. Hence the sample is tilted to face the ion beam. It also needs to be facing the ion beam for the next part of the procedure, where the ion beam is used to mill trenches from the material, to later enable a lift-out. Figure 17 shows such a platinum protection layer and the two trenches from top view. A circular pattern could also be used for milling in case of needle shaped samples, which was actually done for the very first samples. However for later needle-shaped samples not a cylindrical, but a lamella-shaped sample was lifted out, to have enough material to prepare two needle shaped samples, and thus have a backup. This is reasonable for several reasons: 1) The actual needle shaped sample is never perfectly cylindrical, but has got a conical component. Therefore not the whole sample, but only the top part of the sample will be thin enough for (S)TEM investigations. If the region of interest cannot be identified beforehand (from the surface), like e.g. in case of stochastically distributed precipitates, the region of interest might not be in the investigable sample volume. In such cases the preparation of two samples increases the probability to find the region of interest within the investigable volume by a factor of two. 2) The final thinning step is crucial as the needle shaped sample is fragile. A second needle can simply serve as a back-up sample.

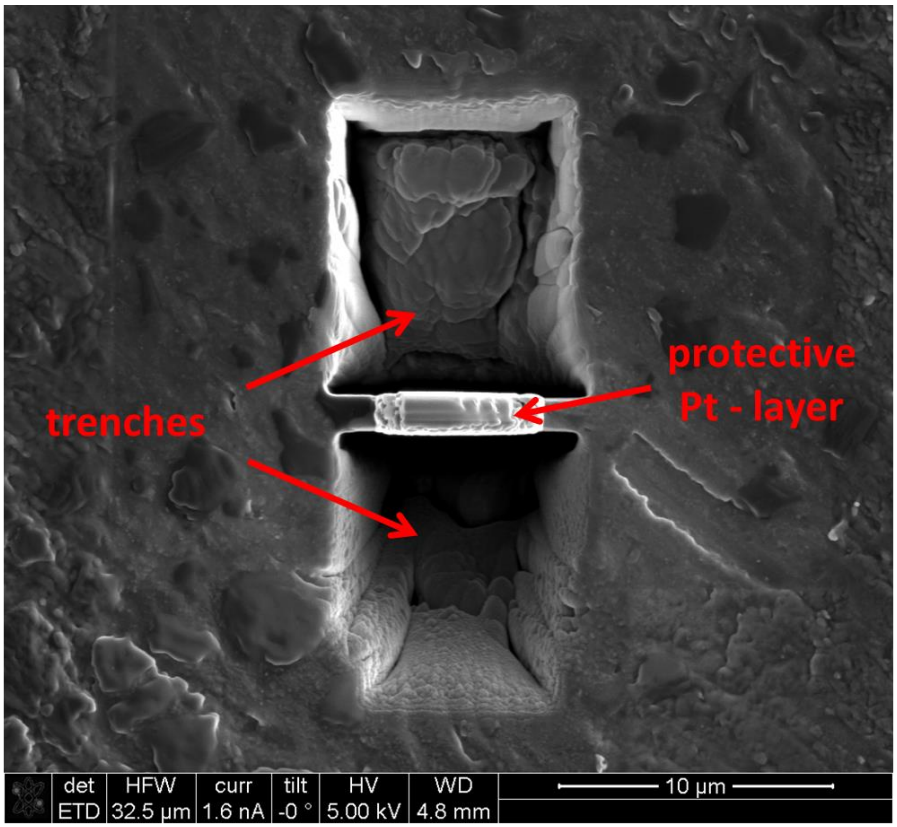

Figure 17: Protective platinum layer and cut trenches from top-view.

After milling the trenches the sample is tilted back to a zero degree stage tilt to get a top view when imaging with electrons (Figure 17) and a tilted side view when imaging with ions, as can be seen in Figure 18. Figure 18 documents the lift-out process. First a so-called U-cut is performed using the ion beam. This U-cut, which can be seen in Figure 18 (2) leaves the lamella attached to the bulk only at one small connective region on the left. Next the OmniProbe needle is carefully approached. The last few micro-meters are overcome by lifting the stage manually, rather than moving the OmniProbe, as the manual stage-lift is more precise. The contact between lamella and OmniProbe can be verified, as there will be a change in contrast in the image, as the OmniProbe carries charge away from the sample. If contact is verified, the OmniProbe can be attached to the lamella via focused ion beam induced platinum deposition. The double-attached position is very critical (Figure 18 (4)). A tiny relative movement of stage and OmniProbe can destroy the lamella. (A slammed door may lead to elimination.) Therefore the connection between lamella and bulk is cut as soon as possible, using the ion beam. When the lamella is detached from the bulk (Figure 18 (5)) it can be lifted away from the sample (Figure 18 (6)). For precision reasons (in our system) it is again better not to lift the OmniProbe, but to manually lower the stage.

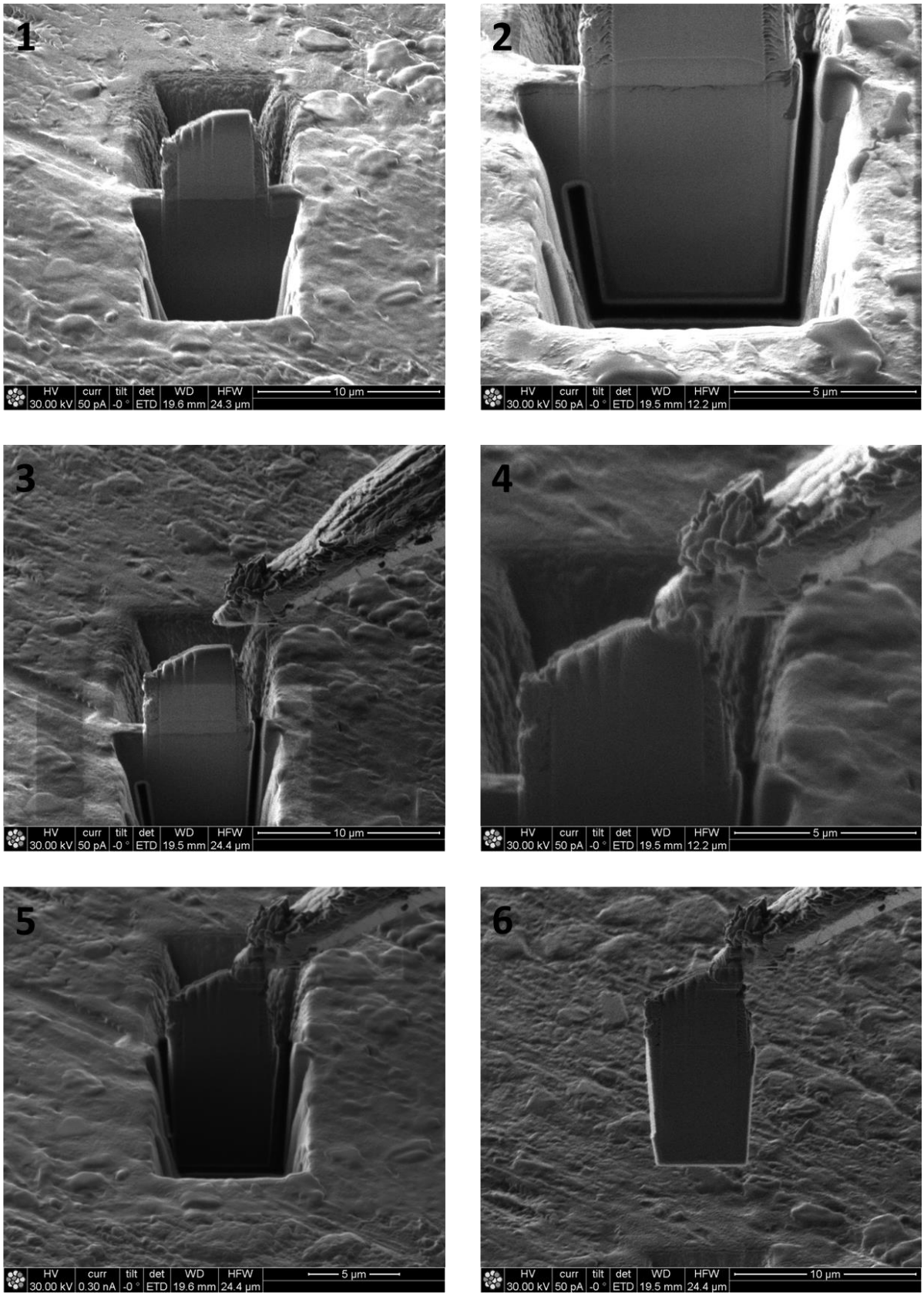

Figure 18: Lift out process imaged with ion beam from side view. 1) Initial conditions after applying protective layer and milling trenches 2) After U-cut: The lamella is now only attached to the bulk at the top left. 3) The OmniProbe is approached to the lamella. 4) The OmniProbe is attached to the lamella. 5) The last connection between bulk and lamella has been cut. 6) The lamella has been lifted away from sample.

Next the lamella is fixed to the sample support (grid or needle). The corner opposite to the OmniProbe is attached, again using FEBID technology. In the example shown in Figure 19 this was the bottom left position. This moment of double-fixation is again critical. Next the lamella is vertically cut in two, so that a pillar shaped sample is left on the sample holding needle, as can be seen in Figure 19. The other half of the sample can be retraced with the OmniProbe and attached to another sample holding needle after the first has been thinned.

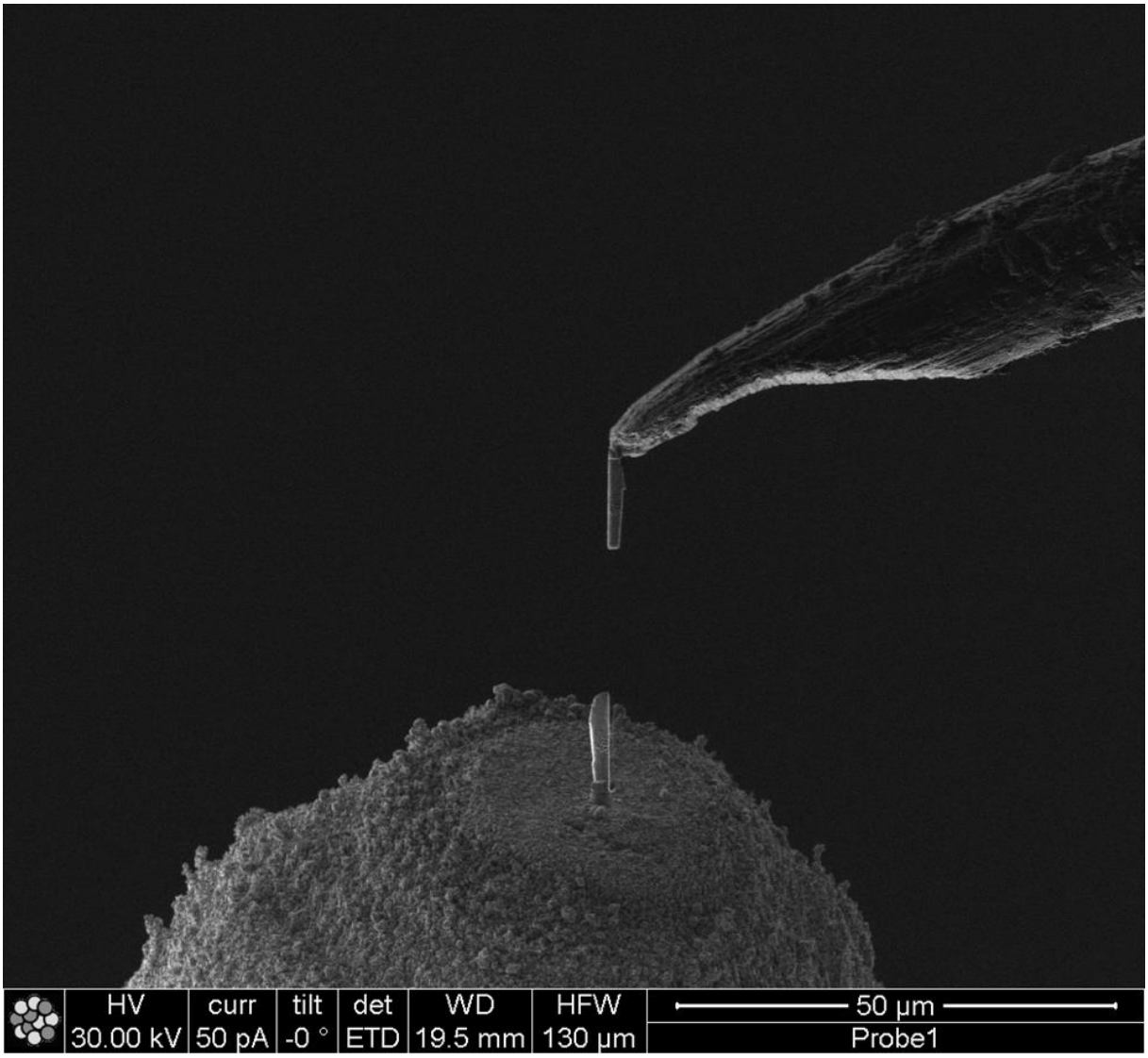

Figure 19: Lamella after attaching the left half to the sample-holder needle, cutting the lamella in two through a vertical scission with the ion beam and lowering the stage to lift away the second part of the lamella.

Finally the pillar shaped sample is cautiously thinned, by adjusting the ion beam current with a circular milling pattern until a needle-shaped electron transparent sample is reached. In the top region a thickness of the needle of below 100 nm is aimed at. Figure 20 shows an example of the thinning process.

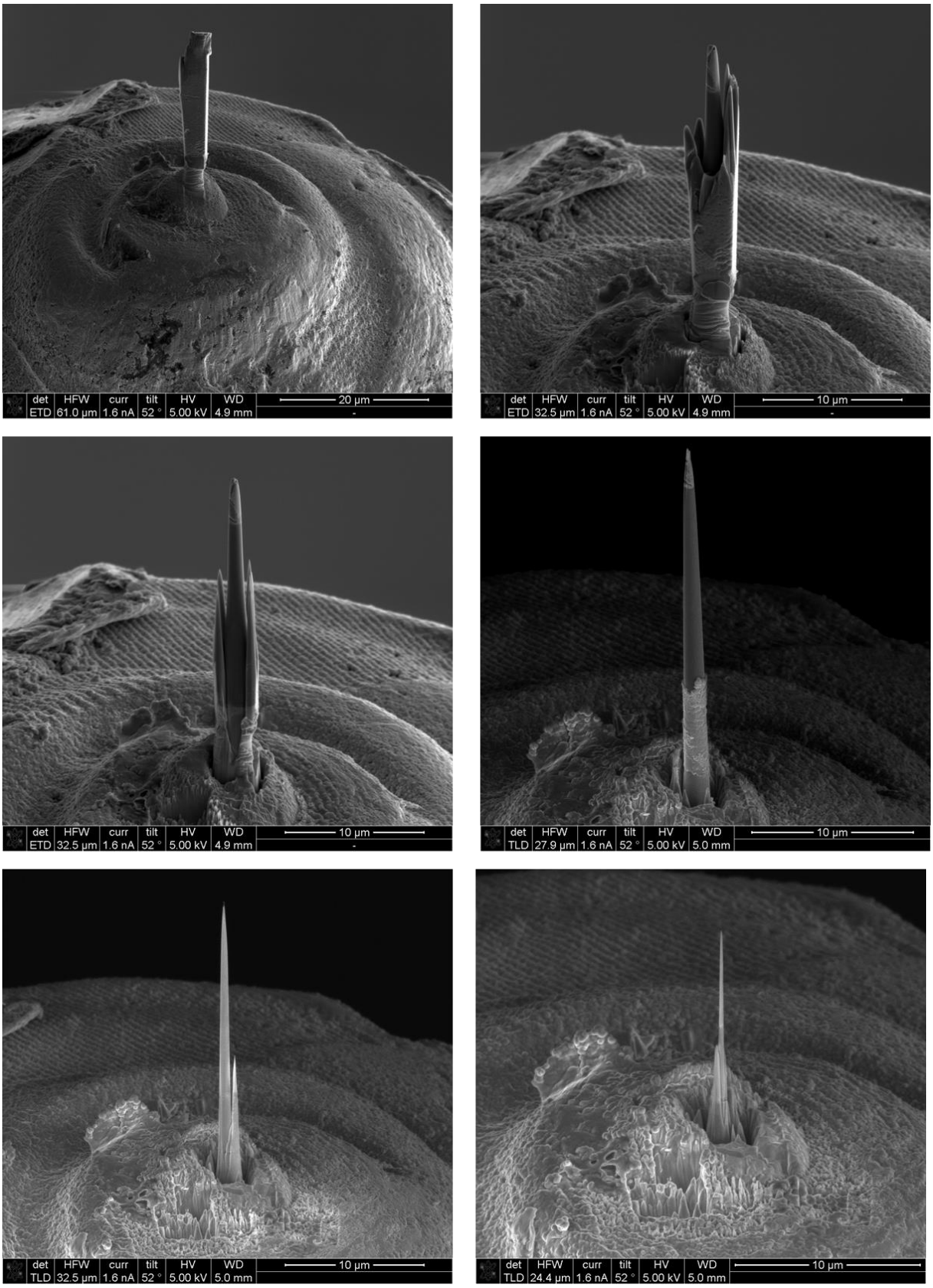

Figure 20: The thinning process. The thinning of needle shaped samples for electron tomography prepared via dual-beam microscope (FIB-SEM).

2.6 Quantitative STEM – STEM Image Simulation via µSTEM

2.6.1 Introduction

Simulations have gained increased interest in (S)TEM, as they allow improved - even quantitative - interpretation of (S)TEM results, and can contribute to the characterisation of instruments, e.g. concerning source, aberrations and detectors.[69–79] In multislice simulations an electron wave function is propagated through a crystal from one atomic plane to the next – referred to as slice, thus the name. Multislice simulations in this thesis were carried out via µSTEM[80] software developed by a group around Les Allen mainly situated at Melbourne university. The multislice based µSTEM uses fast Fourier transforms and allows various applications (HRTEM /STEM, imaging /diffraction, elastic /inelastic signals, ionisation,…) and different models.[81,82] In µSTEM thermal diffuse scattering can be accounted for either via the absorptive scattering potential approach, or a quantum excitation of phonons (QEP)[83] approach, which delivers numerically equivalent results to frozen phonon[84] approaches, but allows to treat elastic and inelastic phonon scattering separately at every stage of the calculation.

In the absorptive scattering potential approach[85–87] thermal diffuse scattering is only accounted for in a way that the intensity of the primary beam is reduced, as part of the beam is "absorbed" by the crystal, but the electron is not further considered as a possible source for further interaction within the crystal. Mathematically this is considered by a local absorptive potential in the Schrödinger equation.[80] As thermally diffuse scattered electrons are further considered in the QEP approach it is the more exact one. This becomes increasingly relevant for thicker samples, as in thick samples multiple scattering becomes more likely.[81,88] The absorptive approach however is a lot quicker, therefore for thin samples, or in case accuracy is less important than speed or only the elastic signal is of interest the absorptive approach can therefore be very useful.[81]

The frozen phonon approach makes use of the fact that the electron moves through the crystal fast enough that the thermal movement of the atoms in the crystal is not registered as movement as such, but rather as a frozen configuration, where the atoms are dislocated according to the mean square displacement or Debye-Waller factor.[80,84,89–91] The QEP approach models thermal scattering on the basis of many-body quantum mechanics. The time independent Schrödinger equation is solved parametrically for the displacement of the atoms in the crystal. For obtaining the total and elastic electron intensities (and also the inelastic intensities as the difference between total and elastic intensities) a Monte-Carlo integration is computed.[80,83] While the frozen phonon approach does not actually treat momentum or energy transfer, the QEP approach treats phonon excitation as a quantum excitation of the crystal (taking into account all possible initial configurations of the system for that electron), where at the inelastic scattering of the incident electron an energy loss occurs.[80,83] Ionization can be included in both models. In the frozen phonon approach the ionization cross section is calculated via the scattering of different electrons from different lattice configurations. In the QEP model inelastic scattering is treated in a quantum mechanical setting, where the ionisation cross section is predicted for a single electron allowing ionisation at every stage.

2.6.2 Important Aspects for the Practical Use of µSTEM

As a reference for future use, I want to summarize the most important aspects for the practical use of µSTEM. µSTEM is a code that runs via exe-files, with merely a command window as user interface. There is a number of files the folder from which µSTEM is started needs to include, for the code to run:

- A folder called ionization data; it is necessary for simulations including EELS and EDX outputs, and is automatically in the folder containing the µSTEM code, if µSTEM is downloaded from the official website of Melbourne university.
- A text file which holds all important data about the crystal to be simulated, but also the high tension with which the virtual electrons are to be accelerated. In this file everything needs to be exactly as described, including line breaks, spaces and commas. Our method of choice therefore was to use the exemplary file provided, and to exchange the values and names in that file. Figure 21 shows such a crystal file and describes the input parameters. The unit cell of the crystal must be a cuboid.

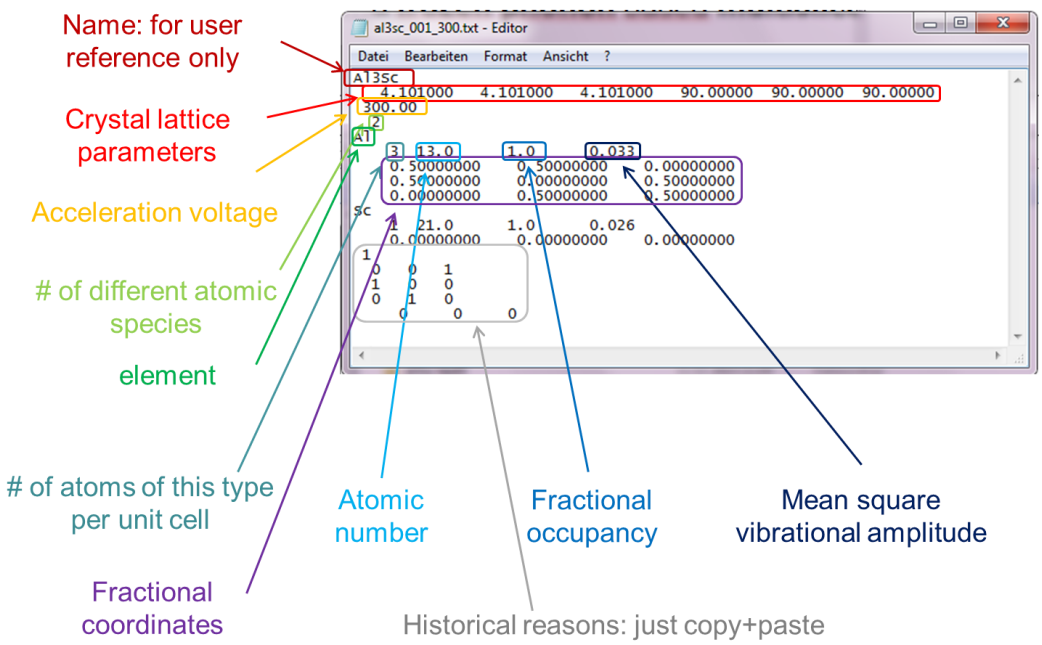

Figure 21: Crystal file for µSTEM and the parameters it must contain.

- Furthermore a txt file called user_input.txt must be in the folder. This file consists of only two lines. The first determining the mode in which µSTEM is run: “play”, “record” or “interactive”. The second determining the file name, under which the inputs are saved in case of the “record” option, or from which file the inputs are read in case of the “play” mode.
- If the “play” mode is chosen, a text file with the file name defined in the user_input.txt file must be in the folder. However, if the “record” mode is chosen, no other file with the file name specified for the recording option in the user input file must be in the folder, otherwise µSTEM will crash.

µSTEM is started by opening the executable file. Depending on the mode chosen either all the parameters are read from a file saved in the folder, or the user is prompted a series of questions

defining all the parameters necessary. In case the record mode is chosen, a text file is saved with all the chosen parameters, which consequently can be modified, and run again with these alterations by choosing the play mode. The advantages of using the "record" (and "play") mode over the "interactive" mode are obvious: 1) The record mode allows the monitoring of the chosen parameters after running the simulation. 2) A lot of time can be saved if a mistake has been made, as the falsely set parameter can be corrected in the saved file, and this file can then be run in "play" mode. 3) Time can be saved and mistakes can be avoided, if several similar simulations are to be run, as the varying parameter only has to be changed in the file, and the file can be rerun in "play" mode. This e.g. is very useful if EDX or EELS simulations of different elements or shells are to be performed, as only one inelastic signal, element and shell/line can be chosen per simulation. To emphasize the relevance of time saving, and the risk of a mistake occurring during parameter choice I need to add that the number of questions prompted is about 20-30, depending on the choices.

2.6.3 PACBED Simulations

Position averaged convergent beam electron diffraction (PACBED) is a technique where a convergent electron beam is scanned over a sample area of at least a unit cell to gain a position averaged diffraction pattern.[92] The diffraction pattern from a static convergent electron beam suitable for imaging at atomic resolution is sensitive to the beam placement within the unit cell. This makes interpretation of the results very complex. The averaging of the diffraction patterns gained by scanning the probe over an area of at least a unit cell will not only solve this problem, but also eliminates the dependence on effective source size and lens aberrations. What remains is a high sensitivity to specimen tilt, strain, polarity and thickness.[92]

The thickness can be determined by visually comparing measured PACBED patterns with simulated ones. It was shown that the absorptive model delivers sufficiently accurate results, even for relatively thick (> 50 nm) samples. [92]

There are several applications where the exact knowledge of thickness of a sample is necessary. The thickness, for instance, is a very important criterion when using multislice HRTEM or STEM or even EDX data simulations and drawing conclusions on the signal delivered from real samples in microscopy by comparison. Without accurate knowledge of the sample thickness a further unknown would significantly increase the possible configurations for simulation and make such an interpretation difficult and prone to misjudgment. For absolute scale comparison of experiment and simulation such an accurate measurement of sample thickness is essential.[70,93] Precise thickness information is also necessary in the approach discussed in section 8.4 where the possibility of drawing conclusions from HAADF intensities on precipitate compositions via an effective atomic number is treated.

3 Material Scientific Basics: The Aluminium Alloy and Solid State Diffusion

Part III of this thesis treats the investigation of an aluminium (Al) alloy, via the experimental techniques described in the previous chapter. This chapter shall give fundamental information of the investigated alloy, but also provide the thermodynamic basics, which were necessary to understand the diffusion processes taking place within the alloy during ageing, and to perform diffusion simulations.

3.1 The Alloy

AlMgScZr alloys are extremely promising for future applications as they combine the advantages of AlMg alloys, such as good welding characteristic, work-hardenability, and corrosion resistance with the high strength which can be achieved through age-hardening, if small amounts of scandium (Sc) and zirconium (Zr) are added to the alloy.[94–96] Therefore this material is ideal as application in aircraft bodies. [96]

Aluminium has a face centred cubic (fcc) crystal structure. Al_3Sc forms a cubic $L1_2$ crystal structure, shown in Figure 22Figure 22: Crystal structure of Al and Al_3Sc, which can be described, as an fcc-lattice, where the corner atoms are occupied by Sc instead of Al. Therefore, and due to the very similar unit cell sizes (4.041 Å for Al and 4.101 Å for Al_3Sc) the small spherical Al_3Sc precipitates, which form during annealing coherently match the Al matrix.

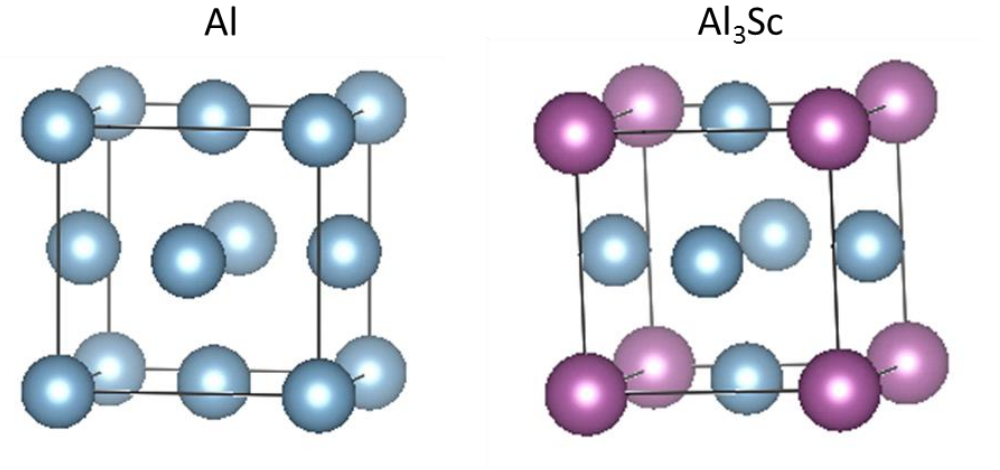

Figure 22: Crystal structure of Al and Al_3Sc.

These precipitates strengthen the alloy, as the movement of dislocations through the precipitate, which is necessary for deformation, disrupts the crystal structure, while the same kind of dislocation may not disrupt the crystal structure of Al, as shown in Figure 23. This disruption entails an increase of energy, thus strongly increasing the mechanical resistance of the material, compared to pure Al.

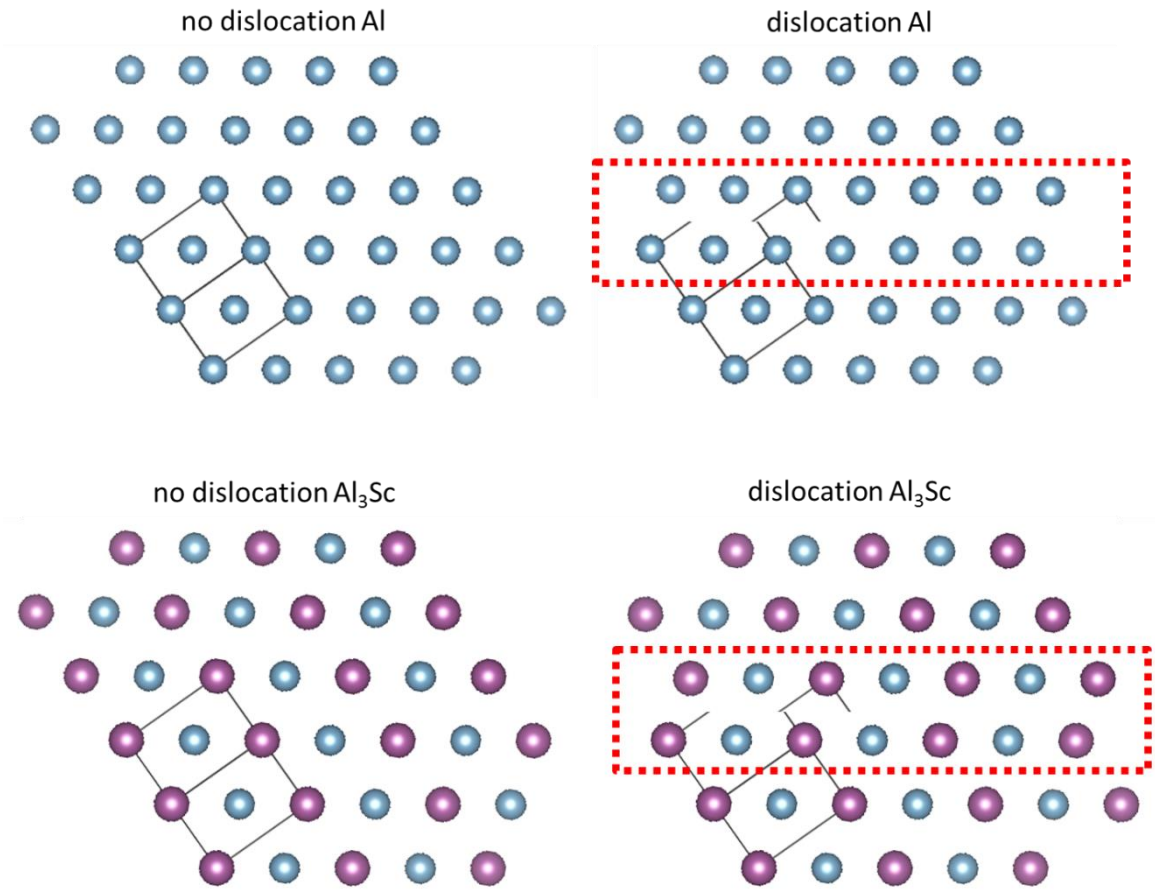

Figure 23: Shows how the movement of a dislocation might disrupt the crystal structure of Al_3Sc, while not disrupting Al.

Zr can be incorporated in the Al_3Sc system, and will occupy the same lattice sites as Sc, leading to an Al_3(Sc,Zr) system. As the solubility of Sc is limited to 0.4% the addition of Zr to the system increases fraction solute atoms that are then available for the formation of the strengthening precipitates.

It is well known from literature that Al_3(Sc,Zr) precipitates exhibit a core-shell structure.[97–103] Clouet et al.[104–106] used ab-initio calculations to show that this can be attributed to the different diffusivities of Sc and Zr in Al. Due to the faster diffusion of Sc the Al_3Sc precipitates will form primarily. Later during ageing a Zr-rich Al_3(Sc,Zr) shell forms around those precipitates.

We investigated an AlMg4Sc0.4Zr0.12 (wt.%) alloy[62,107–109], which had been casted to an 8mm thick, 280mm wide and more than 30m long strand via a continuous belt-casting technology. We could demonstrate that this alloy revealed a solute Sc-content of 0.13 wt.% at room temperature.[62]

Some of the samples will be referred to as electron beam re-solidifed (EBRS). This process was performed to increase the amount of solute Sc and Zr in the Al-matrix, which will finally increase its mechanical resistance.[108] We found, that the percentage of Sc in solid solution increases to 0.37 wt.% after EBRS treatment.[108] During this procedure an electron beam is used to locally rapidly melt and re-solidify the material. An industrially applicable process expected to have a very similar effect and thus lead to a comparable increase of solute Sc and Zr would be rapid melting and solidification via laser beams.

3.2 Thermodynamic Basis of Phase Transformations

One question that will be answered in this thesis is why we find the investigated precipitates in a certain final state. Therefore we have to consider which state of the Al - Al_3(Sc,Zr) system is energetically favourable, and we have to consider diffusion mechanisms. The thermodynamic basics for those considerations are treated in this section.

3.2.1 Gibbs Energy

The internal energy (*U*) of a thermodynamic system can be described as follows:

$$U = TS - PV + \sum_i \mu_i N_i \tag{37}$$

Where *T* and *S* represent temperature and entropy, while *P* and *V* stand for pressure and volume, and μ_i and N_i are the chemical potential and the number of moles of a certain component.[110]

Free energy is the part of the total energy of the system that is available to do thermodynamic work. While the Helmholtz Energy is widely used to describe the energy which is free for chemical processes, the Gibbs Energy (G) is practical for describing energy which is available for solid state phase transformations.[110] The Gibbs energy excludes contributions to the internal energy of purely mechanical work. It is a state function that describes the free energy of isothermal, isobaric systems very well, which are conditions which tend to apply to systems going through solid state phase transformations. The Gibbs energy can be described as

$$G = U + PV - TS \tag{38}$$

It follows:

$$G = \sum_i \mu_i N_i \tag{39}$$

3.2.2 Mechanical Mixture vs. Ideal Solution

If free energy is regarded there are two fundamentally different approaches of mixing matter: The mechanical mixture and the ideal solution represent those two extremes, whereas in nature typically a combination of both will be found.

The mechanical mixture represents the easily imaginable case, where blocks of two substances A and B are broken into smaller pieces (e.g.by grinding) and brought together.[110] So finally we end up with a material consisting of two separate phases A and B. The free energy of the system is then simply given by the weighted sum of the two initial phases. If *g* stands for G/mol, g_i^0 for the pure molar Gibbs energy of the component *i* and X_i for N_i/N we retrieve the molar Gibbs Energy of a mechanical mixture g_{MM} as:

$$g_{MM} = \sum_i X_i g_i^0 \tag{40}$$

Figure 24 shows the resulting linear dependence of the Gibbs energy of the mechanical mixture on concentration.

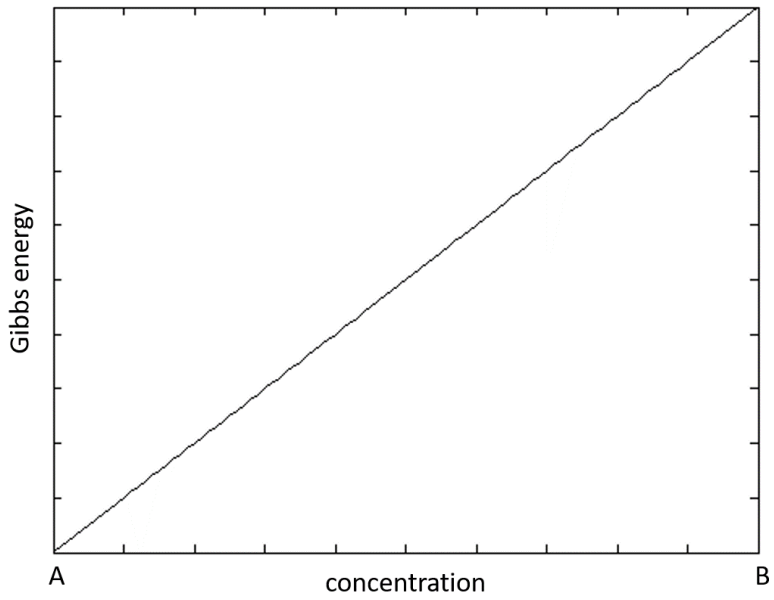

Figure 24: Gibbs energy of a mechanical mixture of two components.

In a solid solution, however, the mixing of the two atom types occurs at the atomic level. This greatly impacts the free energy of the system. Whereas in the case described above the relatively (compared to the atomic scale) large chunks of material are basically immobile, the atoms can move by exchanging lattice positions with vacancies. This stochastic kind of movement is called diffusion.[110]

The driving force for diffusion is entropy. An increase in entropy decreases the free energy of the system. Even though if atoms are regarded at a microscopic scale the principle of time reversal holds, at the macroscopic scale diffusion is an irreversible process.[110] Being more elaborate we can regard a number of atoms and will find that it is just as likely for two atoms to change their places, as it is for them to change them back. But if a huge number of position swaps takes place in a huge volume it becomes statistically very unlikely that the original state is reached again – even though it is as likely, as any other state – due to the large number of states available.

Entropy was described via the microcanonical density of states Ω_{mc} by Ludwig Boltzmann

$$S = k_B \ln \Omega_{mc} \tag{41}$$

Of which Ω_{mc} represents the driving force for diffusion

$$\Omega_{mc} = \frac{N!}{N_A!\, N_B!} \tag{42}$$

With $N = N_A + N_B$

N! can further be approximated by

$$N! = NlnN + N + O(logN) \tag{43}$$

Therefore

$$S \approx k_B(NlnN - N_A lnN_A - N_{\boldsymbol{B}} lnN_B) \tag{44}$$

By substituting $X_A = \frac{N_A}{N}$ and $X_B = \frac{N_B}{N}$ we can get the following form of the equation using concentrations:

$$S = -k_B N(X_A lnX_A + X_{\boldsymbol{B}} lnX_B) \tag{45}$$

This equation can of course also be formulated for a multicomponent system:

$$S = -k_B N \sum_i X_i lnX_i \tag{46}$$

With $R = N_A k_B$ - N_A being Avogadro's number, which equals *N* for one mole of atoms – we obtain

$$s = -R \sum_i X_i lnX_i \tag{47}$$

for the molar entropy of the ideal solution. The molar Gibbs energy component arising from the solid solution then is

$$g = -Ts = RT \sum_i X_i lnX_i \tag{48}$$

The Gibbs energy of a system, which is neither purely mechanical, nor purely solid solution, but a combination of both, can simply be described by the linear combination of the two. [110] Equation 49 gives the molar Gibbs energy of this so-called "ideal solution".

$$g = \sum_i X_i g_i^0 + RT \sum_i X_i lnX_i \tag{49}$$

The Gibbs energy of the ideal solution in dependence on concentration is shown in Figure 25.

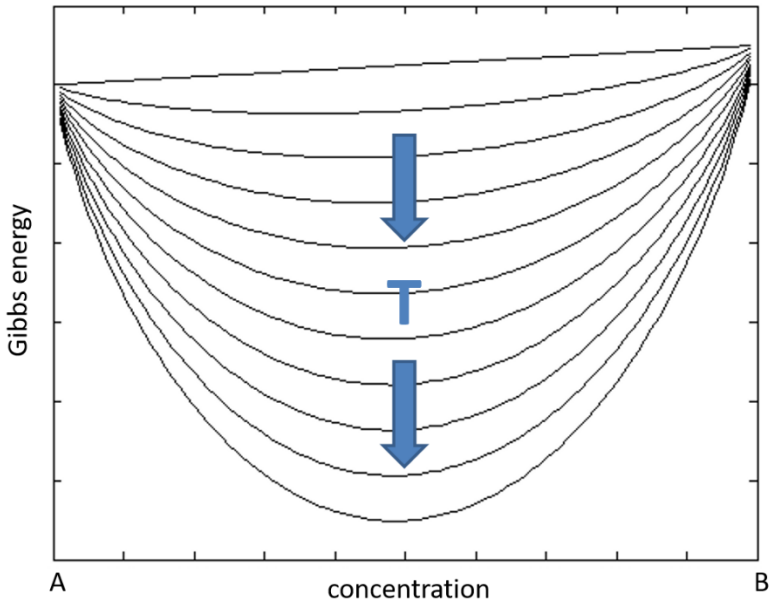

Figure 25: Gibbs energy of an ideal solution of two components for different temperatures.

3.2.3 The Regular Solution Model

In the ideal solution the various types of chemical and mechanical interactions between different types of atoms are not taken into account. This step is covered by the regular solution model.

Bond energies are taken into account. We want to calculate the change of energy of a system that arises purely from the change in bond energies when mixing two pure substances A and B. This energy difference ΔH is called "enthalpy of solution" or "enthalpy of mixing". Therefore we first calculate the bond energies of the pure substances A and B and then subtract these from the sum of the bond energies from the mixed system.

In the pure substance only bonds between atoms of same kinds are possible therefore we only need to calculate total energy of bonds between A and A atoms E_{AA}, and B and B atoms E_{BB}:

$$E_{AA} = \frac{1}{2} z_L N_A \varepsilon_{AA} \tag{50}$$

$$E_{BB} = \frac{1}{2} z_L N_B \varepsilon_{BB} \tag{51}$$

Where z_L is the coordination number, N_A and N_B the number of atoms in substance A and B and ε_{AA} and ε_{BB} are the bond energies between atoms A and A, and B and B, respectively. The factor of ½ makes sure every bond is only counted once.

In case of a solid solution, where atoms of kind A and B are mixed the number of the total energy of bonds of same kind atoms now changes due to the fact that not all neighbouring atoms are of the same kind. If both kinds of atoms are randomly mixed the probability of neighbouring atoms being of the same kind (and therefore the bond being with a same kind atom) will simply depend on the

concentration of that species X_A or X_B. Therefore the total energies of same kind bonds in the solid solution are given by:

$$E_{AA}^{S} = \frac{1}{2} z_L N_A X_A \varepsilon_{AA} \tag{52}$$

$$E_{BB}^{S} = \frac{1}{2} z_L N_B X_B \varepsilon_{BB} \tag{53}$$

In the solid solution we now also find bonds between atoms of type A and B. We first want to count the number of atoms of type A bonding with atoms of type B and then resume the total energy of all those bonds, by multiplying with the bond energy. By following the same train of thought as above, we find that we merely have to exchange X_A for X_B. We therefore get:

$$E_{AB}^{S} = \frac{1}{2} z_L N_A X_B \varepsilon_{AB} \tag{54}$$

In case of atom type B bonding with atom type A we have to exchange X_B for X_A, which leads to:

$$E_{BA}^{S} = \frac{1}{2} z_L N_B X_A \varepsilon_{BA} \tag{55}$$

If we then make use of the relations $N_A = NX_A$ and $N_B = NX_B$, as well as $\varepsilon_{AB} = \varepsilon_{BA}$ we find the obvious:

$$E_{AB}^{S} = \frac{1}{2} z_L N_A X_B \varepsilon_{AB} = \frac{1}{2} z_L N X_A X_B \varepsilon_{AB} = \frac{1}{2} z_L N X_B X_A \varepsilon_{BA} = E_{BA}^{S} \tag{56}$$

And:

$$E_{AB}^{S} + E_{BA}^{S} = 2 * \frac{1}{2} z_L N X_A X_B \varepsilon_{AB} = z_L N X_A X_B \varepsilon_{AB} \tag{57}$$

If we then also use those relations for the number of atoms, on E_{AA}^{S} and E_{BB}^{S}, as well as on E_{AA} and E_{BB} we get

$$H^S = E_{AA}^{S} + E_{BB}^{S} + 2E_{AB}^{S} = \frac{1}{2} z_L N X_A X_A \varepsilon_{AA} + \frac{1}{2} z_L N X_B X_B \varepsilon_{BB} + z_L N X_A X_B \varepsilon_{AB} \tag{58}$$

$$H^S = \frac{1}{2} z_L N [X_A X_A \varepsilon_{AA} + X_B X_B \varepsilon_{BB} + 2 X_A X_B \varepsilon_{AB}] \tag{59}$$

for the enthalpy of the solid solution and

$$H = E_{AA} + E_{BB} = \frac{1}{2} z_L N X_A \varepsilon_{AA} + \frac{1}{2} z_L N X_B \varepsilon_{BB} \tag{60}$$

$$H = \frac{1}{2} z_L N [X_A \varepsilon_{AA} + X_B \varepsilon_{BB}] \tag{61}$$

for the enthalpy of the system of two pure substances.

To gain the enthalpy of mixing we now subtract these two enthalpies:

$$\Delta H = H^s - H \tag{62}$$

$$\Delta H = \frac{1}{2} z_L N [X_A X_A \varepsilon_{AA} + X_B X_B \varepsilon_{BB} + 2 X_A X_B \varepsilon_{AB}] - \frac{1}{2} z_L N [X_A \varepsilon_{AA} + X_B \varepsilon_{BB}] \tag{63}$$

$$\Delta H = \frac{1}{2} z_L N [X_A X_A \varepsilon_{AA} + X_B X_B \varepsilon_{BB} + 2 X_A X_B \varepsilon_{AB} - X_A \varepsilon_{AA} - X_B \varepsilon_{BB}] \tag{64}$$

By further using the relations $X_A = 1 - X_{\boldsymbol{B}}$ and $X_B = 1 - X_{\boldsymbol{A}}$ we get

$$\Delta H = \frac{1}{2} z_L N [(1 - X_B) X_A \varepsilon_{AA} + (1 - X_A) X_B \varepsilon_{BB} + 2 X_A X_B \varepsilon_{AB} - X_A \varepsilon_{AA} - X_B \varepsilon_{BB}] \tag{65}$$

$$\Delta H = \frac{1}{2} z_L N [X_A \varepsilon_{AA} - X_B X_A \varepsilon_{AA} + X_B \varepsilon_{BB} - X_A X_B \varepsilon_{BB} + 2 X_A X_B \varepsilon_{AB} - X_A \varepsilon_{AA} - X_B \varepsilon_{BB}] \tag{66}$$

$$\Delta H = \frac{1}{2} z_L N [-X_B X_A \varepsilon_{AA} - X_A X_B \varepsilon_{BB} + 2 X_A X_B \varepsilon_{AB}] \tag{67}$$

$$\Delta H = \frac{1}{2} z_L N X_A X_B [-\varepsilon_{AA} - \varepsilon_{BB} + 2\varepsilon_{AB}] \tag{68}$$

We can further define the regular solution parameter ω_{AB} as

$$\omega_{AB} = z_L (-\varepsilon_{AA} - \varepsilon_{BB} + 2\varepsilon_{AB}) \tag{69}$$

and get

$$\Delta H = \frac{1}{2} N X_A X_B \omega_{AB} \tag{70}$$

The regular solution parameter is extremely interesting, as we can learn a lot about the behaviour of two substances when joined in solid solution simply by looking at the sign of the regular solution parameter:

In case $\omega_{AB} > 0$ energies of bonds between same atomic species are lower than energies of bonds between atoms of different kinds. The system's striving to minimum energy leads to a phase separation. This may lead to spinodal decomposition.

In case $\omega_{AB} = 0$ the enthalpy term equals zero and mixing is purely random. In this case the ideal solution model holds.

In case $\omega_{AB} < 0$ bonds between unlike atoms are energetically favourable compared to bonds of atoms belonging to the same species. Now second (or even higher order) nearest neighbour energies become relevant. If second nearest neighbours of the same species are favourable, local regions with short range ordering will appear. In case atoms of the other species are favourable, atoms of the

minor species will show large distances from each other in order to maximise the number of unlike neighbours.

After this short excursion to the meaning of the regular solution parameter we want to conclude this section on the regular solution with its Gibbs energy. As the molar version of the Gibbs energy is more practical to work with, we transform *ΔH* to its molar version *Δh*:

$$\Delta h = \frac{1}{2} X_A X_B \omega_{AB} \tag{71}$$

Or for more components:

$$\Delta h = \frac{1}{2} \sum_i \sum_{j>i} X_i X_j \omega_{ij} \tag{72}$$

We then obtain the molar Gibbs energy of the regular solution by adding the molar enthalpy of mixing to the molar Gibbs energy of the ideal solution:

$$g_{RS} = g_{IS} + \Delta h = \sum_i X_i g_i^0 + RT \sum_i X_i ln X_i + \frac{1}{2} \sum_i \sum_{j>i} X_i X_j \omega_{ij} \tag{73}$$

The resulting Gibbs energy of the regular solution in dependence on concentration for different temperatures can be seen in Figure 26.

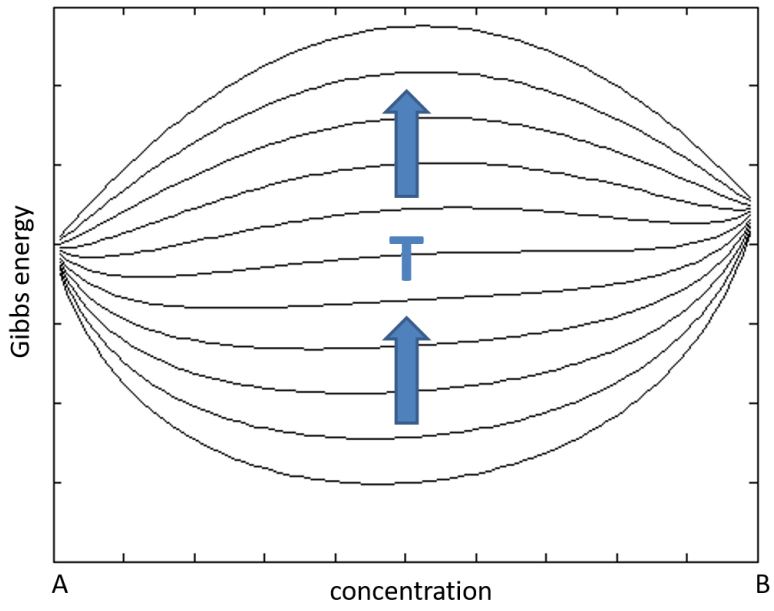

Figure 26: Gibbs energy of a regular solution of two components for different temperatures.

3.3 Fick's Laws of Diffusion

Adolf Eugen Fick stated that the flux of matter J is proportional to the gradient of concentration. This relation is known as Fick's first law of diffusion and for one dimension equals[110] :

$$J = -D\frac{dc}{dx} \tag{74}$$

The proportionality factor *D* is called the diffusion coefficient. For multiple dimensions Fick's first law can be written as:

$$J = -D\nabla c \tag{75}$$

Via chemical potentials Fick's first law for a certain species can be formulated as[110]:

$$J_i = -\frac{D_i c_i}{RT}\frac{\partial \mu_i}{\partial x} \tag{76}$$

Fick's second law describes the change of concentration over time and can be written as:

$$\frac{\partial c}{\partial t} = -\nabla J = -\nabla(-D\nabla c) \tag{77}$$

where Fick's first law was used to rewrite the equation. In case the diffusion coefficient is not dependent on concentration this can be simplified to:

$$\frac{\partial c}{\partial t} = D\nabla^2 c = D\Delta c \tag{78}$$

Part II Development and Evaluation of Methods

4 New Developments in Analytical Electron Tomography

4.1 Introduction

While conventional analytical (S)TEM signals are a very powerful tool for the determination of composition, they suffer from one major disadvantage: The intrinsic property of transmission electron microscopy that the signal will always be a projection - an integrated signal in beam direction. Therefore, while even atomic resolution can be achieved in x- and y-direction, there is no resolution at all in z-direction. Tomography in (S)TEM on the other hand allows us to even resolve the information in z-direction, this information however is only morphological. HAADF tomography might allow us to draw some conclusions on what kind of phases are present if enough prior knowledge of the sample is available through Z-contrast, but no compositional information can be gained. It seems obvious that a combination of those two methods (as symbolically shown in Figure 27) is necessary to gain unambiguous knowledge of samples. Therefore, this was one of the main goals of this thesis.

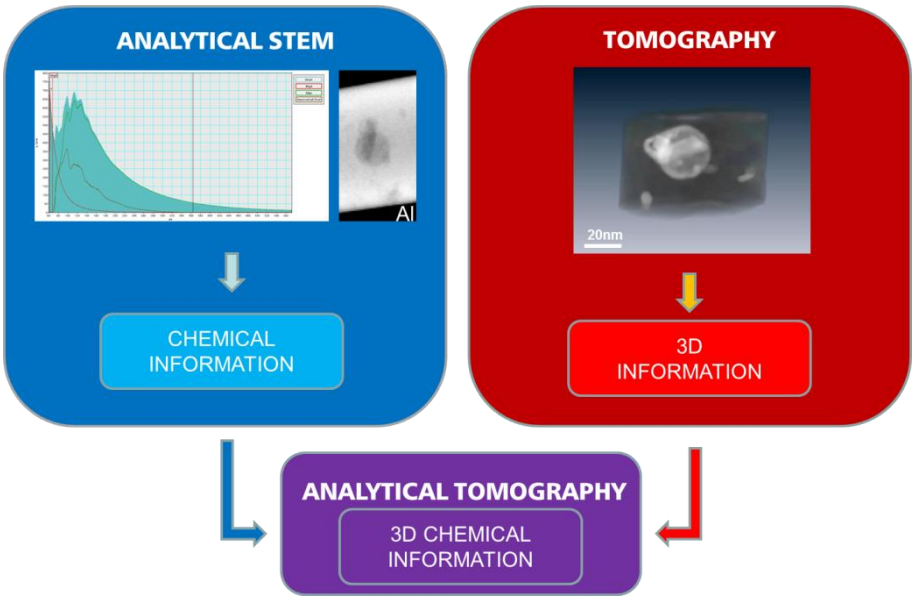

Figure 27: Analytical tomography, the combination of analytical STEM and tomography to gain 3D chemical information

The idea to use signals that do not only give morphological information for performing tomography has not only come up, but was also already followed by several groups in the past decade.[12,18,60,47–49,51–55] But apart from demonstrative examples showing that reconstructions of such signals are possible the method was not widely used for answering material scientific questions. Also its potential was by far not reached, as simultaneous EELS and EDX tomography, as well as the reconstructions of whole spectra have not been done. So at this point two missions were to be accomplished by our workgroup:

1) Establish analytical electron tomography including simultaneous EELS and EDX tomography and reconstruct whole data cubes (as schematically shown in Figure 28) so that compositional information can be retrieved from any region of interest within the sample.[56]
2) Advance from the proof of concept by using the technique on "real" samples to retrieve material scientifically relevant information which is otherwise unavailable.[111]

To reach the first goal a great amount of coding was necessary. The software allowing tomographic alignment and reconstruction for analytical tomography was also created by this workgroup, primarily by Georg Haberfehlner, who created a not yet published, Matlab based software package "ToReAl", which stands for "Tomographic Reconstruction and Alignment".

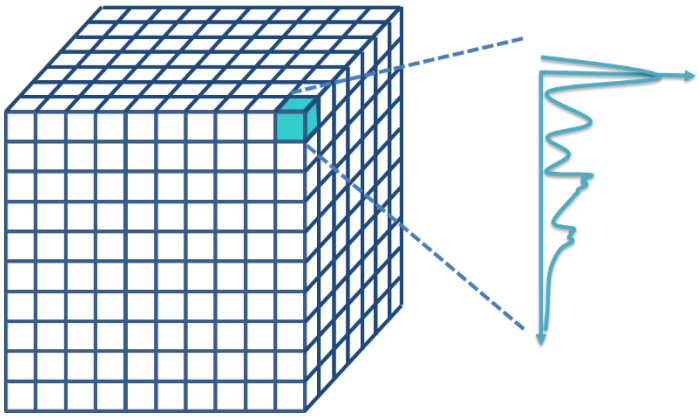

Figure 28: Scheme of a 4D "data cube". In opposition to a data cube received from an SI (see section 2.2.4 and Figure 12), in a 4D "data-cube" every voxel (instead of pixel) contains one or more spectra.

4.2 Basic Procedures

We wanted to tackle analytical tomography in its probably most versatile[iii] approach: Through the acquisition of simultaneous EELS- and EDX spectrum images. The scheme in Figure 29 shows the steps necessary when performing analytical tomography in that sense. Basically the same three steps have to be carried out, as in conventional HAADF tomography: Acquisition, alignment and reconstruction. The main difference lies in the fact, that during acquisition not simple images are acquired, but spectrum images (SIs - see section 2.2.4), which means that every single image pixel contains a whole spectrum. Consequently the signals need to be processed prior to alignment and reconstruction, to again have images for these following steps. This therefore necessary additional step is marked in pink in the scheme shown in Figure 29.

We will later discuss two different types of analytical tomography we developed: 3D elemental mapping and voxel spectroscopy. The acquisition is the same for both methods, and they can therefore both be applied to the same data set. The main difference lies in the processing step (marked pink in the scheme in Figure 29) and the output of course. Roughly summarised, the 3D

[iii]" versatile", because in addition to the image series (typically HAADF) EELS and EDX signals can be acquired simultaneously, each leading to a "4D-data cube" from which basically any signal of interest can be reconstructed further on in the process. This can be useful, not only because, EELS and EDX sometimes deliver complementary information, but especially, because in comparison to EFTEM tomography less prior knowledge of the signal of interest is required at acquisition.

(elemental)[iv] maps allow a more visual analysis, as they give a 3D distribution of a specific element or feature, while in voxel spectroscopy the whole spectroscopic data is reconstructed and left to be analysed after the reconstruction. This allows a quantitative analysis of the 3D spectroscopic data.

It can be a great advantage to use both methods on one dataset: first 3D elemental mapping to get a 3D overview of the elemental distribution. As elemental map reconstructions are computationally less time consuming than the reconstruction of whole spectra, they also allow the use of more elaborate reconstruction algorithms like compressed sensing[33–36] techniques, and therefore may lead to better reconstructions, depending on the sample. The ease at which the 3D elemental maps can be interpreted visually, can be an important aid for planning how to proceed with voxel spectroscopy, concerning the set-up of the reconstruction as well as further (quantitative) analysis.

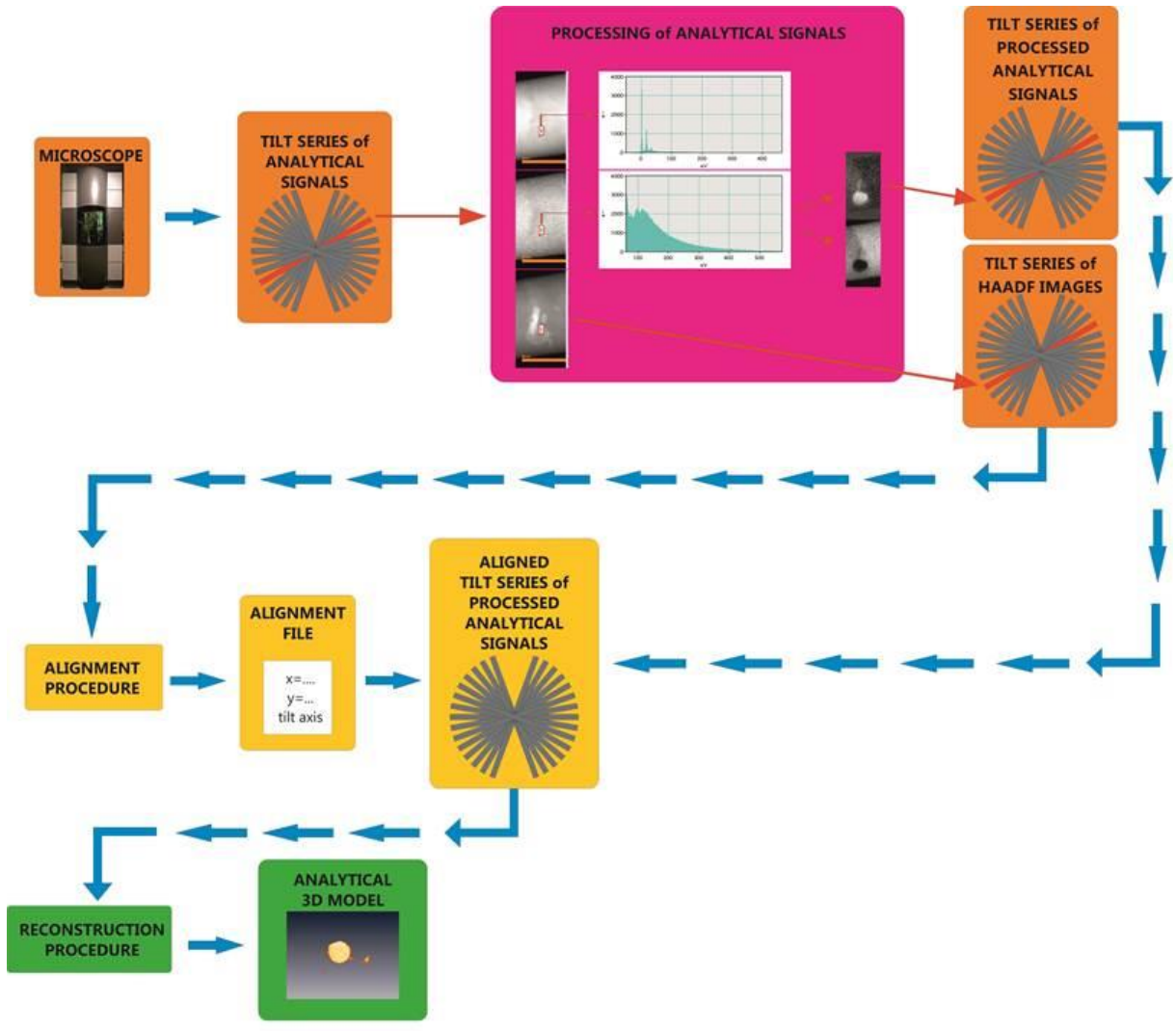

Figure 29: Scheme of the workflow leading to analytical tomographic reconstructions.

[iv] Of course not only elemental distributions can be mapped, but also other interesting features that could be gained from spectroscopic EELS data, like e.g. plasmons, or the fine structure.

4.2.1 Acquisition

Acquisition is a crucial part of the procedure in which perfection is simply not possible – in several ways. The first and probably most crucial factor is time. Figure 30 schematically illustrates how a trade-off between long acquisition times for a good signal to noise ratio, and keeping acquisition times low enough that

1) sample damage or carbon deposits will not change the sample throughout the tilt series
2) the acquired images (especially if they are spectrum images) will not suffer from sample and beam drift leading to distortion

has to be made. Concerning the avoidance of sample change, also the number of tilt angles needs to be taken into account. Therefore this number will typically be lower than for a conventional TEM or STEM tomographic acquisition.

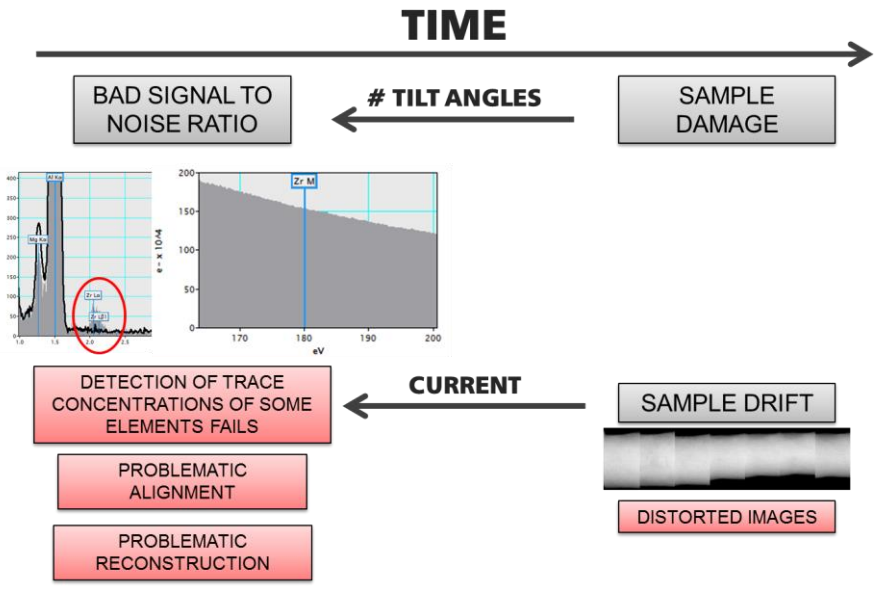

Figure 30: Scheme of key factors (grey boxes) which need to be taken into account when choosing acquisition times in analytical tomography, and possible consequences (red boxes). The EDX and EELS spectrum on the left have been acquired simultaneously and demonstrate a case where Zr could not be detected. The image on the right shows a series of images of a cylindrically shaped sample at different tilt angles and the distortion they suffer at some tilt angles due to drift.

When the work for this thesis was done there was no automated acquisition software for analytical tomography available. Therefore it also had to be taken into account that throughout the tilt series a microscopist had to actively perform the acquisition, which might also be a time limiting factor. As analytical tomography has increasingly aroused interest, commercial software has recently become available, that not only allows automated acquisition of EDX tomographic series, but will also close the column valves of the microscope after acquisition.[112] Consequently it is possible to acquire at least an EDXS tilt series without the constant presence of a microscopist, at least after a thorough set up of the system.

4.2.2 Alignment

Alignment does not differ from conventional tomographic alignment[v], except for one major advantage. In analytical tomography performed via spectrum images you will typically have several

[v] As long as image distortions could be avoided during acquisition.

different kinds of images/maps acquired simultaneously. Therefore the signal most useful for alignment can be used to get the alignment data – these may even be a different signals for shifts in x and y and also the tilt axis. The alignment data can then be applied to all the signals.

4.2.3 (Elemental) Map Reconstructions – "Analyse First – Reconstruct Second"

Basically not only elemental maps can be reconstructed, but any kind of feature from a spectrum which can be mapped. One very prominent and important example, where this work group has contributed major publications, are plasmons.[113,114] In this thesis, however, the elemental maps are the central feature. The focus lay on EELS and EDX elemental maps.

Characteristic for map reconstructions (as opposed to voxel spectroscopy) is that the analysis is performed before the reconstruction. The output of the processing step has to be a series of images, as this is the necessary input for the next step in the sequence – the alignment.

To allow an easy, but most importantly, identical processing of the whole tilt series, the whole tilt series of SIs was stitched with a Matlab script to have one large spectrum image. That way the whole tilt series can be processed at once so time can be saved, and human errors (leading to unequal processing of SIs at different tilt angles) can be avoided. Figure 31 shows an example of an elemental map of the whole tilt series resulting from a stitched SI. The maps obtained after processing have to be saved as a tilt series again, therefore the mrc file format was used. The processing of the stitched SIs was done via the Digital Micrograph software of Gatan[21].

Figure 31: Horizontally stitched EDX elemental map from stitched SI resulting from SI tilt series. All spectrum images acquired throughout the tilt series are horizontally aligned next to each other to form one large SI that can be processed at once. The variation of intensities throughout the tilt series stems from shadowing of the EDX detectors and is discussed in section 5.1.1

A model based approach was used for extracting 2D EDX elemental maps. A Kramers[115] model was applied for the background and fitting Gaussians to the K-peaks of each element. In Digital Micrograph this can be done for each pixel of the EDX spectrum images simultaneously. The integrated intensities are then mapped, leading to an image where high intensities correspond to high amounts of the mapped element in projection.

For EELS maps two windows were used for modelling the background (one in front of the edge and one after the edge – with some distance) if possible without interfering with other edges, and a signal window capturing the edge. A power law was used as a modelling approach for the background. For modelling the cross-section a Hartree-Slater[116] model was applied.

4.2.4 Voxel Spectroscopy – "Reconstruct First – Analyse Second"

In voxel spectroscopy every single energy channel of a tilt series of spectrum images is reconstructed. This results in a 4D "data-cube" (schematically shown in Figure 28) where every single voxel (3D pixel) contains a whole spectrum. Figure 32 shows the manifold of possibilities that come with that type of reconstruction. It is possible to obtain spectra from any region of interest within the data

cube. And it is possible to create maps of certain elements, or other features of interest within a spectrum.

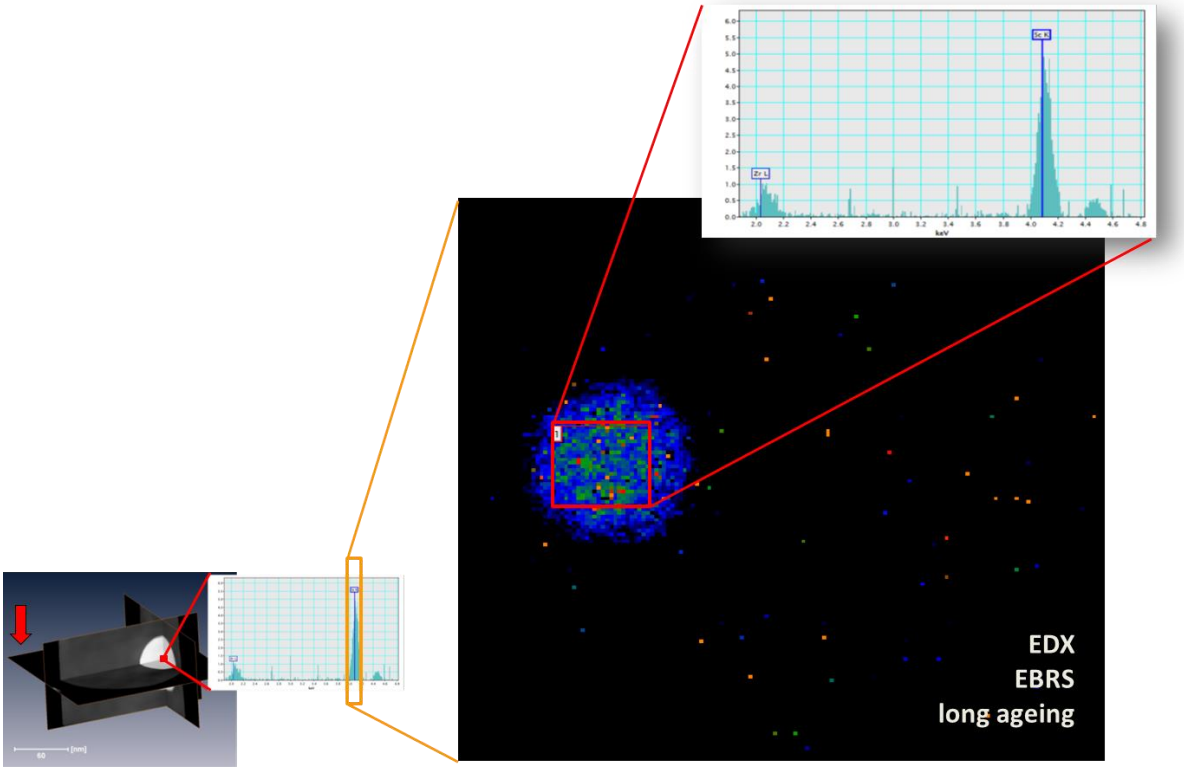

Figure 32: Voxel spectroscopy. Scheme of the different kind of information that can be obtained through the 4D "data cube" obtained via voxel spectroscopy. The red arrow in the image on the left indicates the plane that was chosen for the elemental map of Sc shown further on the right.

The reconstructions for voxel spectroscopy were performed using the multiplicative SIRT[31] algorithm. Multiplicative SIRT (as described in section 2.3.3) is often the method of choice, partly because it is a lot faster than TV minimisation. This becomes significant in voxel spectroscopy, because the number of channels of the spectrum equals the number of reconstructions performed, so the time difference between two algorithms per reconstruction needs to be multiplied by the number of channels, to get the final time difference. E.g. for a spectrum with 1024 channels and a time difference of 5 min per reconstruction the final time difference is three and a half days. But even if the time difference were not relevant in case the sample may have non-discreet compositional variations TV minimization is not a good choice, as it minimises gradients and therefore might not give a realistic representation of the sample. Furthermore it is in particular problematic, as every channel is treated independent of the others in reconstruction. Multiplicative SIRT is an ideal method of choice for any sample for which gradual variations of the reconstructed characteristics cannot be excluded, as it makes no prior assumptions at all. It needs to be mentioned that very recently (2019) another method was developed, which does allow the reconstruction of gradual changes and makes use of correlation between different datasets, like e.g. HAADF and EDXS or EELS data: The Total Generalized Variation (TGV) regularization[117] This method however was not available yet, when the work for this thesis was executed. At that time multiplicative SIRT was the best available method and therefore the method of choice.

4.2.4.1 Masks

To extract spectra from specific 3D regions of interest a segmented HAADF reconstruction can be used to create a mask. The segmentation can be - and was - performed using the Amira software package. Each voxel of the mask is then assigned a value, depending on what region it was assigned to during segmentation. This was done with the Image J software package[118]. Further a Matlab script was used to sum the spectra from the voxels with the same value. Due to the different amount of voxels in the different mask-regions, normalisation of the spectra might be useful for easier visual comparison. Figure 33 shows an example of such a mask, and the summed and normalised voxel spectra retrieved with it.

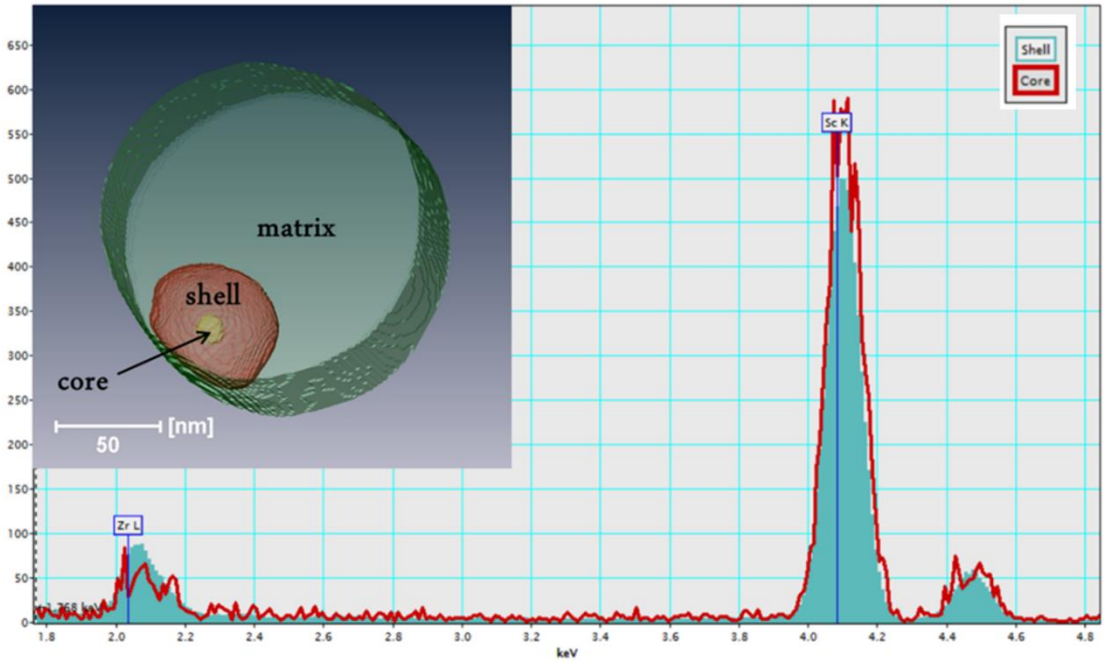

Figure 33: Normalised spectra extracted from a 4D EDX data cube via the mask shown in the left top corner.

5 Approaching 3D Quantification: Evaluation of Influences on Analytical Electron Tomography and Improvements

If we want to quantitatively evaluate tomographic results we need to consider the influences on resulting reconstructions. It is known[119] that channelling can have a significant influence on analytical signals determined in a crystalline sample. It is an open question, whether this is also true for analytical tomographic investigations. The second major influence we want to investigate is the absorption of X-rays within the sample during the tilt series. But before these questions can be answered there is still a long route to go: Sample preparation, acquisition conditions and data processing are developed further and improved. All these steps are taken to approach reliable quantitative analytical tomography.

5.1 Optimising Acquisition Conditions for Analytical Tomography

5.1.1 The X-ray Shadowing Problem

First analytical tomographic investigations were performed with a Fischione 2020 holder[120] and OmniProbe girds for support of FIB milled samples. It became clear, that the holder-detector geometry might lead to shadowing effects under some tilt angles. In a first approach to reduce shadowing the OmniProbe grids were modified, by cutting the M-shaped features off, with a razorblade under the light microscope. This, however, did not solve our problems, as the holder itself was the main source of shadowing of the Super-X detector system in the Titan[3]. Figure 34 shows EDX elemental map intensities over tilt angle, which reveal varying intensities throughout the whole tilt series, with the most shadowing at zero tilt.

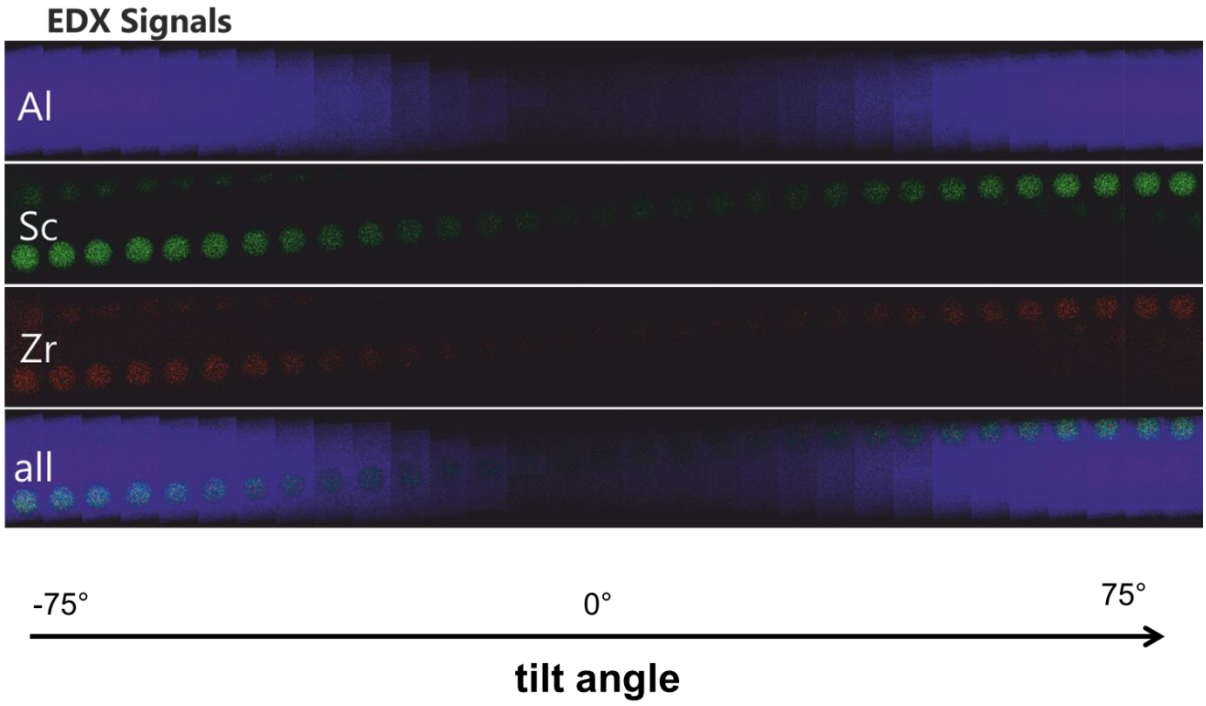

Figure 34: Series of EDX elemental maps for various tilt angles and elements obtained with the Fischione 2020 sample holder.

To analyse all the (geometric) influences of the holder-detector system on the finally detectable signal intensities a circular-symmetric sample was chosen. A layered Si sample was found fitting due to its radial symmetry, which ensures that there is no tilt-angle dependent absorption in the sample, and its high contrast enabling a precise alignment to ensure acquisition is performed at the same sample region at all tilt angles. A tilt series of EDX spectrum images was acquired, as shown in Figure 35.

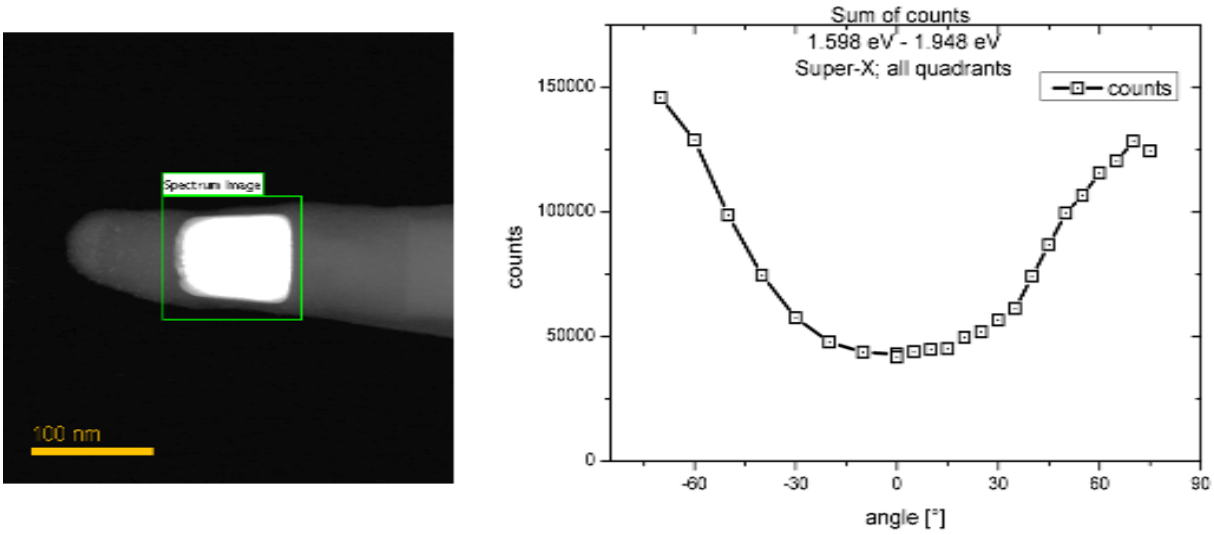

Figure 35: Left: Survey Image of one of the SIs acquired for the tilt series which was performed for the interpretation of the tilt dependant shadowing of the Fischione 2020 tomography holder. Right: Summed detector intensities of all 4 quadrants of the FEI Super-X detector summed over the Si Kα peak.

The intensities of the Si peaks were summed for each SI and are shown in Figure 35. The summation was performed from 1598 eV to 1948 eV without subtraction of the background. Just as it was visible for the Al sample, the signal is minimal at a tilt angle of 0°. The shadowing curve resembles a sine function. As the sample is tilted to higher angles the signal increases, as the X-rays can pass through the hole where the grid is mounted. But what is remarkable, is the quantity of the difference: At the lowest tilt angle the intensity is larger by a factor of three. Another interesting fact is that there are two different values for zero. This arose because first the tilt series was performed in two sequences: First from zero to 75° in 5° tilt steps. Then the sample was tilted back to 0° and then the sample was tilted from 0 to -70° in -10° tilt steps. The two different values for the zero degree intensity are explicable through the non-perfect tilting of the stage, refocussing with z-height, variations in the beam current or measurement uncertainty.

These investigations made it clear that the shadowing is too severe to neglect. The first approach was to account for this intensity variation by normalising the SIs prior to reconstruction via the total counts per SI. The second approach was to use a different sample holder, which is discussed in the next section.

5.1.2 Sample Holders for Tomography

The acquisition of a new sample holder, the Fischione 2050[121] (see Figure 36 on the right) was supposed to solve the shadowing problem. Additionally the holder is equipped with a mechanism, which allows to tilt the sample-holding part of the holder to a number of indicated positions without tilting the stage. By combining stage tilt and the mechanical sample tilt via the holder it is

consequently possible to tilt the sample a full 360°. Figure 36 shows images of the front parts of the Fischione 2020 and 2050 holders for comparison. The major improvement of the Fischione 2050 is that the sample is mounted on a needle. This results in the absence of shadowing parts on the sides of the holder, as can be seen in Figure 36. For analytical tomography this holder geometry should therefore eliminate the tilt dependent shadowing effect and even allow a full illumination of all 4 quadrants of the FEI Super-X detector.

Figure 36: Comparison of sample holders for tomography: Left: Fischione model 2020, where a FIB-grid can be mounted. The side parts of this holder cast shadows on the EDX detectors. The amount of shadowing is tilt angle dependent. Right: Fischione model 2050, where the sample is mounted on the tip of the needle in the front. This holder allows a 360° tilt. Furthermore the tilt dependent shadowing effect should be removed.

5.1.3 Sample Preparation – The Needle on Top of the Needle

The new sample holder also necessitates a revision of the sample support. For the previous holder model, the Fischione 2020, the needle shaped sample was mounted on the top of the finger of a conventional copper FIB-grid as can be seen in Figure 37. (To be specific, we used FIB grids from the manufacturer OmniProbe).

For the Fischione 2050 holder (see Figure 36 on the right) the samples were mounted on the tips of a needle-shaped support. As can be seen in Figure 38 the needles provided by Fischione are not needle shaped at microscopic scale. The “tip” actually is a flat region of about 50 µm. Compared to the needle shaped samples, this is a very large area. This has dramatic consequences for EDX investigations with the Super-X detector: The back two detectors are shadowed by the sample support. This is schematically shown in Figure 39.

Our next approach was to cut this plateau with the focused ion beam. But even after hours of milling with maximum currents, the situation was improved, but still not good enough. A next step was to cut unusually long needle shaped samples and to use FEBID technology to create a podium for the sample before it was mounted. The result of a combined approach – the podium, the extra-long sample and the milling – which still was not sufficient can be seen in Figure 40. Finally the decision was made, to buy needles made for electrical probing and to use them instead of the needles

provided by Fischione. Figure 41 shows a needle shaped sample mounted on such needle. This approach finally resulted in a non-shadowing geometry for tomographic EDX investigations.

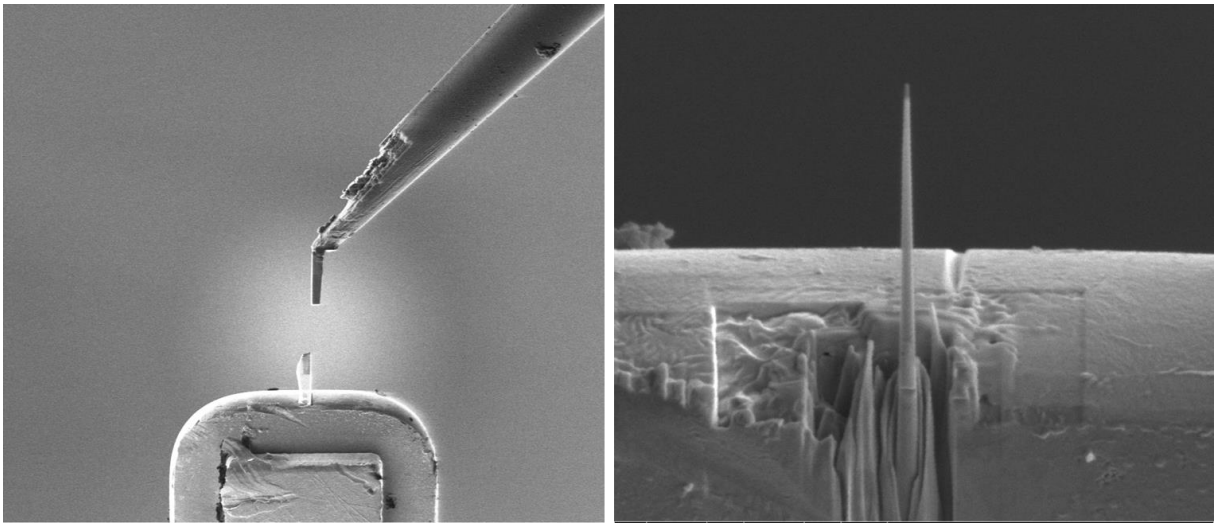

Figure 37: Needle shaped sample mounted on a FIB-gird. Left: During the process. Right: After milling and final thinning.

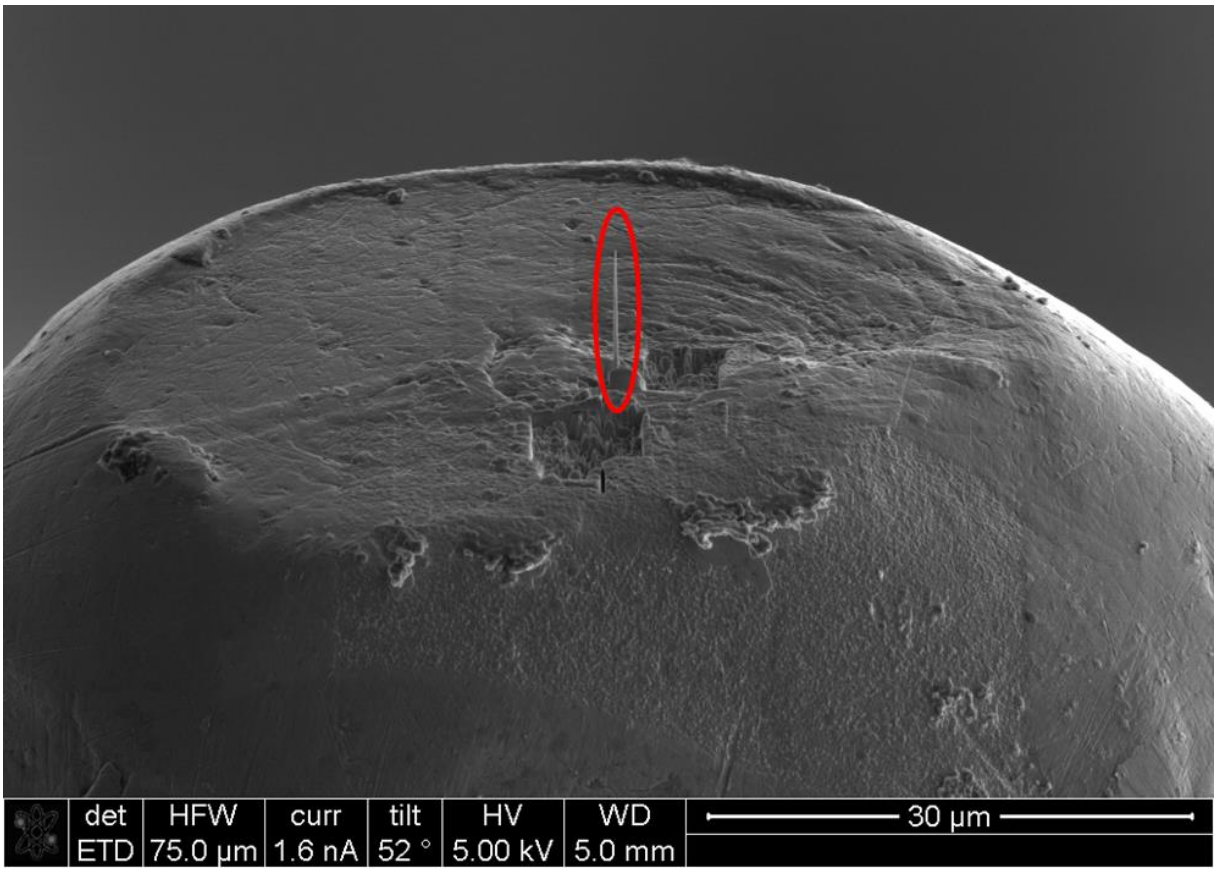

Figure 38: Needle shaped sample on needle of holder as supplied. The sample is highlighted with the red ellipse.

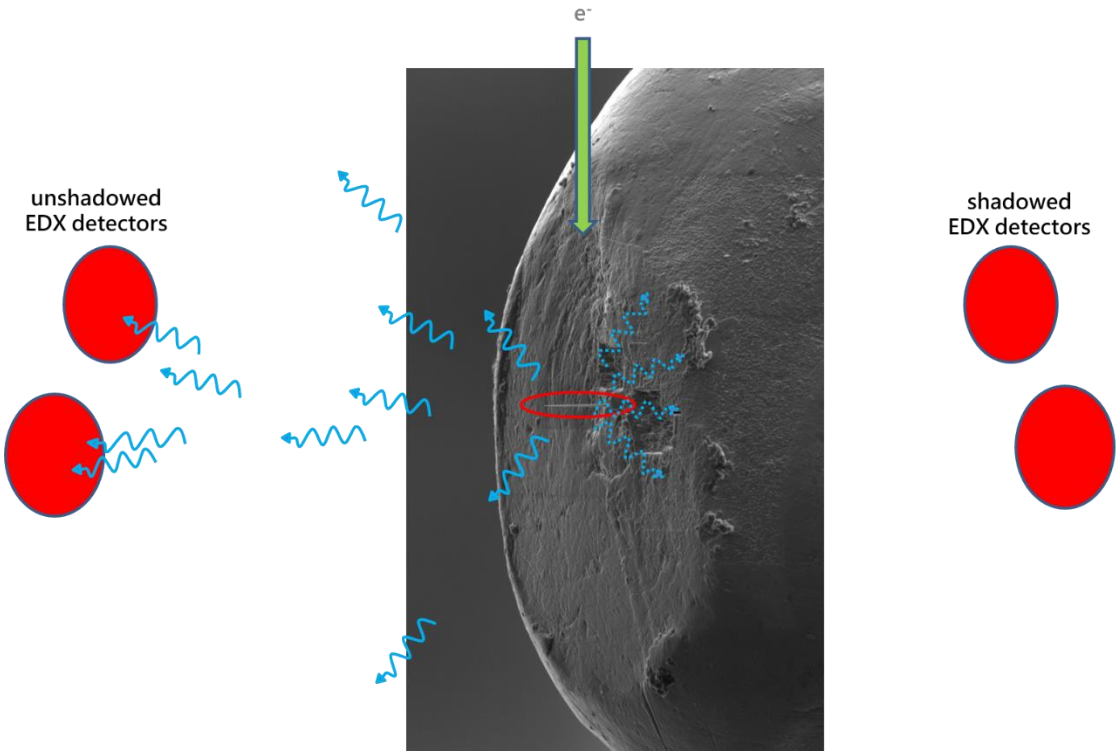

Figure 39: Scheme of how the tip of the sample support of the Fischione 2050 holder shadows the two of the four detectors of the Super X EDX detector system. The actual sample is marked with the red ellipse in the centre of the SEM image.

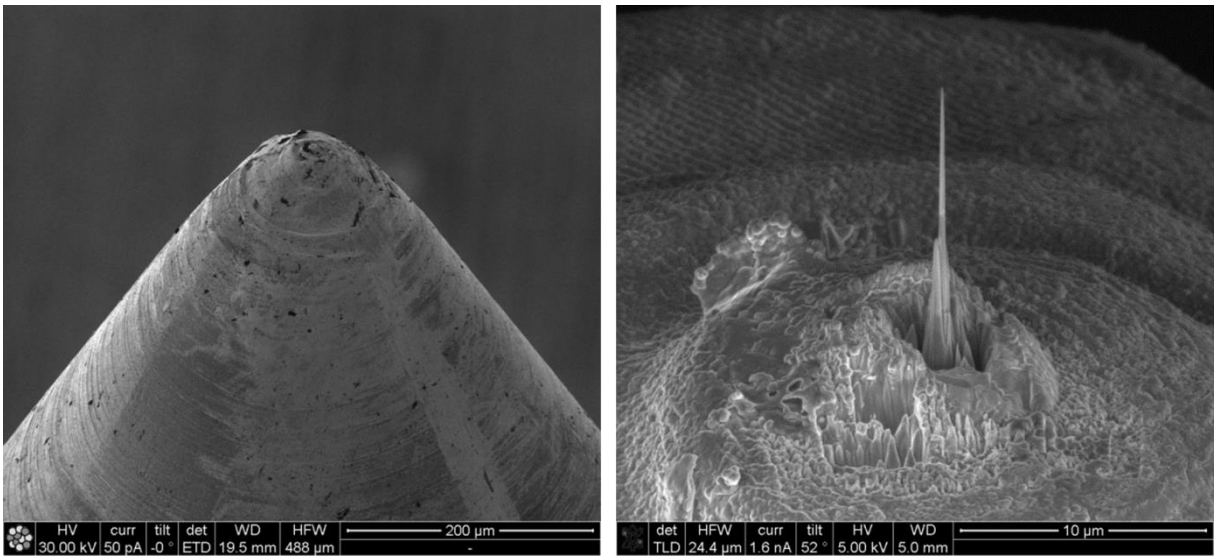

Figure 40: Left: Needle of the holder by supplier sharpened via FIB. Right: Needle shaped sample mounted on the sharpened holder needle on top of a platinum-podium.

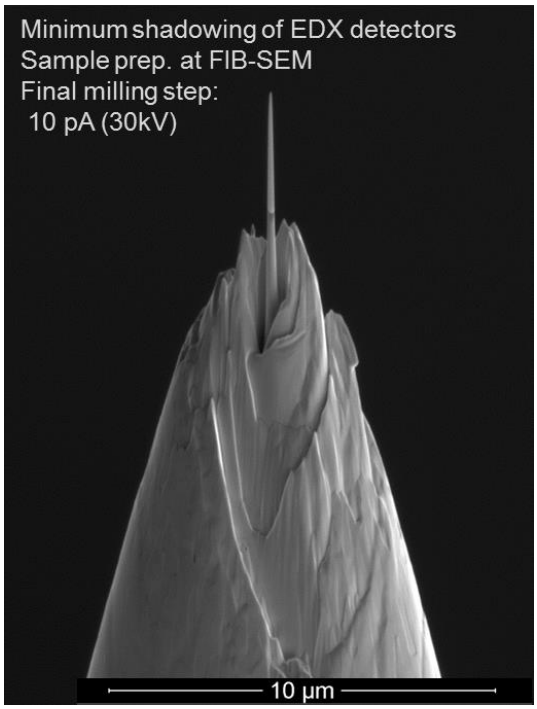

Figure 41: Ideal sample preparation to avoid shadowing of the EDX detectors, using sample-holding probes originally not produced for STEM investigations.

With this final geometry the improvement was obvious, as can be seen in Figure 42. Here we can see comparative tilt series of EDX elemental maps, of the same type of sample acquired with the two different holder systems. It is obvious, that with the Fischione 2050 system there is no angle dependent intensity variation. The overall intensity also is improved.

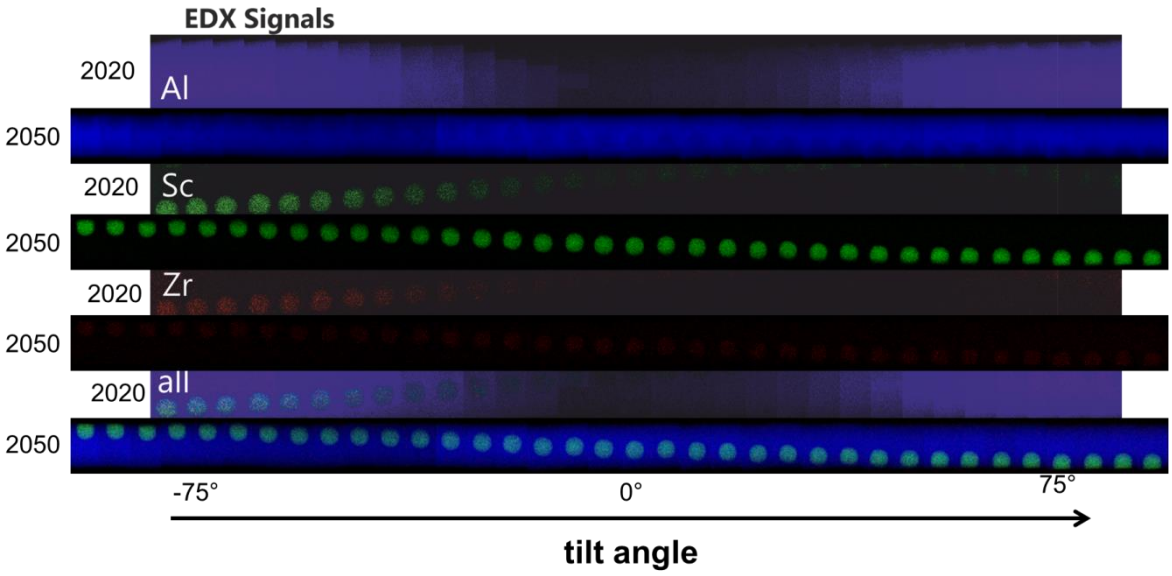

Figure 42: Comparison of EDX elemental maps obtained with the Fischione 2020 sample holder (marked 2020) and the Fischione 2050 sample holder (marked 2050).

5.2 Improvements in Data Processing and Evaluation of Data analysis

Additionally several improvements in data processing were made, like the creation of asymmetric filters for cross correlation, and a Matlab script, which removes spikes from EELS spectra prior to reconstruction. These spikes are basically a form of noise and do not represent the real energy distribution. They have, however, been found to cause artefacts in reconstructions.

The script was written as a function, so that it can easily be applied within another script. The function checks all projections channel by channel. A spike is identified by being larger that a certain factor (that can be chosen) multiplied with the average value of the corresponding pixels of the neighbouring projections. If a spike is identified, the value of this channel is replaced by this value. The EELS spike removal was performed on the data sets used for the EELS signal reconstruction in chapter 9.

To improve alignment for all cross-correlation based methods asymmetric filters were introduced. The asymmetric filters are useful, because we only use a small region of the sample for the SIs in tomography. Therefore, the edges of the images may considerable influence the cross-correlation. Using a filter that only allows information in x-direction to influence the alignment in x-direction can eliminate that influence. This asymmetric filter for cross correlation was used for the data shown in chapter 9 as well as the data published in Nature Materials[122].

Error analysis for voxel spectroscopic EDX quantification was carried out by evaluating error propagation due to the calculation of concentrations via k-factor method. Following Poisson statistics the error attributed to each peak was calculated via $\sigma = \sqrt{N}$, where N is the number of counts attributed to a certain peak after the background has been subtracted. For absolute concentration values the errors of the k-factors were assumed to equal 10 %. For relative data analysis, where compositions of different volumetric sample regions were compared, the error of the k-factors could be neglected, as it affects all analysed voxels the same. For concentration values, the error of the k-factor was included. This error analysis was performed on the data published on the diffusion-defining atomic-scale spinodal decomposition within nanoprecipitates[111].

All the Matlab scripts used for improved data processing and error calculation can be found in the appendix.

5.3 Evaluation of the Influence of Channelling

Channelling will influence an analytical investigation if it is performed in zone axis. This comes from that fact that differently occupied atomic columns have different potentials. This not only influences the HAADF signal, but also the EELS and EDXS signal of the elements occupying this column.[119] While electrons approaching one atomic column might be attracted onto the column and thus deliver an increased signal of the elements occupying this column, it may be nearly unaffected by another column, thus not enhancing its signal. This is schematically shown in Figure 43. The probably most prominent example is that published by Kothleitner et al.[119]of strontium titanate (STO). There is the same number of oxygen atoms on the pure oxygen (O) column as on the titanium-oxygen (Ti-O) column. But due to channelling the signal on the Ti-O column is a lot higher.

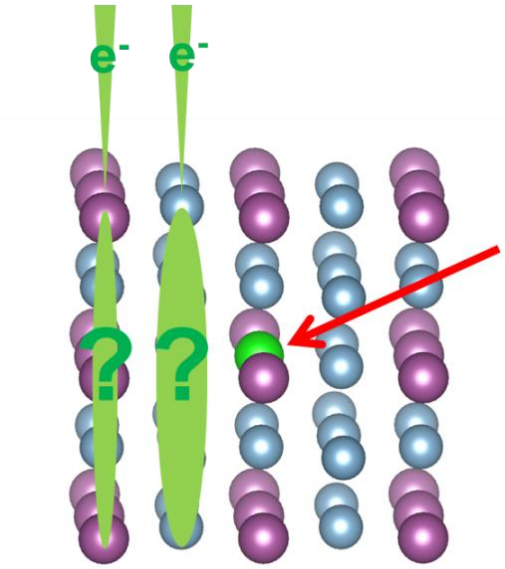

Figure 43: Channelling: Differently occupied atomic columns have a different impact on incoming electrons and therefore may, or may not lead to the enhancement of analytical signals.

The open question is, whether the influence of channelling in analytical tomographic investigations of crystalline samples is significant. We designed an experiment to evaluate this, which is schematically shown in Figure 44. For this investigation a rod shaped Al sample was chosen with an $Al_3(Sc,Zr)$ precipitate on one side, as symbolically shown in Figure 44 (top). Assuming channelling conditions, it makes a difference whether the beam first moves through the precipitate, and then through the Al or vice versa, as the beam will experience a different potential (schematically shown in Figure 44 – middle). From tomographic point of view (assuming non-channelling conditions) two sets of projections form exactly opposite sides (180° difference in tilt) will lead to the same reconstructed object. Therefore the comparison of two reconstructions from opposing sides of a crystalline sample with a precipitate on one side allows us to judge, whether channelling has a significant influence on tomographic reconstructions of our samples.

The experiment was performed with various convergence angels (10 mrad, 19 mrad and 28 mrad), because channelling conditions are expected to change with convergence angle. For the reconstructions the multiplicative SIRT algorithm was chosen, as it makes no primary assumptions on the sample, and therefore is most likely not to influence the result. Due to the high tilt range (180° per reconstruction) and the use of the HAADF signal, which has a very low noise level, artefacts are not expected to be dominant. Figure 45 shows a diffraction pattern exhibiting Kikuchi lines acquired via screenshot from the Flucam (camera recording image on viewing screen in the Titan[3]), proving crystallinity of the sample.

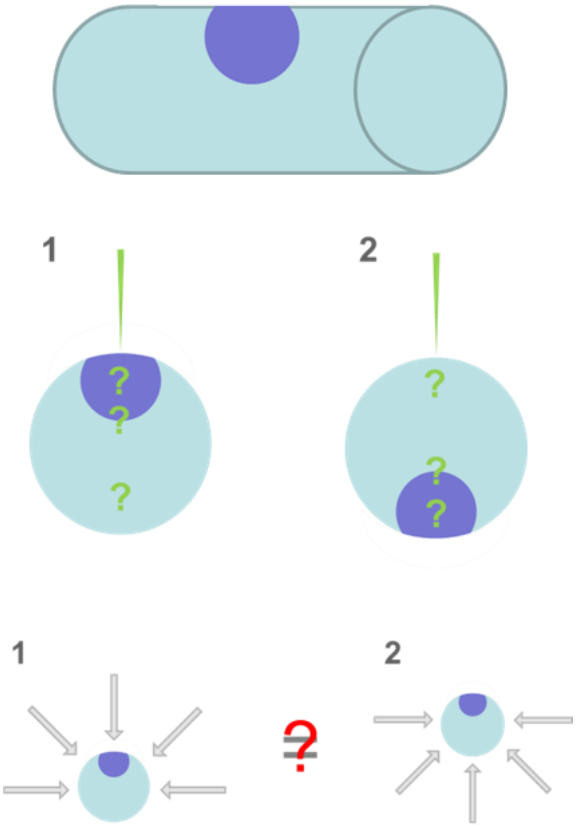

Figure 44: Channelling in tomography. Concept of experiment.

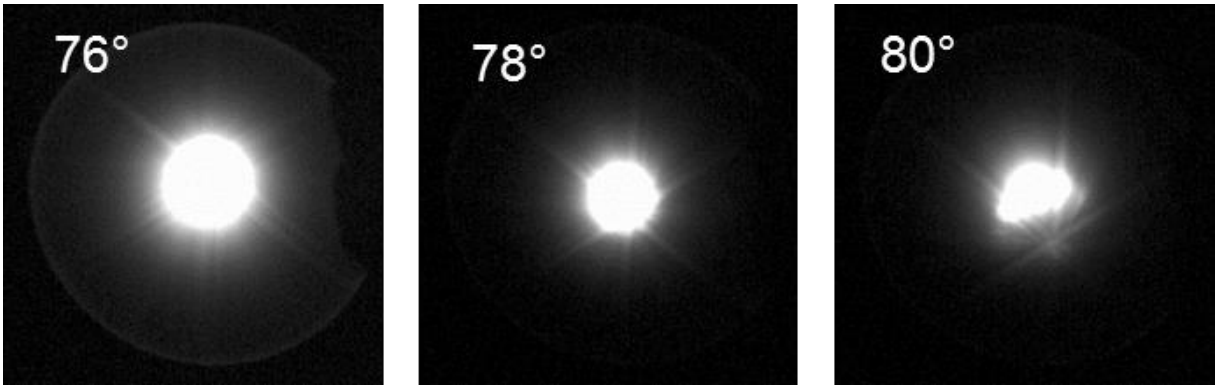

Figure 45: Diffraction pattern exhibiting Kikuchi lines and proving that a zone axis was sampled during the tilt series

Figure 46 shows a slice through an HAADF reconstruction of one of the two reconstructed tilt series, and the difference between the two reconstructions at the same slice. The main difference between the two reconstructions can be found at the edges. This difference can be attributed to non-perfect alignment. No difference can be seen in the intensity at the site of the precipitate, which would be attributed to channelling.

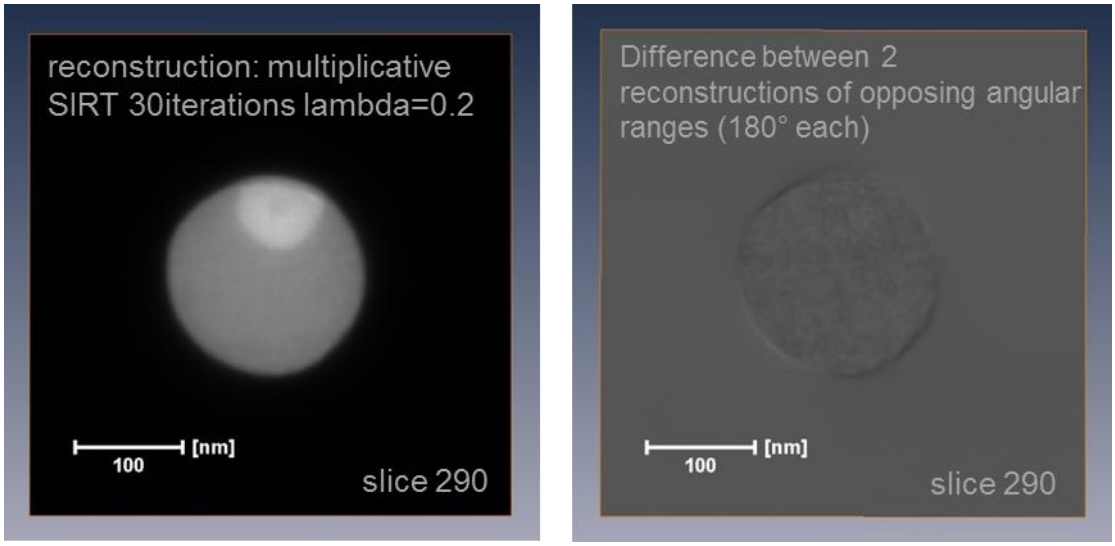

Figure 46: HAADF reconstruction and difference between the two HAADF reconstructions.

Figure 47 and Figure 48 show a surface rendering of the difference of the two reconstructions for a variety of convergence angles. Figure 47 shows the surface for a difference of 1 sigma, Figure 48 for a difference of 0.25 sigma. For one sigma, all the disparity that can be observed comes from differences in alignment of the two reconstructions. A difference of 0.25 sigma can be seen at the edge of the precipitate, especially for high convergence angles. This can be explained via the depth of field that is very low for very high tilt angles. Therefore it actually does make a difference whether the precipitate is at the beam entrance, or exit surface during acquisition, as it will be very well focussed at the entrance, but not well focussed at the exit surface, and thus result in a difference in the reconstruction at the edge of a feature. But except for this small difference no significant difference in the intensity of the features can be seen in the HAADF reconstructions. As the influence of channelling would show the HAADF signal, the absence of a significant difference in the HAADF reconstruction can be used to interpret the possibility of an influence of the analytical signals. As no significant difference can be overserved it follows that the influence of channelling is negligible in the analytical tomographic analysis of this material system.

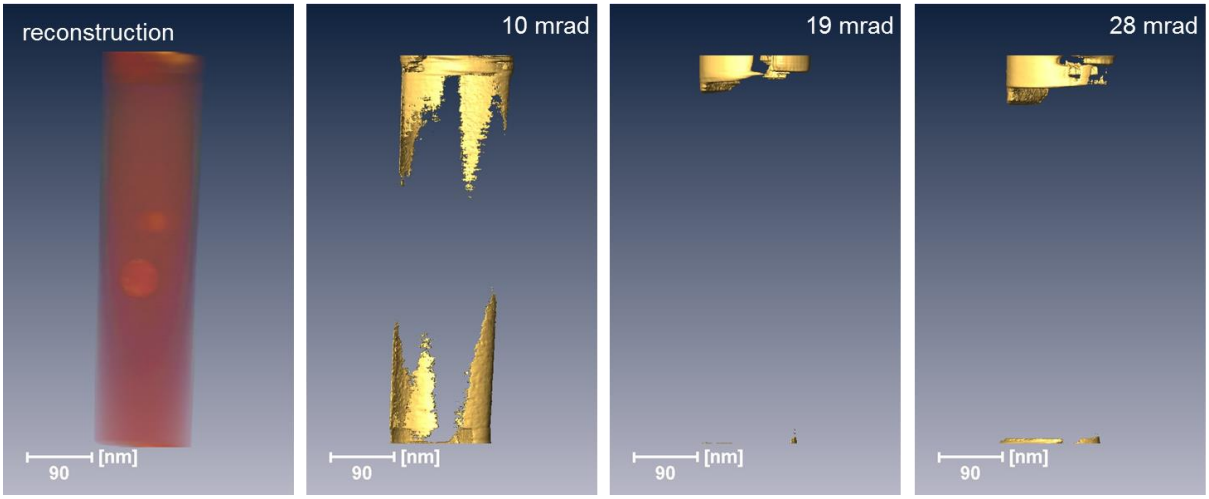

Figure 47: Left: HAADF reconstruction of the test sample. Right: Difference of HAADF reconstructions performed with projections acquired from opposing sides. Surface rendering for a sigma of 1.

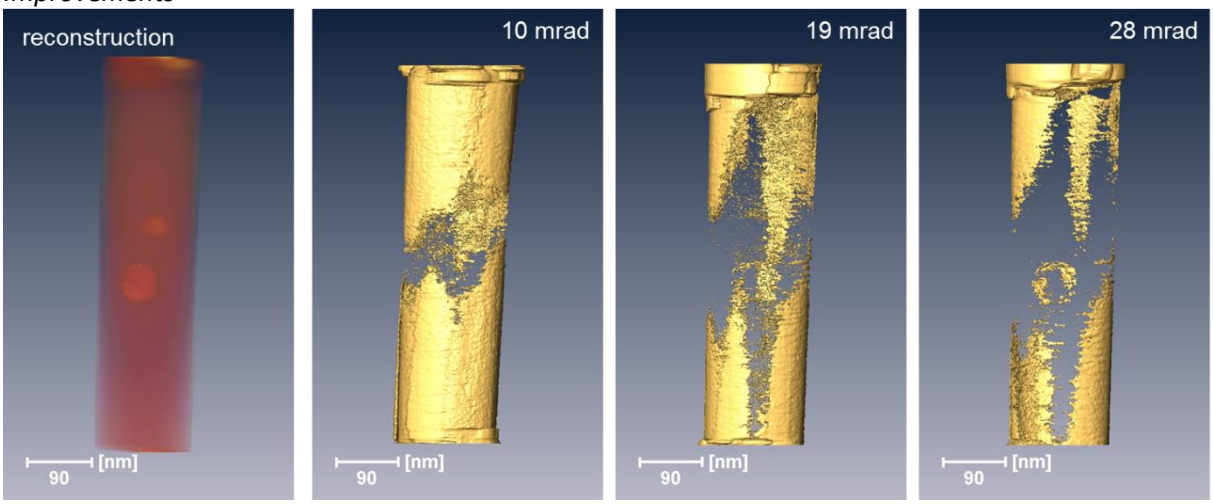

Figure 48: Left: HAADF reconstruction of the test sample. Right: Difference of HAADF reconstructions performed with projections acquired from opposing sides. Surface rendering for a sigma of 0.25.

It is still an open question, whether this comes from "averaging out" as so many different projections are used for reconstruction, and thus is an intrinsic property of tomography. Amorphous surface regions due to sample preparation could also be a reason. The influence of channelling could, however, also be dependent on the material system. To make a generally applicable conclusion on the influence of channelling in tomography further investigations would be necessary. As this is only a side aspect of the thesis, we conclude that the influence of channelling is not significant in our investigation.

5.4 Absorption of X-rays

For EDX tomographic investigations the absorption of X-rays in the sample also needs to be taken into account. The shadowing of X-rays through the holder was already treated above. A Matlab based simulation of the absorption of X-rays originating from a point like precipitate of element A surrounded by element B in a cylindrical sample was performed. The absorption within a material was calculated using an exponential law for the intensity loss:

$$I = I_0 e^{-C_{abs} * \rho * x} \tag{79}$$

Where I is the X-ray intensity after leaving the sample in direction of the detector, with I_0 the initial intensity emitted at the point-shaped precipitate in direction of the detector. C_{abs} is the absorption coefficient, describing the absorption of radiation with a energy corresponding to the characteristic X-ray peak of interest of material A in material B. ρ stands for the density of material B. x describes the distance the X-rays move through material B on their way to the detector.

Figure 49 schematically shows the idea of the calculation. It is also directly obvious that for a precipitate located off-centre, the length of the path of the X-rays through the sample on the way to the detector varies with tilt angle of the sample. As absorption is a function of this path length, the measured intensities, and consequently also the determined compositions, can depend on the angular range of the tilt series.

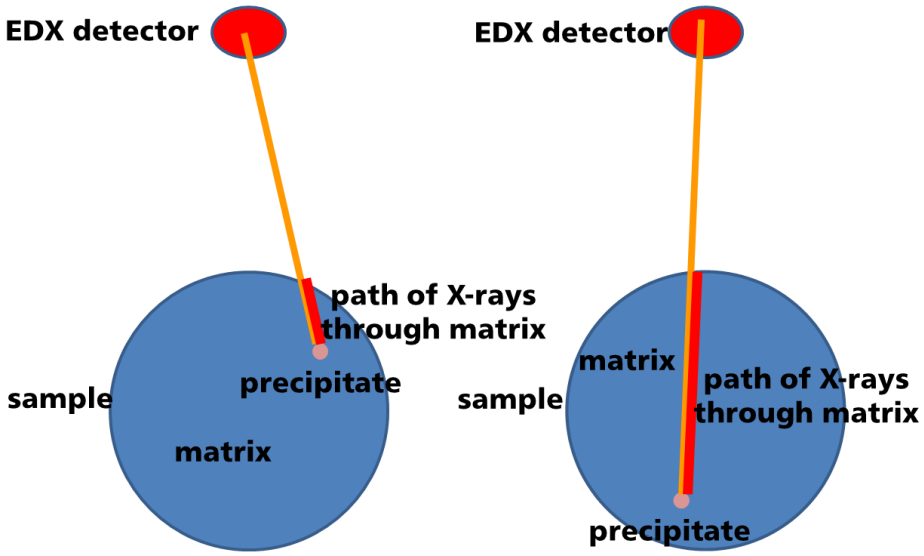

Figure 49: Different paths of X-rays through the sample for a point-like precipitate in a homogeneous matrix of a cylindrical sample

Figure 50 shows the results of such a calculation performed for Sc in Al for a sample with a radius of 60 nm and a system with one EDX detector. The detector is placed on the same z-height of the cylinder as the precipitate to probe the path dependence of the intensity in the x-y plane. The fraction of intensity not absorbed is plotted in dependence of the tilt angle and distance of the precipitate from the centre of the cylinder. The angular dependence of the absorption increases with the precipitates distance from the sample centre.

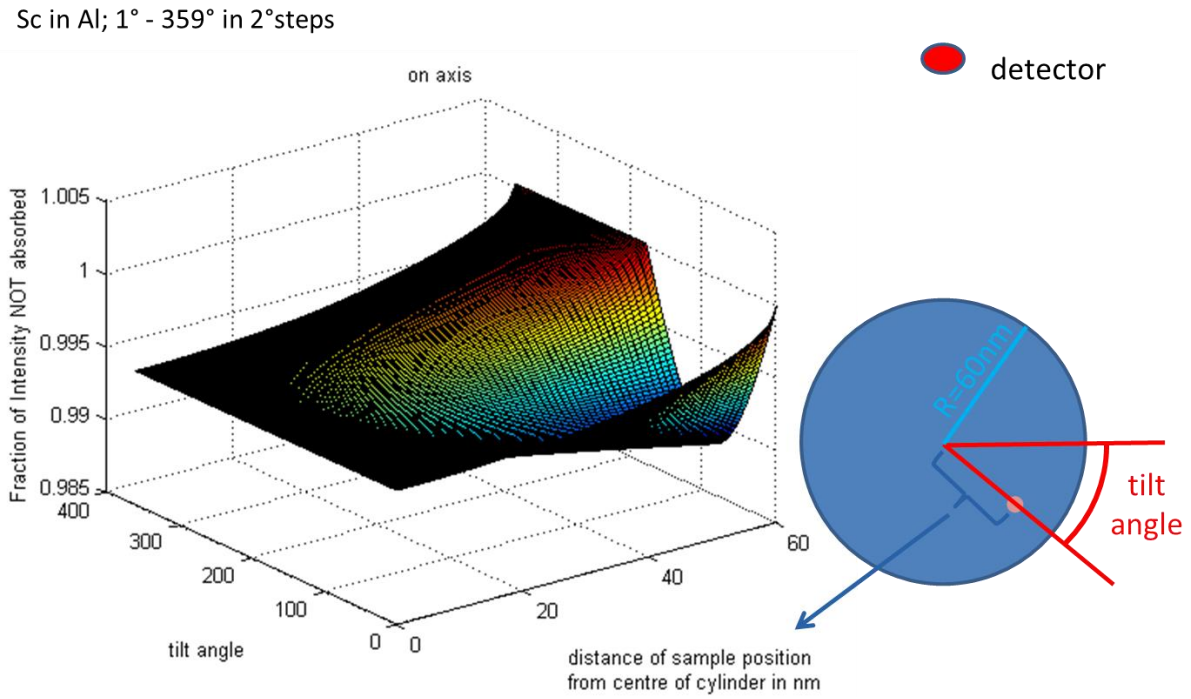

Figure 50: Left: Fraction of non-absorbed intensity of Sc in Al depending on the tilt angle and the distance of the precipitate from the central axis on the cylinder; Right: Scheme of parameters.

Figure 51 shows the average non-absorbed intensity for different tilt angle ranges in dependence of the distance of the precipitate from the centre of the cylindrical sample, for one detector, and a Sc precipitate within an Al matrix. It can be seen that there are very different dependences on the precipitates distance from the sample centre for different tilt angle ranges.

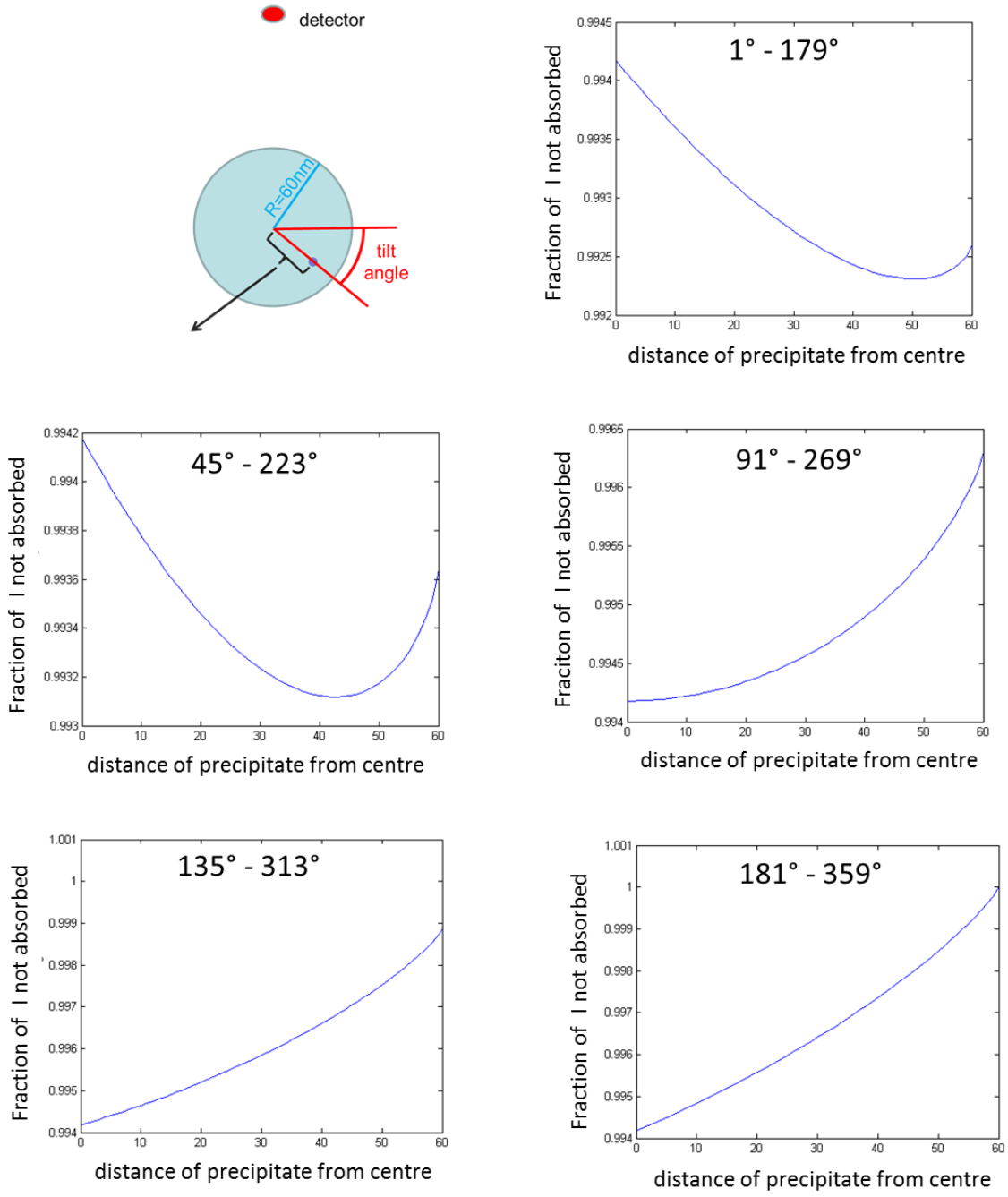

Figure 51: Average fraction of non-absorbed intensity in detector direction for a tilt series of the indicated angular ranges.

In the ASTEM we have the Super-X detector system with four quadrants. Therefore we adjusted the geometry of the absorption simulation to that geometry. Figure 52 shows the fraction of non-absorbed intensity for the same tilt angles as Figure 51. What already becomes obvious is that for this geometry the absorption behaviour becomes qualitatively more similar for all tilt ranges. We find that the most intensity is transmitted for a precipitate close to the sample surface for all tilt angles.

Due to the fact, that Al is a light element compared to the element of interest – Sc - the absorption in general is so small, that this is not relevant. As can be seen in Figure 53 and Figure 51, the average absorption of the Sc signal throughout a tilt series is below 1% of the emitted signal. For the maximum measured Sc concentrations of about 17 at.% this leads to an absorption of signal corresponding to below 0.17 at.%. Consequently the absorption of X-rays plays a negligible role in the investigated material system. These values are even lower for Zr, as can be seen in Figure 53, which shows the not absorbed intensity of Zr for an off-axis detector, like a quadrant of the Super-X detection system.

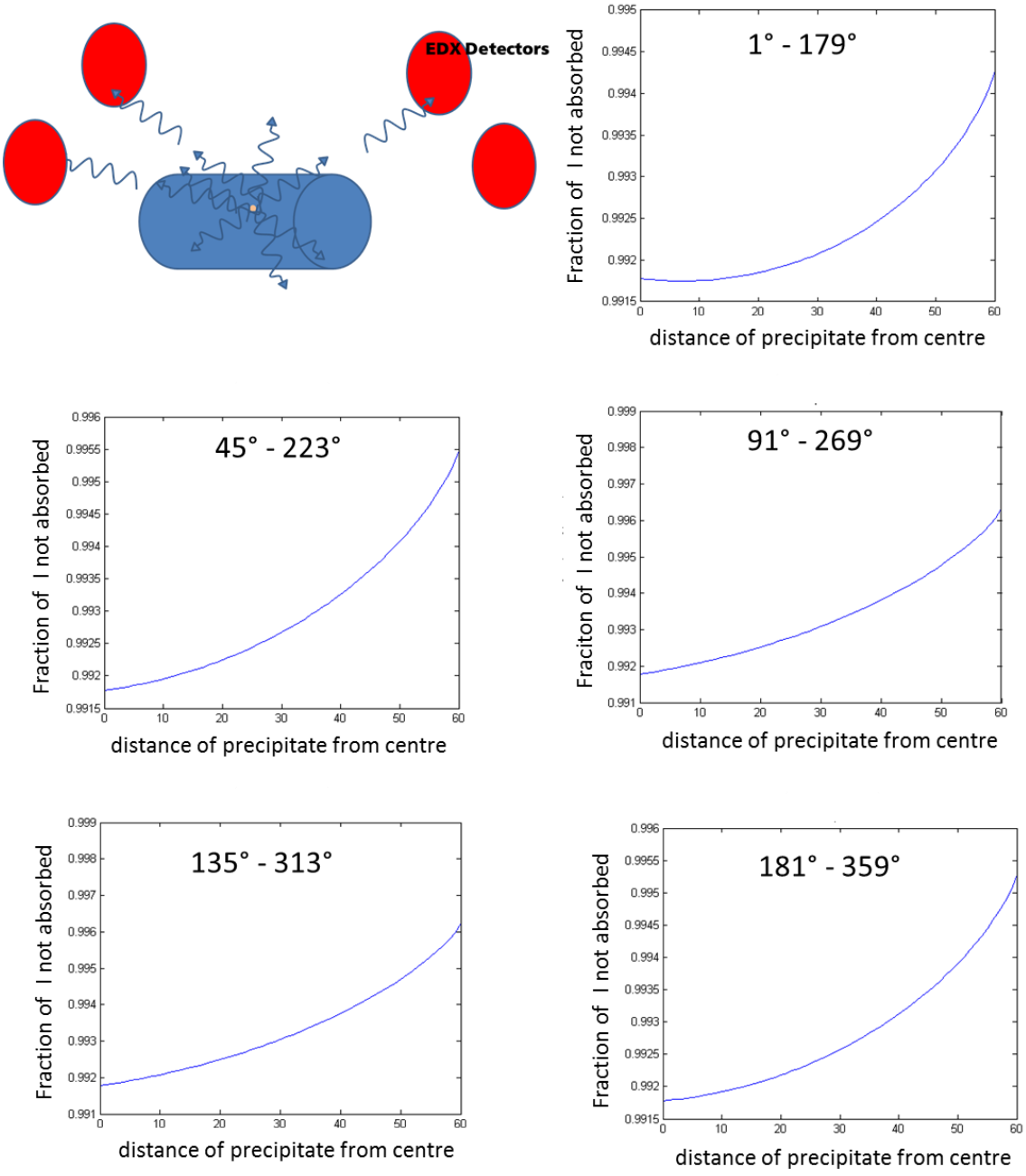

Figure 52: Average fraction of non-absorbed intensity in detector direction for a tilt series of the indicated angular ranges, for the Super-X detector system.

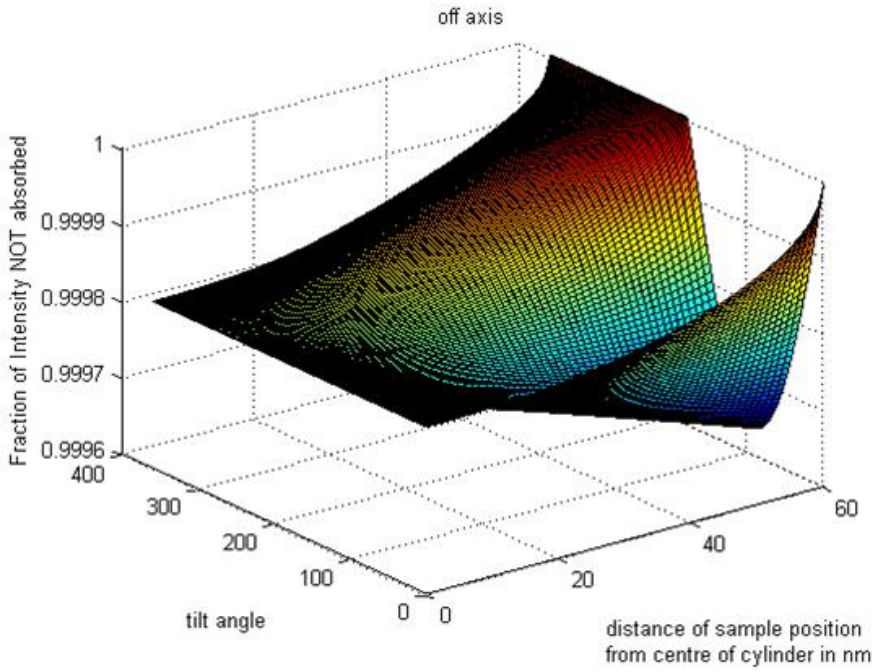

Figure 53: Fraction of non-absorbed intensity of Zr in Al depending on the tilt angle and the distance of the precipitate from the central axis on the cylinder. The calculation is performed for an X-ray path to an off-centred detector.

It must be emphasised that this is a consequence of the material composition: A precipitate of heavy elements within a light element matrix. For other material systems the absorption might not be low enough to neglect. In those cases caution is necessary. Figure 54 shows the opposite situation: the absorption of Al in Sc and Zr. Here the situation is far more dramatic. For the single detector conditions we find variation of the signal with the tilt angle of up to almost 10 % for Al in Sc and about 17 % for Al in Zr.

From the performed analysis we can learn the following: In cases, where light elements are supposed to be quantified within a heavier matrix great care needs to be taken with acquisition conditions. Systems with more than one detector improve conditions, as they minimise the variance in the dependence of transmitted intensity from the tilt angle range. If elemental quantification is performed on a one detector system the acquisition over a full 360° tilt range is advisable and will lead to a similar effect as a system with more detectors.

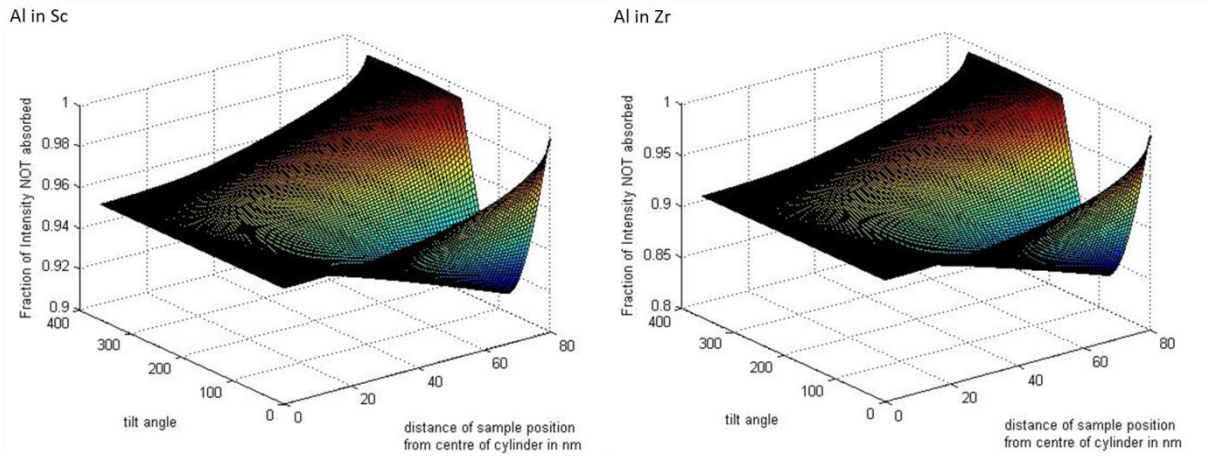

Figure 54: Shows the absorption for Al in Sc (left) and Zr (right)

5.5 Evaluation of Signal Types and Reconstruction Algorithms

The choice of signal to be reconstructed and reconstruction algorithm used are further important aspects that should be evaluated to make sure the desired information is retrieved as good and artefact-free as possible. For the samples of interest various signals have been reconstructed with different algorithms. This section will show, that there is not one perfect signal or algorithm, but that it depends also on the purpose of reconstruction which are the ideal choices.

Figure 55 shows a TV-minimization reconstruction of different signals of a short and long aged non-EBRS treated sample. (For details on the sample, see part III.) For Al and Sc the EELS signal is a lot stronger than the EDX signal, therefore its reconstruction contains less artefacts. However, Zr cannot reliably be detected in the EELS signal, due to a combination of the delayed M edge and the low Zr concentration in the sample, but EDX enables its reconstruction.

Therefore this material system is a very interesting example showing the advantages of analytical tomography via SIs, which enables the simultaneous acquisition of EELS and EDX data. EELS and EDX complement each other, as the EELS signal can be harder to retrieve for heavier elements, while very light elements can be difficult with EDX. This combined approach enables us to retrieve the maximum information and gives us the freedom to choose our signals after acquisition, or even reconstruct various signals. That can be helpful for understanding whether observed features are “real” or might be artefacts.

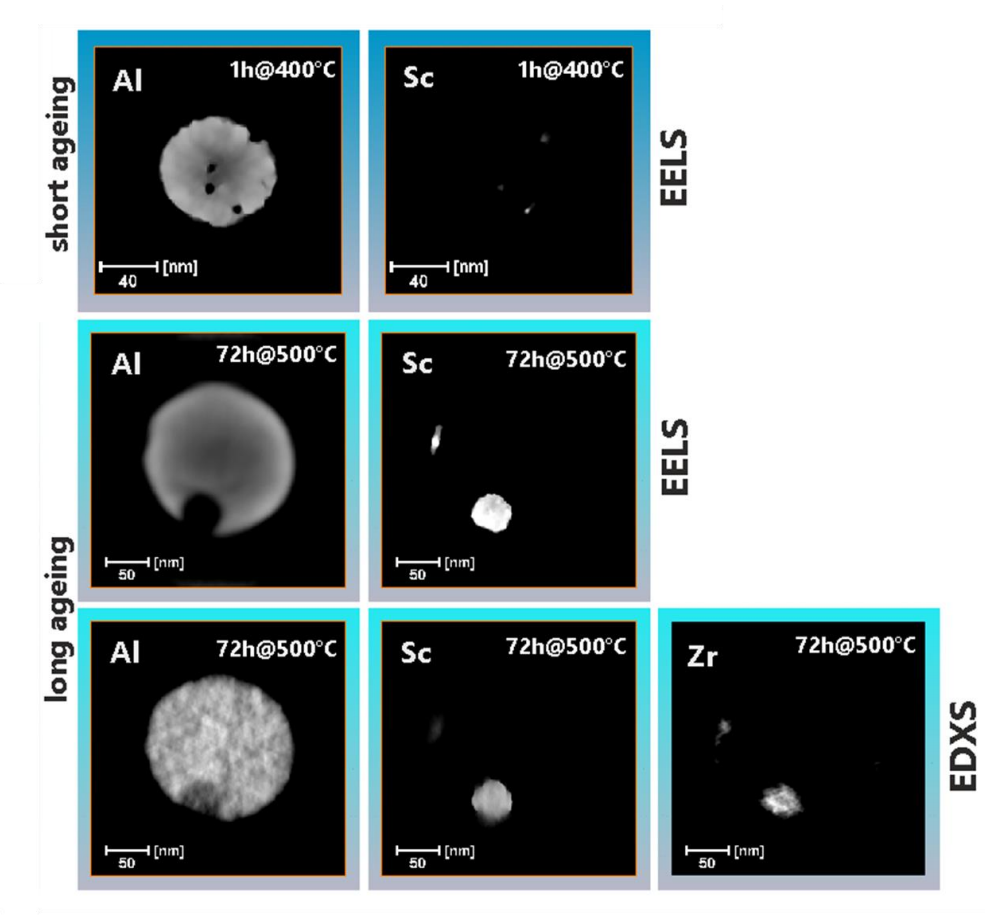

Figure 55: Slices through reconstructions of various signals from a short and long aged sample.

That the distinction between real features and artefacts is sometimes not an easy task becomes apparent in the following examples shown in Figure 56 and Figure 57. For both, the EELS and the EDX signal we see a very different structure when regarding the multiplicative SIRT (mSIRT) and the TV minimization reconstructions. We can observe a very inhomogeneous mSIRT reconstruction, while we find a rather homogeneous Sc-rich region if investigated via TV minimization. If only the knowledge we have from literature is applied the conclusion might be drawn that the results obtained via TV minimisation represent the Sc distribution more truthfully, attributing the intensity variations in the mSIRT reconstruction purely to noise. Our atomic resolution HAADF investigations and Gibbs energy calculations (see part III) however suggest further decomposition of the precipitates, in Al_3(Sc,Zr) and Al regions, which rather matches representation gained via the mSIRT reconstruction.

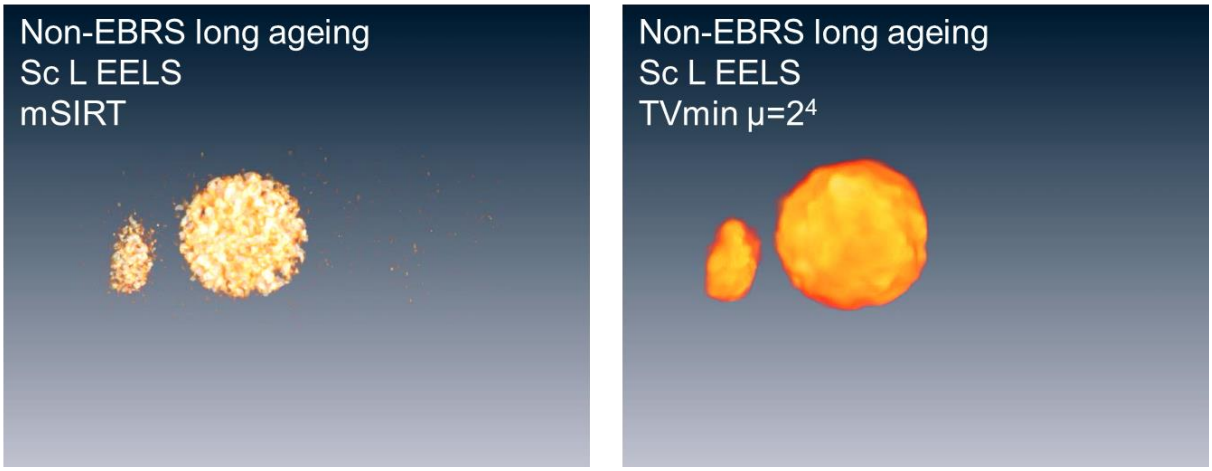

Figure 56: Volume rendered reconstructions of Sc L EELS signal of a non-EBRS treated long aged sample with two different reconstruction algorithms: multiplicative SIRT (left) and TV minimization (right) where the μ parameter was chosen to be 2^4.

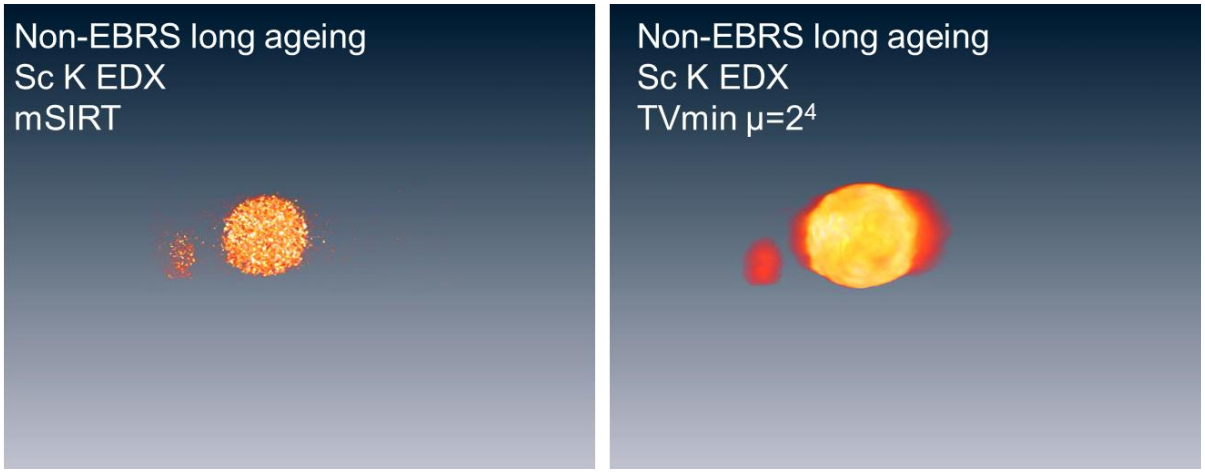

Figure 57: Volume rendered reconstructions of Sc K EDXS signal of a non-EBRS treated long aged sample with two different reconstruction algorithms: multiplicative SIRT (left) and TV minimization (right) where the μ parameter was chosen to be 2^4.

This example clearly shows that reconstruction algorithms need to be applied with care. Not all algorithms are suitable for all samples and goals. The TV minimization algorithm, for instance, minimises gradients, and is therefore primarily suitable for samples with well-defined phases. It is not ideal for retrieving a realistic distribution of compositions in the AlMgScZr (see part III) sample. It is however ideal to define a border between different regions for the creation of masks for voxel spectroscopic analysis. For that purpose the TV-minimization algorithm was used for data presented in section 9.3 and in the publication resulting as the main output of this thesis.[111]

6 Quantitative STEM Investigations Using Simulations - µSTEM

The basics of µSTEM were already described in chapter 2.6, and can be found in more detail in the µSTEM manual[123]. While µSTEM is considered to be the most accurate tool for STEM simulation including analytical data, through the "quantum excitation of phonons" approach, it is also rather complex to handle and has a considerable limitations. The most problematic of those limitations when dealing with real samples probably is the necessity of using cuboid unit cells perpendicular to the incoming beam (as shown in Figure 58) for simulation, and the fact that the whole crystal used for simulation is built up through a sequence of that defined unit cell in x, y and z direction. Consequently, no defects can be simulated, as the defect would be repeated in every unit cell of the crystal.

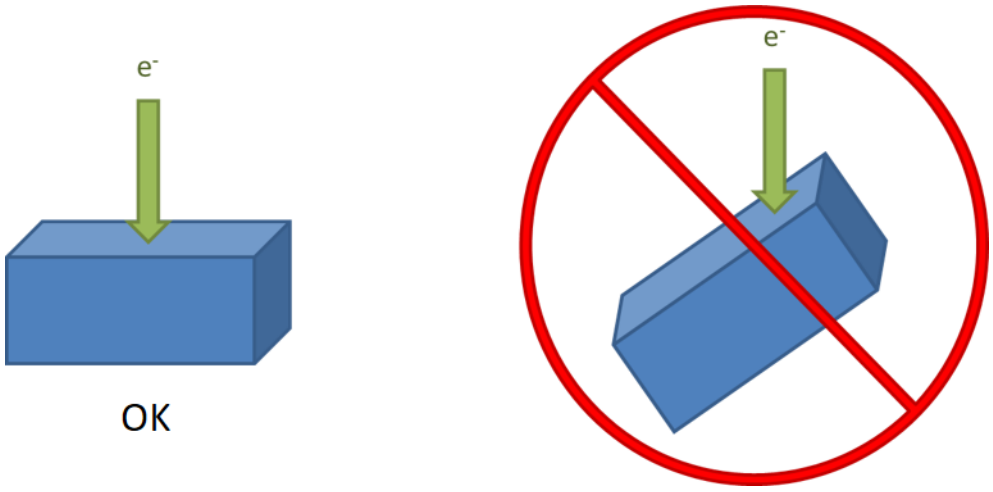

Figure 58: Scheme of unit cell constraints in µSTEM. The defined unit cell must be cuboid and perpendicular to the incoming beam, as shown on the left. On the right a unit cell is shown, which is still cuboid, but tilted compared to the incoming beam. This unit cell cannot be used in µSTEM, but must be redefined.

Therefore µSTEM used directly as intended is limited in its use for real material scientific problem solving. It can be used to gain knowledge on detector intensities that can be expected for certain crystals in TEM, STEM as well as EELS and EDX, and for thickness determination via position averaged convergent beam electron diffraction (PACBED)[92]. But in case of orientations other than <100> and samples with defects µSTEM cannot be used straightforwardly.

6.1 Construction of a Unit Cell

For performing simulations in µSTEM a unit cell needs to be created, which:

1) Is in fact a unit cell (gaplessly fills space, correctly reproducing the crystal)
2) Reproduces the physical sample and sample-beam-situation, where the electron wave function is propagated along the z-axis (the z coordinate is equal to depth)
3) Is a cuboid.
4) Is described via fractional coordinates, where 1 corresponds to the length of the unit cell. (If the unit cell is not cubic, the scale will be different in x, y and z direction.)

To receive all parameters necessary for a correct crystal file for the situation present, we developed a method combining a program of choice, for crystal structure visualisation (e.g. VESTA[124]), which can produce xyz-files, and a self-written Matlab code, which can be found in the attachments. The visualisation program is used to find a unit cell, which is shaped like a cuboid in the correct crystal

orientation. The Matlab file can be used to further manipulate the unit cell and retrieve the correct coordinates and other parameters, which need to be in the crystal file.

With the visualisation software, a cuboid unit cell is chosen as depicted in Figure 59 a - including the atoms at fractional coordinates 1. This makes the visual unit cell determination easier. But as a stacking of such unit cells would not represent the crystal correctly, as there would be two atoms at the same position (atoms at coordinate 0 and 1 – as schematically depicted in Figure 59 b), they have to be removed before transferring the data to µSTEM (so they can be stacked as schematically shown in Figure 59 c). This is automatically done by the Matlab script, which also allows an arbitrary stacking of unit cells in x, y and z direction.

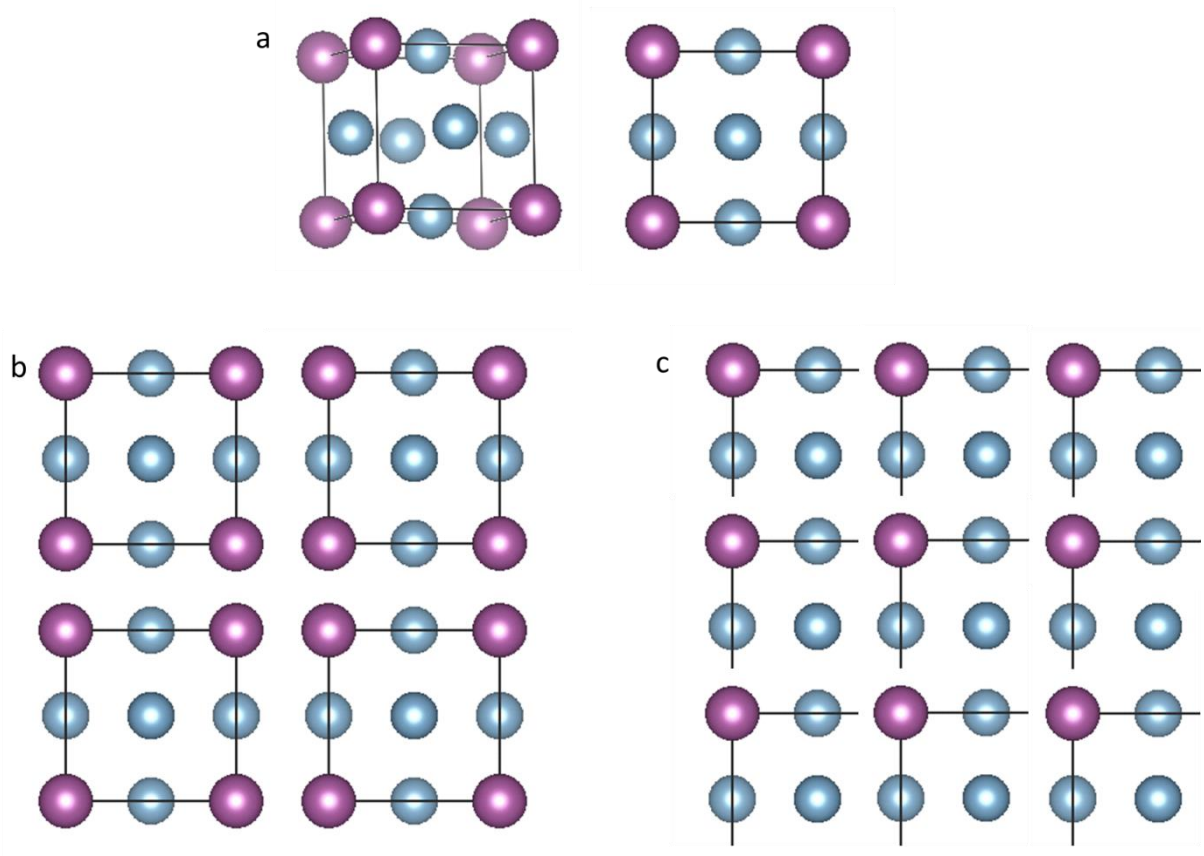

Figure 59: Unit cell choice for µSTEM. a) unit cell of Al_3Sc from two perspectives; b) stacking of such unit cells, if atoms at fractional corrdinate = 1 are not removed; b) stacking of unit cell a) after removing atoms at fractional coordinate = 1, which delivers a correct unit cell representing the crystal structure, which can be used for µSTEM

6.2 Incorporating Defects

This kind of stacking is necessary if defects are to be simulated in µSTEM, as µSTEM simply stacks the unit cells provided in x, y and z direction. Figure 60 is an example of how 20% anti-site atoms can be incorporated in the column indicated with the green arrow. Therefore 5 unit cells were stacked, to have five atoms of type “purple” in the column of interest. Then one of the atoms of type “purple” (indicated with the red arrow) was exchanged for an atom of type “blue”. This stack of five unit cells in z direction (and 3 in x or y direction) now represents our new unit cell, with which we can simulate a situation, where one out of three of the “purple”-rich columns contains 20% of “blue” atoms, where “purple” ones should be. If single atomic site defects are to be simulated, the unit cell stack

has to be large enough (in z-direction) to cover the whole sample depth, so that no stacking in z-direction is performed by µSTEM to achieve the desired sample thickness.

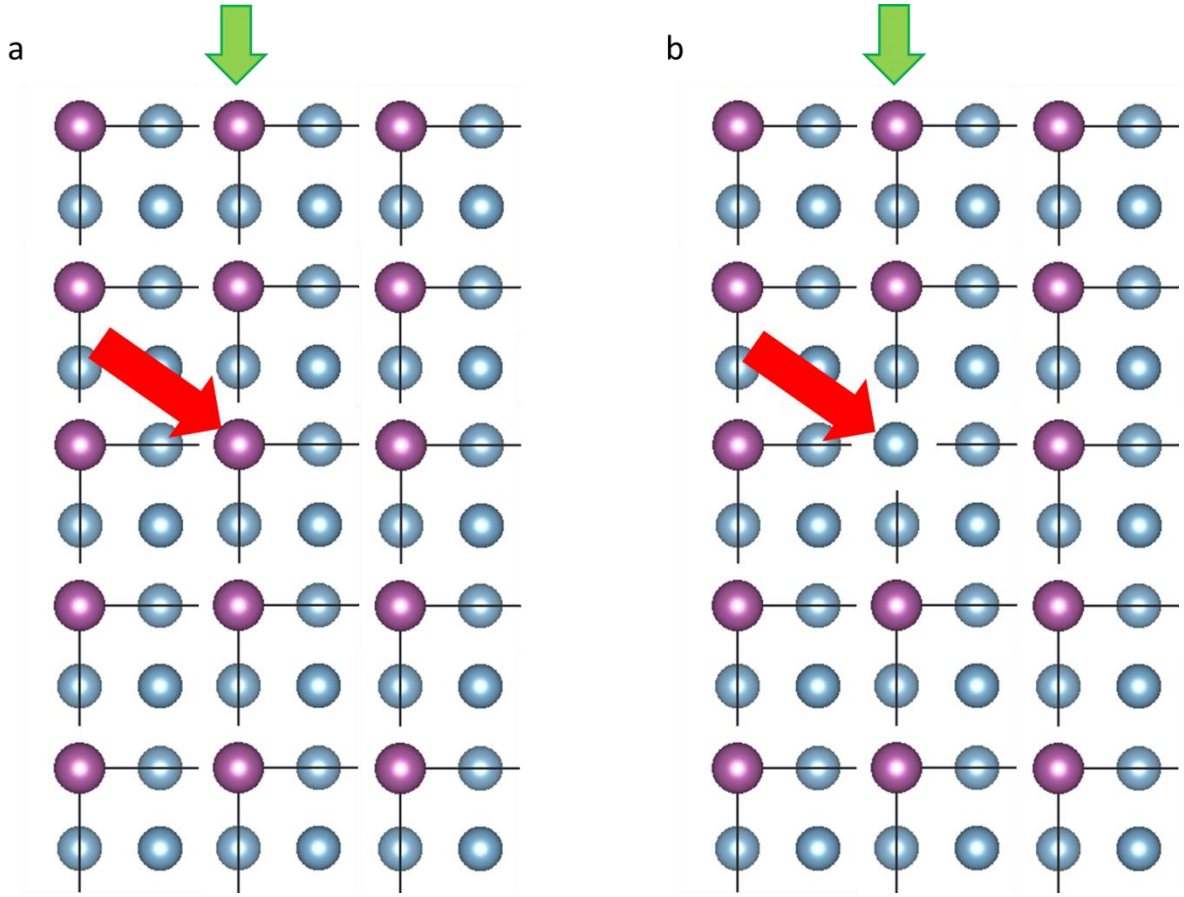

Figure 60: Unit cell design for a µSTEM simulation, where one column has 20% antisite defects.

It needs to be noted that the greater amount of atoms due to such stacking of unit cells in z-direction prior to importation in µSTEM impacts the GPU memory necessary to perform the simulation. The run time of the simulation performed is not increased compared to a simulation performed with the same unit cell but stacked by µSTEM, as the number of slices on which the simulation is performed stays the same.

At this point I want to use an example to describe step by step what needs to be done to finally create a crystal file, which describes a crystal with defects. The defect crystal we want to create is schematically depicted in Figure 60. We use VESTA[124] as a visualisation program to export the xyz file of the unit cell depicted in Figure 59 a. This text file is opened and the first two lines are deleted, the file is saved as a text file. In the Matlab script the input options are chosen as described in the comments of the script. It consequently calculates the correct new fractional coordinates and sorts them by atom type. Number of atoms of each type and the new unit cell size are also calculated. These results can directly be copied from the output window to the crystal file (the text file determining crystal parameters, which serves as an input for µSTEM). Defects can be included by altering the fractional atomic coordinates as follows:

- For anti-site atoms the fractional coordinates have to be copied from one atom type to another. The number of atoms per type has to be changed accordingly.

- For vacancies fractional coordinates of one atom are to be deleted from the list. The number of atoms for this type consequently has to be reduced by one.
- For interstitial atoms the fractional coordinates have to be added to the atom type of choice. (Again, the number of atoms per type has to be changed accordingly.)

Examples of the application of the µSTEM simulations at different angles and including defects can be found in the following chapter and in Part III, chapter 10.1, where µSTEM simulations were used to gain insights on the structural composition of nano-precipitates in an Al alloy at the atomic scale.

7 Elemental Quantification of Atomic Columns

Acquiring atomic resolution STEM HAADF images does not represent a great challenge anymore, since aberration corrected systems are available. Consequently one might assume that EDX elemental quantification at the atomic level should be possible. Kothleitner et al.[119], however, showed that this endeavour is much more challenging than its "black-and-white" counterpart. The reason therefore lies to a great part in the channelling effect: The different potential of differently occupied atomic columns leads to a difference in attraction of an atomic column for an electron, and thus a different probability of interaction and thus a higher signal. Kothleitner et al. showed that even though in STO <100> there is the same amount of oxygen on the pure oxygen column as on the mixed titanium-oxygen column, the mixed column will deliver a significantly higher oxygen signal due to channelling. Furthermore thermal diffuse scattering will lead to an overlap of signals from different columns. Consequently elemental quantification at the atomic level fails.

Very recently, however G. Kothleitner found that the elemental quantification of spectra integrated over lines along atomic columns (as indicated with blue lines in Figure 65) under specific circumstances can deliver the right results. Quickly the idea was born that this allows us to calculate the correct atomic column compositions simply through solving a system of linear equations for every element present:

$$Ax = b \tag{80}$$

Where *A* represents a matrix describing the performed line integrals, *x* and *b* are vectors: *b* is a vector of integrated line compositions, while *x* is the number of atoms of the element in question on the column per unit cell. The atomic column concentrations can be calculated from the *x*-values as follows:

$$c_{ln} = \frac{x_{ln}}{\sum_n x_{ln}} \tag{81}$$

Where *l* is the index of the atomic column and *n* is the index of the type of atom.

What needs to be known for this method is the crystal structure – the positions where atoms can be found, but not what kind of atoms. By performing elemental concentration quantification over linearly integrated pixels and solving a system of linear equations the correct elemental column concentrations can be extracted. The possible line integrals, and consequently the matrix *A* depend on the crystal structure and orientation. One of the probably easiest choices for the $Al_3(Sc,Zr)$ system in <100> direction is shown below in Figure 61. This system can also be used for STO, CTO and many more. The matrix A, however, is different for STO and CTO in <100> direction compared to Al_3Sc. As there is the same number of atoms on every column in Al_3Sc, a1, a2, a3 and a4 all equal ½. For STO and CTO, however, the Ti-O column has two atoms per unit cell, while the others have one. So if the scheme shown in Figure 61 is applied such, that x_4 is the Ti-O column, a3=1/3.

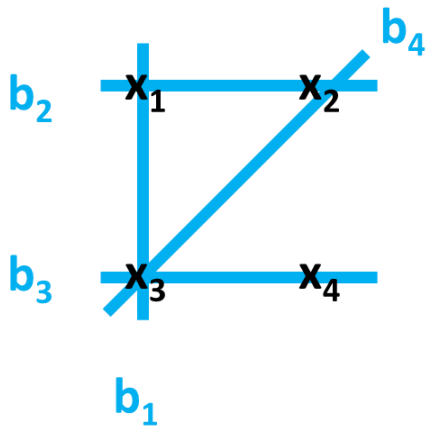

$$A = \begin{matrix} a1 & 0 & a1 & 0 \\ a2 & a2 & 0 & 0 \\ 0 & 0 & a3 & a3 \\ 0 & a4 & a4 & 0 \end{matrix}$$

a1= 1/(#atoms along b1 per unit cell)
a2= 1/(#atoms along b2 per unit cell)
a3= 1/(#atoms along b3 per unit cell)
a4= 1/(#atoms along b4 per unit cell)

Figure 61: Option to set up a system of linear equations for atomic column elemental quantification.

This back-calculation from correct line integrals to correct atomic column concentrations can be tested via a gedankenexperiment[vi], which we want to pursue for STO, CTO, PZO and Al_3Sc. Figure 62 shows the crystal structure of STO, CTO and PZO and the placement of the line integrals b_1 to b_4, which was chosen so that the atomic column with two atoms per unit cell depth are all represented by x_4. The other atomic columns only have one atom per unit cell depth. Therefore the matrix *A*, which describes which atomic columns contribute to the compositional line integrals and weighs them according to the number of atoms per unit cell depth, is the same for all systems.

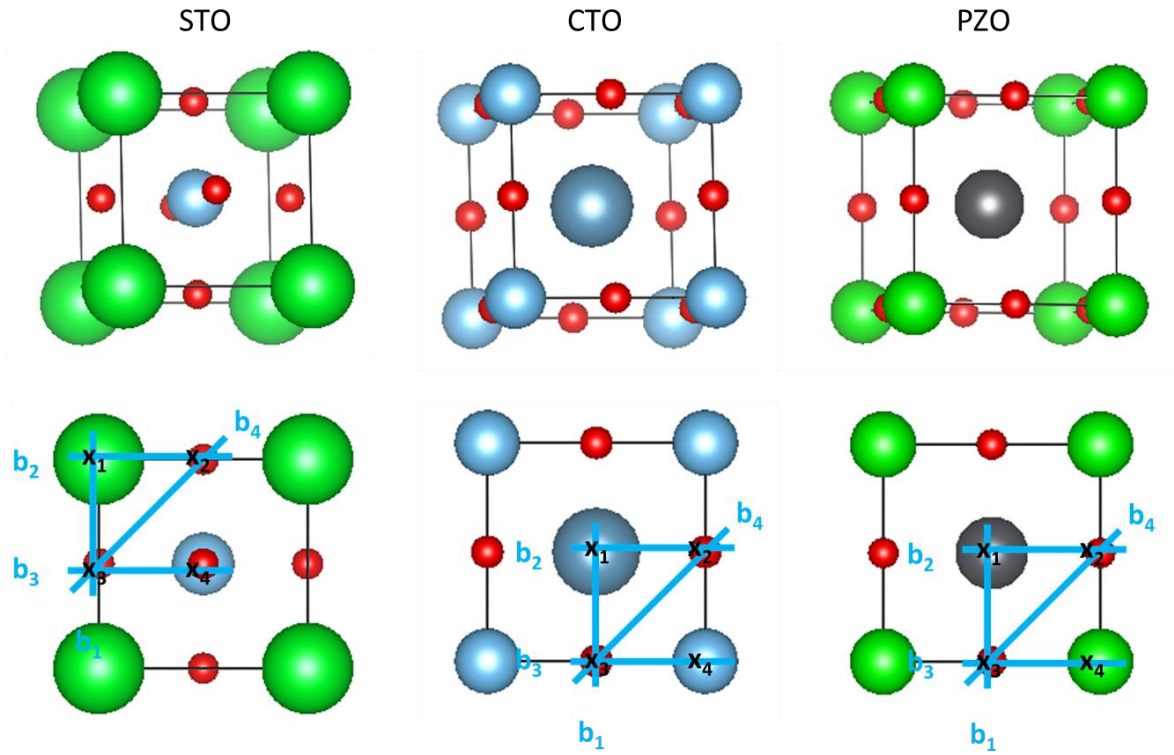

Figure 62: Scheme for gedankenexperiment, where system of linear equations is solved for STO, CTO and PZO.

[vi] It's a gedankenexperiment because we do not use actually measured line integrals, but assuming correct line integrals we use what they theoretically should be, to show that (and how) the back-calculation to correct column compositions via solving systems of linear equations works.

Consequently the left side of the systems of linear equations to be solved is also the same:

$$\begin{aligned}\frac{1}{2}x_1 + \frac{1}{2}x_3 &= b_1\\ \frac{1}{2}x_1 + \frac{1}{2}x_2 &= b_2\\ \frac{1}{3}x_3 + \frac{1}{3}x_4 &= b_3\\ \frac{1}{2}x_2 + \frac{1}{2}x_3 &= b_4\end{aligned} \tag{82}$$

The system of linear equations has to be solved for every element separately. These are the compositions that ideally can be found for the linearly integrated spectra, for the different systems and different elements as indicated in Figure 62:

Table 1: The b-vectors for all elements of STO, CTO and PZO.

STO

b_{Sr} =	b_{Ti} =	b_O =
0.5	0	0.5
0.5	0	0.5
0	0.333	0.667
0	0	1

CTO

b_{Ca} =	b_{Ti} =	b_O =
0.5	0	0.5
0.5	0	0.5
0	0.333	0.667
0	0	1

PZO

b_{Pb} =	b_{Zr} =	b_O =
0.5	0	0.5
0.5	0	0.5
0	0.333	0.667
0	0	1

We want to exemplarily talk the attainment of the b-vectors through for oxygen in STO: Along b_1 we find one O atom and one Sr atom per unit cell depth - hence an oxygen concentration of 0.5. The same is true for b_2. Along b_3 we find two oxygen atoms and one Ti atom per unit cell depth. Consequently we have an oxygen fraction of 0.66667. Along b_4 we have only oxygen atoms, hence b_4 equals 1. The linear equation system that needs to be solved for oxygen in STO therefore is:

$$\begin{aligned}\frac{1}{2}x_1 + \frac{1}{2}x_3 &= 0.5\\ \frac{1}{2}x_1 + \frac{1}{2}x_2 &= 0.5\\ \frac{1}{3}x_3 + \frac{1}{3}x_4 &= 0.66667\\ \frac{1}{2}x_2 + \frac{1}{2}x_3 &= 1\end{aligned} \tag{83}$$

There are various different methods that can be used to solve the system. A number of online linear equation system solvers are available. We used the "wims"[vii] linear solver and chose the matrix method. The solution of the equation gives us the number of O atoms per unit cell depth along the columns x_1 to x_4. For oxygen we get x_O=(0,1,1,1). To get the oxygen composition we can either solve

[vii] provided by the Université Nice Sophia Antipolis (UNS); accessible online

the equation for all other elements and use the formula described above, or divide the vector x element by element with the vector *nx* = (*nx1, nx2, nx3, nx4*) of the number of atoms per column per unit cell which for STO equals (1, 1, 1, 2). Through performing this division we get c_O = (0, 1, 1, 0.5) for the oxygen composition along the columns. By solving the systems of linear equations for the b-vectors of Sr and Ti, we get x_{Sr} = *(1,0,0,0)* and x_{Ti} = (0,0,0,1), respectively. For the concentrations of the elements Sr and Ti on the four columns in question we finally get: c_{Sr} = (1,0,0,0) and c_{Ti} = (0,0,0,0.5).

As not only the A matrix, but also the b-vectors are the same for CTO and PZO, we also get the same *x*- and *c*-vectors, as can be seen in the following Table 2. If the *x*-vectors and *c*-vectors are compared to the crystal structures shown in Figure 62 it can be seen that they deliver the correct number of atoms per column per unit cell depth and correct atomic column concentrations respectively. (For all vectors given, the first element stands for the column marked x_1, the second for column x_2, and so on.)

Table 2: x-vectors and concentrational vectors for STO, CTO and PZO. The vector elements from top to bottom stand for x_1 to x_4 and c_1 to c_4, respectively. They apply to the atomic columns indicated with x_1 to x_4 in Figure 62.

STO

x_{Sr} =	x_{Ti} =	x_O =
1	0	0
0	0	1
0	0	1
0	1	1

CTO

x_{Ca} =	x_{Ti} =	x_O =
1	0	0
0	0	1
0	0	1
0	1	1

PZO

x_{Pb} =	x_{Zr} =	x_O =
1	0	0
0	0	1
0	0	1
0	1	1

STO

c_{Sr} =	c_{Ti} =	c_O =
1	0	0
0	0	1
0	0	1
0	0.5	0.5

CTO

c_{Ca} =	c_{Ti} =	c_O =
1	0	0
0	0	1
0	0	1
0	0.5	0.5

PZO

c_{Pb} =	c_{Zr} =	c_O =
1	0	0
0	0	1
0	0	1
0	0.5	0.5

Different choices of line integrals (with which a linearly independent system of equations can be set up) are possible to determine atomic column compositions. As an example we want to choose different line integrals on CTO and again solve the system of linear equations. Figure 63 shows the alternate paths chosen for the integrals and the resulting matrix A describing those paths. Table 3 gives the values of compositional line integrals for all three elements and the x-vectors (and compositions) that are obtained by solving the system Ax=b for each element. We find that also for this choice of line integrals the resulting compositions are correct.

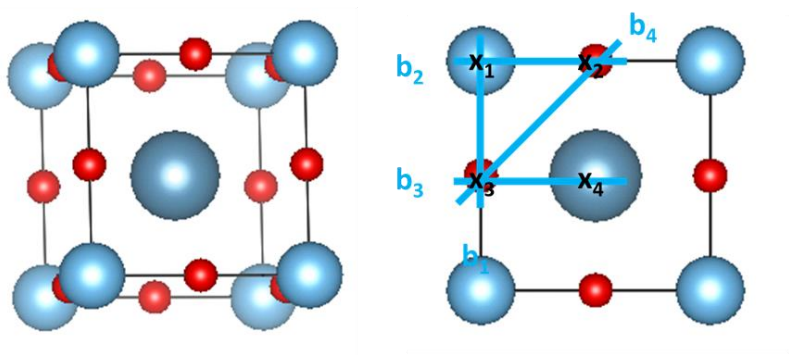

$$A = \begin{matrix} 1/3 & 0 & 1/3 & 0 \\ 1/3 & 1/3 & 0 & 0 \\ 0 & 0 & 1/2 & 1/2 \\ 0 & 1/2 & 1/2 & 0 \end{matrix}$$

Figure 63: Alternate choice of line integrals for CTO and resulting A-matrix.

Table 3: b, x and c values for CTO for an alternate choice of the line integrals.

CTO

b_{Ca} =	b_{Ti} =	b_O =
0	0.333	0.667
0	0.333	0.667
0.5	0	0.5
0	0	1

CTO

x_{Ca} =	x_{Ti} =	x_O =
0	1	1
0	0	1
0	0	1
1	0	0

CTO

c_{Ca} =	c_{Ti} =	c_O =
0	0.5	0.5
0	0	1
0	0	1
1	0	0

We want to perform the same gedankenexperiment for Al_3Sc in the <100> direction. As can be seen in Figure 64 we can apply the same directions for line integrals. The A-matrix, however, is different compared to STO, CTO, PZO, due to the different crystal structure. In this case there is one atom per unit cell depth for all columns investigated. Consequently all line integrals are performed over two atoms per unit cell depth and all weighing factors in the A-matrix are ½.

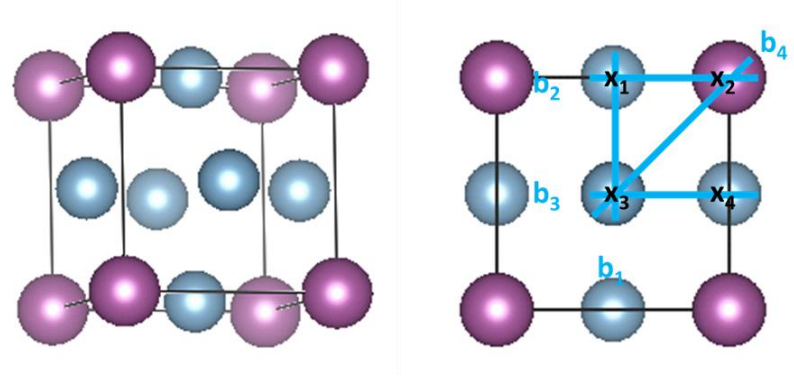

$$A = \begin{matrix} 1/2 & 0 & 1/2 & 0 \\ 1/2 & 1/2 & 0 & 0 \\ 0 & 0 & 1/2 & 1/2 \\ 0 & 1/2 & 1/2 & 0 \end{matrix}$$

Figure 64: Possible choice of line integrals for Al_3Sc and resulting A-matrix.

After solving this system we again retrieve the correct compositions, as can be seen in Table 4.

Table 4: b, x and c values for Al_3Sc for the choice of the line integrals shown in Figure 64.

Al_3Sc	
b_{Al} =	b_{Sc} =
1	0
0.5	0.5
1	0
0.5	0.5

Al_3Sc	
x_{Al} =	x_{Sc} =
1	0
0	1
1	0
1	0

Al_3Sc	
c_{Al} =	c_{Sci} =
1	0
0	1
1	0
1	0

In the examples above we could show how the method works for different model systems, with assumed perfect line integrals. Now we want to go one step further and approach a useful application of the system: In the Al-Al_3Sc-system the Al_3Sc precipitates coherently match the fcc-Al-matrix. In the Al_3Sc precipitates the position of the Sc atoms can be described as taking up the corner positions of the fcc crystal structure, as can be seen in the figures above. Consequently in an HR STEM investigation of the system one might come across the situation that the crystal structure, but not the compositions of individual columns, are known, as in the corner positions in the fcc crystal structure can be taken up by Al and Sc. In such a case, this method can be used to determine the unknown atomic column concentrations. As we found evidence of an Al-network within the Al_3Sc-precipiates, this method could be used to find and quantify Al channels in an Al_3Sc-precipiate. Therefore we want to test the method on simulated data of the system.

The elemental maps in Figure 65 were simulated from an artificially created crystal structure. The top three lines represent an $Al_3(Al,Sc)$ system, where the column marked with the yellow circle contains 40 at.% of Al and 60 at.% of Sc. The line below contains pure Sc columns and was inserted for reference reasons, as the linear equations solving needs to be done with concentrations, but the simulations merely deliver intensities. The lines of pure Sc and Al could be used as a 100% -reference for line integrals. For real experimental data such a reference is not necessary, as elemental concentrations can be retrieved from the acquired data via the necessary processing software, like e.g. Gatan Digital Micrograph.

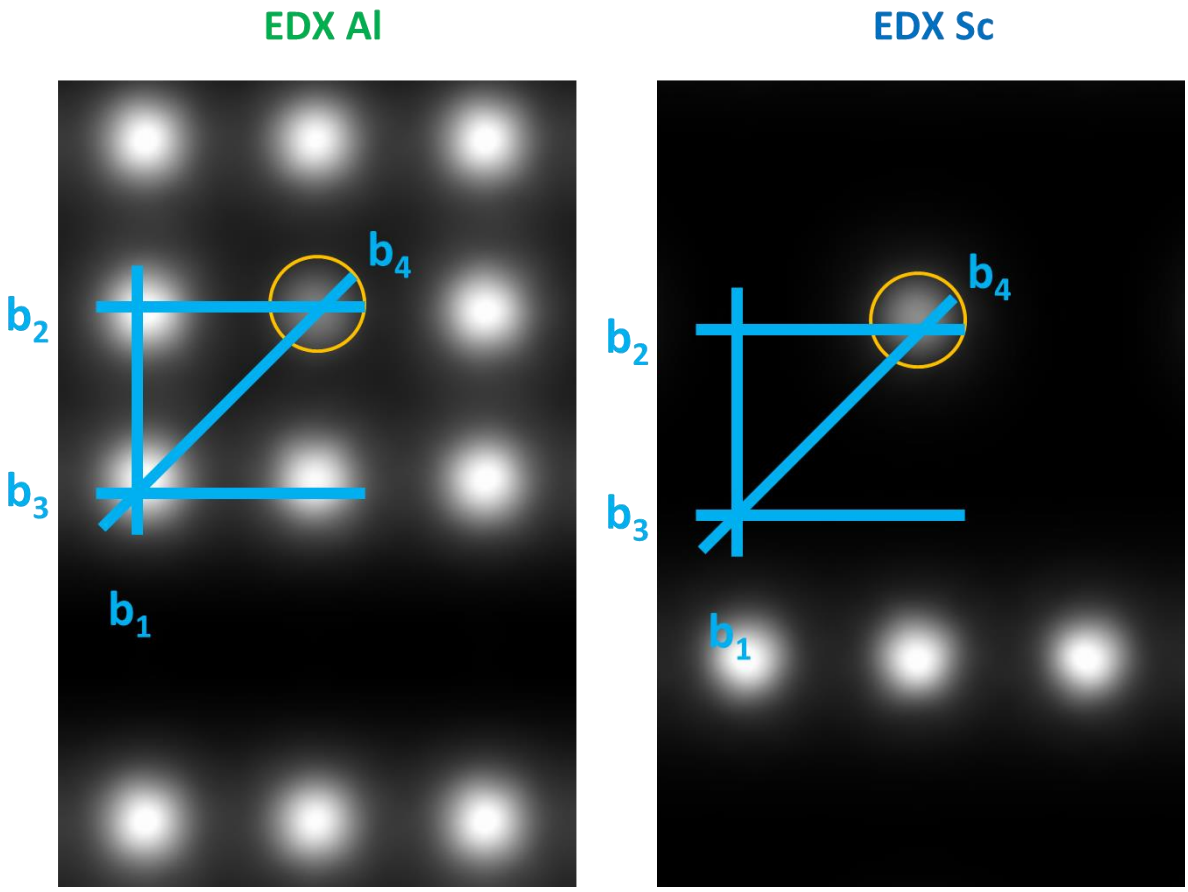

Figure 65: EDX elemental maps of an artificially manufactured crystal structure simulated via µSTEM. Line integrals indicated in blue.

The simulations and quantification were performed for two thicknesses: 10nm and 50nm. After simulation a source broadening was performed with a Gaussian shaped source of 0.8 Å. For 50nm, however, the impact of artificial source broadening was so big that a significant Al signal was found on pure Sc sites and vice versa. Consequently the line integrals performed on such columns will not deliver correct concentrations, which means the fundamental requirement for this method is not fulfilled. As no reasonable quantification can be performed like that the quantification for 50 nm was performed without source broadening.

Table 5: b, x and c values for Al_3Sc 10 nm thick, where 2 of 5 Sc atoms were substituted by Al atoms. The line integrals performed on simulated EDX maps for this system, as shown in Figure 65.

$Al_3(Al_{0.4}Sc_{0.6})$	
b_{Al} =	b_{Sc} =
1	0
0.72	0.28
1	0
0.71	0.29

$Al_3(Al_{0.4}Sc_{0.6})$	
x_{Al} =	x_{Sc} =
1.01	-0.01
0.43	0.57
0.99	0.01
1.01	-0.01

$Al_3(Al_{0.4}Sc_{0.6})$	
c_{Al} =	c_{Sci} =
1.01	-0.01
0.43	0.57
0.99	0.01
1.01	-0.01

The results for 10 nm are already very close to the correct results, only 3 at.% off. For 50 nm (without source broadening) the composition was reached perfectly. One reason might be, that due to the greater thickness, the compositions obtained from the line integrals are less sensitive to the

placement of the line integrals. It needs to be noted that prior knowledge was introduced in the evaluation: We know (also if this were data from a real sample) that the Al columns are Sc-free.

Table 6: b, x and c values for Al_3Sc 50 nm thick, where 2 of 5 Sc atoms were substituted by Al atoms. The line integrals performed on simulated EDX maps for this system, as shown in Figure 65.

$Al_3(Al_{0.4}Sc_{0.6})$

b_{Al} =	b_{Sc} =
1	0
0.7	0.3
1	0
0.7	0.3

$Al_3(Al_{0.4}Sc_{0.6})$

x_{Al} =	x_{Sc} =
1	0
0.4	0.6
1	0
1	0

$Al_3(Al_{0.4}Sc_{0.6})$

c_{Al} =	c_{Sci} =
1	0
0.4	0.6
1	0
1	0

The open question is only the composition of the one column marked with the yellow circle. Therefore we know, that the line integrals b_1 and b_3 contain only Al and no Sc: It follows that $b_{1Al} = b_{3Al} = 1$ and $b_{1Sc} = b_{3Sc} = 0$. Had this knowledge not been included, the 50 nm evaluation would have been clearly worse, as significant Sc intensity spreads onto the Al columns due to the thickness, even if no source broadening is applied.

We can conclude that especially for thick samples it is essential for improvement of the method to include prior knowledge. Not only knowledge of the material, but also the shape of the profile and other profiles of elemental maps can indicate, whether intensity should be included or dismissed as tail from a neighbouring column. A more advanced possibility to gain that knowledge is the performance of a Gaussian fit to all the profiles. As can be seen in Figure 66, this approach was applied in an attempt to perform this procedure on simulated data from STO. STO, however, is very problematic, as the oxygen is anti-bonding, and therefore spreads very far into neighbouring columns. The fit algorithm used was not good enough to produce very good results. The line integrals have to be performed through the centre of the columns, not averaged, which corresponds to a maximum for elements present in the column.

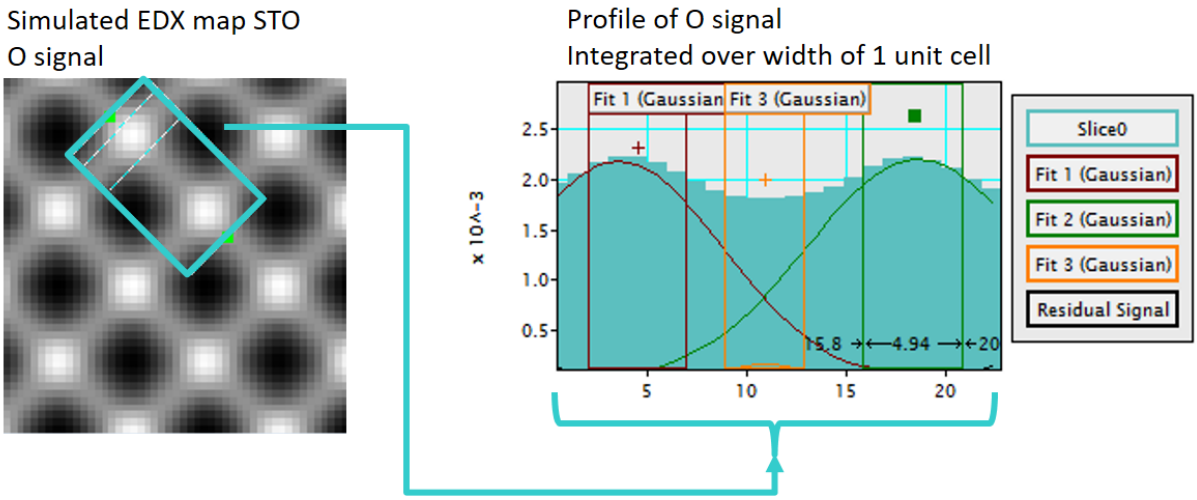

Figure 66: Gaussian fits applied to simulated oxygen EDX map of STO.

Part III - Investigation of an Industrially Cast AlMgScZr Alloy

In cooperation with the *Institute of Material Science, Joining and Forming* at TU Graz and the aircraft producer *Airbus* an AlMgScZr alloy was investigated. This alloy is relevant for applications in aircrafts due to its light weight and good welding characteristics.[96,125,126] The basic properties of the alloy and its precipitation hardening characteristics are described in part I - chapter 3.1.

The AlMg4Sc0.4Zr0.12 alloy was belt cast at industrial scale and investigated at a wide range of temperatures. Additionally electron beam re-solidification (EBRS) - see also part I, chapter 3.1 was performed on some samples, to increase the amount of Sc in solid solution.

8 Pre - Characterisation of the Industrially Cast AlMgScZr System

8.1 EFTEM and STEM Imaging Investigations

To get an overview of the alloy and its precipitation kinetics EFTEM and STEM investigations were performed. EFTEM was used especially for short aged samples, which exhibited very small precipitates, as the contrast in EFTEM could be chosen to exceed HAADF contrast, by imaging electrons with energy losses which are attributed unspecific background at 40 eV with a slit width of 10 eV. The EFTEM investigations were performed at an FEI Tecnai F20 operated at 200 kV and equipped with a Gatan Tridiem post column imaging filter. The STEM HAADF investigations were performed at the ASTEM (described in section 2.1.3) operating in non-monochromatic conditions after corrector tuning to have an aberration free zone of at least 24 mrad. Findings on precipitation kinetics, the influence of the EBRS treatment (see section 3.1) and recrystallization have been published in cooperation with the Institute of Material Science, Joining and Forming[107,108]. The results discussed here are from non-EBRS treated samples, if not explicitly noted otherwise. A comparison of images from a short aged sample (Figure 67) and a long aged sample (Figure 68) shows the expected size increase of the precipitates accompanied by a decrease in number of precipitates. Both samples showed that the precipitates exhibited the expected $L1_2$ crystal structure and coherently matched the Al-matrix. These findings and the HAADF intensity increase of the precipitates compared to the matrix, which suggest a higher average atomic number (Z) of the spherical precipitates, allowed the assumption that the spherical precipitates are in fact the expected $Al_3(Sc,Zr)$ precipitates. Clarity concerning the atomic species, however, can only be gained via spectroscopic investigations.

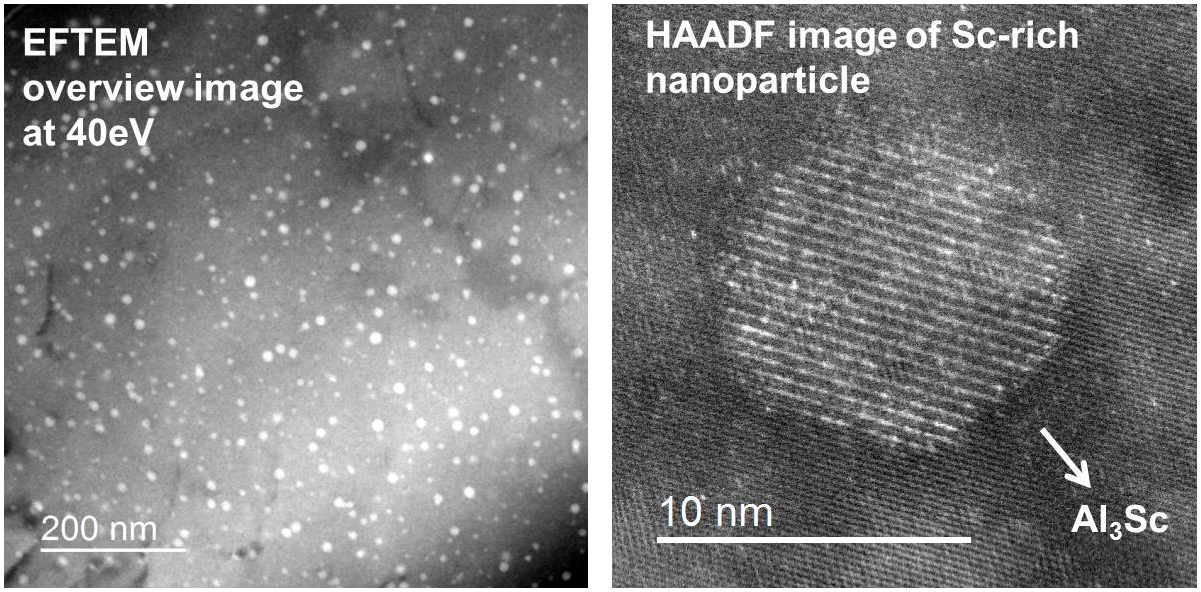

Figure 67: Overview image and precipitate of short aged non-EBRS sample. On the left there is an EFTEM overview image of a short aged sample. The image was acquired at 40 eV with a slit width of 10 eV. Under those conditions the precipitates appear bright compared to the matrix. The image on the right is a probe corrected HAADF STEM image.

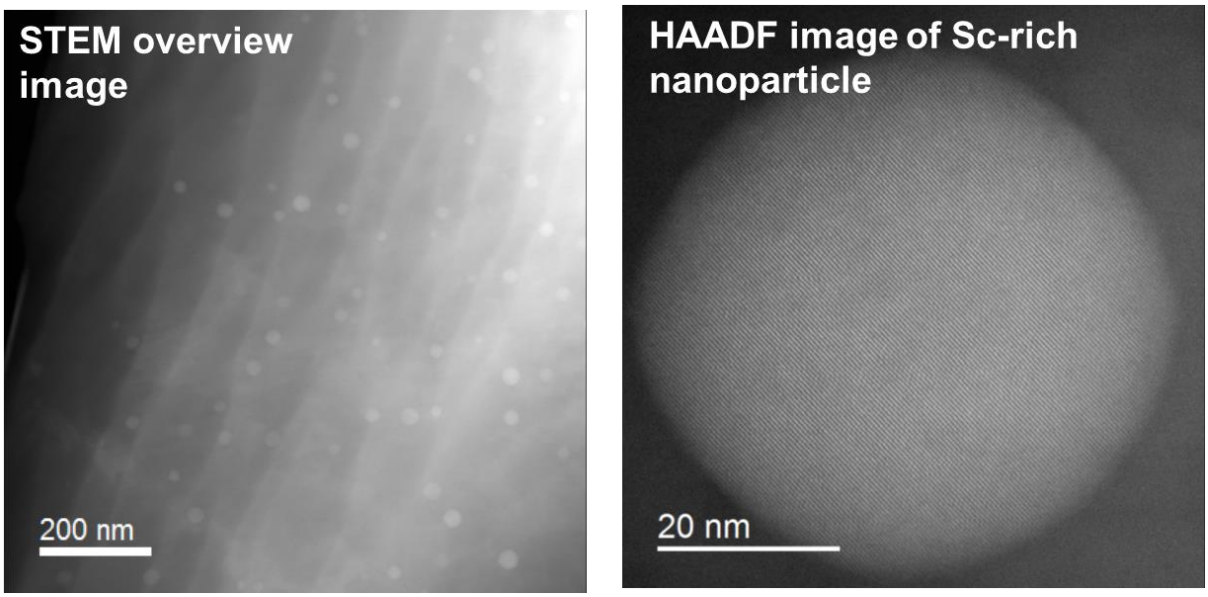

Figure 68: Overview and precipitate of long aged non-EBRS sample. Both acquired via HAADF STEM imaging at the ASTEM.

In Figure 69 the magnification was chosen to allow a direct comparison of a short and a long aged precipitate. Here the dramatic difference in size becomes very clear.

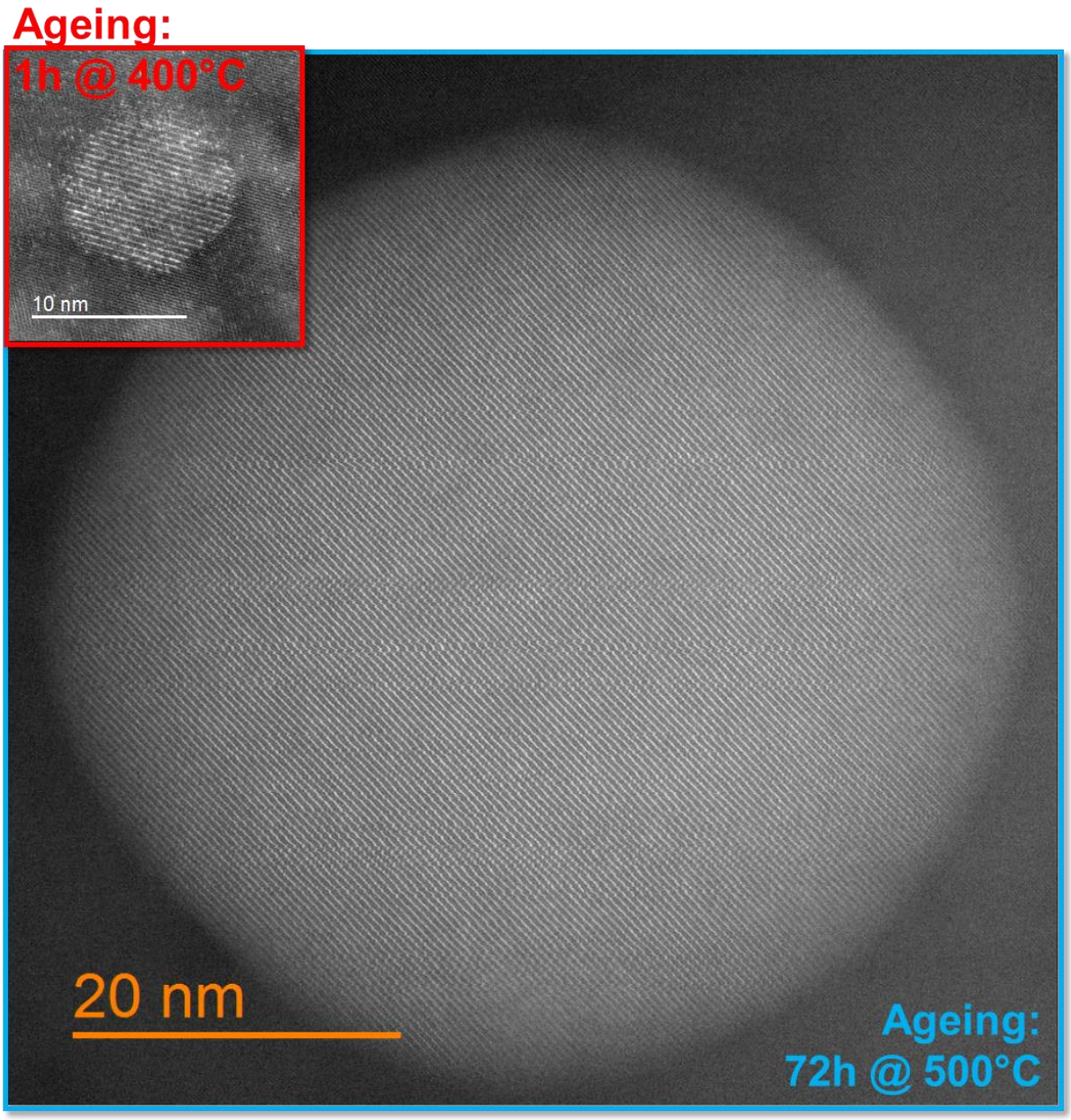

Figure 69: Direct comparison of two precipitates in short and long aged non-EBRS samples.

While all the findings discussed so far (size and distribution, dependence on ageing and $L1_2$ crystal structure coherently matching matrix) match present knowledge on $Al_3(Sc,Zr)$ precipitates documented in literature, as described in chapter 3, there is one clear difference not discussed yet: The core-shell structure. Previous investigations of similar material systems found precipitates with core-shell structures, for ageing times long enough to allow Zr-diffusion to the Sc-rich precipitates. This core-shell structure had been explained via the slower diffusion of Zr in the Al-matrix and the impossibility of Zr diffusion in Al_3Sc and Sc diffusion in Al_3Zr.[104] Our preliminary investigations show no evidence of such a core-shell structure, which should be easily detectable via HAADF STEM due to the great difference in atomic numbers of Sc and Zr (21 and 40). This issue will further be discussed later in this chapter.

8.2 In Situ Heating Experiments

In situ experiments were carried out to experience the evolution of the AlMgScZr system over time. Therefore an as-cast sample was prepared as a lamella and mounted on a heatable chip of the DENS solutions heating holder[127].[viii] The system was heated to 500°C. Two processes can be witnessed in the first minutes of heating: The formation of small Sc rich precipitates and a phase transformation originating from one side of the lamella, spreading and finally capturing the whole lamella. Figure 70 shows the comparison of the lamella before heating and during the phase transformation, which appears to be a recrystallization. The border region of the recrystallized phase in Figure 70 shows a hexagonal feature, which is in line with the fcc crystal structure in <111> direction, which was observed in the sample.

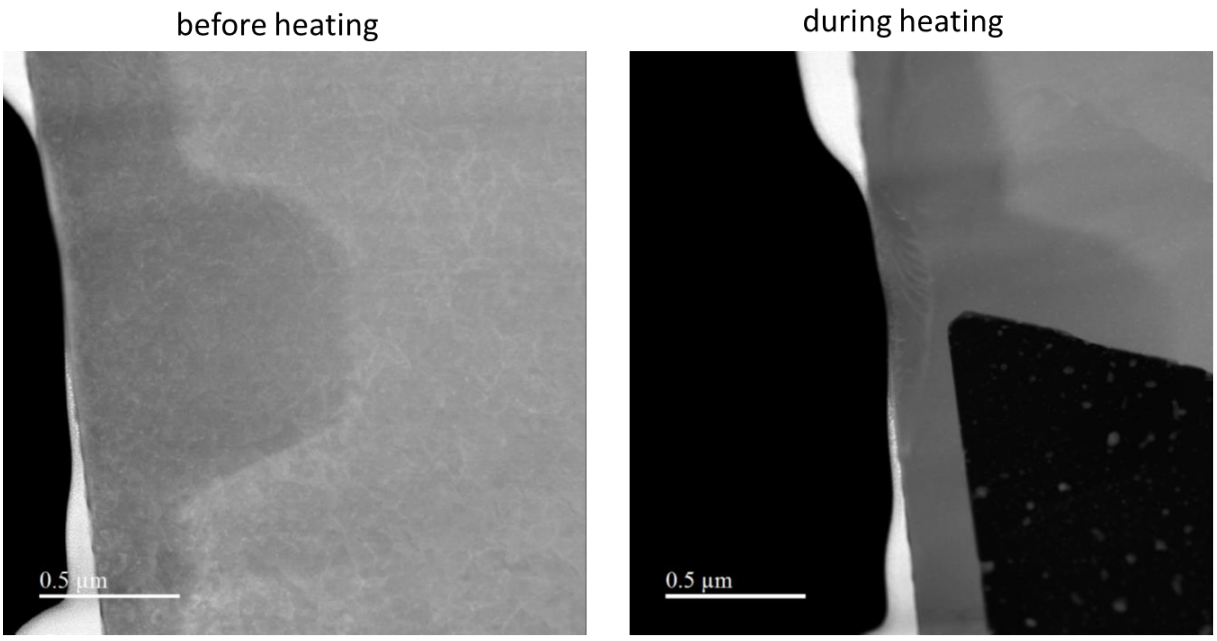

Figure 70: HAADF STEM overview of the phase transformation which occurred during heating of the untreated AlMgScZr sample at 500°C.

Figure 71 shows a smaller region of the sample during the recrystallization process, over time. The movement of the grain boundary can be observed. A close look at precipitates at the border regions shows how the precipitates pin the boundary, for short moments and slow down its movement in the process. The precipitates encircled in blue in Figure 71, for instance, prevent the recrystallization of the sample volume "behind" them, until the recrystallization boarder has moved clearly past them.

[viii] The sample preparation for the in situ experiments was performed by Martina Dienstleder.

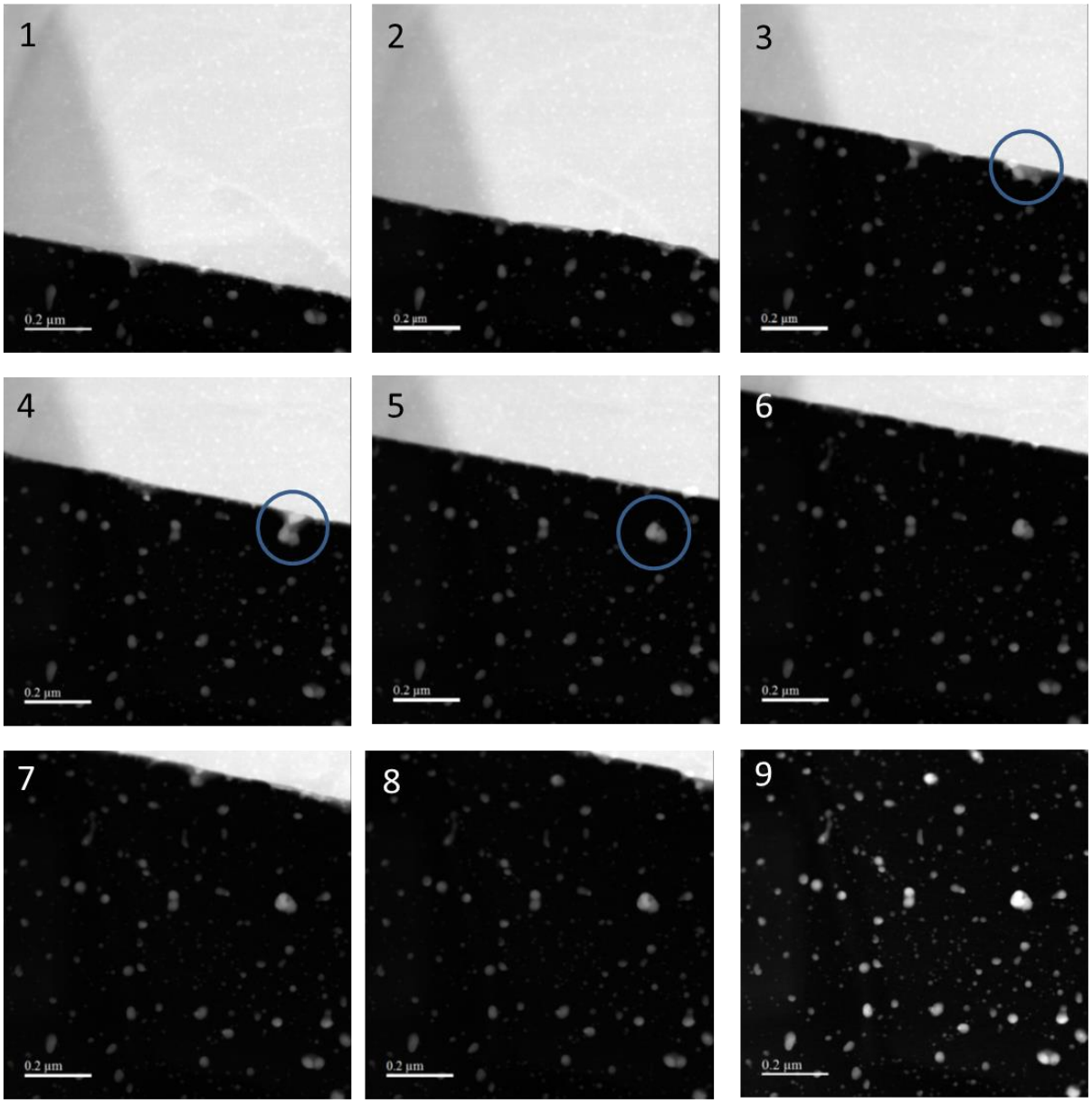

Figure 71: Movement of the re-crystallisation boundary over time at 500°C. The blue circles indicate the evolution of a small group of Sc-rich precipitates.

Figure 72 shows HR images of the sample after several hours of heating. At that point in time not only Sc rich precipitates have formed but also agglomerates of Zr atoms. These Zr agglomerates move through the sample. This can be seen on two videos provided in the electronic supplementary information.

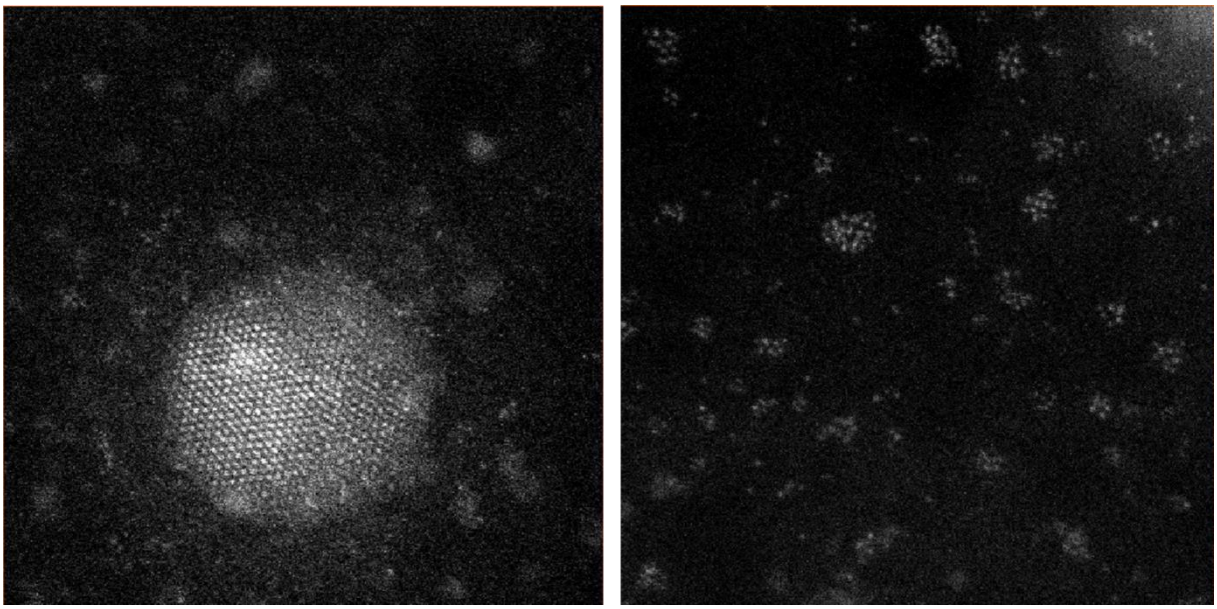

Figure 72: HR images of in situ experiments at 500°C after several hours. Left: Sc-rich precipitate surrounded by several Zr agglomerates: Right: Zr agglomerates. *both also available as videos, see electronic supplements

8.3 2D Spectroscopic Investigations

Spectroscopic data is necessary to determine the actual composition of the sample. All spectroscopic signals described in the following were acquired at the Titan[3] in STEM mode. Offline analyses were performed via digital micrograph software. EDX and EELS Spectrum images (see section 2.2) were acquired. Elemental maps, as shown in Figure 73 for a short aged (1h at 400°C) sample, were calculated using Kramers[115] model for background subtraction in EDX. It could be verified that these short aged precipitates are Sc-rich. No Zr enrichment was found near the samples. This was to be expected, due to the lower diffusivity of Zr in the Al-matrix.

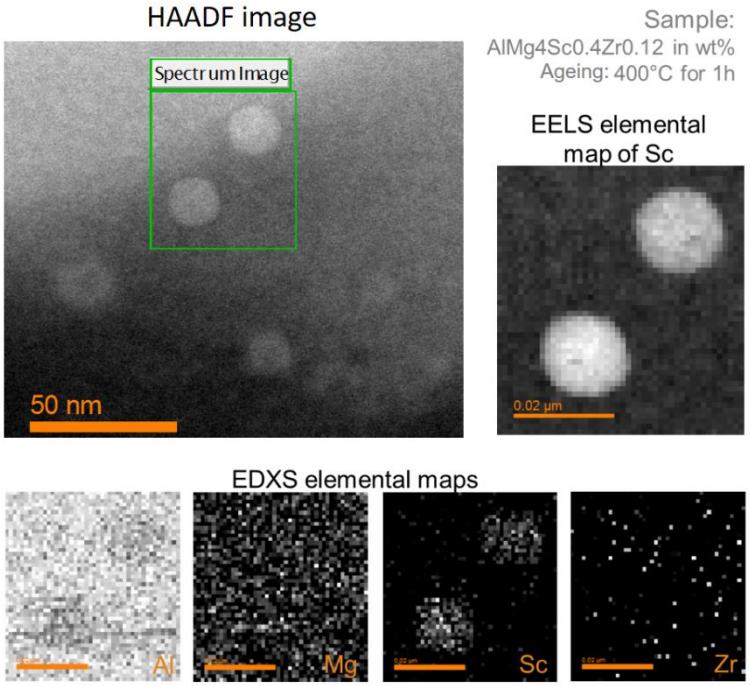

Figure 73: EELS and EDX spectrum images of precipitates in a short aged non-EBRS treated sample.

Elemental maps of a long aged (72h at 500°C) sample (see Figure 74) showed, that the precipitates are not only Sc, but also Zr rich. At this point also the precipitates' Sc-richness after short ageing and Sc- and Zr-richness after long ageing, which were described in literature could be shown to be true also for our samples, but the core-shell structure could not yet be verified, even though some HAADF images seemed to show it very faintly. To shed more light on the core-shell debate another spectroscopic investigation was conducted.

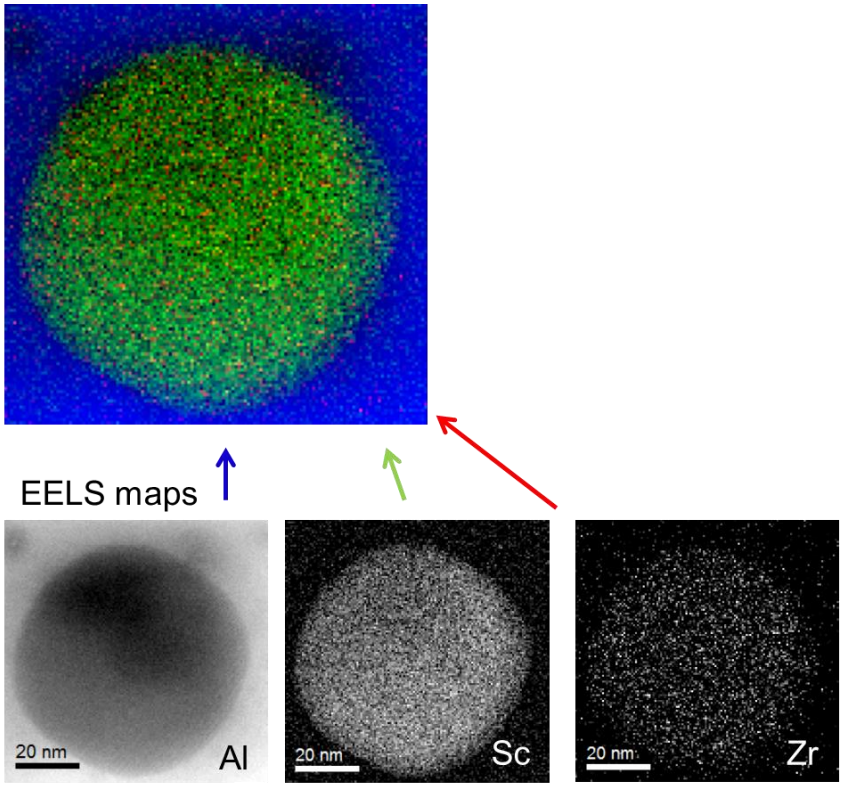

Figure 74: Spectroscopic investigation of precipitates in a long aged sample via EELS spectrum images.

EDX spectra were acquired while scanning a region in the centre of the precipitate – for gaining information including the core region - and a region on the side of the precipitate to gain a signal that only stems from the shell. A difference in Sc/Zr ratio could be found in those experiments, allowing us to conclude that there is some kind of core-shell structure, however different from the kind described in literature[97,98,101,104], which has a clearly defined shell, easily detectable in HAADF images through the high contrast to the core region.

Figure 75 shows the Sc/Zr concentration ratio (in at.%/at.%) for numerous precipitates determined via the EDX signal measured at the Titan[3]. It can be seen, that with the exception of one precipitate we found that the core contained more Sc than the shell. Another very interesting observation that can be made is that small precipitates are richer in Zr than larger precipitates, at a relative scale. One possible explanation is that the Zr diffusion happens after the Sc diffusion and the smaller precipitates have a larger surface to volume fraction: As Zr can diffuse more easily in pure Al the greater surface leads to an increased Zr uptake per unit volume.

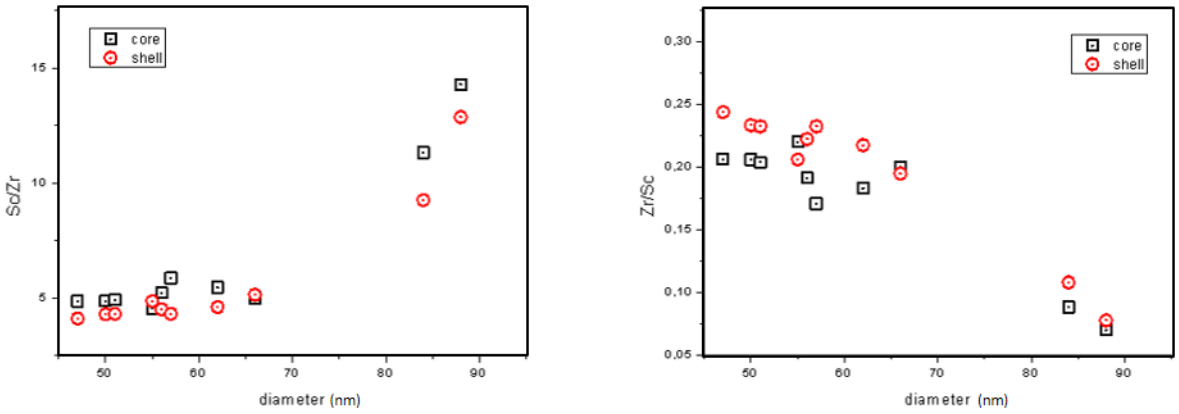

Figure 75: Sc/Zr and Zr/Sc concentration ratios in (in $\mathbf{at.\,\%/at.\,\%}$) for core and shell measured in 2D

It needs to be noted that this analysis was performed in 2D. Consequently there is no pure core or shell signal. On the one hand both signals are mixed with the signal of the matrix, which might cover the precipitate on top, bottom, or both. This hinders the retrieval of core and shell compositions, but it does not influence our results too badly, as long as we only compare the Sc/Zr ratios of core and shell, as the matrix should mainly consist of Al and some Mg. Problematic however is the fact, that the core is always surrounded by the shell, thus we cannot get a real core Sc/Zr ratio, but only a mixed signal of the following kind:

$$a * \left(\frac{Sc}{Zr}\right)_{core} + b * \left(\frac{Sc}{Zr}\right)_{shell} \tag{84}$$

where a and b are unknown. For simplicity this mixed signal was still referred to as core signal in the description above.

8.4 The Effective Atomic Number

This superposition of signal stemming from a precipitate and matrix will also be reflected in the HAADF signal. The scattering from a column is approximately proportional to the mean square atomic number $\overline{Z^2}$. In the HAADF signal the exponent can be smaller than two, depending on detector geometry.[8] Thus assuming non-channelling conditions, we can draw some conclusions on composition from HAADF intensity. To better understand the influence of the superposition of matrix and precipitate a Matlab code was written (see attachments), to calculate an effective Z that an HAADF signal would correspond to at a certain distance from the centre of a precipitate with a certain composition and radius, embedded in matrix for a certain sample thickness. Figure 76 shows the resulting effective Z Z_{eff} for a particle with a diameter of 50 nm, once the overall sample thickness displayed on the x-axis, and once the distance from the centre of the precipitate as the x-value. In this case it was assumed that the precipitate is perfectly spherical and complete within the matrix. Already for this simple case it becomes apparent that the effective Z is influenced by various factors. If a conclusion on composition is to be drawn from the HAADF signal there are still a few unknowns that need to be eliminated. One of those would be the exact Z-dependence of the signal delivered by the detector system. Figure 78 shows the results of the calculation performed with the exact same values as the one, of which the results are displayed in Figure 76 except for the Z-dependence, which was chosen to be $Z^{1.7}$, as opposed to Z^2. Comparison of the effective Z-values shows a reduction.

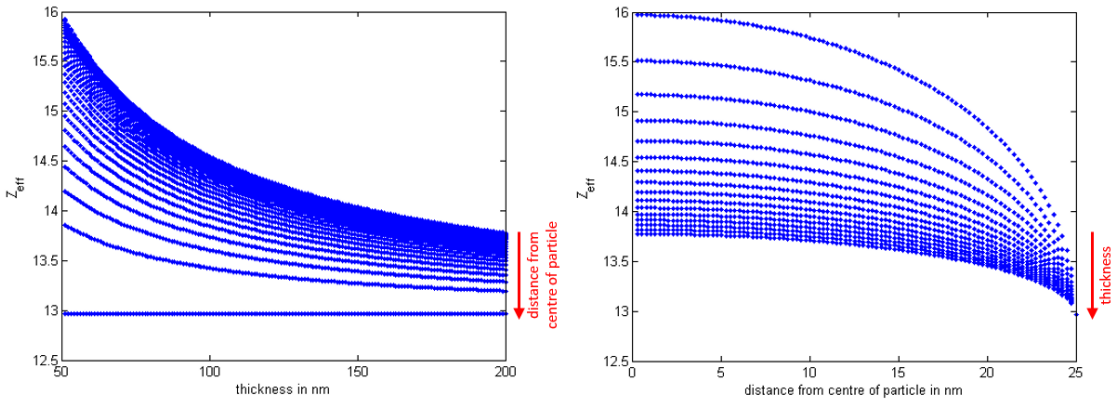

Figure 76: Effective atomic number. $Al_3Sc_xZr_{1-x}$ with a Sc/Zr ratio (in at. %/at. %) of 15 in an AlMg matrix; partice size: 50 nm. The figure on the left shows the change in effective Z with sample thickness for different distances from the centre of the particle. The graph on the right shows the variation of effective Z with the distance from the centre of the particle for different sample thicknesses. Z-dependence was considered to equal Z^2.

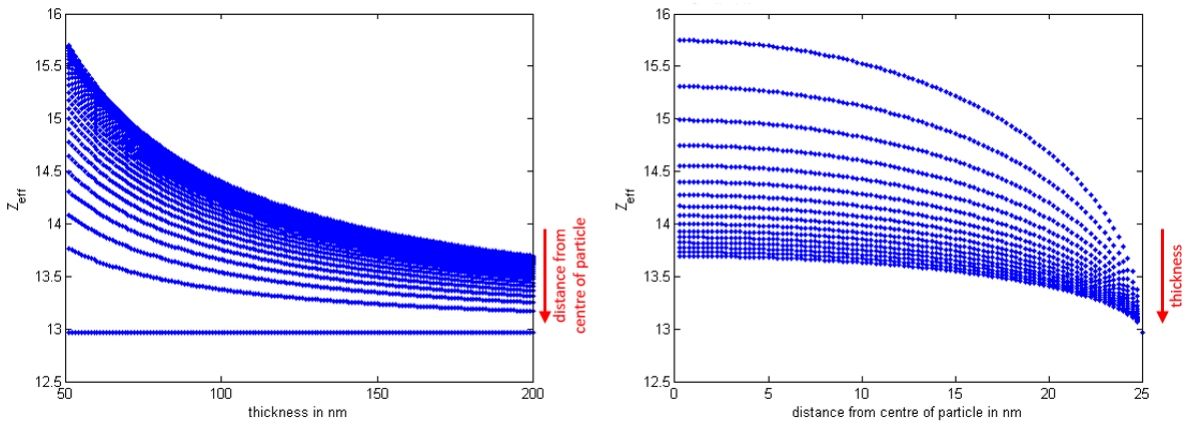

Figure 77: Effective atomic number. $Al_3Sc_xZr_{1-x}$ with a Sc/Zr ratio (in at. %/at. %) of 15 in an AlMg matrix; partice size: 50 nm. The figure on the left shows the change in effective Z wih sample thickness for different distances from the centre of the particle. The graph on the right shows the variation of effective Z with the distance from the centre of the particle for different sample thicknesses. Z-dependence was considered to equal $Z^{1.7}$.

Furthermore the thickness of the sample region investigated needs to be known precisely. As can be seen in Figure 76 and Figure 77 it significantly affects the effective atomic number, especially at low thicknesses typically preferred in (S)TEM investigations. Position averaged convergent beam electron diffraction (PACBED)[92] (see also part I section 2.6.3) allows a highly accurate thickness determination. Figure 78 shows how we determined the thickness of an AlMgScZr sample region in the Al-matrix near a precipitate. Visual comparison of simulated PACBED patterns for various thicknesses with a measured PACBED pattern (Figure 78 right), allows the determination of thickness through the best match, which was found to be 23 nm in the case depicted in Figure 78. Such a thickness determination via comparison with a PACBED simulation would have to be performed as close as possible to any analysed precipitate, which means a lot of effort. Unfortunately the thickness is not the only information needed to evaluate composition of a precipitate embedded in matrix.

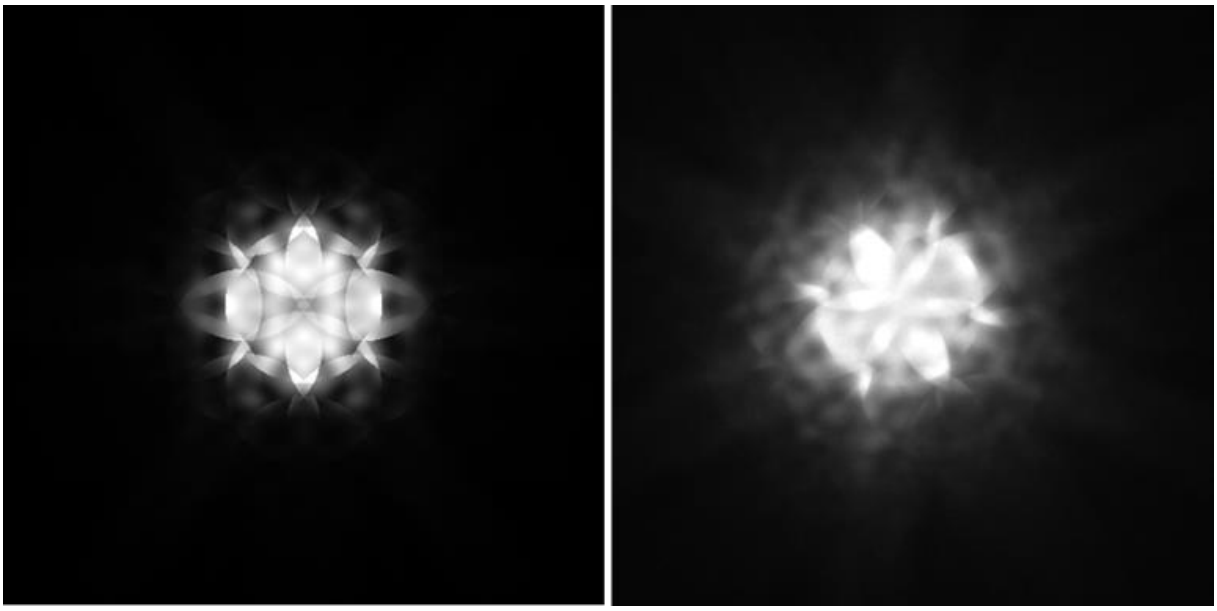

Figure 78: Thickness determination via position averaged convergent beam electron diffraction (PACBED). Left: simulated PACBED pattern of Al in <111> orientation. Right: Experimentally acquired PACBED pattern of Al in <111> orientation.

In that context it needs to be emphasised that before we were treating a simplified case, by assuming a perfectly spherical precipitate completely embedded in matrix. The main problem lies in the fact that in case of a real sample we do not know whether the precipitate is complete in the sample. It may be cut-off at the top or bottom due to sample preparation as schematically shown in Figure 79. This would lead to a smaller amount of precipitate contributing to the detected signal. One might say that there could be a way to determine this via the radial intensity gradient. This however could only be done if the precipitate's composition was known and constant. Apart from the obvious problem that the precipitate's composition is not known, as it is the variable of interest, it has also already been shown (see Figure 75) that the composition can vary throughout the precipitate.

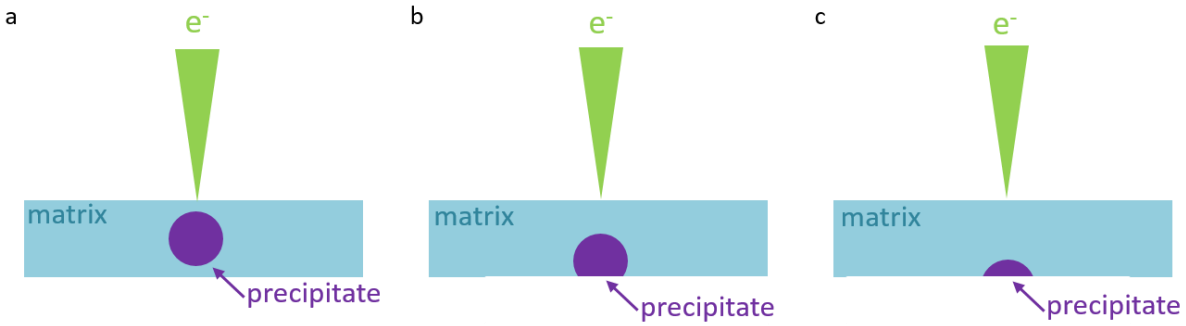

Figure 79: Schematic representation of the side view of a sample demonstrating that a precipitate embedded in matrix could be cut due to sample preparation, thus reducing its contribution to the detected signal. a) Precipitate complete within sample; b) and c) precipitate cut to different extents, thus reducing its contribution to the detected signal to different extents.

Consequently this evaluation of theoretical effective Z values leaves us with the conclusion that the only way to gain pure compositional information from different regions of interest within the precipitate is to make use of tomography.

9 Analytical Tomographic Investigations of the AlMgScZr System

9.1 Introduction

Analytical tomographic investigations on the AlMgScZr were performed on the following samples:

	Non-EBRS	EBRS
Short ageing	400° 1h	
Long ageing	500° 72h	500° 72h

As described in part I, section 3.1, EBRS stands for electron beam re-solidification, or electron beam re-solidified. The alloy is rapidly melted and solidified via electron beam. During this process the amount of Sc in solid solution is increased from 0.13 wt.% to 0.37 wt.%. [62]

9.2 Elemental Map Reconstructions

Figure 80 shows segmented reconstructions of the EELS and EDX signals of Al, Sc, Zr of a short aged (left) and long aged (right) non-EBRS sample. The most distinctive differences are that in the short aged sample the precipitates are an order of magnitude smaller, than in the long aged sample, and that the short aged precipitates are only Sc rich, while the long aged precipitates are Sc and Zr rich. If a comparison with our 2D studies and with studies performed on the Al-Sc-Zr system found in literature[104] is drawn, this is not surprising. A detailed look at the short aged sample, however, reveals a rather interesting fact: Regions that contain less Al than the threshold value defined for the Al matrix, but also contain less Sc than the threshold value for the Al_3Sc precipitates can be found. It can be concluded that the short aged precipitates do not exhibit the expected composition of perfect $L1_2$ crystal structure. This is a novel finding for this material system.

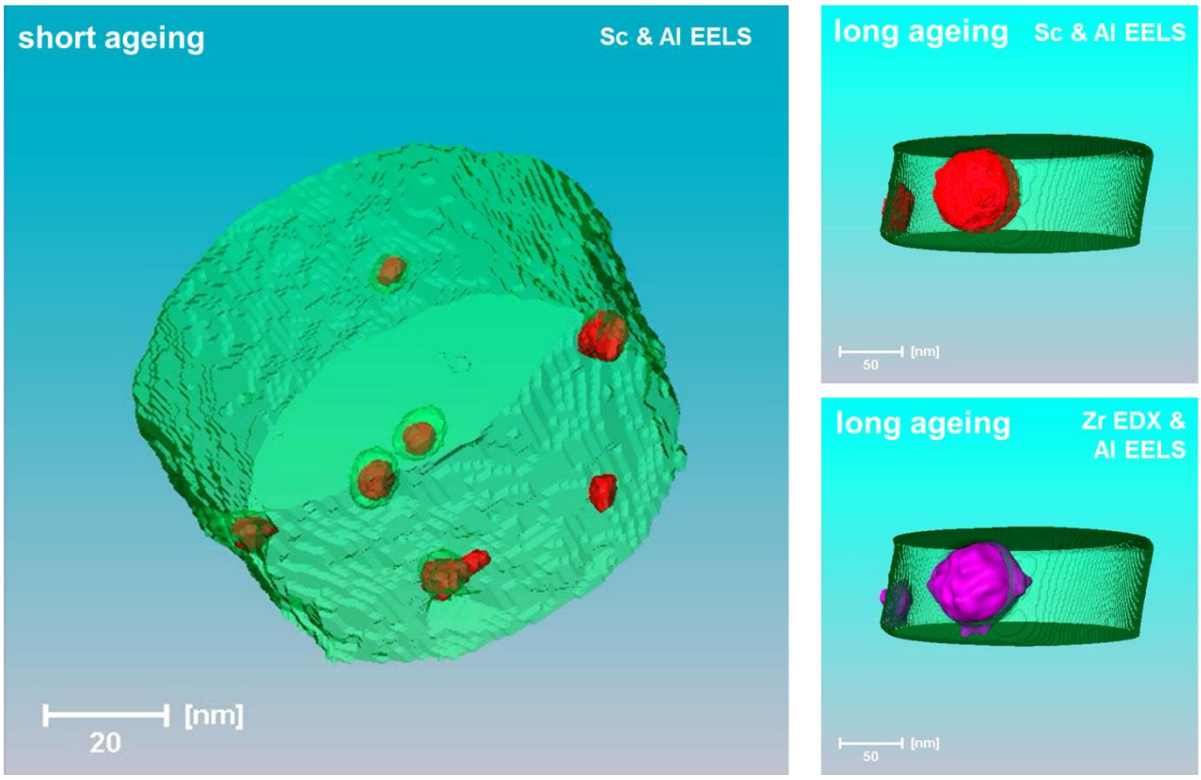

Figure 80: Segmented elemental map reconstructions of short aged (left) and long aged (right) non-EBRS treated samples. The Al-signal is shown in green, the Sc-signal in red and the Zr-signal in purple.

The volume rendered reconstructions of the Sc L signal of the same samples can be seen in Figure 81. They not only give a good overview of the Sc distribution, but confirm the conclusion drawn above: In the short aged precipitates the Sc distribution is not uniform. As the short aged precipitates are Zr-free, it follows, that the $L1_2$ crystal structure is not perfectly pronounced. In the long aged precipitate inhomogeneity can also be seen. But due to the presence of Zr, the present system is not Al_3Sc, but $Al_3(Sc,Zr)$, so no further conclusion concerning stoichiometry can be drawn merely from a visual analysis of the Sc distribution. To do that a quantitative compositional analysis is necessary. This can be done via voxel spectroscopy.

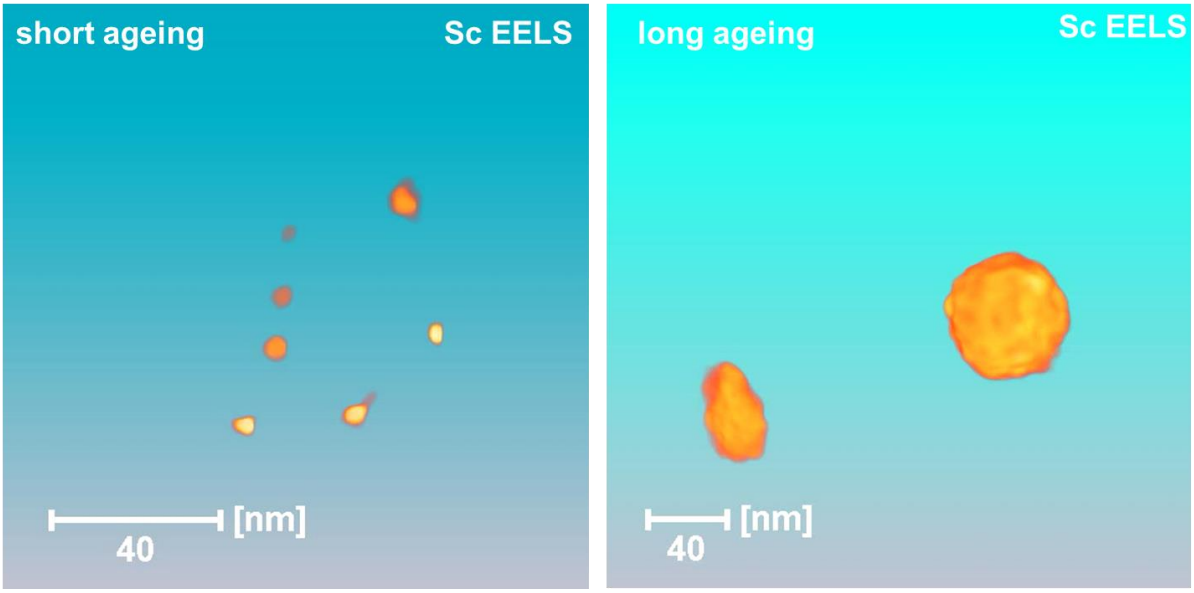

Figure 81: Volume rendered elemental map reconstructions of short aged (left) and long aged (right) non-EBRS treated samples. The Sc-K EELS signal was reconstructed.

9.3 Voxel Spectroscopy

As discussed above the predicted core shell structure could not be seen very well in HAADF images of long aged samples, could however be verified via analytical investigation. Figure 82 shows how tomographic reconstruction brings out the core shell structure of the precipitates in a long aged EBRS treated sample, which is nearly impossible to see in a single image. This reconstruction revealed that every precipitate in the investigated volume exhibited a core-shell structure - even if only weak.

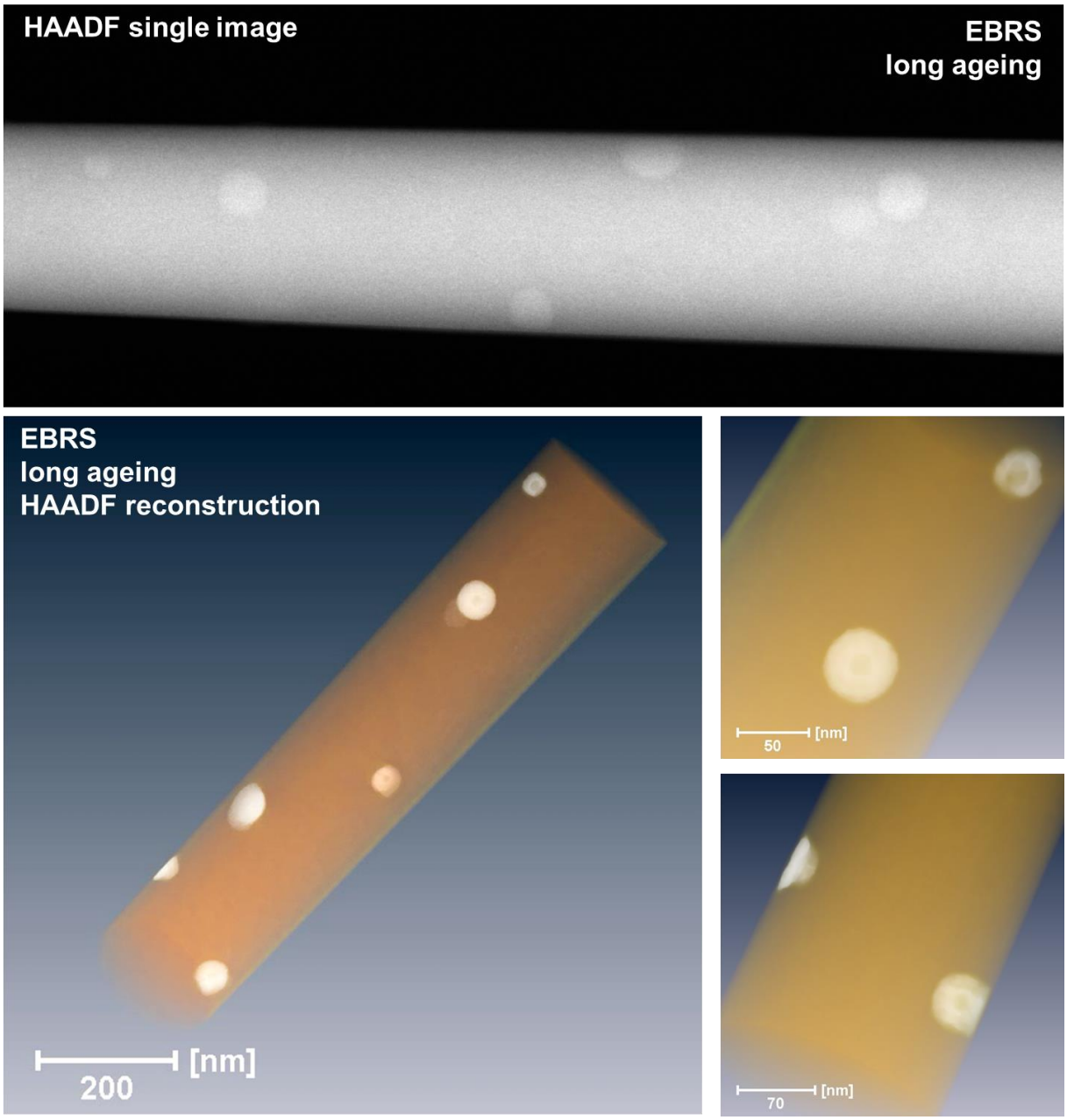

Figure 82: Needle shaped long aged EBRS treated sample comparison of single HAADF image (top) and tomographic reconstruction via TV minimisation (bottom).

One of our major interests in the investigation of the AlMgScZr alloys was the retrieval of pure analytical (EELS or EDX) signals from core, shell and matrix region. As TV minimisation reconstructions of the HAADF signal allow the distinction of those regions, the next step was to use these reconstructions to create masks, which allow the retrieval of spectra from regions of interest from a 4D data cube containing reconstructed EELS or EDX signals in every voxel. Consequently SI tilt series containing HAADF, EELS and EDX data were acquired, and aligned. TV minimisation was used to reconstruct the HAADF signal and create masks of the reconstructed volume, where each voxel was assigned to either core, shell or matrix. By summing all the pixels of the same type, integrated spectra could be obtained. For visual comparison of the spectra (as shown in Figure 83) they need to be normalised, as the three regions contain different amounts of voxels.

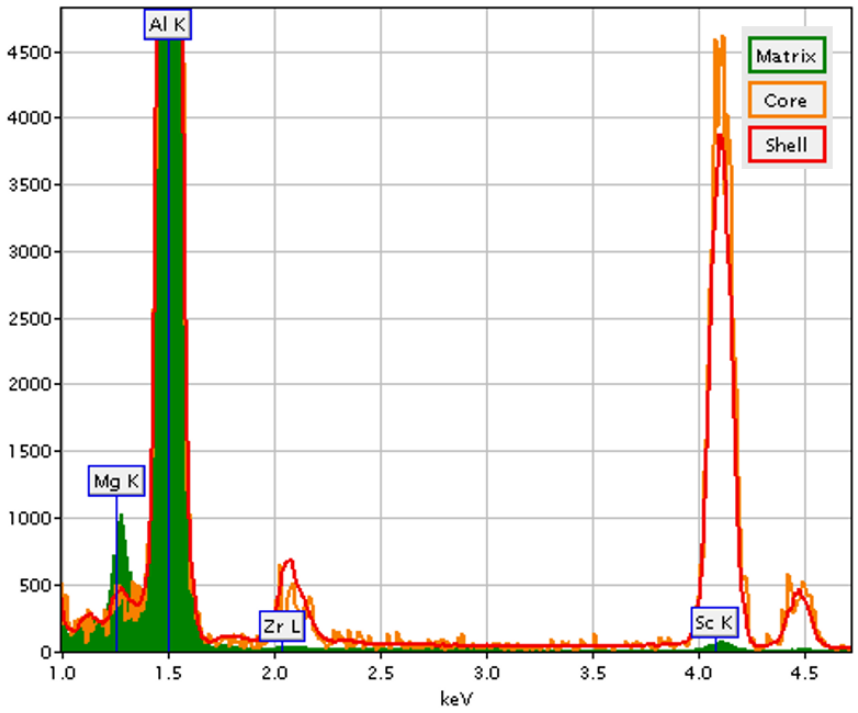

Figure 83: Comparison of normalised spectra from the core, shell and matrix region of a long aged EBRS treated precipitate.

The voxel spectroscopic analysis shown in Figure 83 now confirms that the core holds more Sc than the shell. It also shows that less magnesium (Mg) is present in the precipitate than in the matrix. But most importantly it gives one very interesting new insight that could not be obtained via 2D methods and has major consequences: **We find Zr within the core of the long aged precipitate.**

Short aged precipitates make up the core of the long aged precipitate. All previously described results show that the short aged precipitates are Zr-free. Consequently the Zr found within the core of long aged precipitates indicates, that **diffusion took place within the precipitate** during the ageing process. This contradicts the currently accepted theory[104] that there is no diffusion within the precipitates and thus the resulting core-shell structure of the precipitate is merely a result of different diffusivities of Sc and Zr within Al.

The retrieval of summed spectra via masks also allows to perform compositional analysis of 3D regions of interest. EDX voxel spectra were analysed using the Kramers[115] model for background subtraction and the standardless k-factor method of Gatan Digital Micrograph software. Error analysis was performed as described in section 5.2. The result was again unexpected: We found that the composition of the precipitate does not match that of $Al_3(Sc,Zr)$, but can be described as Al(Al,Sc,Zr). This crystal structure is schematically shown in Figure 84 b. We found that the amount of Al on the (Sc,Zr) – sublattice was 0.32 ± 0.06 at. % for the EBRS treated and 0.53 ± 0.05 at. % for the non-EBRS treated sample. As the absence of diffusion within such precipitates was explained[104] via the high activation energy of six jump cycles necessary for the diffusion of Zr in Al_3Sc or Sc in Al_3Zr, this compositional deviation explains why diffusion is possible within the precipitate.

Driving forces for diffusion are entropy, and the energetic advantage of Sc and Zr as second nearest neighbours[104]. Following those rules there is no further reason why we should still find a core-shell structure. However, if we again regard the reconstruction of precipitates in Figure 82 we can

observe, that independent of their size, all the precipitates exhibit a core-shell structure. And this independence of size, in combination with the extremely long ageing times, indicates that the occurrence of the core-shell structure is not a matter of time. Apparently the diffusion process is somehow stopped. These findings, lead to a new open question: What makes diffusion stop?

Another peculiarity arises, when comparing the difference between core and shell concentrations, which are shown in Table 7 for the EBRS treated sample and Table 8 for the non-EBRS treated sample. It seems remarkable that the core-shell structure is visible in the tomographic reconstructions, even though the compositional variation is so small.

Table 7: Al, Sc and Zr concentrations in core, shell and matirx of an EBRS treated sample in at %

	Al	*Sc*	*Zr*
Core	79.3	18.1	0.9
Shell	80.9	15.9	1.1
Matrix	94.8	0.3	0.1

Table 8: Al, Sc and Zr concentrations in core, shell and matirx of an EBRS treated sample in at %

	Al	*Sc*	*Zr*
Core	82.8	14.1	1.2
Shell	86.0	10.3	1.3
Matrix	95.9	0.2	0.2

In a next step we wanted to find out, whether the composition of the shell is uniform or whether we find a compositional gradient. Therefore new masks were generated, where the shell was divided into several subshells, as schematically shown in Figure 84 a. Figure 84 c shows the resulting compositions for the core and the first 15 subshells. The most prominent feature of the radial compositional deviation can be found at the interface between core and shell: Here the Al-concentration drops to a minimum, while the Sc concentration reaches its maximum. So the interface between core and shell marks the region with minimum compositional deviation from that of the $L1_2$ crystal structure. This same behaviour was also found for the compositional variation of the non-EBRS treated sample.

This minimum deviation from the $L1_2$ crystal structure indicates a region of minimum diffusion – possibly even a diffusion barrier. Consequently whatever is responsible for the formation of this region might be responsible for stopping the diffusion process.

It also shall be noted that this high Sc region at the edge of the shell appears bright in the HAADF images and thus increases the contrast with the core, which is darker in the HAADF signal. This explains the visibility of the core-shell interface, even for small overall compositional deviations between core and shell.

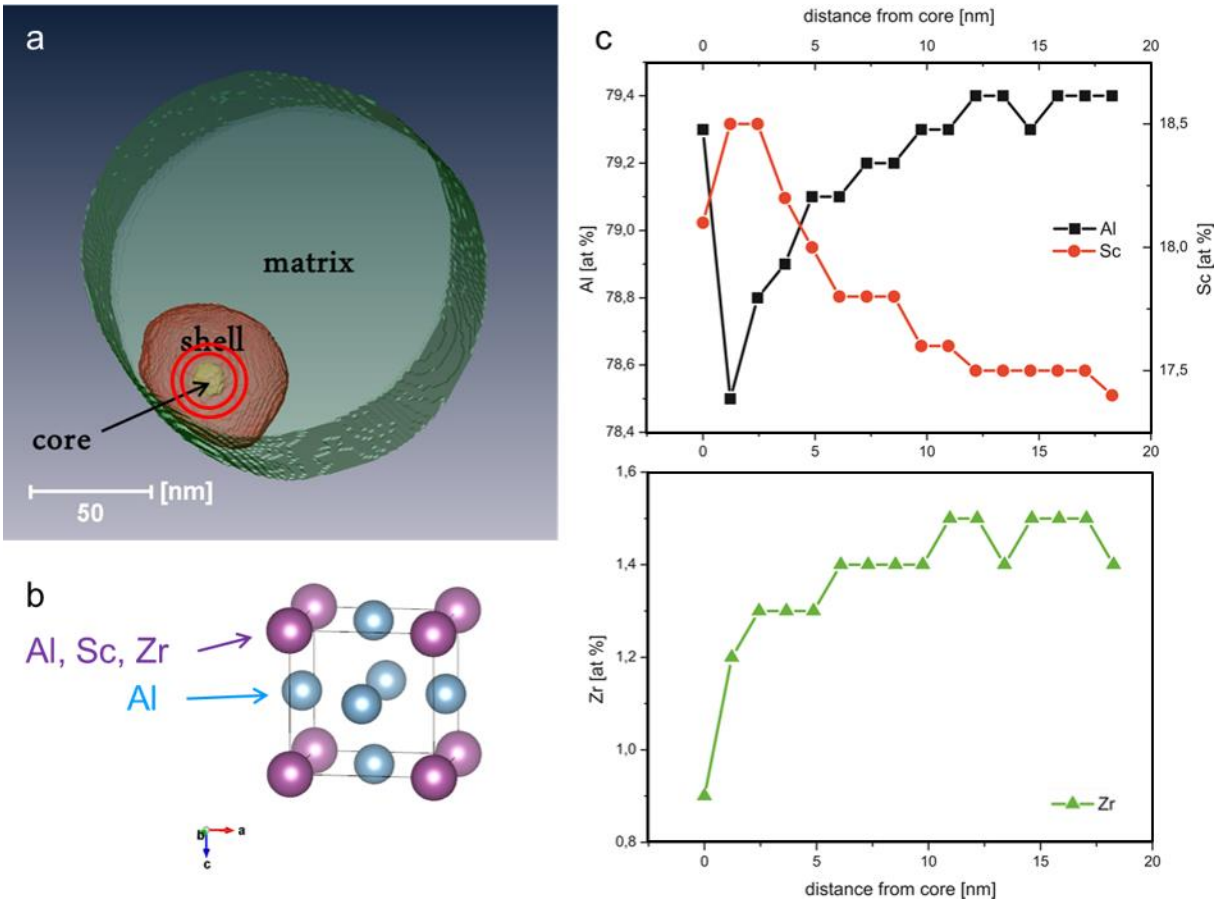

Figure 84: Voxel spectroscopic analysis of subshells. a) Image of mask indicating subshells; b) Crystal structure and possible occupation c) Al, Sc and Zr compositional distribution over subshells

10 Advanced (HR) STEM HAADF Investigations

10.1 HR STEM HAADF Investigations and QEP Simulations

In an attempt to understand the creation of the minimum diffusion region, or diffusion barrier a HR HAADF investigation of short and long aged precipitates supported by frozen phonon multi-slice simulations was conducted. Figure 85 shows a HR HAADF STEM image of a precipitate in a long aged EBRS treated sample. In the bottom right region the coherent transition from precipitate to Al-matrix can be seen. Throughout the precipitate (but especially close to its edge) some columns appear significantly brighter than the others.

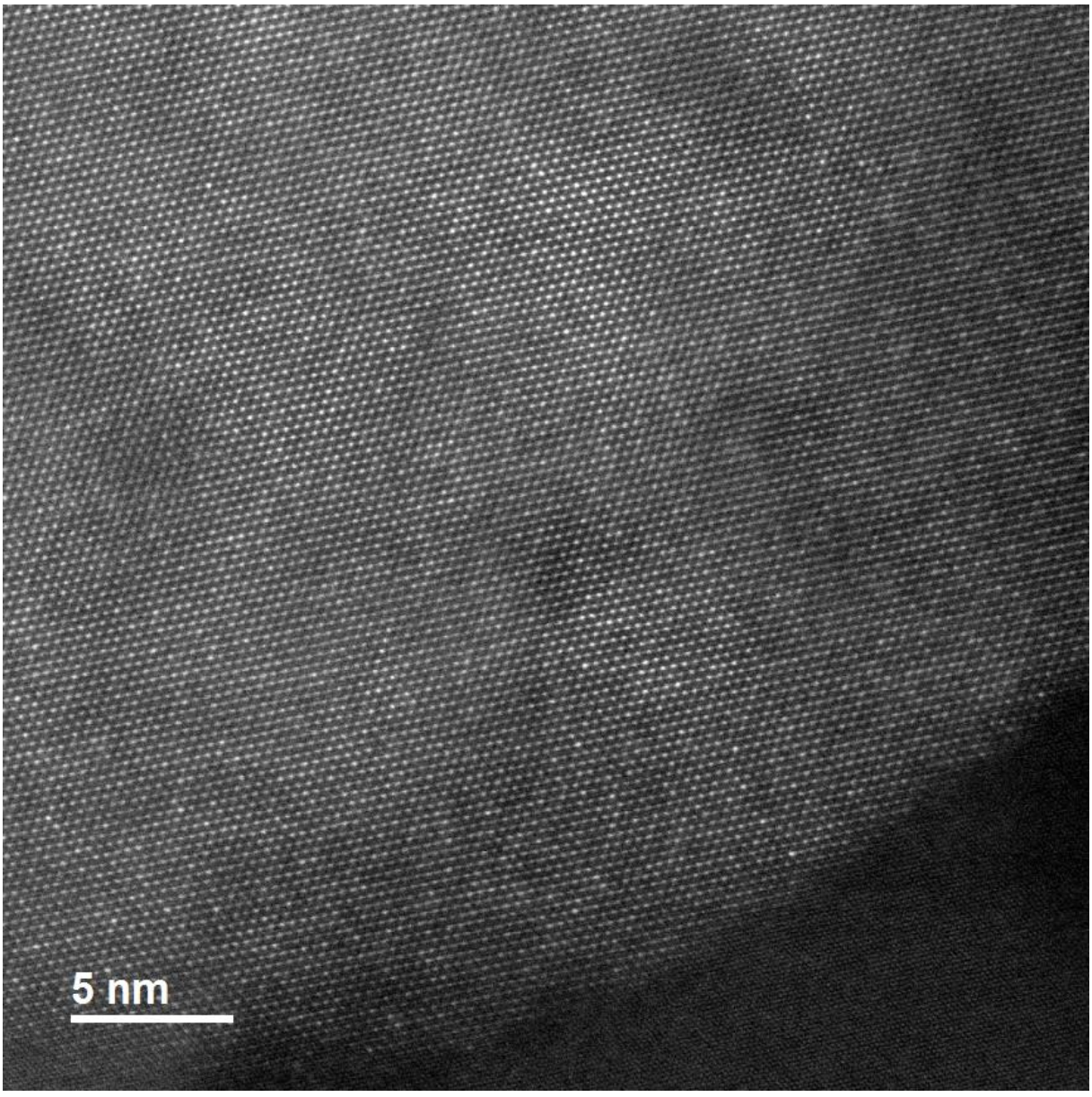

Figure 85: STEM HAADF image of the edge of a spherical precipitate in a long aged EBRS treated sample.

To follow the assumption that this could be caused by Zr atoms QEP simulations (see section 2.6) were performed. Figure 86 shows a µSTEM simulation of Al_3Sc in <100> direction, where on every second Sc-rich column in *x* and *y* every 8th Sc atom was replaced by a Zr atom. It becomes apparent

that already small amounts of Zr are visible in the HAADF signal, indicating that especially close to the edge of the precipitate the higher brightness of columns could hint at single Zr atoms.

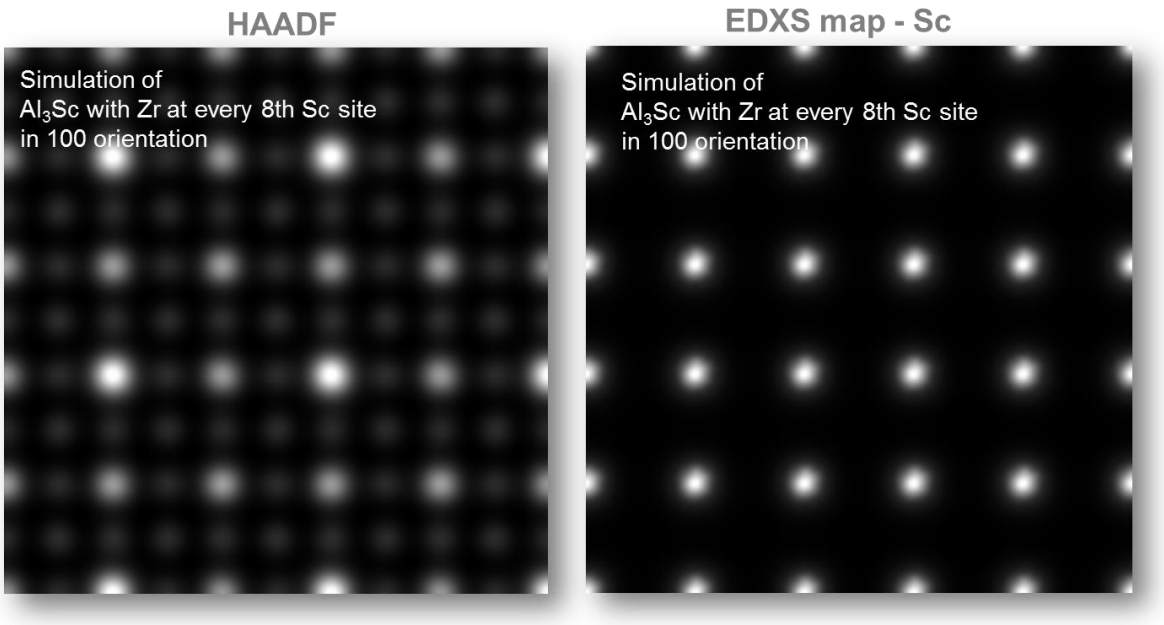

Figure 86: µSTEM simulation results of the $Al_3(Sc,Zr)$ system. Left: HAADF signal. Right: Sc-K EDXS signal.

Figure 87 shows the comparison of experimental results with µSTEM simulations of Al_3Sc, both in <111> direction. The simulation is five unit cells thick. In every second Sc-rich row one of the five Sc atoms was exchanged for a Zr atom. A model unit cell is shown in top-view and side view in Figure 87 bottom c and d. The comparison of intensity profiles from experiment and simulation suggests that the bright blobs may indicate Zr atoms on Sc sites. The sample region depicted on the top might be thicker than simulated, as suggested by the smaller intensity difference, between the columns. In the images below an intensity decrease close to the precipitate border can clearly be identified. As the possible Zr atom is found close to this border, the strong contrast can be explained by the probably small number of Sc atoms in beam direction.

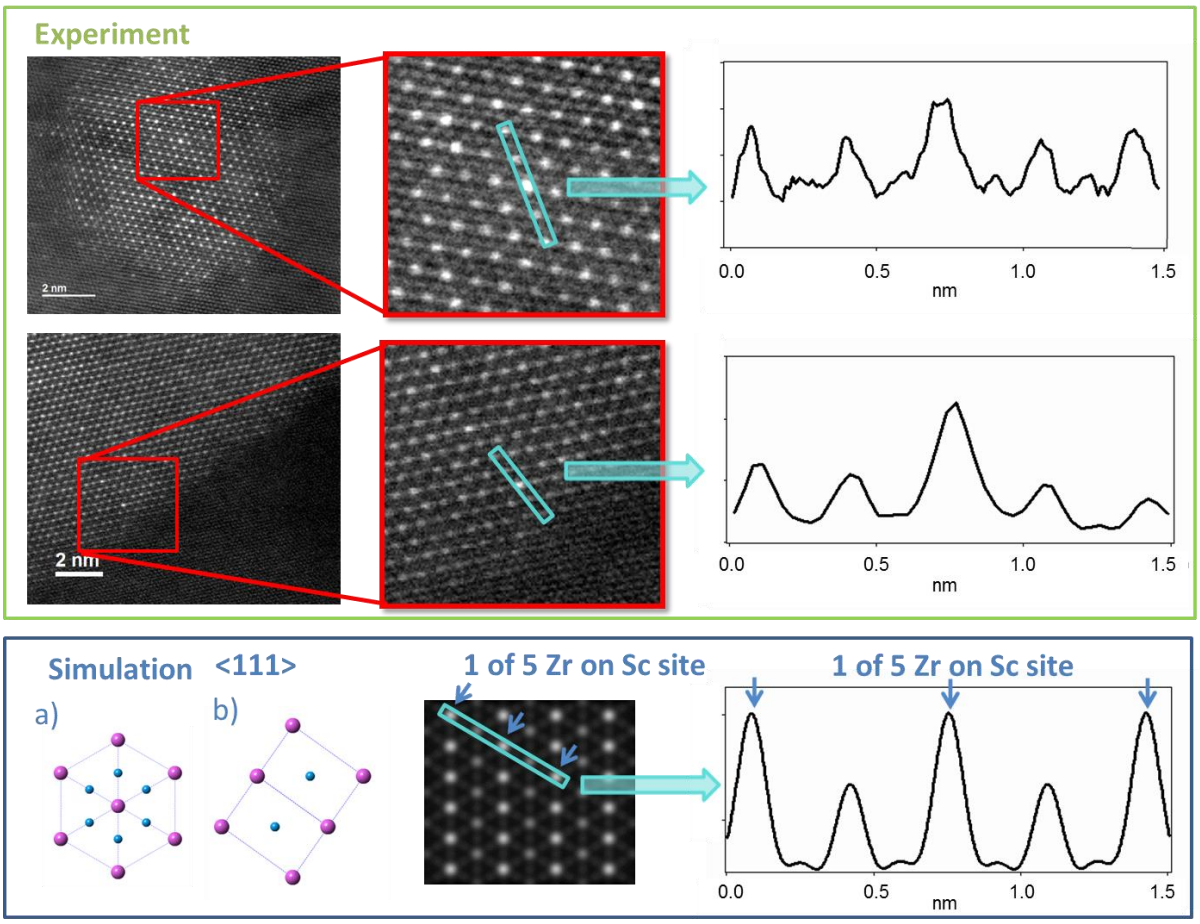

Figure 87: High resolution images and profiles of short (top) and long (below) aged EBRS treated precipitates revealing higher intensity columns on the Sc/Zr sublattice. a) and b): Model of Al_3Sc structure in <111> orientation as used for simulation in beam direction (a) and perpendicular to it (b). Sc atoms are depicted in purple and Al atoms in blue. Bottom middle and right: Simulated HR STEM image and profile from QEP simulation of Al_3Sc, where in the indicated columns 1 of 5 Sc atoms was substituted by a Zr atom.

The top region Figure 88 shows a larger version of the top most HAADF image of Figure 87 - a precipitate in a short aged EBRS treated sample. We find, that there are not only some very bright Sc-rich columns, which may indicate single Zr atoms within the precipitate, but we find various darker Sc-rich columns, hinting at inhomogeneities in the Sc distribution. In the enlarged region we even find a Sc column with the same HAADF intensity as the surrounding Al columns, suggesting that this column holds no Sc. It appears to be an Al channel within the Al_3Sc precipitate. To evaluate, whether slight grey scale variations could also hint at such channels we performed QEP simulations of the Al_3Sc system (also in <111> direction to match the experiment) and varied the number of Al atoms replacing Sc atoms in every second vertical row. We find that with the naked eye channels that are only a single atomic column wide can hardly be seen, even for extremely thin samples (5 unit cells in z-direction), if they run rather perpendicular to the beam direction, and therefore only lead to one or two Al atoms per Sc site per column in beam direction. It follows that only channels can be noted that run in a direction close to the beam and the less intense Sc-rich columns might indicate such channels.

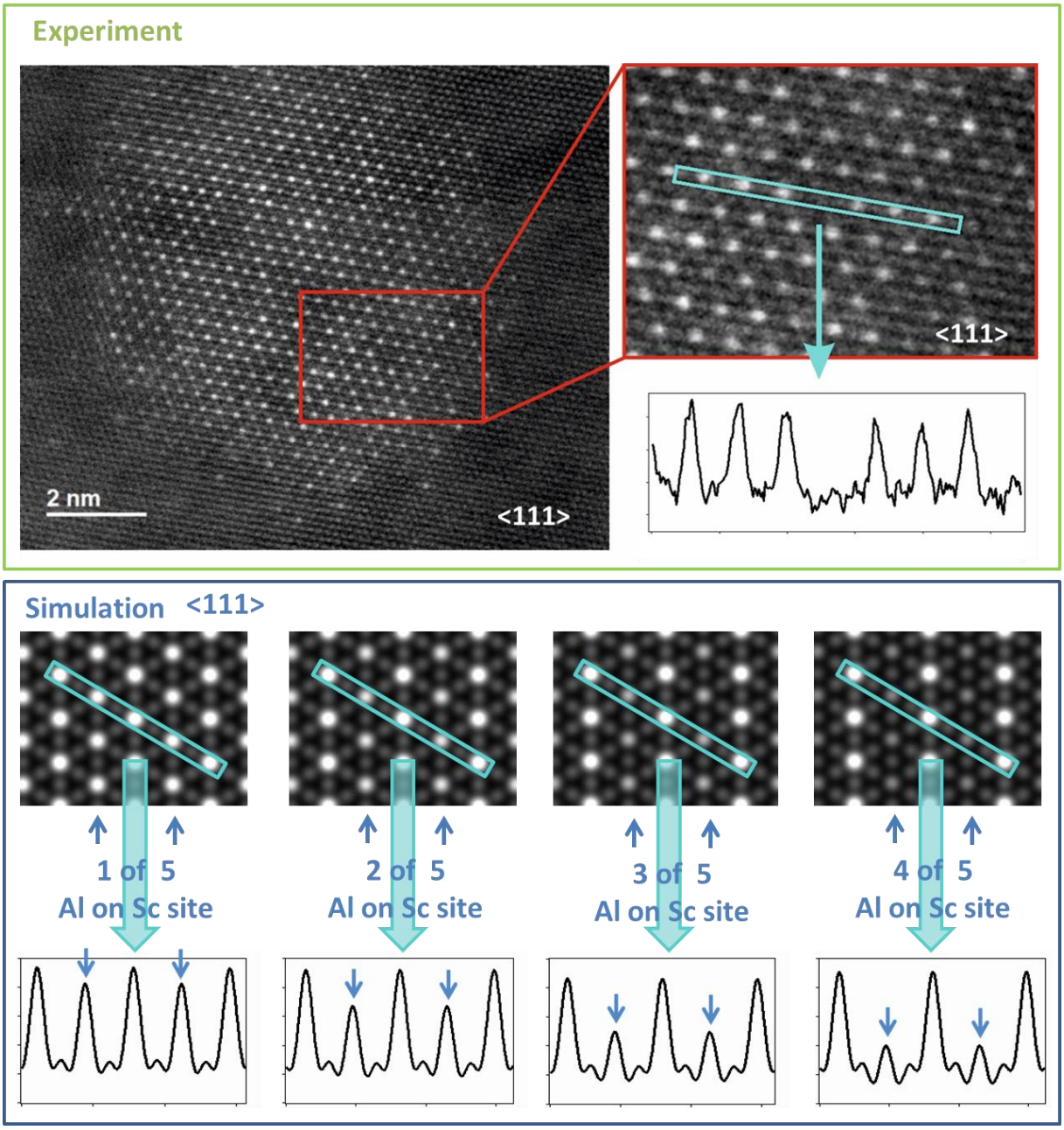

Figure 88: Top: Atomic resolution HAADF image and intensity line profile of a short aged precipitate revealing a matrix like channel with single column width in the Sc/Zr sublattice allowing 1D diffusion of Sc and Zr. Bottom: Images and line profiles from QEP simulations of Al_3Sc, where Sc atoms were substituted by 1, 2, 3 and 4 Al atoms in the indicated columns.

Assuming that this channel is not a random occurrence, but that Al atoms tend to arrange in channels rather than creating random point defects on the Sc-sublattice, the phenomenon of diffusion occurring and stopping can be explained: 1) As Sc and Zr are able to diffuse in Al these channels allow diffusion within the precipitate. 2) If those channels are very narrow (as indicated by the channel witnessed in Figure 88) the encounter of Sc and Zr atoms during diffusion might block the channels, as the diffusing atoms also represent the "building blocks of the walls of those channels". Such a self-limiting diffusion (schematically shown in Figure 89) process would explain the region of minimum compositional deviation from the $L1_2$ crystal structure which we found at the interface between core and shell (see Figure 84).

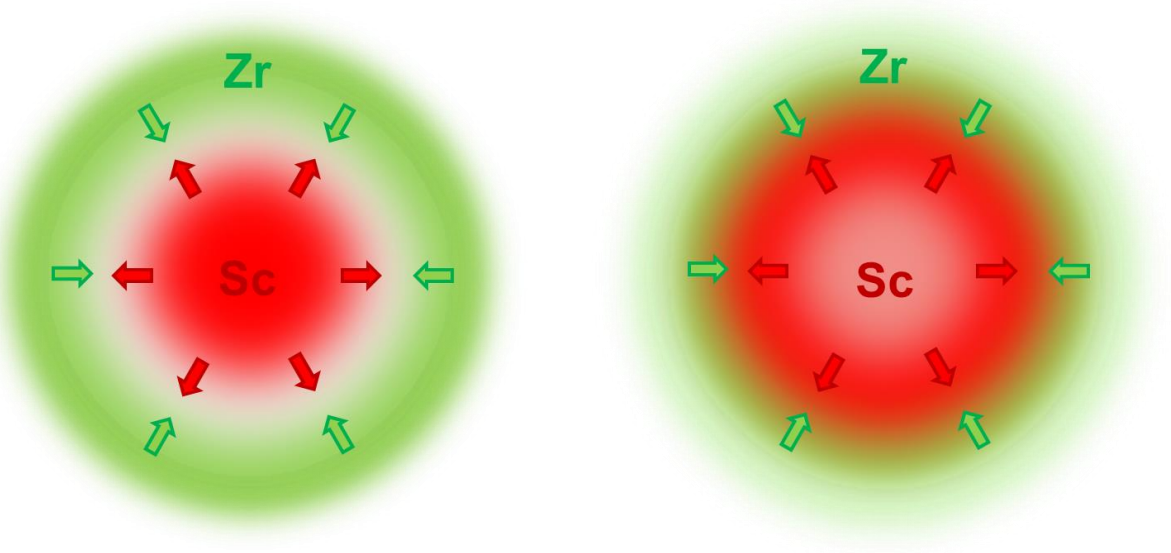

Figure 89: Schematic representation of suggested self-limiting diffusion process leading to a hollow spherical region with minimum compositional deviation from the $L1_2$ crystal structure.

At this point this is merely a hypothesis, which needs to be tested. As a first step this behaviour of separation of the Al and $Al_3(Sc,Zr)$ phases reminding of an atomic scale spinodal decomposition needs to be understood. Therefore theoretical thermodynamic analyses were performed.

11 Theoretical Thermodynamic Analysis

To find out whether at all and if yes, at which concentrations the separation of Al_3(Al,Sc,Zr) into Al and Al_3(Sc,Zr) is energetically favourable, a Gibbs Energy calculation was set up. [ix]

11.1 Gibbs Energy Calculation

The Gibbs Energy of the Al_3(Al,Sc,Zr) system was calculated using the regular solution model (see chapter 3), where the Gibbs energy per unit cell is given by:

$$g_{RS} = g_{IS} + \Delta h = \sum_i X_i g_i^0 + RT \sum_i X_i ln X_i + \frac{1}{2} \sum_i \sum_{j>i} X_i X_j \varepsilon_{ij} \tag{85}$$

The first term describes the mechanical mixture, the second term will be referred to as the entropy part, and the third describes the enthalpy of the system. Consequently the Gibbs energy can be written as:

$$\boldsymbol{G} = \sum_i X_i g_i^0 + \boldsymbol{H} - T\boldsymbol{S} \tag{86}$$

Figure 90 shows a scheme of the main routine set up for calculation of the Gibbs energies. The calculation was set up in a way, that the main routine calculates the Gibbs energy of the system for varying amounts of (Sc+Zr), but with a fixed Sc:Zr ratio. It relies on several sub-routines, for calculating the interaction energies, filling the matrix and calculating the enthalpy and entropy for certain configurations. The colour code in the equation above marks the different subroutines used for the calculation, in accordance with the scheme depicted in Figure 90.

The inputs for the main routine are the Sc/Zr ratio and the number of steps *n*, defining the number of different concentrations for which the calculation was performed, thus defining the resolution of the calculation in terms of concentration. The temperature needs to be defined right in the beginning of the calculation, as it not only influences the Gibbs energy as obviously visible in equation 86 above, but also has an impact on the interaction energies ε_{ij} ($\varepsilon_{ij} = f(T)$) which appear in the enthalpy term of equation 85. Said interaction energies were taken from the supplementary information of Clouet et al.[104], where they were calculated using ab initio methods.

[ix] The Gibbs Energy calculation was originally coded by Bernhard Sonderegger. My contribution to the code was merely its adaption to allow arbitrary (Sc+ Zr) and Zr concentrations which originally were limited. This adaption is described in the end of the chapter.

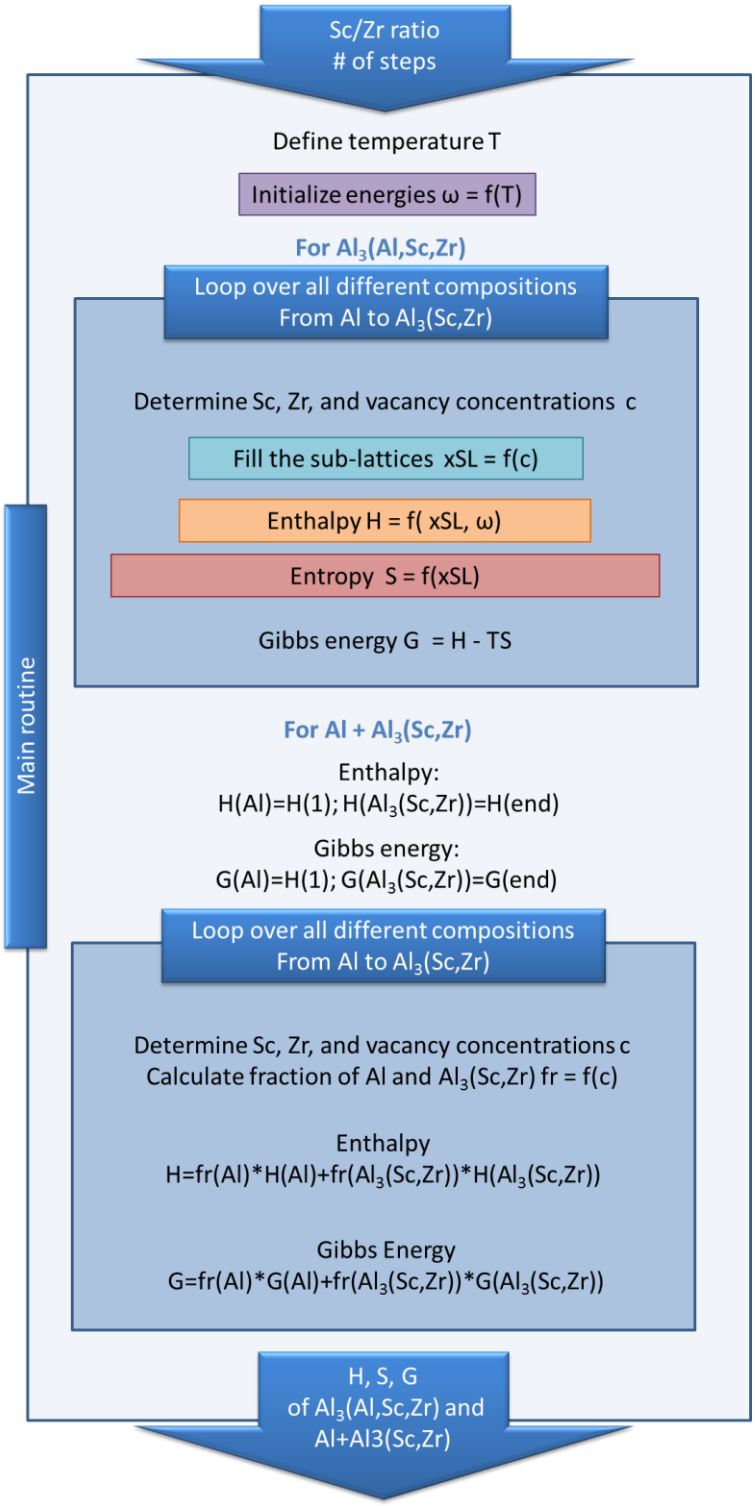

Figure 90: Scheme describing the main routine for calculation of the Gibbs energies.

In a next step the Gibbs energy of the $Al_3(Al,Sc,Zr)$ system is calculated for *n* different compositions in a loop. To account for the $L1_2$ crystal structure, and because the interaction energies indicate that the ordered crystal structure is energetically more favourable than random intermixing of atoms primarily a system of two sublattices (SL) was set up: Sublattice one (SL1) was populated only with Al atoms, according to the ordered $L1_2$ crystal structure and sublattice two (SL2) was filled with Sc and

Zr, as well as with the remaining Al, to reach specific concentrations depending on the loop cycle. Figure 91 schematically shows the two sublattice system. This filling of the sublattices was performed in a separate subroutine, as a function of concentration.

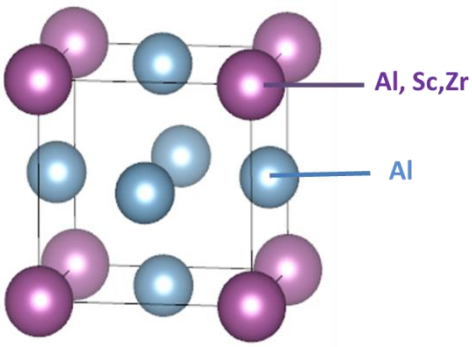

Figure 91: Two sublattice system: SL1 (blue) is populated with Al atoms; SL2 (purple) is populated with Al, Sc, and Zr.

A further look at the interaction energies reveals negative binding energies for Sc and Zr as second nearest neighbours, which suggests, a further split of SL2. Therefore the calculation was also performed for a 3 SL system. The resulting enthalpies, however, were nearly identical with those of the 2 SL system, with a maximum deviation of 0.069eV (which is roughly 0.69%).

With the filled sublattices all parameters are at hand for the calculation of the enthalpy of the system:

$$H = \frac{1}{2} \sum_{\substack{k=A,B,C \\ l=A,B,C \\ NN=1,2}} \left\{ \alpha_k n_{kl}^{(NN)} \sum_{ij} \left(x_i^{(k)} x_j^{(l)} \varepsilon_{ij}^{(NN)} \right) \right\} \tag{87}$$

with *A*, *B* and *C* representing the 2 or 3 SLs. *NN* represents the first or second nearest neighbour. α_k stands for the number of atoms in SL *k* per unit cell. $n_{kl}^{(NN)}$ indicates the coordination number of *NN*th nearest neighbours in SL *k* with reference to SL *l*. $x_i^{(k)}$ and $x_j^{(l)}$ represent the concentrations of atom types *i* and *j* on SL *k* and *l*. Finally, $\varepsilon_{ij}^{(NN)}$ stands for the interaction energy between *NN*th nearest neighbors of type *i* and *j*, calculated as described above – depending on temperature and according to Clouet et al[104].

The configurational entropy according to the regular solution model, including the application of the sublattices as described above can be expressed as:

$$S = -k_B \sum_{k=A,B,C} \left\{ \alpha_k \sum_i \left[x_i^{(k)} ln \left(x_i^{(k)} \right) \right] \right\} \tag{88}$$

where k_B is the Boltzmann constant and the remaining variables are defined as described for the enthalpy above.

While the first part of the main routine calculates the Gibbs energy of the Al_3(Al,Sc,Zr) system with compositions reaching from pure Al to Al_3(Sc,Zr) in *n* steps, the second part of the main routine

calculates the energy of Al and Al_3Sc existing as separate phases. The enthalpy and Gibbs energy of the first element calculated in the loop corresponds to pure Al (as $c_{Sc+Zr} = 0$), while the Gibbs energy of Al_3Sc corresponds to the last element calculated in the loop ($c_{Sc+Zr} = 0.25$). The resulting Gibbs energy of the separately existing phases can consequently be calculated as:

$$G = x_{Al}G_{Al} + x_{Al_3(Sc,Zr)}G_{Al_3(Sc,Zr)} = x_{Al}G(1) + x_{Al_3(Sc,Zr)}G(end) \quad (89)$$

$$x_{Al} + x_{Al_3(Sc,Zr)} = 1 \quad (90)$$

Where x_{Al} and $x_{Al_3(Sc,Zr)}$ are the fractions of Al and Al_3Sc phase.

Figure 92 shows a comparison of the Gibbs energy of the $Al_3(Al,Sc,Zr)$ system with the Gibbs energy of separated Al and Al_3Sc phases, which makes it obvious that for any possible composition between Al and $Al_3(Sc,Zr)$ a separation of the phases is energetically more favourable compared to a $Al_3(Al,Sc,Zr)$ phase where the additional Al atoms on SL2 are randomly distributed. Regions of the Gibbs energy curve exhibiting negative curvature, such as the Gibbs energy curve of the $Al_3(Al,Sc,Zr)$ phase are called spinodal[110,128] and indicate the energetic advantage of a system's decomposition. In Figure 92 the main routine was carried out for a Sc/Zr ration of 10 to match experimental findings.

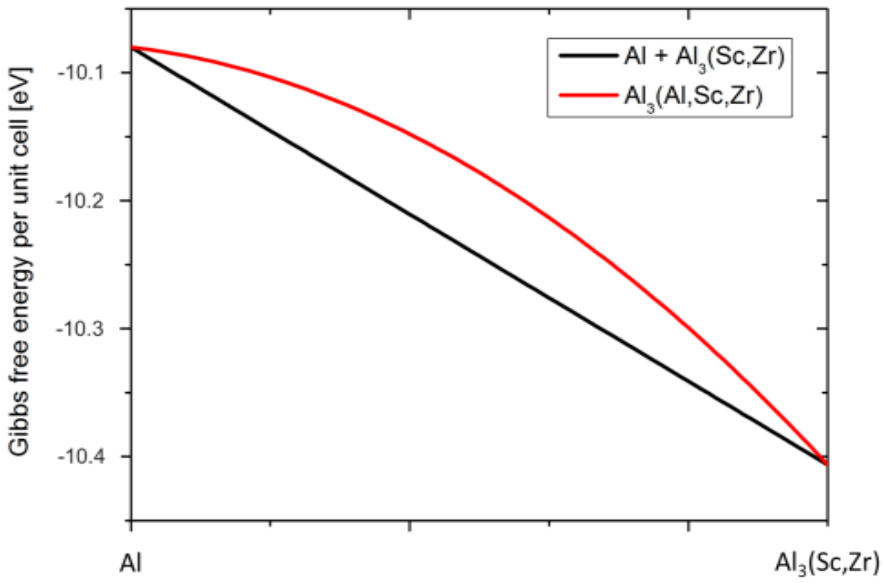

Figure 92: Comparison of Gibbs energy of $Al_3(Al,Sc,Zr)$ (red curve) and of Al and $Al_3(Sc,Zr)$ as separate phases (black curve).

In a next step the calculation was performed for all possible Sc/Zr ratios. Figure 93 shows the Gibbs energy curves for different Sc/Zr ratios. Spinodal behaviour can be seen for all ratios. It can also be seen that for higher amounts of Zr the $Al_3(Sc,Zr)$ phase decreases in energy. Consequently the slope of the Gibbs energy curves becomes steeper. This might have an influence on the evolution of the system over time.

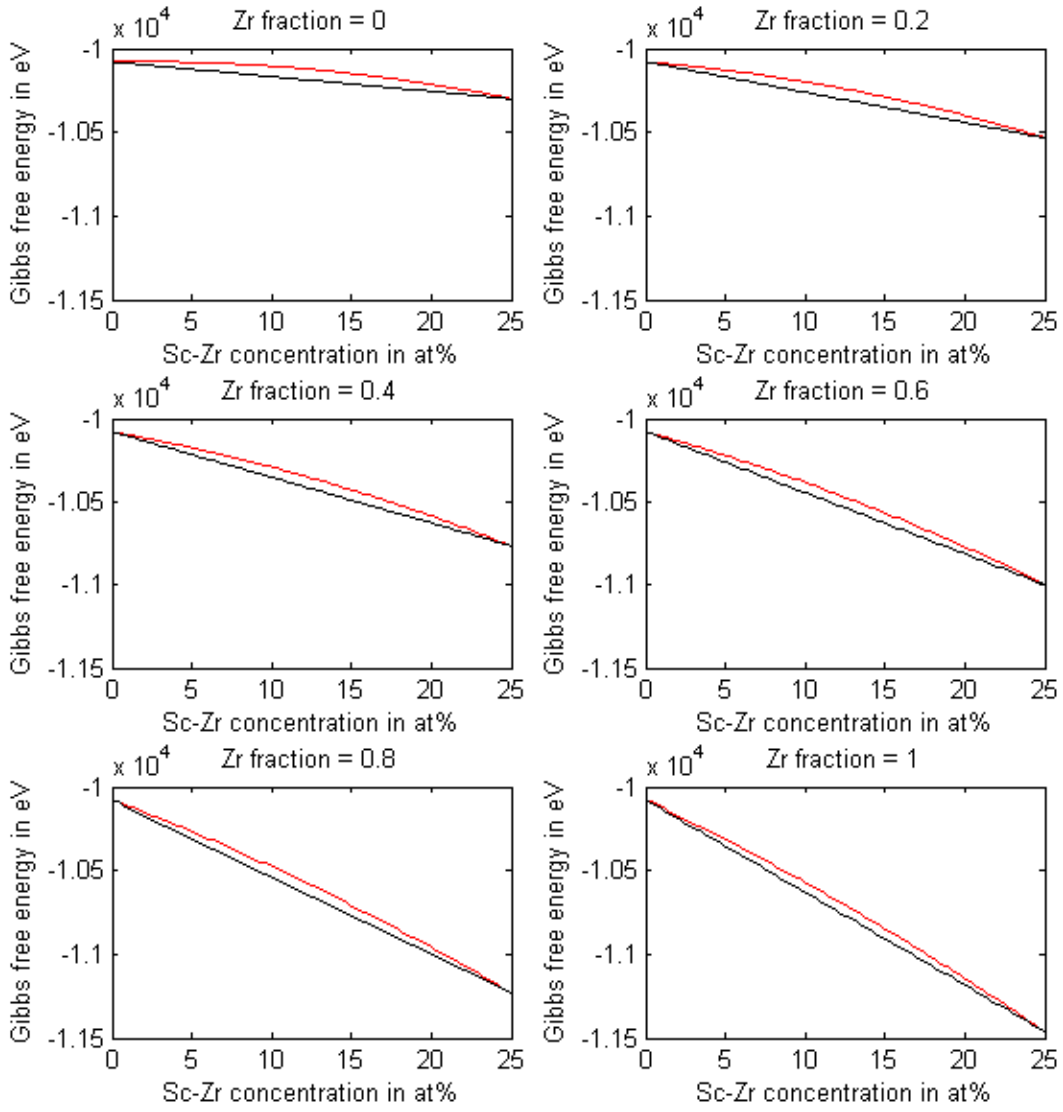

Figure 93: Gibbs energy curves dependant on concentration from Al to Al_3(Sc, Zr) for different Sc/Zr ratios. As in the figure above the red curve stands for the Al_3(Al,Sc,Zr) system, while the black curve gives the Gibbs energy of Al + Al_3(Sc,Zr).

Furthermore $c_{Sc+Zr} > 0.25$ were allowed in the simulation. This was done by distinguishing two cases: In case $c_{Sc+Zr} \leq 0.25$ the sublattices were filled as described above, but in case $c_{Sc+Zr} > 0.25$ SL2 was filled completely with Sc and Zr, and any remaining Sc/Zr was added to SL1. Figure 94 shows the results of this calculation. If the whole image is regarded, it can be seen that up to Zr/(Zr+Sc) ratios of about 0.9 the Al_3(Sc,Zr) concentration represents an absolute minimum in the Gibbs energy, but for Zr concentrations higher than that a phase consisting almost purely of (Sc,Zr) is lower in Gibbs energy. This adaption of the Gibbs energy calculation to allow arbitrary Sc/Zr ratios and $c_{Sc+Zr} > 0.25$ was necessary for its use in the 2D diffusion simulation described in the next section.

While this Gibbs energy calculation proved, that a decomposition of the Al_3(Al,Sc,Zr) system into Al and Al_3Sc is favourable for any composition between Al and the Al_3(Sc,Zr) system, we still do not know whether such a separation would lead to the fine channels observed in HR STEM investigations,

or whether a large volume phase separation is more likely. This was to be answered via the diffusion simulation discussed in the next section.

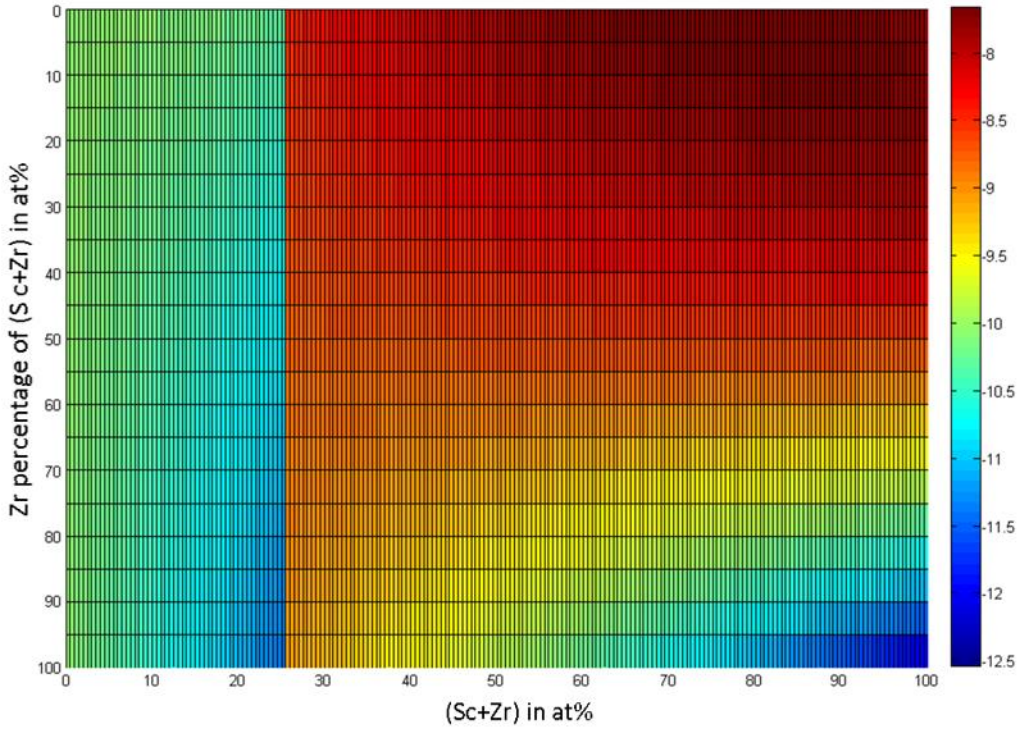

Figure 94: Gibbs energies for different compositions.

11.2 2D Diffusion Simulation

A 2D diffusion simulation based on Fick's laws of diffusion (see chapter 3.3) was set up.[x] Figure 95 schematically shows the program flow. The simulation treats an area of *n*n* cells with certain initial concentrations. The system is then left to evolve following Fick's laws of diffusion.

[x] Bernhard Sonderegger guided and supported me with the 2D diffusion simulation.

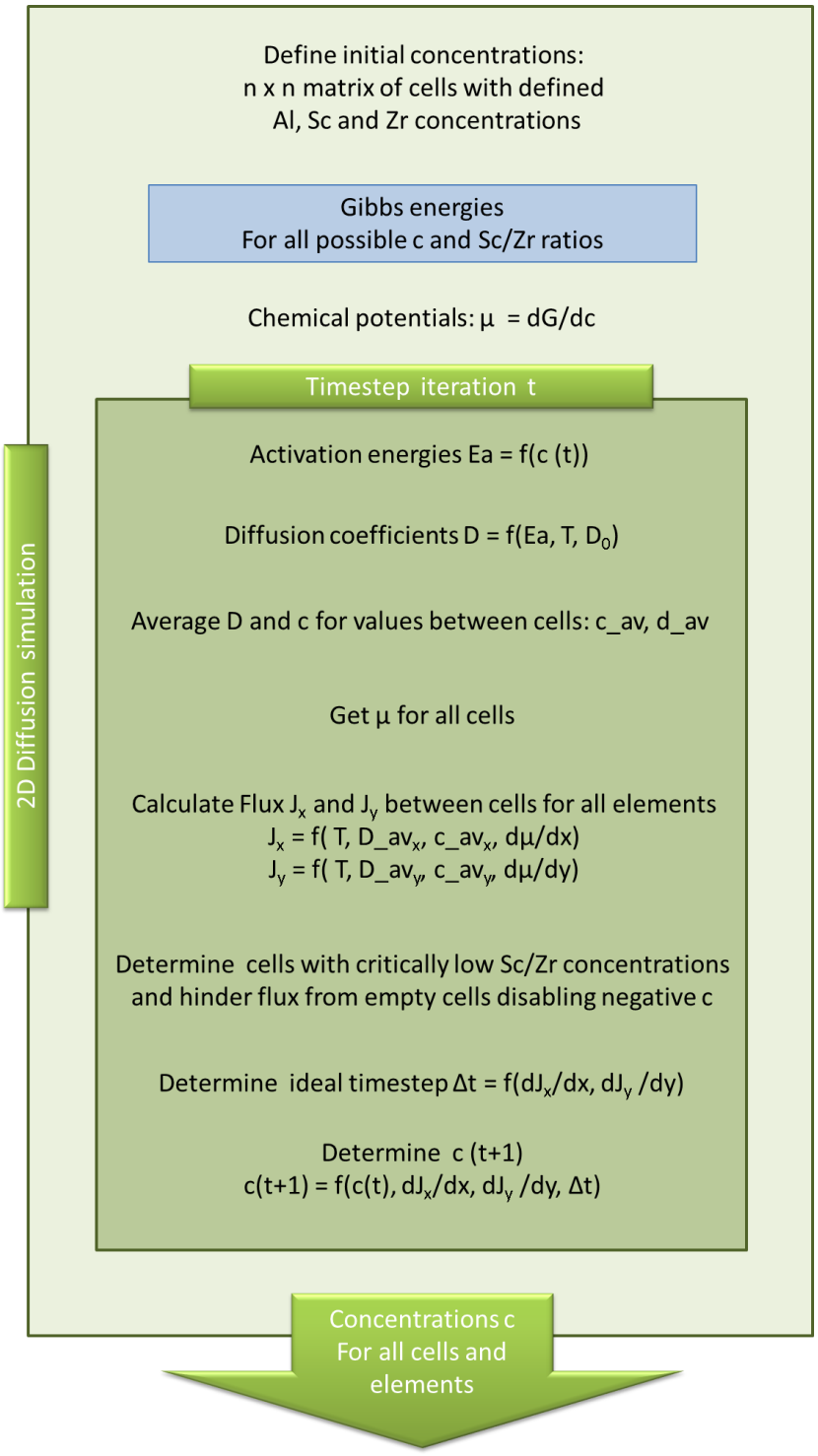

Figure 95: Scheme of 2D diffusion simulation.

For calculating the flux *J* between cells, fields of flux cells are set up for each species *k* and each direction.

$$J_k = -\frac{D_k c_k}{RT}\frac{\partial \mu_k}{\partial x} \tag{91}$$

The sizes of the flux fields are *(n+1)*n* for the fluxes in *x* direction, and *n*(n+1)* for the fluxes in *y* direction. Positive values of flux between two cells $c_{i,j}$ and $c_{i+1,j}$ denote a flux from $c_{i,j}$ to $c_{i+1,j}$. Negative values stand for fluxes in the opposite direction (from $c_{i+1,j}$ to $c_{i,j}$). The chemical potentials necessary for flux calculation were gained from deriving the Gibbs energies as calculated in the "main routine" described above. Concentrations for all cells and fluxes, for all flux-cells are calculated for each time step. To make the calculation as fast as possible while also ensuring stability of the simulation an automatic time step regulation was incorporated. As Fick's laws mathematically allow negative concentrations it was necessary to implement an additional constraint that does not allow the flux of a species out of a cell into another, if the concentration of the species is below a critical value very close to zero. This critical value set to 10^{-5} for all simulations, which appeared to be expedient.

Initially the initial concentrations were chosen such that a circular precipitate with a homogeneous non-EBRS – like or EBRS – like concentration was surrounded by a homogeneous region with matrix – like concentration. This lead to a highly symmetric concentration distribution after an evolution of 300s, as can be seen in Figure 96. The cells sizes were chosen to be 4.101 Å wide in x and y direction to match the unit cell size of the Al_3Sc system in <100> direction.

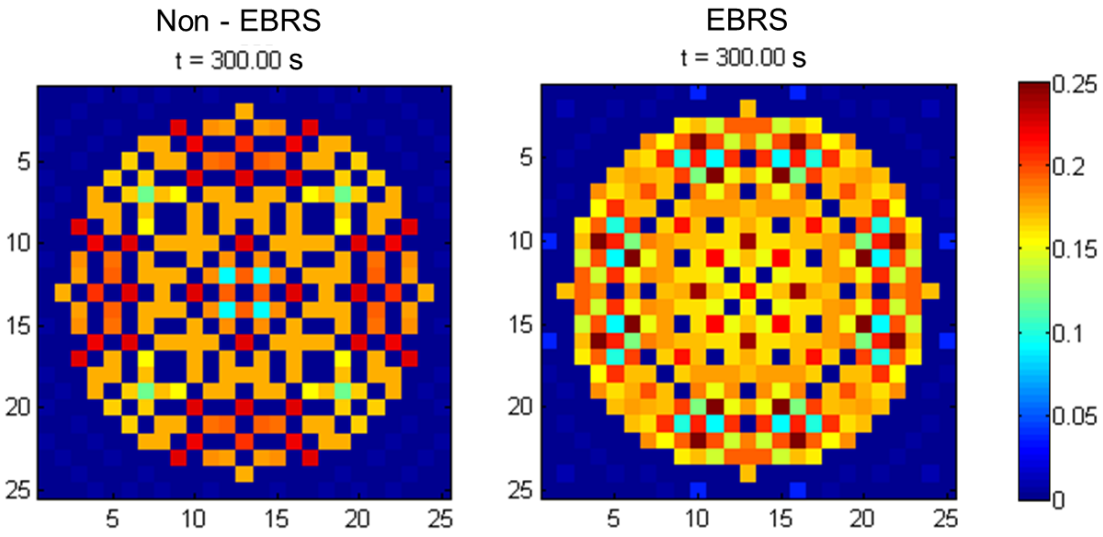

Figure 96: Results of 2D diffusion simulation for non-EBRS - like and EBRS - like homogeneous initial concentrations of a circular region surrounded by cells with matrix – like concentrations. The scale shows the Sc + Zr concentrations.

In a next step a slight (±0.0018) randomization of the homogeneous initial concentration was implemented, to create more realistic initial conditions. Figure 97 shows the results of the simulation performed under these conditions, also for 300s. The symmetry of the final concentration is broken. Just as for the initially homogeneous precipitate, the shape of the precipitate stays the same and channels of matrix-like material are formed, as regions with low Sc/Zr content are decomposed into pure Al channels, and regions with high Sc/Zr content. The Al channels are mostly only one cell wide. In the precipitate with the higher matrix content, there are more channels, and also some channels, that are more than a cell wide.

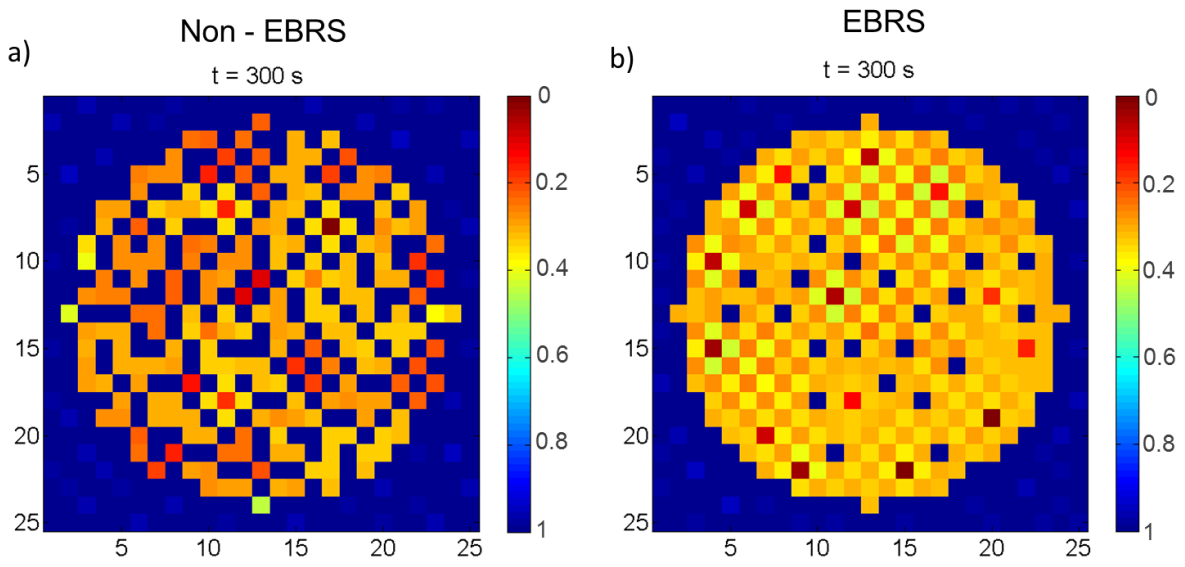

Figure 97: Results of 2D diffusion simulation for non-EBRS - like (a) and EBRS – like (b) non-homogeneous initial concentrations of a circular region surrounded by cells with matrix – like concentrations. The scale shows the Sc + Zr concentrations.

The results of these diffusion simulations therefore confirm that the formation of very fine (down to the width of one unit cell) Al channels within the $Al_3(Sc,Zr)$ precipitates is energetically favourable, over the formation of a larger area phase separation. This is in line with the experimental findings through HRSTEM and analytical electron tomography. With these findings the formation of an atomic scale spinodal decomposition within the nanoprecipitates is understood, and the theory of the self-limiting diffusion process within these channels, explaining the remaining weak core-shell structure is supported.

12 Publications Resulting from the Investigations of the Industrially Cast AlMgScZr Alloy

The most important results of the cooperation with the *Institute of Material Science, Joining and Forming* at TU Graz and the aircraft producer *Airbus* can be found in the following publications:

Diffusion Defining Atomic-Scale Spinodal Decomposition within Nanoprecipitates
A. Orthacker, G. Haberfehlner, J. Taendl, M. C. Poletti, B. Sonderegger G. Kothleitner
Nature Materials 17 (2018) 1101-1107

In-situ observation of recrystallization in an AlMgScZr alloy using confocal laser scanning microscopy
J. Taendl , S. Nambu, A. Orthacker, G. Kothleitner, J. Inoue, T. Koseki, C. Poletti
Materials Characterization (2015) 108, 137.

Influence of the degree of scandium supersaturation on the precipitation kinetics of rapidly solidified Al-Mg-Sc-Zr alloys
J. Taendl , A. Orthacker, H. Amenitsch, G. Kothleitner, C. Poletti
Acta Materialia 117 (2016) 43-50

12.1 Diffusion Defining Atomic Scale Spinodal Decomposition within Nanoprecipitates

One of the publications above I would like to emphasise, as it is probably the most direct outcome of this thesis: The most important findings of part III were published as article in *Nature Materials*. Therefore the next pages hold the Natrure Materias Publication “Diffusion Defining Atomic Scale Spinodal Decomposition within Nanoprecipitates”

12.1.1 Main Text

The next pages hold the main part of the publication including the methods section:

nature materials

ARTICLES

https://doi.org/10.1038/s41563-018-0209-z

Diffusion-defining atomic-scale spinodal decomposition within nanoprecipitates

Angelina Orthacker[1,2*], Georg Haberfehlner[1,2], Johannes Taendl[3], Maria C. Poletti[3], Bernhard Sonderegger[3] and Gerald Kothleitner[1,2*]

Stoichiometric precipitates owe their fixed composition to an ordered crystal structure. Deviations from that nominal value, however, are encountered at times. Here we investigate composition, structure and diffusion phenomena of ordered precipitates that form during heat treatment in an industrially cast Al–Mg–Sc–Zr alloy system. Experimental investigations based on aberration-corrected scanning transmission electron microscopy and analytical tomography reveal the temporal evolution of precipitate ordering and formation of non-equilibrium structures with unprecedented spatial resolution, supported by thermodynamic calculations and diffusion simulations. This detailed view reveals atomic-scale spinodal decomposition to majorly define the ongoing diffusion process. It is illustrated that even small deviations in composition and ordering can have a considerable impact on a system's evolution, due to the interplay of Gibbs energies, atomic jump activation energies and phase ordering, which may play an important role for multicomponent alloys.

Ordered precipitates with non-equilibrium composition are frequently encountered in various material systems[1–3]. An important question is whether the observed non-equilibrium structure is stable, or if it merely represents an intermediate step in a system's transition towards equilibrium. Understanding diffusion within the precipitate requires the consideration of atomic jump activation energies and Gibbs energy gradients with respect to chemical composition. Three cases are conceivable. First, if the activation energy is low enough with the Gibbs energy monotonously decreasing as far as the equilibrium composition, the equilibrium composition will be reached. Second, if the activation energy is low enough, but the Gibbs energy does not decrease monotonously, a local minimum of the Gibbs energy is encountered. Third, if the activation energy for atomic jumps is too high, diffusion is not possible and the non-equilibrium state is stable.

However, these considerations make no premises concerning the atomic order of the phase, which may vary locally and temporally. As the order of the phase can influence both the activation and the Gibbs energy, the system may undergo the formation of several phases during its kinetic evolution. For the technologically relevant Al–Sc–Zr system[4–13] it was previously shown[1] that the ordered $L1_2$ phase stabilizes the system in a non-equilibrium condition.

The as-cast alloy hosts solute Mg, Sc and Zr atoms in an Al matrix[4,5,10] due to rapid solidification. Ageing of the alloy enables Sc and Zr diffusion in the matrix and the formation of spherical $Al_3(Sc,Zr)$ precipitates with $L1_2$ crystal structure, coherently matching the surrounding face-centred cubic (fcc) Al. The initially formed $L1_2$ precipitates are Sc-enriched due to the element's faster diffusion in the Al matrix[14]. With ongoing ageing, a Zr-rich shell develops around the core. According to the literature[1], the differences in diffusivity between Sc and Zr in Al account for the final composition of the precipitates, as no more diffusion of Sc or Zr is possible in $Al_3(Sc,Zr)$.

Previous studies[1,15,16] examined laboratory-cast model systems with perfect composition and crystal structure, which have been homogenized to suppress micro-segregation. For a better comprehension of the precipitation process, this study investigates differently pre-treated samples far beyond peak ageing, as described in detail in the following section. It turns out that the understanding derived under ideal conditions is insufficient to describe more complex systems, such as industrially cast AlMgScZr alloys.

Atomic-resolution STEM and analytical tomography

The experiments were performed on differently processed samples of an AlMg4Sc0.4Zr0.12 alloy. To reduce micro-segregation and to enhance Sc and Zr solution in the Al matrix, an electron beam re-solidification (EBRS)[4] was performed (the material is rapidly melted locally and solidified via an electron beam) and the results were compared with non-EBRS-treated samples (see Supplementary Information). The main difference between the two conditions is the concentration of Sc in solid solution (0.37 wt% in EBRS- and only 0.13 wt% in non-EBRS-treated samples). The EBRS samples were also subject to ageing at 500 °C for 5 min and 72 h for a so-called 'short-aged EBRS' and 'long-aged EBRS' sample, respectively.

High-resolution (HR) high-angle annular dark-field (HAADF) scanning transmission electron microscopic (STEM) investigations were performed to get an overview as well as atomic-resolution information on the crystal lattice of the precipitates and to gain insight into the order of the phases at the different stages of ageing. In addition, the HR STEM results were compared to frozen phonon multi-slice simulations. Energy-dispersive X-ray (EDX) spectroscopy was conducted for compositional information on the precipitates. To overcome the intrinsic projection problem of STEM investigations and to enable resolution in the beam direction, EDX tomography was carried out to retrieve three-dimensional (3D) compositional information via voxel spectroscopy[17]. Thermodynamic calculations were performed, delivering the Gibbs energy of the system as a function of composition. Moreover, locally resolved diffusion simulations were conducted.

[1]Institute of Electron Microscopy and Nanoanalysis, Graz University of Technology, Graz, Austria. [2]Graz Centre for Electron Microscopy, Graz, Austria. [3]Institute of Materials Science, Joining and Forming , Graz University of Technology, Graz, Austria. *e-mail: angelina.orthacker@tugraz.at; gerald.kothleitner@felmi-zfe.at

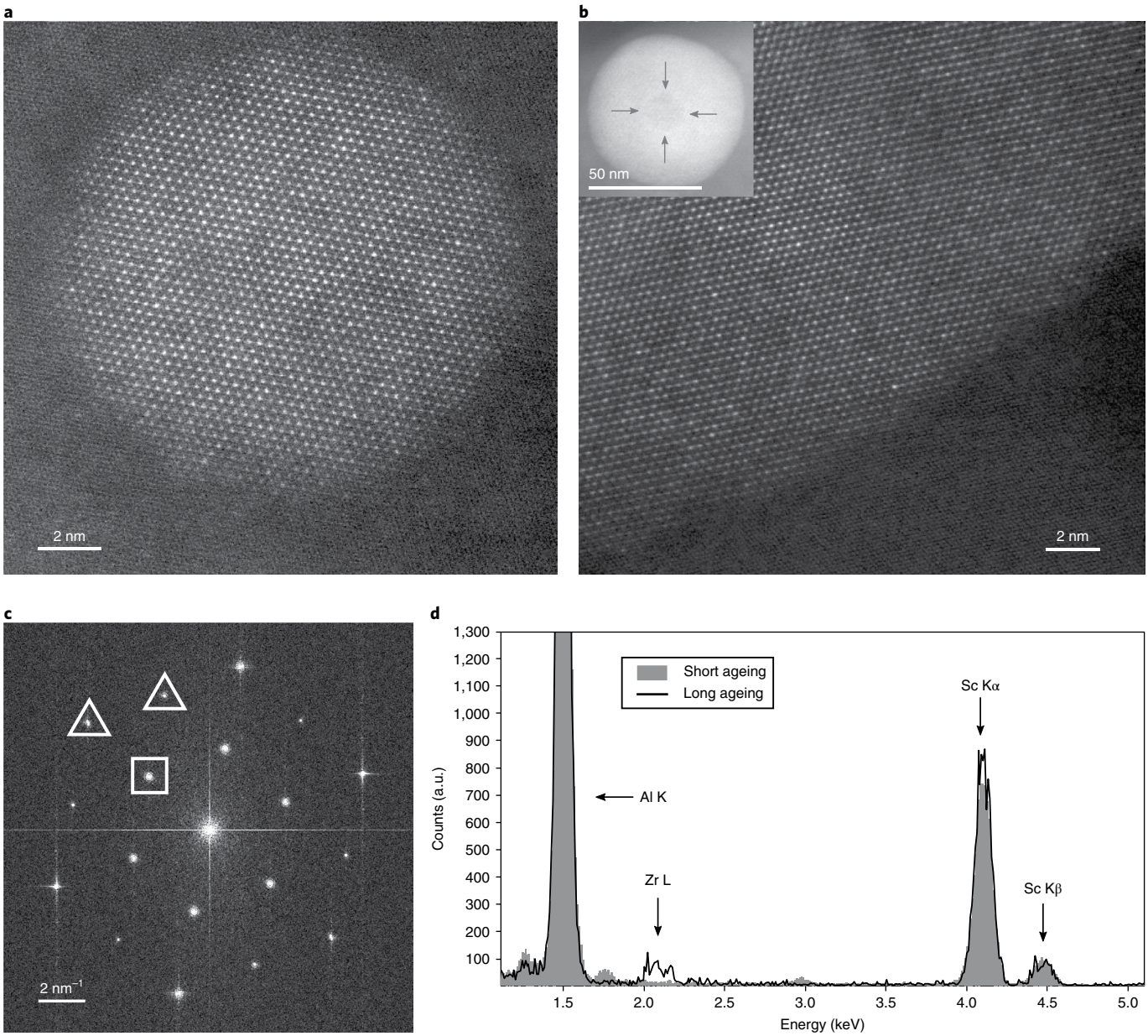

Fig. 1 | Structure and composition of short-aged and long-aged precipitates. a,**b**, (HR) STEM images of a short-aged (**a**) and part of a long-aged (**b**) precipitate. The inset of **b** shows the whole long-aged precipitate with the arrows indicating the interface between the core and the shell. **c**, Fast Fourier transform of **a**, demonstrating the coherent embedding of the precipitate in the matrix, the spots on the outer hexagon (marked with triangles) stemming from the Al matrix, the inner spots (marked by a square) originate from the $L1_2$ crystal structure. **d**, EDX spectrum from a precipitate after a short ageing process (grey-filled) and integrated voxel spectra of the core region of a precipitate after a long ageing process (black line), normalized with the Al-Kα peak, showing differences in Zr content.

HR HAADF STEM investigations as depicted in Fig. 1a,b revealed the formation of spherical, coherently matching (confirmed by fast Fourier transform; see Fig. 1c) Sc- and Zr-rich precipitates. Previous findings[1], explaining precipitate formation solely on the basis of different diffusivities of Sc and Zr in the matrix, would suggest a thin shell and strong HAADF contrast between the core and the shell. This is in contradiction to our experimental data that expose surprisingly large shell regions with low contrast between the core and the shell in the long-aged samples (Fig. 1b).

The precipitation forming process over time shall be illustrated on a short-aged sample and a sample aged long enough to ensure that the system was fully equilibrated. The short-aged precipitates, forming the cores of the long-aged core–shell-type precipitates, are rich in Sc and contain no Zr, as visible by its EDX spectrum in Fig. 1d (grey). By isolating the spectroscopic signal of the core region from shell and matrix effects, through the analytical tomographic method of voxel spectroscopy[17], in the long-aged sample, however, significant amounts of Zr become apparent, even though the precipitate was Zr-free after short ageing. A quantitative analysis of the spectra furthermore revealed that the stoichiometric composition of the $L1_2$ structure—75 at% Al and 25 at% (Sc + Zr)—was not reached in the precipitates. The actual global composition is described by $Al_3(Al,Sc,Zr)$. Introducing x, as the concentration of non-Sc/Zr atoms on the Sc/Zr lattice sites, a perfect $L1_2$ crystal structure corresponds to a composition with $x = 0$, whereas $x = 1$ represents the pure Al matrix (see Methods for details).

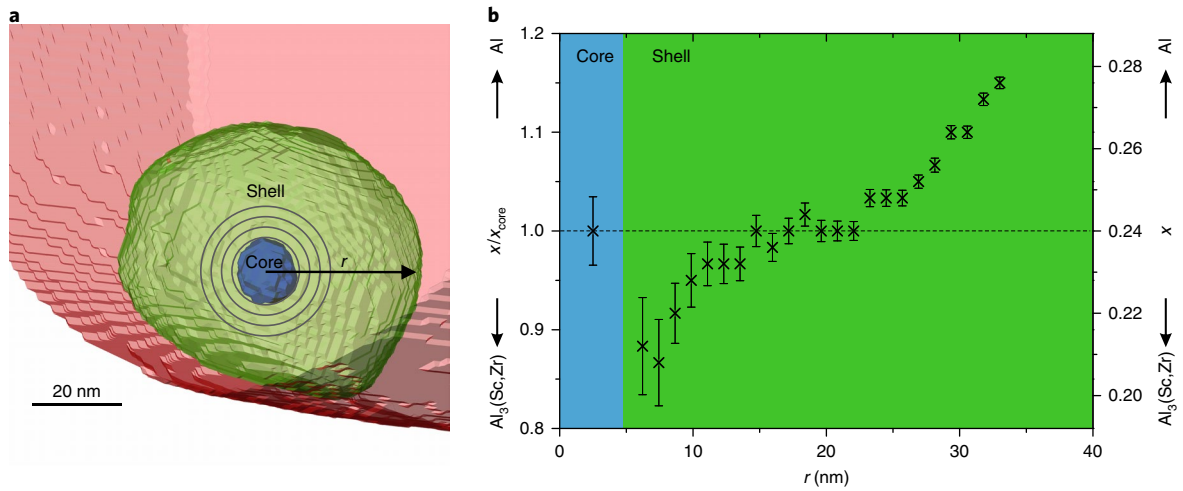

Fig. 2 | Analysis of radial compositional variation of a precipitate in a long-aged EBRS-treated sample. a, Mask of the core (blue), shell (green) and matrix (red) region gained from a 3D reconstruction of the HAADF signal**. b**, Average relative compositional deviation x/x_{core} from the $L1_2$ crystal structure measured radially away from the core. Here x represents the deviation from stoichiometry as defined for $Al_3(Al,Sc,Zr)$, quantified via 3D voxel spectroscopy and x_{core} represents this deviational value found for the core. Absolute elemental concentrations are given in the Supplementary Information (see Supplementary Fig. 2a). The error bars were calculated as described in the Methods.

Voxel spectroscopic[17] analysis delivered $x=0.32\pm0.06$ for a precipitate in the EBRS-treated and $x=0.53\pm0.05$ in the non-EBRS-treated sample, implying that these precipitates contain about 30% and 50% of matrix material, respectively. (The Mg concentration within the precipitate was found to be only up to 2 at%; consequently Mg can play only a minor role in this deviation.) Figure 2a shows the segmented HAADF reconstruction of the EBRS sample including a precipitate, which was used as a mask for the voxel spectroscopic analysis (see Methods). In Fig. 2b, we compare the radial dependency of this deviation x in the shell with the deviation found in the core x_{core}. This radial composition profile of the precipitate (Fig. 2b) yields a minimum deviation from the stoichiometric $L1_2$ ($x=0$) composition at the interface between the core and the shell. In the Supplementary Information (Supplementary Fig. 1), the same voxel spectroscopic analysis performed on a non-EBRS-treated sample can be found, which also shows a minimum deviation from the $L1_2$ crystal structure at the core–shell interface. It should be noted that this deviation corresponds to a mean, 3D-azimuthally averaged value for a given radial shell, which varies locally.

Atomic-resolution HAADF imaging furthermore reveals an inhomogeneous distribution of Al atoms on Sc/Zr positions (antisite defects) within the $Al_3(Al,Sc,Zr)$ phase. A collection of matrix-like channels with widths down to one single atomic column on the Sc/Zr sublattice can be seen in Fig. 3. The enlarged area (Fig. 3b) and a line profile (Fig. 3c) suggest matrix-like composition of that channel, being oriented exactly in the beam direction. In other regions of the precipitate, columns are found, which show higher intensity than matrix columns, but lower intensity than a full Sc/Zr column, implying that not all of the Sc/Zr sites are occupied by Sc/Zr. Additional experimental evidence for non-perfect $L1_2$ composition and an inhomogeneous distribution of additional Al atoms within precipitates, in terms of elemental map reconstructions and additional STEM HAADF images, is displayed and discussed in the Supplementary Information (Supplementary Figs. 3 and 5).

Frozen phonon multi-slice simulations (μSTEM[18] software) were then performed to understand STEM image contrast (see Methods). Al_3Sc in the <111> orientation was used as a basis, to ensure comparability with experimental data. In a column containing five Sc atoms in the beam direction, different numbers of Sc atoms were replaced by Al atoms, as can be seen in Fig. 3d–g. The simulations show that even in very thin samples single atom channels running perpendicular to the beam direction are difficult to detect. It can be deduced that only matrix-like channels that run through the crystal in a direction parallel to the beam can be identified. The appearance of single Zr atoms within a precipitate is discussed in the Supplementary Information (see Supplementary Fig. 4).

Calculation of Gibbs energies and atomic-scale diffusion

The observed concentration profiles and local anomalies in the precipitate dictate the need for different thermodynamic calculations: a calculation depicting the Gibbs free energy of the phases, assuming a homogeneous distribution of the elements within the phase; and a spatially resolved analysis of diffusion processes within the precipitate to indicate whether a minimization of the Gibbs free energy leads to local decompositions and inhomogeneities. Both tasks consider a three-component system, consisting of Al, Sc and Zr atoms.

The first calculation computes the Gibbs free energy on the basis of a regular solution model with an enthalpy and an entropy part, as further described in the Methods. This approach yields values for the Gibbs free energy of the ordered $Al_3(Sc,Zr)$ phase as well as the energy of the Al matrix, oversaturated with Sc and Zr. Deviations from the ideal stoichiometric composition of the precipitate can be considered by assuming a composition $Al_3(Al,Sc,Zr)$. The calculations refer to a Zr/Sc ratio of 1:10 to match the experimental findings.

Figure 4a (compact curve) depicts the transition from a pure Al matrix (left side of the diagram) to an ordered stoichiometric $Al_3(Sc,Zr)$ compound. The negative curvature of the Gibbs free energy over nearly the whole composition range suggests a decomposition of the system. This finding is supported by comparison to the Gibbs free energy curve of the two-phase system matrix (pure Al) plus precipitate (stoichiometric composition), indicated as a dashed curve in Fig. 4a, along with the difference between the two cases shown in Fig. 4b. There are only very small compositional ranges—in the order of 10^{-5} at%, adjacent to Al and Al_3Sc composition—where a separation is less favourable than a mixture (see Fig. 4c,d). For every other possible system composition, a decomposition into the two phases (matrix and stoichiometric precipitate) is energetically more favourable than a one-phase system. Consequently, an $Al_3(Al,Sc,Zr)$ precipitate should divert into

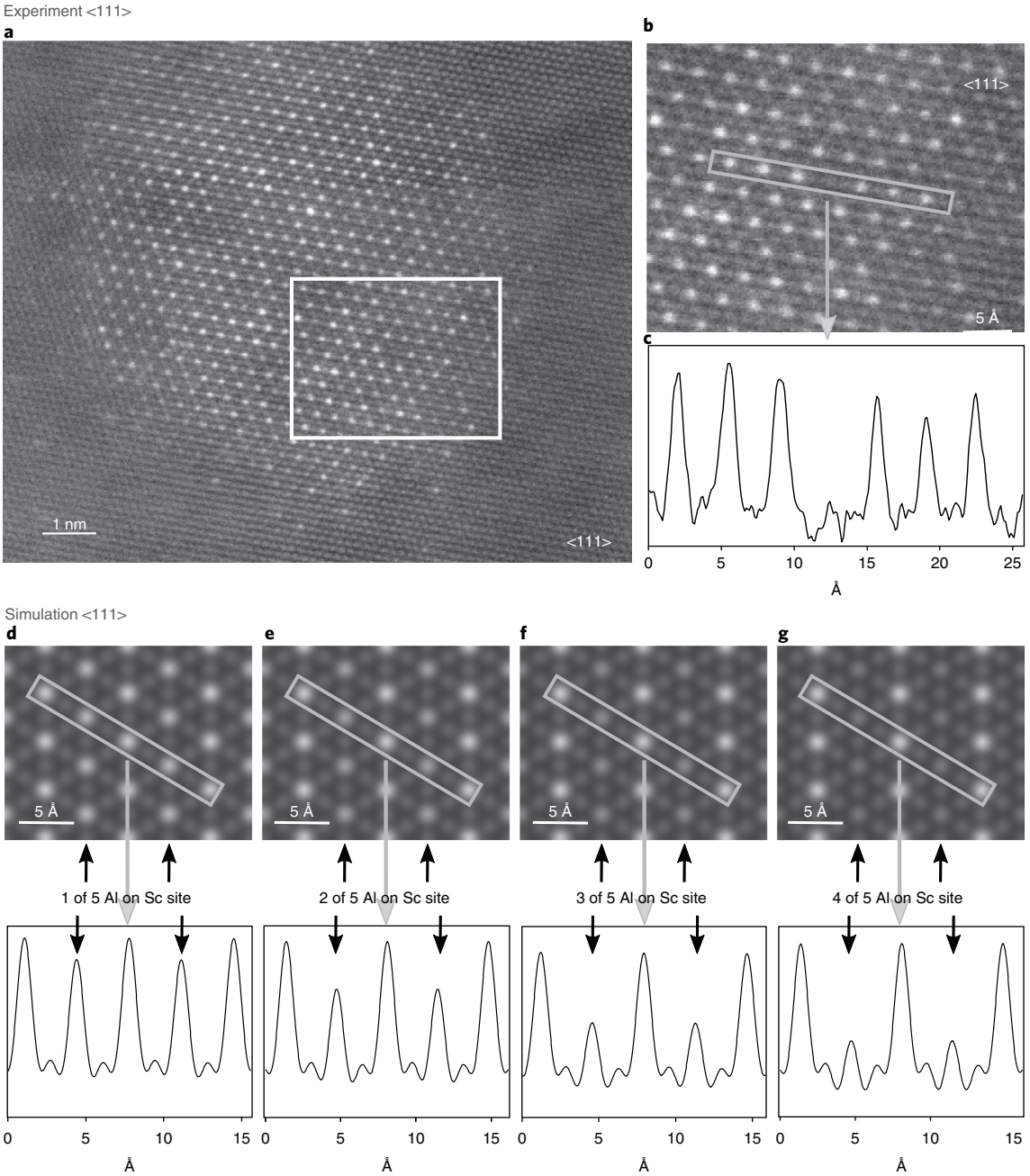

Fig. 3 | Comparison of HAADF images and simulations of $L1_2$ precipitates with different numbers of Al atoms on Sc sites. a, An atomic-resolution HAADF image of a short-aged precipitate. **b**, A detailed view of the region indicated in **a**. **c**, Intensity line profile as indicated in **b**. Panels **a**–**c** reveal a matrix-like channel with single column width in the Sc/Zr sublattice allowing 1D diffusion of Sc and Zr. **d**–**g**, Images and line profiles from frozen phonon multi-slice simulations of Al_3Sc, where Sc atoms were substituted by 1 (**d**), 2 (**e**), 3 (**f**) and 4 (**g**) Al atoms in the indicated columns.

stoichiometric $Al_3(Sc,Zr)$ and separate Al regions to minimize its Gibbs free energy, provided according diffusion processes are possible.

For the second calculation—the spatially resolved diffusion simulation—a 3D atomistic diffusion simulation was set up to study the evolution of diffusion channels (channels of Al matrix) within the precipitate (see Methods). It should be emphasized that the purpose of this simulation is not simulating the concentration profiles within the core–shell structure of the precipitate, but to demonstrate the formation of Al-rich diffusion channels within the otherwise ordered crystal. The starting condition is a simulation box representing the interior of an ordered $Al_3(Al,Sc,Zr)$ structure and accordingly two sublattices. The composition of the simulated volume was chosen to be 80 at% Al, 18 at% Sc and 2 at% Zr and the temperature was chosen to be 773 K to match experimental findings. Most important results of the simulation are the formation and evolution of the diffusion channels, in case they are present. Figure 5 confirms their presence, increase and growth over time. Figure 5a shows a comparison of Al atoms contributing to channels that are at least 20 atoms long at the first and last time step of the simulation, while in Fig. 5b Al atoms on Sc/Zr positions are summed over atomic columns. Figure 5c shows the temporal evolution of the ratio of Al atoms contributing to chains, which shows a clear increase from roughly 0.55 to roughly 0.75 and Fig. 5d gives the fraction of Al atoms contributing to chains with a certain length

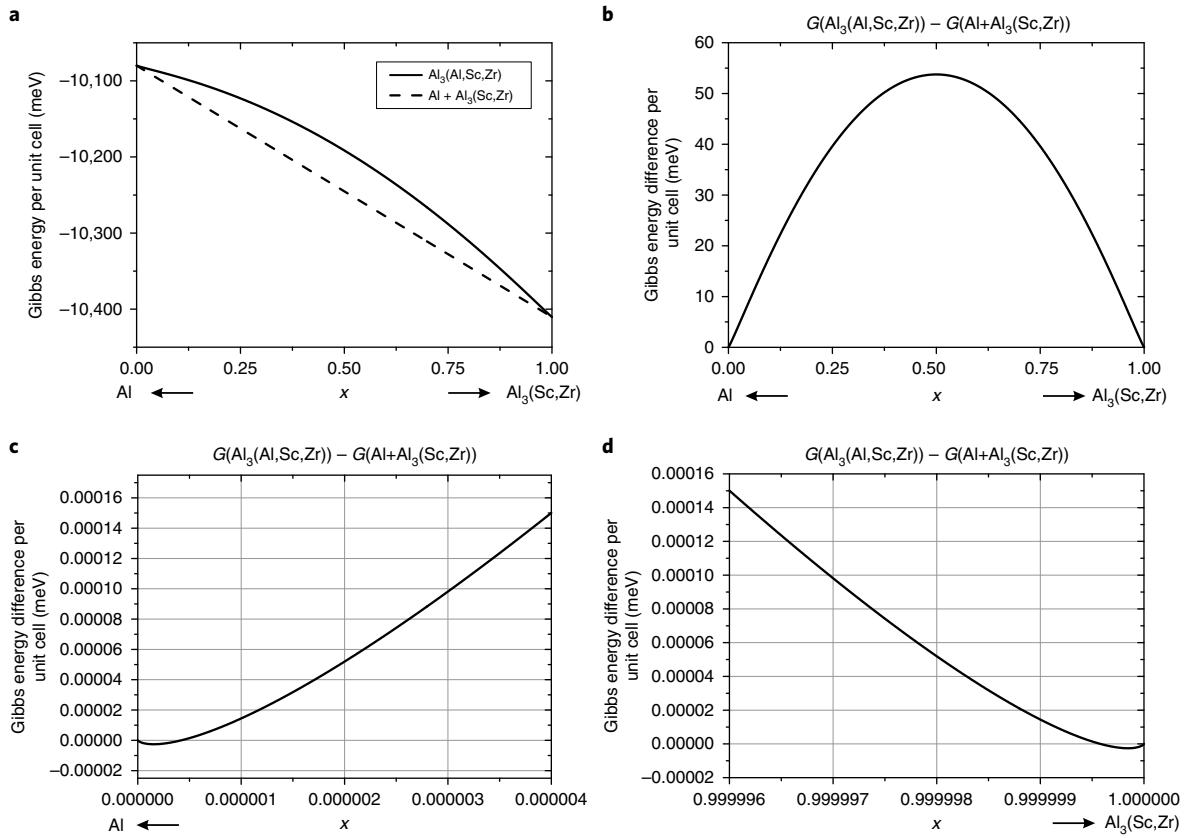

Fig. 4 | Gibbs free energy calculations. a, Gibbs free energy as a function of concentration for separate Al and $Al_3(Sc,Zr)$ phases (dashed line) and for Al treated as defects in $Al_3(Sc,Zr)$ (compact line). **b**–**d**, Differences in Gibbs energy in the Al–Sc–Zr system treated as $Al_3(Al,Sc,Zr)$ and as separate Al and $Al_3(Sc,Zr)$ phases depending on concentration. **b** shows the whole range from Al to $Al_3(Sc,Zr)$, while **c** and **d** show a zoom into the regions of extremely high and low (Sc,Zr) concentrations, which show a very small region, where a separation into Al and $Al_3(Sc,Zr)$ is energetically less favourable than a mixture. Except for these very limited compositional ranges, however, a separation into Al and Al_3Sc is more favourable.

at the beginning and the end of the simulation, indicating a growth of the chains.

Diffusion enabled by atomic-scale spinodal decomposition

The experimental observation of diffusion inside the precipitates can be ascribed to their imperfect $L1_2$ structure, with varying composition x. Matrix-like regions ($x=1$) are formed as a network of channels, evoking the picture of an atomic-scale spinodal decomposition. This is supported by the characteristic negative curvature of the Gibbs free energy[19,20]. It implies that for non-perfect stoichiometry, the formation of clustered Al antisite defects in the precipitate is favoured over the implementation of Al point antisite defects randomly distributed on the Sc/Zr sublattice. Being in line with experimental observations and Gibbs energy calculations the 3D atomistic diffusion simulation confirms the formation of matrix-like channels within precipitates with Sc concentrations lower than necessary for a perfect $L1_2$ crystal structure.

Al channels then represent a diffusion pathway for Sc and Zr in the precipitate, while regions of perfect $L1_2$ structure allow no diffusion. Two driving forces lead to the intermixing of Sc and Zr atoms: entropy and the interaction energies of Sc and Zr, which slightly favour Sc and Zr as second-nearest neighbours. If Sc and Zr were allowed to diffuse until equilibrium conditions are reached, compositional differences and the core–shell structure would vanish, which is clearly not the case.

From this, it can be concluded that regions with perfect $L1_2$ structure acting as diffusion barriers are formed during this secondary diffusion process. Following diffusion in the network, the encounter of a small number of Sc and/or Zr atoms, situated on neighbouring sites of their sublattice, can lead to the immobilization of these atoms, as they are gradually incorporated into the $L1_2$ system. Our hypothesis is that a gapless $L1_2$ shell seals off the core and diffusion becomes self-limiting, finally leading to a stabilization of the core–shell structure of the precipitate. In atomically narrow channels, enabling only 1D diffusion, it is intuitively understandable that two atoms diffusing in opposite directions can block the channel at encounter. As the encounter of atoms is a stochastic process, the radial average composition will not deliver a well-defined threshold radius of perfect $L1_2$ structure composition. Instead, a radial region spanning several nanometres is observed with lower x values than in the rest of the precipitate.

Variations from the ideal $L1_2$ composition have been mentioned in previous publications: while on the one hand, precipitates were found with (Sc,Zr) concentrations of around 30 at%[21], on the other hand, Al-rich precipitates were reported, which despite their $L1_2$ superstructure had a composition close to $Al_4(Sc,Zr)$[15]. Our detailed investigation of systems where the deviation from the $L1_2$ structure is very pronounced gives clear insights into indicators for a secondary diffusion processes taking place. One of those would be an increase of (Sc,Zr) in combination with a decrease of Al in the border region between the core and the shell of the precipitate, which in an HAADF image would appear as a high-intensity region. If this knowledge is applied to previously published work on the Al–Sc–Zr systems, undiscussed evidence of a secondary diffusion process can also be found[1]. (However, the effect is less prominent due to the reduced amount of matrix material within

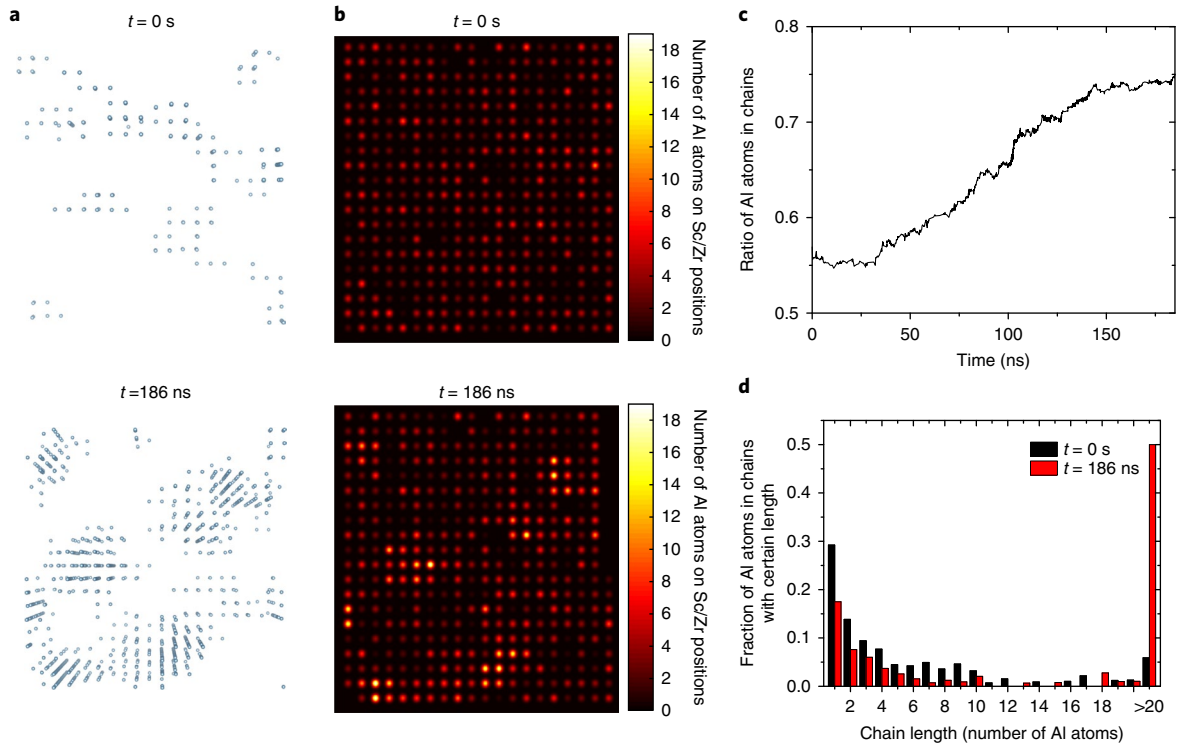

Fig. 5 | Results of 3D atomistic diffusion simulation showing the evolution of diffusion channels. a, Visualizations of Al channels on the Sc/Zr sublattice including at least 20 Al atoms at the first ($t = 0$ s) and last ($t = 186$ ns) time step of the simulation. **b**, Al atoms on Sc/Zr positions summed up over atomic columns for the first ($t = 0$ s) and last ($t = 186$ ns) time step; atomic columns with a high number of Al atoms correspond to darker columns in the HAADF image due to missing Sc/Zr atoms. **c**, Ratio of Al atoms contributing to channels (Al atoms with at least one Al atom as the nearest neighbour on the Sc/Zr sublattice) at all time steps during the simulation. **d**, Histograms comparing the amount of atoms contributing to chains with certain lengths at the first ($t = 0$ s) and last ($t = 186$ ns) time step. The newly formed aluminium channels stem from previously randomly distributed Al atoms or shorter chains.

the precipitate resulting from laboratory-casting as opposed to industrially casting the alloy.) Atom probe investigations (shown in Fig. 2 of ref. [1]) present an increase in Sc with a simultaneous decrease in Al, visible at about −1.5 nm, right at the interface between the Sc-rich core and the Zr-rich shell. Moreover, in the HAADF image of Fig. 4d in ref. [1] an intensity discrepancy with respect to the simulation can be noted.

A comparison of the non-EBRS- (for details, see Supplementary Information) and EBRS-treated samples with the homogenized samples of the above reference hints at a direct relation between the amount of initially dilute Sc and Zr and the final composition of the precipitates. While x, the concentration of non-Sc/Zr on Sc/Zr sites, equals almost 0 in precipitates in homogenized samples[1], it takes on a value of $x = 0.32 \pm 0.06$ in the EBRS-treated and $x = 0.53 \pm 0.05$ in the non-EBRS-treated sample. A precipitate composition closer to the perfect $L1_2$ composition features less matrix-like channel material. Consequently, the early stage composition of the precipitate directly controls the amount of material that can diffuse until the barrier has formed. In an EBRS sample, exhibiting less Al, less Zr finally reaches the core (0.87 at%) compared to the non-EBRS sample (1.2 at%). A very thin shell with more Zr than Sc points at a diffusion process that stopped very quickly. In contrast, precipitates of higher matrix content, allowing far more diffusion to take place, lead not only to core, but also to shell compositions that exhibit an order of magnitude more Sc than Zr. This now explains the difference in core and shell thickness and composition that can be observed if our results are compared to those of previous publications[1]. The influence of sample pre-ageing treatment and its impact on the resulting nanostructure, and thus the performance of the material, cannot be emphasized enough.

Interplay of ordering, Gibbs and activation energies

The Al–Sc–Zr system is a perfect example of the dynamic interaction of Gibbs energy, the ordering of phases and the activation energy for the necessary jump cycles that ultimately determines the finally stable precipitate. This interplay necessitates detailed investigations at atomic resolution and analytical 3D studies to be able to understand the underlying process: as long as Sc and Zr are not equally distributed, the precipitate is in a non-equilibrium state. If the precipitate exhibited a perfect $L1_2$ composition, no diffusion would be possible within the precipitate, as the activation energy for atomic jumps is too high. The negative curvature of the Gibbs energy, however, leads to an atomic-scale spinodal decomposition process, as long as the $L1_2$ structure shows imperfections. This leads to the formation of matrix-like channels, enabling diffusion, as the activation energy is decreased. The diffusion of Sc and Zr atoms in opposite directions (radially inward and outward) introduces new order and $L1_2$ structure forms at sites where diffusing atoms meet. On encounter and because of high activation energy, local diffusion stops. When a gapless $L1_2$ surface is formed, this diffusion barrier between the core and the shell stabilizes the non-equilibrium core–shell structure. Whether such an atomic-scale network (or its counterpart, the agglomerate of nanoprecipitates) entails influences on properties or processes other than diffusion, or whether the quantum character of 1D diffusion can be of further use, is still an open question.

We anticipate that such an interplay of energies and ordering may play an important role for other multicomponent alloys. A spatially and time-resolved investigation of composition and order in combination with resulting activation and Gibbs energy calculations sheds light on these processes and allows one to explain formerly unnoticed deviations.

Online content

Any methods, additional references, Nature Research reporting summaries, source data, statements of data availability and associated accession codes are available at https://doi.org/10.1038/s41563-018-0209-z.

Received: 3 August 2017; Accepted: 26 September 2018;
Published online: 12 November 2018

References

1. Clouet, E. et al. Complex precipitation pathways in multicomponent alloys. *Nat. Mater.* **5**, 482–488 (2006).
2. Hald, J. Prospects for martensitic 12 % Cr steels for advanced steam power plants. *Trans. Indian Inst. Met.* **69**, 183–188 (2016).
3. Danielsen, H. K. Review of Z phase precipitation in 9–12wt-%Cr steels. *Mater. Sci. Technol.* **32**, 126–137 (2016).
4. Taendl, J., Orthacker, A., Amenitsch, H., Kothleitner, G. & Poletti, C. Influence of the degree of scandium supersaturation on the precipitation kinetics of rapidly solidified Al-Mg-Sc-Zr alloys. *Acta Mater.* **117**, 43–50 (2016).
5. Taendl, J. et al. In-situ observation of recrystallization in an AlMgScZr alloy using confocal laser scanning microscopy. *Mater. Charact.* **108**, 137–144 (2015).
6. Williams, J. C. & Starke, E. A. Progress in structural materials for aerospace systems. *Acta Mater.* **51**, 5775–5799 (2003).
7. Cavanaugh, M. K., Birbilis, N., Buchheit, R. G. & Bovard, F. Investigating localized corrosion susceptibility arising from Sc containing intermetallic Al_3Sc in high strength Al-alloys. *Scr. Mater.* **56**, 995–998 (2007).
8. Sawtell, R. R. & Jensen, C. L. Mechanical properties and microstructures of Al-Mg-Sc alloys. *Metall. Mater. Trans. A* **21**, 421–430 (1990).
9. Filatov, Y., Yelagin, V. & Zakharov, V. New Al–Mg–Sc alloys. *Mater. Sci. Eng. A* **280**, 97–101 (2000).
10. Taendl, J., Palm, F., Anders, K., Gradinger, R. & Poletti, C. Investigation of the precipitation kinetics of a new Al-Mg-Sc-Zr alloy. *Mater. Sci. Forum* **794–796**, 1038–1043 (2014).
11. Novotny, G. M. & Ardell, A. J. Precipitation of Al_3Sc in binary Al-Sc alloys. *Mater. Sci. Eng. A* **318**, 144–154 (2001).
12. Røyset, J. & Ryum, N. Kinetics and mechanisms of precipitation in an Al-0.2wt.% Sc alloy. *Mater. Sci. Eng. A* **396**, 409–422 (2005).
13. Røyset, J. & Ryum, N. Scandium in aluminium alloys. *Int. Mater. Rev.* **50**, 19–44 (2005).
14. Clouet, E., Barbu, A., Laé, L. & Martin, G. Precipitation kinetics of Al_3Zr and Al_3Sc in aluminum alloys modeled with cluster dynamics. *Acta Mater.* **53**, 2313–2325 (2005).
15. Tolley, A., Radmilovic, V. & Dahmen, U. Segregation in $Al_3(Sc,Zr)$ precipitates in Al-Sc-Zr alloys. *Scr. Mater.* **52**, 621–625 (2005).
16. Forbord, B., Lefebvre, W., Danoix, F., Hallem, H. & Marthinsen, K. Three dimensional atom probe investigation on the formation of $Al_3(Sc,Zr)$-dispersoids in aluminium alloys. *Scr. Mater.* **51**, 333–337 (2004).
17. Haberfehlner, G., Orthacker, A., Albu, M., Li, J. & Kothleitner, G. Nanoscale voxel spectroscopy by simultaneous EELS and EDS tomography. *Nanoscale* **6**, 14563–14569 (2014).
18. Allen, L. J., D'Alfonso, A. J. & Findlay, S. D. Modelling the inelastic scattering of fast electrons. *Ultramicroscopy* **151**, 11–22 (2015).
19. Kozeschnik, E. *Modeling Solid-State Precipitatio*n (Momentum, New York, 2012).
20. Jones, R. A. L. *Soft Condensed Matter* (Oxford Univ. Press, Oxford, 2002).
21. Fuller, C. B., Murray, J. L. & Seidman, D. N. Temporal evolution of the nanostructure of Al(Sc,Zr) alloys: Part I-Chemical compositions of $Al_3(Sc_{1-x}Zr_x)$ precipitates. *Acta Mater.* **53**, 5415–5428 (2005).

Acknowledgements

The authors thank the Austrian Cooperative Research Facility, the Austrian Ministry for Transport, Innovation and Technology (project GZ BMVIT- 612.011/0001-III/I1/2015) and the Austrian Research Promotion Agency FFG (TAKE OFF project 839002) for funding. We would like to express our gratitude to F. Hofer for supporting the project and to W. Sprengel for advice concerning the manuscript. Furthermore, we would like to thank L. Allen and his group for support with μSTEM and M. Weyland, J. Etheridge and S. Findlay for support concerning quantitative STEM.

Author contributions

A.O. performed all STEM investigations including sample preparation for tomography and STEM HAADF simulations, interpreted the results and wrote the bigger part of the manuscript. G.H. provided the software for tomographic alignment and reconstruction and supported its application. J.T. and M.C.P. provided the samples and information and performed the re-solidification and ageing process. B.S. coded the Gibbs energy calculation and the 3D atomistic diffusion simulation and wrote the parts of the manuscript treating them. G.K. supervised the project and the writing of the manuscript.

Competing interests

The authors declare no competing interests.

Additional information

Supplementary information is available for this paper at https://doi.org/10.1038/s41563-018-0209-z.

Reprints and permissions information is available at www.nature.com/reprints.

Correspondence and requests for materials should be addressed to A.O. or G.K.

Publisher's note: Springer Nature remains neutral with regard to jurisdictional claims in published maps and institutional affiliations.

Methods

Material. The investigated material was an AlMg4Sc0.4Zr0.12 (wt%) alloy casted to an 8-mm-thick, 280-mm-wide and more than 30-m-long strand using a continuous belt-casting technology. It was demonstrated[6] that this alloy exhibited a solute Sc content of 0.13 wt% at room temperature in the non-EBRS condition and 0.37 wt% in the EBRS condition.

Sample preparation. Samples for HR investigations were prepared via conventional ion beam thinning after dimpling and polishing. For (analytical) tomographic investigations, needle-shaped samples were cut and thinned via focused ion beam milling at an FEI Nova 200 dual-beam instrument.

Acquisition. HR HAADF STEM and analytical tomographic STEM investigations were carried out at a probe-corrected FEI TITAN[3] operated at 300 kV at a convergence angle of 20 mrad, equipped with a GIF quantum[22] energy filter (Gatan) and a Super-X EDX detector[23] (FEI). The corrector tuning was performed such that the approximate aberration-free zone easily exceeded the aperture cutoff. For analytical tomographic investigations, STEM spectrum image tilt series were acquired. For the non-EBRS-treated sample, 4° tilt steps were carried out from −76° to 76°. For the EBRS-treated sample, a tilt series from −90° to 90° was carried out in 5° steps. At each tilt angle, HAADF and EDX data were acquired with a size of 158×64 pixels and a pixel size of 1.13 nm for the EBRS sample and 64×199 pixels with a pixel size of 1.22 nm for the non-EBRS sample.

Calculation of elemental maps. For extracting 2D EDX elemental maps, a model-based approach was used, applying a Kramers model[24] for the background and fitting Gaussians to the K-peaks of each element. This was done for each pixel of the EDX spectrum images. The integrated intensities are then mapped, leading to an image per tilt angle, where high intensities correspond to high amounts of the mapped element in projection.

Tomographic alignment and reconstructions. All tomographic data processing was done in Matlab. The alignment of the tomographic tilt series was carried out using centre-of-mass methods for the *x* direction (perpendicular to the tilt axis) and tilt axis[25] and projection re-projection matching for the *y* direction (parallel to the tilt axis)[17,26]. The alignment data were calculated for the HAADF STEM tilt series and applied to all (simultaneously acquired) data.

HAADF STEM reconstructions and 3D elemental maps were carried out using total variation minimization[17,27,28]. Total variation minimization assumes sharp interfaces between different regions in the sample. Even though this assumption is not strictly valid in our sample, this reconstruction technique allows the determination of morphology and in particular the retrieval of the core–shell structure of the precipitates.

The segmentation was performed in Amira by choosing intensity thresholds for the primary regions of interest—core, shell and matrix. The EBRS-treated sample showed a very clear border region between the core and the shell, which allowed a purely intensity-based segmentation of the core, shell and matrix regions. With the non-EBRS-treated sample, manual corrections of the regions had to be performed, as the border between the core and shell regions was not clear enough to produce meaningful results without manual corrections.

Voxel spectroscopy. For quantitative analysis of 3D EDX data, the reconstruction was performed using the simultaneous iterative reconstruction technique with a multiplicative update. The acquired EDX spectra from all tilt angles were reconstructed channel-by-channel to obtain a 3D reconstruction for each channel, which can then be combined to get local 3D resolved EDX spectra (voxel spectroscopy[17]). This '4D data cube' then allows the extraction of summed spectra from individual regions of interest.

Segmented HAADF reconstructions were used to create masks for different regions of interest, for showing the radial dependency of the composition. The mask of the core was used as a seed. All neighbouring voxels fulfilling the condition of being part of the shell were chosen as the first subshell. All further subshells were created by choosing neighbouring voxels from the previous subshells, which fulfilled the conditions of being part of the shell, but not part of one of the previous subshells.

EDX and 3D compositional analysis. The EDX elemental quantification was performed using the standardless k-factor approach provided by digital micrograph on the K-peaks of each element. The background correction was performed with a model-based approach using the Kramers model[24]. The concentration of non-(Sc,Zr) atoms on (Sc,Zr) sites, *x*, was obtained from the determined concentrations as follows:

$$x = \frac{(0.25 - (c_{Sc} + c_{Zr}))}{0.25}$$

While this method also allows single voxel spectra to be retrieved, they are too noisy to deliver reliable results. This issue arises because long acquisition times necessary for sufficient noise reduction for single voxel spectroscopy entail problems such as sample drift and sample damage. Therefore, acquisition times had to be kept short. To nevertheless ensure a reliable analysis of the voxel spectroscopic data, spectra of sufficiently large numbers of voxels were summed before elemental quantification. Consequently, the core region was not further subdivided. It should be noted that this averaging process levels out local variations, thus never delivering pure matrix or $L1_2$ concentrations, but indicating radial variations of the amount of matrix-like material within the precipitate.

Error analysis was performed by calculating the error propagation due to the calculation of concentrations via the k-factor method, with $\sigma = \sqrt{N}$ (N being the number of counts attributed to a certain peak after background subtraction) as the error attributed to each peak. The error of each k-factor was assumed to be 10%. For relative analysis, the errors of the k-factors were omitted, as they have the same impact on all measured points and therefore do not influence the relative analysis.

Frozen phonon multi-slice calculations. Frozen phonon multi-slice calculations were performed via μSTEM[18] in the <111> direction to be comparable to experimental results, which were also obtained in the <111> direction. Therefore, a cuboid unit cell that spans the crystal in the <111> direction was defined, measuring 5.7997 Å and 3.3485 Å in the directions perpendicular to propagation. The code was run in quantum excitation of phonons mode. The supercell was created by repeating the unit cell 4 by 6 times. The number of phase grates was chosen to be 24. Two hundred and fifty Monte Carlo iteration steps were carried out. The detector inner and outer angles were 60 mrad and 150 mrad, respectively, to mimic HAADF conditions. A convolution with a Gaussian of 1 Å full-width at half-maximum was performed on the simulated HAADF images to compensate for the finite source size in the experiment and any aberrations not accounted for in the simulation. The small sample thickness of 5 unit cells, which equals about 3.5 nm, was chosen to assess the detectability of single atomic channels running perpendicular to the beam direction for the best case scenario of extremely thin samples. Non-detectability in this case immediately implies non-detectability for thicker samples.

Calculation of Gibbs energy of the system. The phases' enthalpy was calculated using data found in the literature[1] (Supplementary Information), which indicated temperature-dependent first- and second-nearest-neighbour interaction energies in an fcc Al–Sc–Zr system by ab initio methods. Since the obtained interaction energies strongly favour an ordered crystal structure over random intermixing of atoms, we set up a 2-sublattice (SL) model with Al in SL1 and Al, Sc and Zr in SL2. The SLs were set up according to an ordered $L1_2$ fcc structure. Since experimental findings suggest concentrations of more than 75 at% Al in the precipitates, no Zr or Sc had to be considered in SL1; any deviation from the stoichiometric composition $Al_3(Sc,Zr)$ was achieved by including Al in SL2. Previous publications[1] also suggest an attractive negative binding energy of second-nearest neighbours Sc and Zr, which would lead to a further split into three SLs: Al in SL1, Zr predominantly in SL2 and Sc predominantly in SL3. Again, any deviation from a stoichiometric $Al_3(Sc,Zr)$ composition was compensated by including Al in SL2 and SL3, and Sc in SL2, respectively. It turns out that the Gibbs free energies derived from the 2-SL and 3-SL are practically identical with a maximum deviation of 0.069 eV; thus, only one line is plotted in the graph in Fig. 4. At a given composition, the enthalpy, normalized to one unit cell $Al_3(Sc,Zr)$, can then be depicted as:

$$H = \frac{1}{2} \sum_{\substack{k=A,B,C \\ l=A,B,C \\ NN=1,2}} \left\{ \alpha_k n_{kl}^{(NN)} \sum_{ij} (x_i^{(k)} x_j^{(l)} \varepsilon_{ij}^{(NN)}) \right\} \quad (1)$$

where *A*, *B* and *C* represent the 2 or 3 SLs respectively. *NN* indicates the first- or second-nearest neighbour. α_k indicates the number of atoms in SL *k* per unit cell. $n_{kl}^{(NN)}$ denotes the coordination number of *NN*th nearest neighbours in SL *k* with respect to SL *l*. $x_i^{(k)}$ and $x_j^{(l)}$ are the concentrations of atom types *i* and *j* in SL *k* and *l*. Finally, $\varepsilon_{ij}^{(NN)}$ is the temperature-dependent interaction energy between *NN*th nearest neighbours of type *i* and *j* according to the literature[1].

Note that not only the enthalpy of the precipitate phase can be calculated by equation (1), but also the enthalpy of the Al matrix with solute Zr and Sc atoms. Furthermore, equation (1) automatically indicates the enthalpy correctly in the case of mixing between the SLs and does not need any adaption for this case (downwardly compatible with respect to the number of SLs).

In addition to the (temperature-dependent) enthalpy of the precipitate phase and aluminium matrix, we consider the entropy contribution to the Gibbs free energy. In the regular solution model, the entropy is defined as configurational entropy, which is expressed as

$$S = -k_B \sum_{k=A,B,C} \left\{ \alpha_k \sum_i [x_i^{(k)} \ln(x_i^{(k)})] \right\} \quad (2)$$

in a multi-sublattice crystal. k_B is the Boltzmann constant; the other variables are defined according to equation (1).

As well as the enthalpy in equation (1), equation (2) automatically indicates the entropy correctly in the case of total mixing between the sublattices and thus does not need any adaption.

With this set-up, the Gibbs free energy of the ordered $Al_3(Sc,Zr)$ phase can be calculated as well as the energy of the Al matrix oversaturated with Sc and Zr. Furthermore, any deviation from the ideal stoichiometric composition of the precipitate can be considered by assuming the composition $Al_3(Al,Sc,Zr)$. Calculations, as depicted in Fig. 4, further assume a Zr/Sc ratio of 1:10 approximating the experimental findings.

3D atomistic diffusion simulation. The simulation box is set up as $20\times20\times20$ unit cells with 4 atoms each, in total 32,000 atoms. The box is set up with periodic boundary conditions. To improve the statistical evidence of the simulation, the vacancy density is set as 3.75×10^{-3}, as compared to the real value of 0.9×10^{-4} to 1.8×10^{-4} for 480 °C to 520 °C according to Simmons and Balluffi[29]. This increase leads to a faster diffusion process by a factor of 42 to 21. More importantly, the simulation can operate with 120 vacancies within the simulation box instead of 3 to 6, providing reasonable statistical evidence.

Since the Al concentration is assumed to be higher than 75 at% for every simulation, SL1 is completely filled with Al atoms as starting conditions. SL2 is filled randomly with Al, Sc and Zr atoms, considering the respective concentrations.

For the diffusion, only position exchanges of vacancies with neighboring atoms are considered; thus, the diffusion is completely driven only by vacancy jumps. The simulation operates in discrete time steps; the length of each time step is adaptive with respect to the vacancy jump with the highest probability per time. Each vacancy can potentially jump to 1 of its 12 first-nearest neighbours. The probability per time, dw/dt, is calculated according to the height of the potential wall and the jump frequency as

$$\frac{dw}{dt} = f_j \times \exp\left\{-\frac{E}{k_B T}\right\} \tag{3}$$

with the jump frequency f_j, where j is the type of atom the vacancy is exchanging its position with and E is the energy barrier for the jump. By generalizing the data found in the literature[1], the energy barrier can be calculated by

$$E = e_i + e_j - E_{\mathrm{sum},i} - E_{\mathrm{sum},j} + E_{\mathrm{inter},i,j} \tag{4}$$

where e_i and e_j are the saddle point energies of atom types i (here: the vacancy) and j (the atom potentially exchanging its place with the vacancy). $E_{\mathrm{sum},i}$ is the sum of all the interaction energies of the vacancy including first- and second-nearest neighbours; $E_{\mathrm{sum},j}$ is the according interaction energies of the atom j. The bond energy $E_{\mathrm{inter},i,j}$ between atom i (vacancy) and atom j has to be subtracted, because it would otherwise be considered twice (once in $E_{\mathrm{sum},i}$ and $E_{\mathrm{sum},j}$, respectively). All data on interaction energies, saddle point energies and jump frequencies are taken from the literature[1].

Using equations (3) and (4), all dw/dt are evaluated for every potential jump direction for every vacancy. The duration of the time step Δt is then calculated as

$$\Delta t = 1 \Big/ \left\{\frac{dw}{dt}\right\}_{\max}$$

The probability for a specific jump within this time step is then computed according to

$$w = 1 - \exp\left\{-\frac{dw}{dt}\Delta t\right\}$$

The applied jump direction of each vacancy is then determined as a Monte Carlo step considering the according probabilities.

Since most (starting condition: all) atoms in the first SL are Al atoms in the first place, we define a matrix channel as a line of Al atoms in the second SL. Al atoms in the second SL are thus categorized into two groups: (i) Al atoms that have at least two other Al atoms in their second sublattice neighbourhood—these atoms are assumed to belong to a network and are interpreted as 'channel atoms'; and (ii) Al atoms that are isolated with respect to this criterion. Even with a random distribution of Al atoms as the starting condition, a certain amount of Al atoms will fulfil condition (i). One important output of the simulation is the time evolution of the fraction of atoms of type (i) and (ii) respectively, and the evolution of the type (i) network in the course of the simulation.

For the graphic representation of the 3D atomistic simulation results in Fig. 5a VESTA[30] was used.

Data availability

The data sets generated and/or analysed during the current study as well as any custom code used during this study are available from the authors on reasonable request.

References

22. Gubbens, A. et al. The GIF Quantum, a next generation post-column imaging energy filter. *Ultramicroscopy* **110**, 962–970 (2010).
23. Schlossmacher, P., Klenov, D. O., Freitag, B. & von Harrach, H. S. Enhanced detection sensitivity with a new windowless XEDS system for AEM based on silicon drift detector technology. *Micros. Today* **18**, 14–20 (2010).
24. Kramers, H. A. XCIII. On the theory of X-ray absorption and of the continuous X-ray spectrum. *Philos. Mag.* **46**, 836–871 (1923).
25. Azevedo, S. G., Schneberk, D. J., Fitch, J. P. & Martz, H. E. Calculation of the rotational centers in computed tomography sinograms. *IEEE Trans. Nucl. Sci.* **37**, 1525–1540 (1990).
26. Uusimäki, T. et al. Three dimensional quantitative characterization of magnetite nanoparticles embedded in mesoporous silicon: local curvature, demagnetizing factors and magnetic Monte Carlo simulations. *Nanoscale* **5**, 11944–11953 (2013).
27. Leary, R., Saghi, Z., Midgley, P. A. & Holland, D. J. Compressed sensing electron tomography. *Ultramicroscopy* **131**, 70–91 (2013).
28. Saghi, Z. et al. Compressed sensing electron tomography of needle-shaped biological specimens - potential for improved reconstruction fidelity with reduced dose. *Ultramicroscopy* **160**, 230–238 (2016).
29. Simmons, R. O. & Balluffi, R. W. Measurements of equilibrium vacancy concentrations in aluminum. *Phys. Rev.* **117**, 52–61 (1960).
30. Mommaa, K. & Izumia, F. VESTA 3 for three-dimensional visualization of crystal, volumetric and morphology data. *J. Appl. Crystallogr.* **44**, 1272–1276 (2011).

12.1.2 Supplementary Information

Diffusion Defining Atomic Scale Spinodal Decomposition within Nano-Precipitates

Angelina Orthacker[(1,2),*], Georg Haberfehlner[(1,2)], Johannes Taendl[(3)], Maria C. Poletti[(3)], Bernhard Sonderegger[(3)] and Gerald Kothleitner[(1,2),*]

(1) Institute of Electron Microscopy and Nanoanalysis, Graz University of Technology, Graz, Austria

(2) Graz Centre for Electron Microscopy, Graz, Austria

(3) Institute of Materials Science, Joining and Forming, Graz University of Technology, Graz, Austria

[*] angelina.orthacker@tugraz.at; gerald.kothleitner@felmi-zfe.at

1) Radial symmetric compositional analysis on a non-EBRS treated sample

The investigation of a non-EBRS treated precipitate also showed a core shell system. A radial symmetric investigation of the average compositional deviation from the $L1_2$ crystal structure (see figure S1) shows the same general behaviour as the average compositional deviation of the EBRS treated sample: a minimum of x/x_{core} can be found at the interface between core and shell. The absolute values of x, however, are higher: The average value of x for the precipitate in the non-EBRS treated sample equals 0.53 ± 0.05 while it equals 0.32 ± 0.06 for the precipitate in the EBRS treated sample. This increase in deviation from the perfect $L1_2$ composition can be attributed to the smaller initial amount of dilute Sc and Zr in solid solution in the non-EBRS treated sample.

2) Absolute quantification of radial composition variation

3D elemental quantification of Al, Sc and Zr serves as basis for the analysis of the compositional variation shown in Fig. 2b and S1b. The absolute radial compositions from core to shell for the long aged EBRS treated sample and for a long aged non-EBRS treated sample are shown in Figure S2a and S2b respectively. It should be noted that the error of the absolute quantification is higher than for relative compositional variations due to uncertainties of k-factors.

3) Elemental map reconstruction of a short aged non-EBRS treated sample

To get an overview of the elemental distribution in various samples 3D elemental maps[56] were created. The elimination of ambiguities that signals in projection (as usually obtained in transmission electron microscopy) entail, allows the drawing of conclusions concerning the distribution of certain elements. While elemental maps do not allow an absolute quantitative analysis of the composition, they give a 3D overview of the system while enabling a relative analysis of composition. Figure S3a shows surface rendered 3D reconstructions of the Al –K (green) and Sc-K (red) EDX signal of a short aged non-EBRS treated sample. Several Sc rich precipitates can be seen within the Al- matrix. Figure

S3b, c and d show the volume rendered 3D reconstructions of the Sc-K EDX signal of the same sample. Simply looking at the volume rendered representation allows us to draw the following conclusions: In the close ups on two particles (figure S3c and d) regions of precipitates can be seen, which contain Sc, but clearly less than other regions of the same precipitates. Through this varying composition it can immediately be concluded that the precipitates are not purely made up of perfect Al_3Sc in $L1_2$ crystal structure. This conclusion is supported if different precipitates are compared in figure S3b: If all the precipitates had the same perfect Al_3Sc composition, precipitates of similar size would give similar Sc signals. This is not the case. It can even be observed that small precipitates give stronger signals than larger precipitates. Figure S3a further supports these conclusions, as regions can be observed, which give a weaker Al – signal than the threshold chosen for matrix regions, but also weaker Sc signals than that chosen as a threshold for Sc-rich precipitates – thus appear as regions that are neither part of the Al-matrix, depicted in green, nor part of the Sc-rich precipitates, depicted in red. All these observations serve as further evidence that early in the ageing process precipitates vary in composition and thus do not have Al_3Sc stoichiometry, but can be described as $Al_3(Al,Sc)$.

4) HR STEM investigations combined with HR STEM simulations

As discussed in the main text HR STEM investigations of precipitates showed atom columns on the Sc/Zr sublattice with varying intensities. The substitution of Sc atoms with Al atoms was discussed in the main text. In this section the substitution of Sc atoms with Zr atoms shall be discussed. A simulation of Al_3Sc in <111> orientation (model unit cell shown in top-view and side view in figure S4 bottom c and d) where in every second column one Sc atom was replaced by a Zr atom was performed. The comparison of intensity profiles from the regions of interest with that of the simulation suggest that the bright blobs might be Zr atoms. The smaller intensity difference between the Al columns and the column containing the possible Zr atom in the short aged sample (figure S4a) compared to the simulation suggests that the thickness of the precipitate is higher than in the simulation. The strong contrast in the long aged sample (figure S4b) is easily understandable, as the possible Zr atom is at the border region of the precipitate, where the number of Sc atoms in beam direction might be smaller than five. An intensity decrease approaching the border region of the precipitate can also clearly be seen in the profile.

Figure S5 shows additional examples of HR STEM images of precipitates in short aged samples exhibiting a non-perfect $L1_2$ structure, as can be seen from the varying intensities of the bright Sc-rich columns.

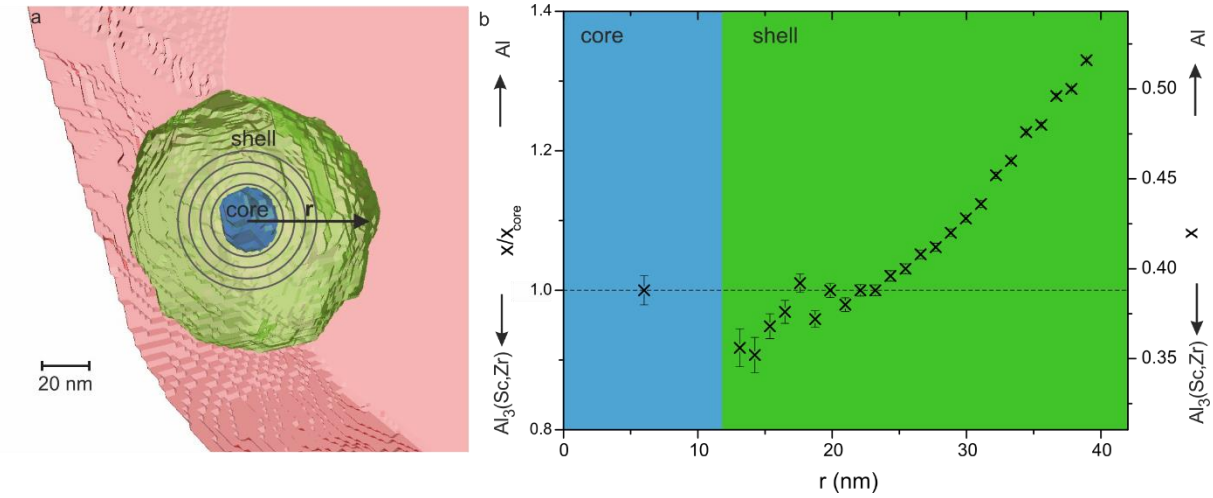

Figure S1: Analysis of radial compositional variation of a precipitate in a long aged non-EBRS treated sample. a) Mask of core (blue), shell (green) and matrix (red) region gained from a 3D reconstruction of the HAADF signal; b) Average relative compositional deviation x/x_{core} from the $L1_2$ crystal structure measured radially away from the core. Here x represents the deviation from stoichiometry as defined for $Al_3(Al,Sc,Zr)$, quantified via 3D voxel spectroscopy, and x_{core} represents this deviational value found for the core . Absolute elemental concentrations are given in Fig. S2b.

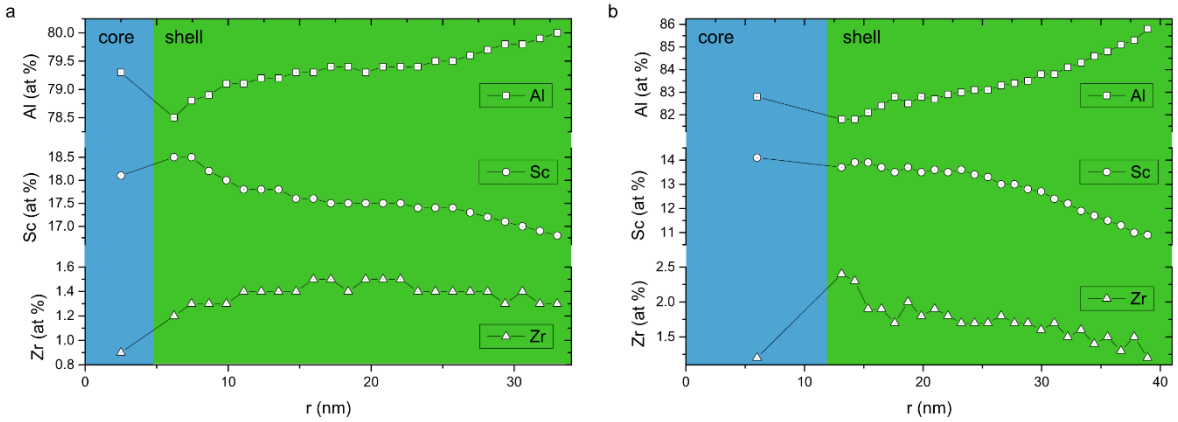

Figure S2: Absolute radial compositional variation of a precipitate in a) a long aged EBRS treated sample and b) a long aged non-EBRS treated sample.

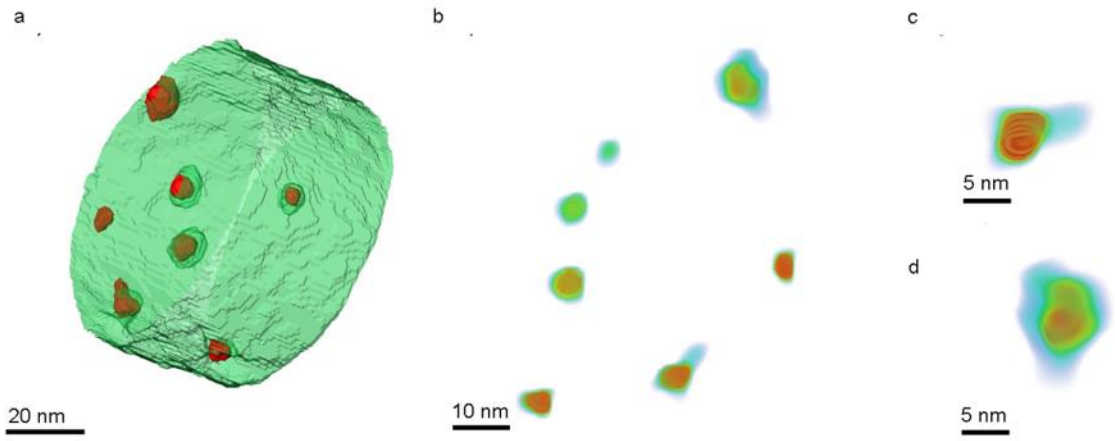

Figure S3: Elemental map reconstructions of a short aged sample. a) Segmentation of Al-rich (green) and Sc-rich (red) regions b) Volume rendered representation of the Sc-K EDX signal. The colour scale going from dark blue, via cyan, green yellow and orange to red indicates the amount of Sc detected, where red represents a maximum of the signal and the other colours respectively less. c) and d) show precipitates with clearly inhomogeneous Sc distributions.

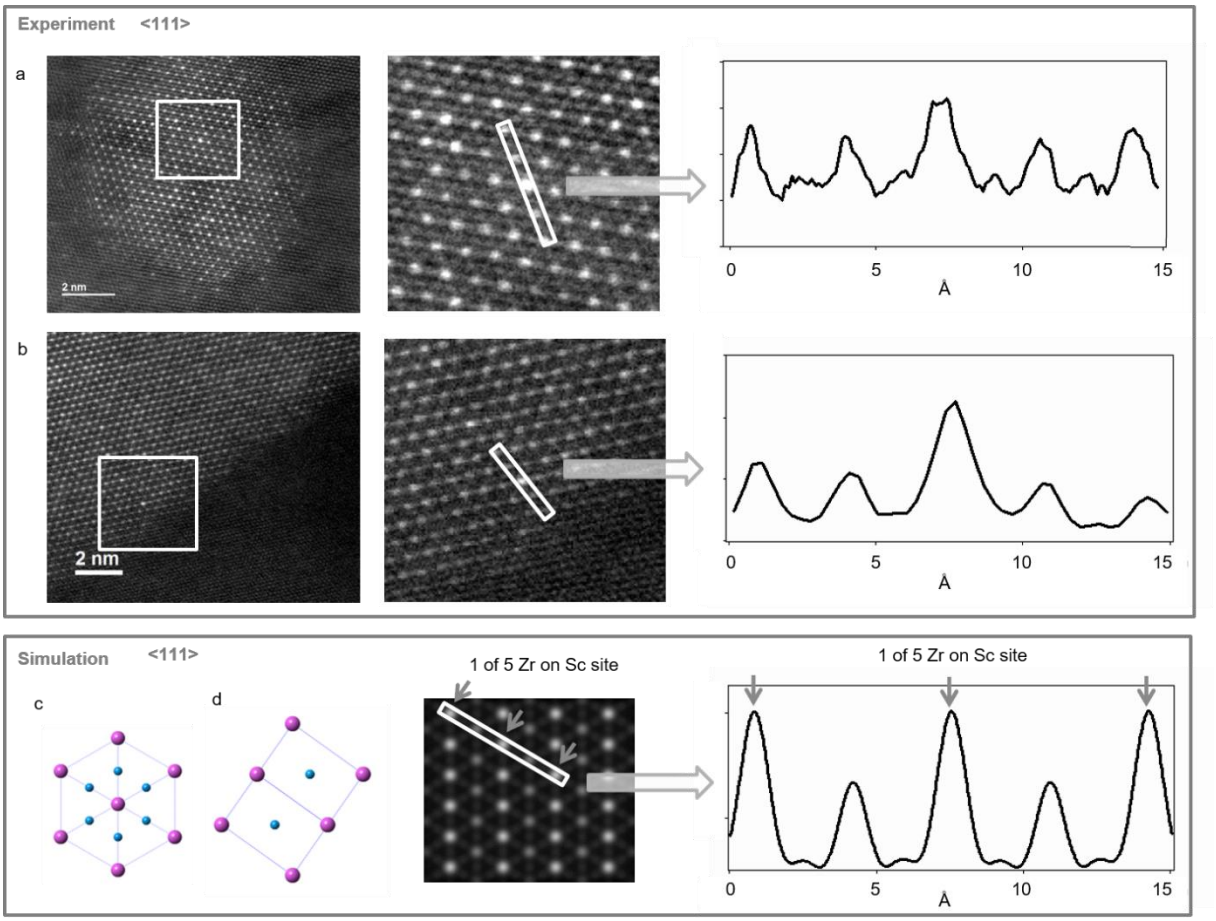

Figure S4: High resolution images and profiles of short (a) and long (b) aged EBRS treated precipitates revealing higher intensity columns on the Sc/Zr sublattice. c) and d): Model of Al_3Sc structure in <111> orientation as used for simulation in beam direction (c) and perpendicular to it (d). Sc atoms are depicted in purple and Al atoms in blue. e): Simulated HR STEM image and profile from frozen phonon multi-slice calculation of Al_3Sc, where in the indicated columns 1 of 5 Sc atoms was substituted by a Zr atom.

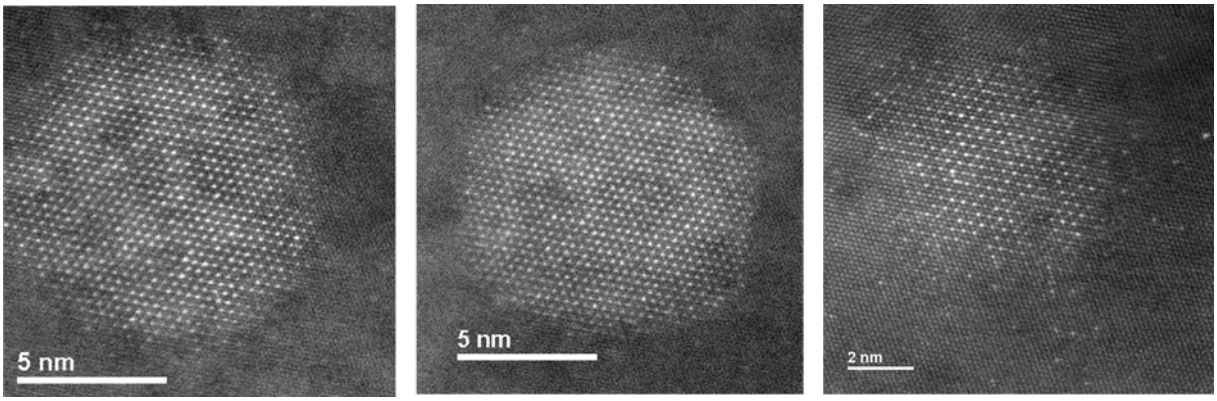

Figure S5: HR STEM images of different short aged precipitates all showing inhomogeneous Sc distribution.

13 Summary and Conclusions

During this thesis developmental work has been done in analytical tomography and quantitative HR (EDX) STEM imaging and interesting material scientific discoveries were made during the investigation of an aluminium alloy.

Developmental work in analytical tomography:

- In EDX tomography a shadowing problem was identified and analysed. We found that the Fischione 2020 holder causes shadowing of the Super X (FEI) EDX detection system in the Titan^3. The shadowing per tilt angle was analysed using a radial-symmetric needle-shaped sample and intensities were found to vary by a factor of three. To account for this intensity variation SIs were normed prior to reconstruction via the total counts per SI.
- To eliminate the shadowing problem and additionally maximise the detectable EDX counts and thus reach a better signal without increasing dose a new sample holder (Fischione 2050) was purchased. However, it was soon found that if used with the provided sample holding needles two of the four detectors, of the Super-X system were shadowed. In a first step we tried to adjust the sample holding needle via FIB milling and create very long sample needles as well as attach them on a FEBID built podium. Finally the most effective way to avoid all shadowing and thus enable the unlimited use of all four quadrants of the Super-X detector was the use of other sample-holding tips, which are actually produced for electric sensing.

Evaluation of the quantitative reliability of analytical tomographic results:

- The effects of channelling on analytical tomographic investigations were investigated through the comparison of reconstructions performed on two sets of tilt series shifted by 180° performed on a non-radially symmetric sample. Investigation was performed using a set of different probe convergence angles. It was found, that the effect of channelling is negligible for our samples of interest.
- X-ray absorption in analytical tomography was investigated by calculating the absorption within a needle shaped sample. It was found that absorption can have a non-negligible influence, depending on sample composition and detector geometry. It was found that the Super-X detector system has the advantage of significantly reducing the tilt angle dependence compared to single detectors. We found that for our samples of interest Al-matrix and Al_3(Al,Sc,Zr) precipitates the absorption can be neglected.
- Reconstruction algorithms were compared and it was found that compressed sensing methods need to be handled with care. In our case multiplicative SIRT proved to be the ideal method for voxel spectroscopy, while TV minimisation was best for mask generation. This comparative study also proved the advantage of simultaneous EELS, EDX and HAADF acquisition, not only for complementary information, but also for evaluating reconstruction algorithms and distinguishing sample features from artefacts.

Developments concerning quantitative HR STEM including simulations:

- A method was developed, which allows performing STEM simulations via µSTEM for non-perfect crystals. The combined use of a crystal illustration software (e.g. Crystal Maker or VESTA) and a self-written Matlab script allows the simulation of crystal defects like anti-site atoms, interstitial atoms, vacancies, surfaces, or even varying compositions via µSTEM.

- A method, which enables the calculation of atomic column EDX concentrations from averaged plane concentrations, was developed. This method gives channelling corrected atomic column concentrations in case a set of criteria is fulfilled.

The AlMgScZr alloy:

- TEM, EFTEM, STEM, EELS and EDX investigations of differently aged and pre-treated samples showed that
  - EBRS treatment increases the amount of Sc in solid solution.
  - Precipitates (short and long aged) exhibit $L1_2$ crystal structure and coherently match the Al matrix.
  - Short aged precipitates are Sc-rich, but show no increased Zr concentration compared to the matrix.
  - Long aged precipitates show increased Sc and Zr concentrations, compared to the matrix.
  - The core-shell structure is significantly less pronounced, than previously reported in literature, but could be confirmed.
- In situ heating experiments showed a recrystallization process. It confirmed the ability of the precipitates to pin the recrystallization boundary. The formation of Sc-rich precipitates was observed, as well as the formation of groups of Zr atoms, and their slow diffusion through the Al matrix.

Analytical tomographic investigations of the AlMgScZr alloy:

- Elemental map reconstruction showed an inhomogeneous Sc distribution within the precipitates. While in long aged precipitates this could be caused by the incorporated Zr, in short aged precipitates this has to stem from occupation of some Sc-lattice sites by Al or Mg atoms.
- High Al concentrations and low Mg concentrations within the precipitates found via voxel-spectroscopic investigations allowed the conclusion that considerable amounts of Al atoms occupy Sc/Zr lattice sites.
- A voxel spectroscopic analysis of the core composition showed the presence of Zr in the core region of long aged precipitates. As precipitates are Zr-free after short ageing, this finding proves Zr diffusion within precipitates.
- A radially symmetric averaged voxel spectroscopic analysis of long aged precipitates shows a minimum deviation from the $Al_3(Sc,Zr)$ composition at the interface between core and shell, for EBRS treated and non-EBRS treated samples.

HR STEM investigations of the AlMgScZr alloy including QEP simulations:

- HR STEM investigation in combination with QEP simulations showed the formation of Al channels within the precipitates.

Gibbs energy calculations and diffusion simulations:

- Gibbs energy calculations for an Al(Al,Sc,Zr) phase with varying compositions confirmed the energetic advantage of a decomposition of Al and $Al_3(Sc,Zr)$ compared to a mixed $Al_3(Al,Sc,Zr)$ phase.

- Diffusion simulations of an Al(Al,Sc,Zr) system confirmed that the expected phase separation takes place at the atomic scale.

Combined findings:

- Above findings mark the **discovery of an atomic scale spinodal decomposition** that enables diffusion within the precipitate.
- The still present core-shell structure proves that some process hinders the precipitates from reaching the equilibrium condition.
- The minimum compositional deviation from the $Al_3(Sc,Zr)$ composition at the core-shell interface implies a minimum-diffusion region, possibly even a diffusion barrier.

From the findings and conclusions drawn above, we can formulate the following hypothesis **explaining diffusion within the precipitates, and the reason for its termination**:

> The diffusion process is self-limiting. This is a result of the diffusing atoms being the building blocks of walls of the diffusion channels. Channels with widths down to single unit cells were found. Consequently, the encounter of atoms in a narrow channel can block the channel permanently, as $L1_2$ crystal structure forms, which hinders diffusion. A region with higher than average amounts of $L1_2$ structure reduces diffusion. A closed shell of increased $L1_2$ structure represents a diffusion barrier. The interface region between core and shell spanning several nm in radius, with minimum average deviation from the ideal $L1_2$ composition reduces diffusion between core and shell and indicates such a diffusion barrier.

14 Bibliography

1. Williams, D. B. & Carter, C. B. *Transmission Electron Microscopy A Textbook for Materials Science*. (Springer, 1996).

2. Brydson, R. *Aberration-Corrected Analytical Transmission Electron Microscopy*. (Wiley, 2011).

3. Rose, H. Correction of aperture aberrations in magnetic systems with threefold symmetry. *Nucl. Instruments Methods Phys. Res.* **187**, 187–199 (1981).

4. Rose, H., Berman, P. E. I. & Nguyen, A. E. T. United States Patent (19). (1990).

5. Krivanek, O. L., Dellby, N. & Lupini, A. R. Towards sub-Å electron beams. *Ultramicroscopy* **78**, 1–11 (1999).

6. Pennycook, S. & Nellist, P. Scanning Transmission Electron Microscopy. *Springer, New York* (2011).

7. Pennycook, S. J. Z-contrast stem for materials science. *Ultramicroscopy* **30**, 58–69 (1989).

8. Carter, C. B. & Williams, D. B. *Transmission electron microscopy: Diffraction, imaging, and spectrometry*. (Springer, 2016).

9. Egerton, R. F. *Electron Energy-Loss Spectroscopy in the Electron Microscope*. (Springer, 2011).

10. Gubbens, A., Barfels, M., Trevor, C., Twesten, R., Mooney, P., Thomas, P., Menon, N., Kraus, B., Mao, C. & McGinn, B. The GIF Quantum, a next generation post-column imaging energy filter. *Ultramicroscopy* **110**, 962–970 (2010).

11. Malis, T., Cheng, S. C. & Egerton, R. F. Log-Ratio Technique for Specimen-Thickness Measurement in the TEM. *Jounrnal Electron Microsc. Tech.* 193–200 (1988).

12. Midgley, P. A. & Weyland, M. 3D electron microscopy in the physical sciences: The development of Z-contrast and EFTEM tomography. *Ultramicroscopy* **96**, 413–431 (2003).

13. Moseley, H. High Frequency Spectra of the Elements. *Phil. Mag.* **26**, 1024–1032 (1914).

14. Egerton, R. F., Li, P. & Malac, M. Radiation damage in the TEM and SEM. *Micron* **35**, 399–409 (2004).

15. Egerton, R. F., Wang, F. & Crozier, P. A. Beam-Induced Damage to Thin Specimens in an Intense Electron Probe. *Microsc. Microanal.* **12**, 65–71 (2006).

16. Jenkins, M.L.; Kirk, M. A. *Characterisation of Radiation Damage by Transmission Electron Microscopy*. (2000).

17. Sawyer, L. C., Grubb, D. T. & Meyers, G. F. *Polymer Microscopy*. (Springer New York, 2008).

18. Genc, A., Kovarik, L., Gu, M., Cheng, H., Plachinda, P., Pullan, L., Freitag, B. & Wang, C. XEDS STEM tomography for 3D chemical characterization of nanoscale particles. *Ultramicroscopy* **131**, 24–32 (2013).

19. Newbury, D. E. The New X-ray Mapping: X-ray Spectrum Imaging above 100 kHz Output Count Rate with the Silicon Drift Detector. *Microsc. Microanal.* **12**, 26–35 (2006).

20. Hunt, J. A. & Williams, D. B. Electron energy-loss spectrum-imaging. *Ultramicroscopy* **38**, 47–73 (1991).

21. Kane, J. M. A user' guide to use Digital micrograph. *Acta Psychiatr. Scand.* **123**, 407–8 (2011).

22. Radon, J. Über die Bestimmung von Funktionen durch ihre Integralwerte längs gewisser Mannigfaltigkeiten. *Berichte der Sächsischen Akadamie der Wiss.* **69**, 262–277 (1917).

23. Kak, A. C. & Slaney, M. *Principles of Computerized Tomographic Imaging*. (IEEE Press, 1988).

24. Hawkes, P. W. Electron Tomography: Three- dimensional Imaging with the Transmission Electron Microscope, Plenum Press, New York, London, . [42]No Title. in (ed. Frank, J.) (Plenum Press, New York, 1992).

25. Howie, A. Image Contrast And Localized Signal Selection Techniques. *J. Microsc.* (1979).

26. Hounsfield, G. N. A Method and Apparatus for Examina- tion of a Body by Radiation such as X or Gamma Radiation. (1972).

27. Deans, S. R. *The Radon Transform and Some of its Applications*. (Wiley, New York, 1983).

28. Hoppe, W., Langer, R., Knesch, G. & Poppe, C. Protein-Kristallstrukturanalyse mit Elektronenstrahlen. *Naturwissenschaften* **55**, 333–336 (1968).

29. Crowther, R. A., De Rosier, D. J. & Klug, A. The reconstruction of a three-dimensional structure from projections and its application to electron microscopy - II. Direct methods. *Proc. R. Soc. Lond. B* 319 (1970).

30. Herman, G. T. The Fundamentals of Computerised Tomography. in (Academic Press, 1980).

31. Gilbert, P. Iterative methods for the three-dimensional reconstruction of an object from projections. *J. Theor. Biol.* **36**, 105–117 (1972).

32. Kuba, A. & Herman, G. T. Discrete Tomography: A Historical Overview. in *Discrete Tomography: Foundations, Algorithms, and Applications* (eds. Herman, G. T. & Kuba, A.) 3–34 (Birkhäuser Boston, 1999). doi:10.1007/978-1-4612-1568-4_1

33. Leary, R., Saghi, Z., Midgley, P. A. & Holland, D. J. Compressed sensing electron tomography. *Ultramicroscopy* **131**, 70–91 (2013).

34. Saghi, Z., Divitini, G., Winter, B., Leary, R., Spiecker, E., Ducati, C. & Midgley, P. A. Compressed sensing electron tomography of needle-shaped biological specimens - Potential for improved reconstruction fidelity with reduced dose. *Ultramicroscopy* **160**, 230–238 (2016).

35. Lustig, M., Donoho, D. & Pauly, J. M. Sparse MRI: The application of compressed sensing for rapid MR imaging. *Magn. Reson. Med.* **58**, 1182–1195 (2007).

36. Donoho, D. L. Compressed sensing. *IEEE Trans. Inf. Theory* **52**, 1289–1306 (2006).

37. Mastronarde, D. N. Dual-axis tomography: An approach with alignment methods that preserve resolution. *J. Struct. Biol.* **120**, 343–352 (1997).

38. Tong, J., Arslan, I. & Midgley, P. A novel dual-axis iterative algorithm for electron tomography. *J. Struct. Biol.* **153**, 55–63 (2006).

39. Penczek, P., Marko, M., Buttle, K. & Frank, J. Double-tilt electron tomography. *Ultramicroscopy* **60**, 393–410 (1995).

40. Lawrence, M. C. Least-Squares Method of Alignment Using Markers. in *Electron Tomography: Three-Dimensional Imaging with the Transmission Electron Microscope* (ed. Frank, J.) 197–204

(Springer US, 1992). doi:10.1007/978-1-4757-2163-8_8

41. Brandt, S., Heikkonen, J. & Engelhardt, P. Automatic alignment of transmission electron microscope tilt series without fiducial markers. *J. Struct. Biol.* **136**, 201–213 (2001).

42. Owen, C. H. & Landis, W. J. Alignment of electron tomographic series by correlation without the use of gold particles. *Ultramicroscopy* **63**, 27–38 (1996).

43. Uusimäki, T., Margaris, G., Trohidou, K., Granitzer, P., Rumpf, K., Sezen, M. & Kothleitner, G. Three dimensional quantitative characterization of magnetite nanoparticles embedded in mesoporous silicon: Local curvature, demagnetizing factors and magnetic Monte Carlo simulations. *Nanoscale* **5**, 11944–11953 (2013).

44. Scott, M. C., Chen, C. C., Mecklenburg, M., Zhu, C., Xu, R., Ercius, P., Dahmen, U., Regan, B. C. & Miao, J. Electron tomography at 2.4-ångström resolution. *Nature* **483**, 444–447 (2012).

45. Goris, B., Bals, S., Van Den Broek, W., Carbó-Argibay, E., Gómez-Graña, S., Liz-Marzán, L. M. & Van Tendeloo, G. Atomic-scale determination of surface facets in gold nanorods. *Nat. Mater.* **11**, 930–935 (2012).

46. Kobayashi, A., Fujigaya, T., Itoh, M., Taguchi, T. & Takano, H. Technical note: A tool for determining rotational tilt axis with or without fiducial markers. *Ultramicroscopy* **110**, 1–6 (2009).

47. Jarausch, K., Thomas, P., Leonard, D. N., Twesten, R. & Booth, C. R. Four-dimensional STEM-EELS: Enabling nano-scale chemical tomography. *Ultramicroscopy* **109**, 326–337 (2009).

48. Saghi, Z., Xu, X., Peng, Y., Inkson, B. & Möbus, G. Three-dimensional chemical analysis of tungsten probes by energy dispersive x-ray nanotomography. *Appl. Phys. Lett.* **91**, (2007).

49. Lepinay, K., Lorut, F., Pantel, R. & Epicier, T. Chemical 3D tomography of 28nm high K metal gate transistor: STEM XEDS experimental method and results. *Micron* **47**, 43–49 (2013).

50. Slater, T. J. A., Macedo, A., Schroeder, S. L. M., Burke, M. G., O'Brien, P., Camargo, P. H. C. & Haigh, S. J. Correlating Catalytic Activity of Ag-Au Nanoparticles with 3D Compositional Variations. *Nano Lett.* **14**, 1921–1926 (2014).

51. Möbus, G., Doole, R. C. & Inkson, B. J. Spectroscopic electron tomography. *Ultramicroscopy* **96**, 433–451 (2003).

52. Gass, M. H., Koziol, K. K. K., Windle, A. H. & Midgley, P. A. Four-dimensional spectral tomography of carbonaceous nanocomposites. *Nano Lett.* **6**, 376–379 (2006).

53. Haberfehlner, G., Bayle-Guillemaud, P., Audoit, G., Lafond, D., Morel, P. H., Jousseaume, V., Ernst, T. & Bleuet, P. Four-dimensional spectral low-loss energy-filtered transmission electron tomography of silicon nanowire-based capacitors. *Appl. Phys. Lett.* **101**, (2012).

54. Yedra, L., Eljarrat, A., Arenal, R., Pellicer, E., Cabo, M., López-Ortega, A., Estrader, M., Sort, J., Baró, M. D., Estradé, S. & Peiró, F. EEL spectroscopic tomography: Towards a new dimension in nanomaterials analysis. *Ultramicroscopy* **122**, 12–18 (2012).

55. Goris, B., Polavarapu, L., Bals, S., Van Tendeloo, G. & Liz-Marzán, L. M. Monitoring Galvanic Replacement Through Three-Dimensional Morphological and Chemical Mapping. *Nano Lett.* **14**, 3220–3226 (2014).

56. Haberfehlner, G., Orthacker, A., Albu, M., Li, J. & Kothleitner, G. Nanoscale voxel spectroscopy

by simultaneous EELS and EDS tomography. *Nanoscale* **6**, 14563–14569 (2014).

57. Van Aert, S., Batenburg, K. J., Rossell, M. D., Erni, R. & Van Tendeloo, G. Three-dimensional atomic imaging of crystalline nanoparticles. *Nature* **470**, 374–377 (2011).

58. Bals, S., Goris, B., De Backer, A., Van Aert, S. & Van Tendeloo, G. Atomic resolution electron tomography. *MRS Bull.* **41**, 525–530 (2016).

59. Miao, J., Ercius, P. & Billinge, S. J. L. Atomic electron tomography: 3D structures without crystals. *Science (80-.).* **353**, (2016).

60. Goris, B., De Backer, A., Van Aert, S., Gómez-Graña, S., Liz-Marzán, L. M., Van Tendeloo, G. & Bals, S. Three-dimensional elemental mapping at the atomic scale in bimetallic nanocrystals. *Nano Lett.* **13**, 4236–4241 (2013).

61. Tuned Piezo Cutting Tool. (2008).

62. Taendl, J., Orthacker, A., Amenitsch, H., Kothleitner, G. & Poletti, C. Influence of the degree of scandium supersaturation on the precipitation kinetics of rapidly solidified Al-Mg-Sc-Zr alloys. *Acta Mater.* **117**, 43–50 (2016).

63. Gatan Disc Grinder System. Available at: http://www.gatan.com/products/tem-specimen-preparation/disc-grinder-system. (Accessed: 24th June 2018)

64. Struers 6 µm diamond paste. Available at: https://www.struers.com/en/Products/Grinding-and-Polishing/Grinding-and-polishing-consumables. (Accessed: 24th June 2018)

65. Struers 0.25 µm diamond felt. Available at: https://www.struers.com/en/Products/Grinding-and-Polishing/Grinding-and-polishing-consumables. (Accessed: 24th June 2018)

66. Gatan. Precision Ion Polishing System User ' s Guide. (2008).

67. Omniprobe nanomanipulator. Available at: https://nano.oxinst.com/products/omniprobe/omniprobe-200. (Accessed: 24th June 2018)

68. Van Dorp, W. F. & Hagen, C. W. A critical literature review of focused electron beam induced deposition. *J. Appl. Phys.* **104**, (2008).

69. Dwyer, C., Weyland, M., Chang, L. Y. & Muddle, B. C. Combined electron beam imaging and ab initio modeling of T1 precipitates in Al-Li-Cu alloys. *Appl. Phys. Lett.* **98**, (2011).

70. Chen, Z., D'Alfonso, A. J., Weyland, M., Taplin, D. J., Allen, L. J. & Findlay, S. D. Energy dispersive X-ray analysis on an absolute scale in scanning transmission electron microscopy. *Ultramicroscopy* **157**, 21–26 (2015).

71. Bjørge, R., Dwyer, C., Weyland, M., Nakashima, P. N. H., Etheridge, J. & Holmestad, R. Quantitative HAADF STEM study of β-like precipitates in an Al-Mg-Ge alloy. *J. Phys. Conf. Ser.* **371**, 012015 (2012).

72. Zheng, C. L. & Etheridge, J. Measurement of chromatic aberration in STEM and SCEM by coherent convergent beam electron diffraction. *Ultramicroscopy* **125**, 49–58 (2013).

73. Maunders, C., Dwyer, C., Tiemeijer, P. C. & Etheridge, J. Practical methods for the measurement of spatial coherence-A comparative study. *Ultramicroscopy* **111**, 1437–1446 (2011).

74. Dwyer, C., Maunders, C., Zheng, C. L., Weyland, M., Tiemeijer, P. C. & Etheridge, J. Sub-0.1

nm-resolution quantitative scanning transmission electron microscopy without adjustable parameters. *Appl. Phys. Lett.* **100**, 9–13 (2012).

75. Katz-Boon, H., Rossouw, C. J., Dwyer, C. & Etheridge, J. Rapid Measurement of Nanoparticle Thickness Profiles. *Ultramicroscopy* **124**, 61–70 (2013).

76. Dwyer, C., Erni, R. & Etheridge, J. Method to measure spatial coherence of subangstrom electron beams. *Appl. Phys. Lett.* **93**, 021115 (2008).

77. Dwyer, C., Erni, R. & Etheridge, J. Measurement of effective source distribution and its importance for quantitative interpretation of STEM images. *Ultramicroscopy* **110**, 952–957 (2010).

78. Nguyen, D. T., Findlay, S. D. & Etheridge, J. The spatial coherence function in scanning transmission electron microscopy and spectroscopy. *Ultramicroscopy* **146C**, 6–16 (2014).

79. Rossouw, C. J., Dwyer, C., Katz-Boon, H. & Etheridge, J. Channelling contrast analysis of lattice images: conditions for probe-insensitive STEM. *Ultramicroscopy* **136**, 216–23 (2014).

80. Allen, L. J., D'Alfonso, A. J. & Findlay, S. D. Modelling the inelastic scattering of fast electrons. *Ultramicroscopy* **151**, 11–22 (2015).

81. Alfonso, A. D., Findlay, S., Forbes, B., Allen, L., Brown, H., Cosgriff, E., Forbes, B., Lugg, N., Martin, A., Ruben, G. & Witte, C. µ STEM. 1–24 (2016).

82. D'Alfonso, A. J., Findlay, S. D. & Allen, L. J. Simulating Inelastic Scattering in Scanning Transmission Electron Microscopy using µSTEM. *Microsc. Microanal.* **21**, 1885–1886 (2015).

83. Forbes, B. D., Martin, A. V., Findlay, S. D., D'Alfonso, A. J. & Allen, L. J. Quantum mechanical model for phonon excitation in electron diffraction and imaging using a Born-Oppenheimer approximation. *Phys. Rev. B - Condens. Matter Mater. Phys.* **82**, 1–8 (2010).

84. Loane, R. F., Xu, P. & Silcox, J. Thermal vibrations in convergent???beam electron diffraction. *Acta Crystallogr. Sect. A* **47**, 267–278 (1991).

85. Allen, L. J., Findlay, S. D., Oxley, M. P. & Rossouw, C. J. Lattice-resolution contrast from a focused coherent electron probe. Part I. *Ultramicroscopy* **96**, 47–63 (2003).

86. Bird, D. M. & King, Q. A. Absorptive form factors for high???energy electron diffraction. *Acta Crystallogr. Sect. A* **46**, 202–208 (1990).

87. Hall, C. R. & Hirsch, P. B. Effect of thermal diffuse scattering on propagation of high energy electrons through crystals. *Proc. Roy. Soc. Lond. A* **286**, 158–177 (1964).

88. Forbes, B. D., D'Alfonso, A. J., Williams, R. E. A., Srinivasan, R., Fraser, H. L., McComb, D. W., Freitag, B., Klenov, D. O. & Allen, L. J. Contribution of thermally scattered electrons to atomic resolution elemental maps. *Phys. Rev. B - Condens. Matter Mater. Phys.* **86**, 1–9 (2012).

89. Hillyard, S., Loane, R. F. & Silcox, J. Annular dark-field imaging: Resolution and thickness effects. *Ultramicroscopy* **49**, 14–25 (1993).

90. Loane, R. F., Xu, P. & Silcox, J. Incoherent imaging of zone axis crystals with ADF STEM. *Ultramicroscopy* **40**, 121–138 (1992).

91. A. Muller, D., Edwards, B., J. Kirkland, E. & Silcox, J. Simulation of thermal diffuse scattering including a detailed phonon dispersion curve. *Ultramicroscopy* **86**, 371–380 (2001).

92. LeBeau, J. M., Findlay, S. D., Allen, L. J. & Stemmer, S. Position averaged convergent beam electron diffraction: Theory and applications. *Ultramicroscopy* **110**, 118–125 (2010).

93. Dycus, J. H., Xu, W., Sang, X., D'Alfonso, A. J., Chen, Z., Weyland, M., Allen, L. J., Findlay, S. D. & LeBeau, J. M. Influence of experimental conditions on atom column visibility in energy dispersive X-ray spectroscopy. *Ultramicroscopy* **171**, 1–7 (2016).

94. Filatov, Y. ., Yelagin, V. . & Zakharov, V. . New Al–Mg–Sc alloys. *Mater. Sci. Eng. A* **280**, 97–101 (2000).

95. Sawtell, R. R. & Jensen., C. L. Mechanical properties and microstructures of Al-Mg-Sc alloys. *Metall. Mater. Trans. A* **21**, 421–430 (1990).

96. Williams, J. C. & Starke, E. A. Progress in structural materials for aerospace systems. *Acta Mater.* **51**, 5775–5799 (2003).

97. Lefebvre, W., Danoix, F., Hallem, H., Forbord, B., Bostel, A. & Marthinsen, K. Precipitation kinetic of Al3(Sc,Zr) dispersoids in aluminium. *J. Alloys Compd.* **470**, 107–110 (2009).

98. Deschamps, A., Lae, L. & Guyot, P. In situ small-angle scattering study of the precipitation kinetics in an Al-Zr-Sc alloy. *Acta Mater.* **55**, 2775–2783 (2007).

99. Forbord, B., Lefebvre, W., Danoix, F., Hallem, H. & Marthinsen, K. Three dimensional atom probe investigation on the formation of Al3(Sc,Zr)-dispersoids in aluminium alloys. *Scr. Mater.* **51**, 333–337 (2004).

100. Forbord, B., Hallem, H., R??yset, J. & Marthinsen, K. Thermal stability of Al3(Scx,Zr1-x)-dispersoids in extruded aluminium alloys. *Mater. Sci. Eng. A* **475**, 241–248 (2008).

101. Tolley, A., Radmilovic, V. & Dahmen, U. Segregation in Al3(Sc,Zr) precipitates in Al-Sc-Zr alloys. *Scr. Mater.* **52**, 621–625 (2005).

102. Fuller, C. B., Murray, J. L. & Seidman, D. N. Temporal evolution of the nanostructure of Al(Sc,Zr) alloys: Part I-Chemical compositions of Al3(Sc1-xZrx) precipitates. *Acta Mater.* **53**, 5415–5428 (2005).

103. Fuller, C. B. & Seidman, D. N. Temporal evolution of the nanostructure of Al(Sc,Zr) alloys: Part II-coarsening of Al3(Sc1-xZrx) precipitates. *Acta Mater.* **53**, 5415–5428 (2005).

104. Clouet, E., Laé, L., Épicier, T., Lefebvre, W., Nastar, M. & Deschamps, A. Complex precipitation pathways in multicomponent alloys. *Nat. Mater.* **5**, 482–488 (2006).

105. Clouet, E., Barbu, A., Laé, L. & Martin, G. Precipitation kinetics of Al3Zr and Al3Sc in aluminum alloys modeled with cluster dynamics. *Acta Mater.* **53**, 2313–2325 (2005).

106. Clouet, E., Nastar, M. & Sigli, C. Nucleation of Al3Zr and Al3Sc in aluminum alloys: From kinetic Monte Carlo simulations to classical theory. *Phys. Rev. B - Condens. Matter Mater. Phys.* **69**, 1–15 (2004).

107. Taendl, J., Palm, F., Anders, K., Gradinger, R. & Poletti, C. Investigation of the precipitation kinetics of a new Al-Mg-Sc-Zr alloy. *Mater. Sci. Forum* **794**–**796**, 1038–1043 (2014).

108. Taendl, J., Nambu, S., Orthacker, A., Kothleitner, G., Inoue, J., Koseki, T. & Poletti, C. In-situ observation of recrystallization in an AlMgScZr alloy using confocal laser scanning microscopy. *Mater. Charact.* **108**, 137–144 (2015).

109. Taendl, J., Dikovits, M. & Poletti, C. Investigation of the hot deformation behavior of an Al-Mg-

Sc-Zr alloy under plane strain condition. *Key Eng. Mater.* **611–612**, 76–83 (2014).

110. Kozeschnik, E. *Modeling Solid-State Precipitation*. (Momentum Press, 2012). doi:10.5643/9781606500644

111. Orthacker, A., Haberfehlner, G., Taendl, J., Poletti, M. C., Sonderegger, B. & Kothleitner, G. Diffusion-defining atomic-scale spinodal decomposition within nanoprecipitates. *Nat. Mater.* **17**, 1101–1107 (2018).

112. Velux Software Package - Thermo Fischer Scientific. Available at: https://www.fei.com/software/. (Accessed: 24th June 2018)

113. Haberfehlner, G., Trügler, A., Schmidt, F. P., Hörl, A., Hofer, F., Hohenester, U. & Kothleitner, G. Correlated 3D Nanoscale Mapping and Simulation of Coupled Plasmonic Nanoparticles. *Nano Lett.* **15**, 7726–7730 (2015).

114. Horl, A., Haberfehlner, G., Trugler, A., Schmidt, F. P., Hohenester, U. & Kothleitner, G. Tomographic imaging of the photonic environment of plasmonic nanoparticles. *Nat. Commun.* **8**, 1–6 (2017).

115. Kramers, H. A. XCIII. On the theory of X-ray absorption and of the continuous X-ray spectrum. *Philos. Mag. Ser. 6* **46**, 836–871 (1923).

116. Rez, P. Cross-sections for energy loss spectrometry. *Ultramicroscopy* **9**, 283–287 (1982).

117. Huber, R., Haberfehlner, G., Holler, M., Kothleitner, G. & Bredies, K. Total generalized variation regularization for multi-modal electron tomography. *Nanoscale* **11**, 5617–5632 (2019).

118. Image Processing Program ImageJ. Available at: https://imagej.net/Downloads. (Accessed: 24th June 2018)

119. Kothleitner, G., Neish, M. J., Lugg, N. R., Findlay, S. D., Grogger, W., Hofer, F. & Allen, L. J. Quantitative elemental mapping at atomic resolution using X-ray spectroscopy. *Phys. Rev. Lett.* **112**, 1–5 (2014).

120. Fischione Model 2020 tomography sample holder. Available at: https://www.fischione.com/products/holders/model-2020-advanced-tomography-holder. (Accessed: 24th June 2018)

121. Fischione Model 2050 tomography sample holder. Available at: https://www.fischione.com/products/holders/model-2050-axis-rotation-tomography-holder. (Accessed: 24th June 2018)

122. Orthacker, A., Haberfehlner, G., Taendl, J., Poletti, M. C., Sonderegger, B. & Kothleitner, G. Diffusion-defining atomic-scale spinodal decomposition within nanoprecipitates. *Nat. Mater.* (2018). doi:10.1038/s41563-018-0209-z

123. muSTEM. Available at: http://tcmp.ph.unimelb.edu.au/mustem/muSTEM.html. (Accessed: 24th June 2018)

124. Mommaa, K. & Izumia, F. VESTA 3 for three-dimensional visualization of crystal, volumetric and morphology data. *J. Appl. Crystallogr.* **44**, 1272–1276 (2011).

125. Spierings, A. B., Dawson, K., Voegtlin, M., Palm, F. & Uggowitzer, P. J. Microstructure and mechanical properties of as-processed scandium-modified aluminium using selective laser

melting. *CIRP Ann. - Manuf. Technol.* **65**, 213–216 (2016).

126. Heinz, A., Haszler, A., Keidel, C., Moldenhauer, S., Benedictus, R. & Miller, W. S. Recent development in aluminium alloys for aerospace applications. *Mater. Sci. Eng. A* **280**, 102–107 (2000).

127. DENS Solutions. Available at: http://denssolutions.com/. (Accessed: 25th June 2018)

128. Hyde, J. M., Sutton, A. P., Harris, J. R. G., Cerezo, A. & Gardiner, A. Modelling spinodal decomposition at the atomic scale: beyond the Cahn - Hilliard model. *Model. Simul. Mater. Sci. Eng.* **4**, 33–54 (1996).

129. Hald, J. Prospects for Martensitic 12 % Cr Steels for Advanced Steam Power Plants. *Trans. Indian Inst. Met.* **69**, 183–188 (2016).

130. Danielsen, H. K. Review of Z phase precipitation in 9–12 wt-%Cr steels. *Mater. Sci. Technol.* **0836**, 1743284715Y.000 (2015).

131. Cavanaugh, M. K., Birbilis, N., Buchheit, R. G. & Bovard, F. Investigating localized corrosion susceptibility arising from Sc containing intermetallic Al3Sc in high strength Al-alloys. *Scr. Mater.* **56**, 995–998 (2007).

132. Novotny, G. M. & Ardell, A. J. Precipitation of Al3Sc in binary Al-Sc alloys. *Mater. Sci. Eng. A* **318**, 144–154 (2001).

133. Røyset, J. & Ryum, N. Kinetics and mechanisms of precipitation in an Al-0.2wt.% Sc alloy. *Mater. Sci. Eng. A* **396**, 409–422 (2005).

134. Røyset, J. & Ryum, N. Scandium in aluminium alloys. *Int. Mater. Rev.* **50**, 19–44 (2005).

135. Jones, R. A. L. *Soft Condensed Matter*. (Oxford University Press, 2002).

136. Schlossmacher, P., Klenov, D. O., Freitag, B. & von Harrach, H. S. Enhanced Detection Sensitivity with a New Windowless XEDS System for AEM Based on Silicon Drift Detector Technology. *Micros. Today* **18**, 14–20 (2010).

137. Azevedo, S. G., Schneberk, D. J., Fitch, J. P. & Martz, H. E. Calculation of the Rotational Centers in Computed Tomography Sinograms. *IEEE Trans. Nucl. Sci.* **37**, 1525–1540 (1990).

138. Simmons, R. O. & Balluffi, R. W. Measurements of equilibrium vacancy concentrations in aluminum. *Phys. Rev.* **117**, 52–61 (1960).

15 List of Abbreviations

ABF	*annular bright field*
AC	*as cast*
ADF	*annular dark field*
Al	*aluminium*
ASTEM	*Austrian scanning transmission electron microscope*
BF	*bright field*
DQE	*detection quantum efficiency*
EBRS	*electron beam re-solidified*
EDXS	*energy dispersive X-ray spectroscopy*
EELS	*electron energy loss spectroscopy*
EFTEM	*energy filtered transmission electron microscopy*
fcc	*face centred cubic*
FEBID	*focused electron beam induced deposition*
FIB	*focused ion beam*
G	*Gibbs Energy*
Ge	*germanium*
GIS	*gas injection systems*
HAADF	*high angle annular dark field*
HR STEM	*high resolution scanning transmission electron microscopy*
HRTEM	*high resolution transmission electron microscopy*
Mg	*magnesium*
mSIRT	*multiplicative simultaneous iterative reconstruction technique*
O	*oxygen*
OTF	*object transfer function*
PACBED	*position averaged convergent beam electron diffraction*
PCTF	*phase contrast transfer function*
QEP	*quantum excitation of phonons*
Sc	*scandium*
SEM	*scanning electron microscopy*
Si	*silicon*
SI	*spectrum image*
SIRT	*simultaneous iterative reconstruction technique*
SL	*sublattices*
SL1	*sublattice one*
SL2	*sublattice two*
STEM	*scanning transmission electron microscopy*
STO	*strontium titanate*
TEM	*transmission electron microscopic techniques*
Ti-O	*titanium-oxygen*
U	*internal energy*
YAG	*yttrium-aluminium-garnet*
Z	*atomic number*
Zr	*zirconium*

16 List of Figures

17 Appendix

17.1 Matlab code - EELS Spike Removal

This code was used to remove very high intensity artefact pixels.

```
    % adapted by angie
        function this = removeSpikesAdapted(this, factor,
wholespectrum,threshold)

            if nargin < 2, factor = 100; end
            if nargin < 3, wholespectrum=0; end
            if nargin < 4, threshold=200; end
            %find energy index
            for ii = 1:this.n_dims
                if isa(this.dimensions{ii},'EnergyDimension')
                    energyDimIndex = ii;
                end
            end

            se=this.datasize(energyDimIndex);
            cProjection1 = this.getAllProjections(1);
            scp=size(cProjection1);
            %sp=size(cProjection1,3);
            if ~wholespectrum
                mask=zeros(scp(1),scp(2),scp(3),se);
            else
                mask=zeros(scp(1),scp(2),scp(3));
            end

            channel=[]
            count1=0;
             for ii = 1:se

                cProjections = this.getAllProjections(ii);


cProjections_m1=cat(2,cProjections(:,2:end,:),cProjections(:,end-1,:));

cProjections_p1=cat(2,cProjections(:,2,:),cProjections(:,1:end-1,:));

                refVal = (abs(cProjections_m1)+abs(cProjections_p1))/2;
                spike=(abs(cProjections) > factor*abs(refVal));
                spike(cProjections<threshold)=0;
                if ~wholespectrum
                    mask(:,:,:,ii) = spike;
                else
                    mask = mask+spike;
                end
                if any(spike(:))>0
                    channel=[channel,ii];
                    count1=count1+1;
                end
                ii
             end
```

```
                m1=mask>0;
                count=sum(m1(:))
                channel
                count1


            mind=find(mask);
            maskw=mask;
            [i1,i2,i3]=ind2sub(size(mask),mind);
%             mind=find(mask);
%             maskw=mask;
%             [i1,i2,i3,i4]=ind2sub(size(mask),mind);
%             maskw(i1,i2,i3,:)=1;
%             if wholespectrum==1, mask=maskw; end
            for ii = 1:se
                cProjections = this.getAllProjections(ii);


cProjections_m1=cat(2,cProjections(:,2:end,:),cProjections(:,end-1,:));

cProjections_p1=cat(2,cProjections(:,2,:),cProjections(:,1:end-1,:));

                refVal = (cProjections_m1+cProjections_p1)/2;

                if ~wholespectrum
                    cProjections(mask(:,:,:,ii) > 0) =
refVal(mask(:,:,:,ii) > 0);
                else
                    cProjections(m1) = refVal(m1);
                end
                this.writeAllProjections(cProjections,ii);
                ii2=ii
            end
            count
            count1
            channel
            [i1,i2,i3]
        end

 %end adapted by angie
```

17.2 Matlab Code – Absorption of X-rays in Tomography

```
% EDX Absorption in a cylindrical sample - one detector
% Angelina Orthacker
% 06.10.2015
% in nm
% for a uniform matrix
% point-like precipitate of other material

clear all
close all
%%

%input
d=1300*10^3; %distance centre of cylinder to detector in nm
```

```
a=[0:60]; %distance of sample position from centre of cylinder
%alpha=[0:89,91:269,271:360]*pi/180; %tilt angle
alpha=[1:2:359]*pi/180; %tilt angle ...the function for x has singularities
for 90° und 270°  - therefore leave out those values. These results are
obvious anyway: x(90°)=2*R; x(270°)=0.
R=60; %radius of cylinder
absC=7.96./10; % absorption coefficient in SI (=1000cm^2/g) ...see labbook
2015-10-07
density=2.699*1000; %in g/cm^3 Al:2.699; Mg:1.740; Sc:2.989; Zr:6.506
sigAtSource=1; %signal where it is formed in sample
%disD=500*10^3; %distance detector from ... in nm;

%%
b=d*cos(pi/4);

[aa, alalpha]=meshgrid(a, alpha);
alalpha_deg=alalpha.*180./pi;
alalpha2=alalpha+144*pi/180;

phi= atan(aa.*cos(alalpha)./(b-aa.*sin(alalpha)));
x=R.*sin(alalpha+phi+pi/2-asin(sin(phi).*b./R))./sin(pi/2-alalpha-phi); %
on axis
xd=x./cos(pi/4); % off axis



%xd=x./(cos(atan(disD./(a.*cos(alpha)/sin(phi)))));

xlab1={'distance of sample position','from centre of cylinder in nm'};
figure(1)
surf(aa,alalpha_deg,x)
hold on
xlabel(xlab1)
ylabel('tilt angle')
zlabel('length of X-Ray path through sample')
title('on axis');
hold off

xlab1={'distance of sample position','from centre of cylinder in nm'};
figure(1)
surf(aa,alalpha_deg,xd)
hold on
xlabel(xlab1)
ylabel('tilt angle')
zlabel('length of X-Ray path through sample')
title('off axis');
hold off

sumx=sum(x);
avdist=sumx/numel(alpha);
figure(3)
plot(a,avdist)
hold on
xlabel(xlab1)
ylabel('average path through sample over all tilt angles')
title('on axis');
hold off

sumxd=sum(xd);
avdist2=sumxd/numel(alpha);
```

```
figure(4)
plot(a,avdist2)
hold on
xlabel(xlab1)
ylabel('average path through sample over all tilt angles')
title('off axis');
hold off


%%
xm=x*10^(-9);
sig=sigAtSource.*exp(-absC.*density.*xm); %Fraction of Intensity not
absorbed -  on axis
xdm=xd*10^(-9);
sigd=sigAtSource.*exp(-absC.*density.*xdm); %Fraction of Intensity not
absorbed -  off axis



%  figure - one detector - on axis
figure(5)
surf(aa,alalpha_deg,sig)
hold on
xlabel(xlab1)
ylabel('tilt angle')
zlabel('Fraction of Intensity NOT absorbed')
title('on axis');
hold off

%  figure - one detector - off axis
figure(6)
surf(aa,alalpha_deg,sigd)
hold off
xlabel(xlab1)
ylabel('tilt angle')
zlabel('Fraction of Intensity NOT absorbed')
title('off axis');
hold off

% one detector - all angles - on axis
sumsig=sum(sig);
avabs=sumsig/numel(alpha);
ylab5={'average fraction of intensity','NOT absorbed through sample','over
all tilt angles'};
figure(7)
plot(a,avabs)
hold on
xlabel(xlab1)
ylabel(ylab5)
title('on axis');
hold off

% one detector - all angles - off axis
sumsigd=sum(sigd);
avabs=sumsigd/numel(alpha);
ylab5={'average fraction of intensity','NOT absorbed through sample','over
all tilt angles'};
figure(8)
plot(a,avabs)
hold on
xlabel(xlab1)
```

```
ylabel(ylab5)
title('off axis');
hold off

%%
% 4 detectors:  off axis Super-X conditions

phi2= atan(aa.*cos(alalpha2)./(b-aa.*sin(alalpha2)));
x2=R.*sin(alalpha2+phi2+pi/2-asin(sin(phi2).*b./R))./sin(pi/2-alalpha2-
phi2);
xd2=x2./cos(pi/4);

xdm2=xd2*10^(-9);
sigd2=sigAtSource.*exp(-absC.*density.*xdm2);


sumsigd12=sum(sigd)+sum(sigd2);
avabs12=sumsigd12/(2*numel(alpha));
ylab5={'average fraction of intensity','NOT absorbed through sample','over
all tilt angles and DETECTORS'};
figure(9)
plot(a,avabs12)
hold on
xlabel(xlab1)
ylabel(ylab5)
title('superX');
hold off


sumsigd2=sum(sigd2);
avabs2=sumsigd2/(numel(alpha));
ylab5={'average fraction of intensity','NOT absorbed through sample','over
all tilt angles; det2'};
figure(10)
plot(a,avabs2)
hold on
xlabel(xlab1)
ylabel(ylab5)
title('det2');
hold off

sumxd2=sum(xd2);
avdist2=sumxd2/numel(alpha);
figure(11)
plot(a,avdist2)
hold on
xlabel(xlab1)
ylabel('average path through sample over all tilt angles')
title('on axis');
hold off
```

17.3 Matlab Code - Mustem Unit Cell Creator

```
% author: Angelina Orthacker
% creates cell suitable for muSTEM from xyz file exported from crystal
% maker
% unit cell must contain atomos at relative coordinates 1 in all directions
% (not primitive unit cell!)
```

```
% TO DO before running code:
%open xyz file
%delete the first two lines (# of atoms; blank line)
%save as txt file

clear all
close all

%% input
%Please choose the number of parameters to your needs
stochiometry=[3,1]; %e.g.[3,1] for Al3Sc %must be in the same order as the
atom types in txt file
resize_option='tile'; %'tile' or 'none' ...depending on whether you would
like to tile your unit cell, or not
tiling=[1,3,5]; %choose how you would like to tile your unit cell [x,y,z]
fid=fopen('E:\Projects\line_av\Al3Sc_2.txt'); %choose your text file with
atom types and coordinates
% end input

%% relative coordinates and eliminating extra atoms
A=fscanf(fid,['%*s', '%f', '%f', '%f']);
fclose(fid);

num_at=length(A)./3;
a=reshape(A,3,num_at)';

offset=min(a, [],1);
max_a=max(a, [],1);
diff_a=max_a-offset;
%diff_a=max_a;
o2=repmat(offset,[num_at,1]);
a2=a-o2;
diff_a2=repmat(diff_a,[num_at,1]);
a_rel=a2./diff_a2;
[row,col]=find(a_rel==1);
boarder_at=unique(row);
na=[1:num_at]';
na2=na;
for k=1:numel(boarder_at)
na2=na2(na2~=boarder_at(k));
end
afinal=a_rel(na2,:);
afinal=double(afinal);

cell_size_notiling=diff_a
laf=size(afinal,1);
sum_st=sum(stochiometry);
num_primcell=laf./sum_st;
num_attypes=stochiometry.*num_primcell;
lat=length(num_attypes);

        depths_notiling=unique(afinal(:,3))
        number_of_depths_notiling=numel(depths_notiling)

        cs_at=cumsum(num_attypes);
        at_beg1=[1,cs_at+1];
        at_beg=at_beg1(1:end-1);

        disp('Relative coordinates of atoms soted by atom types; Element1 =
el1; Element2 = el2...')
```

```
        lat_st=num2str(lat);
       switch lat_st
           case '1'
               el1=a_final
           case '2'
               el1=afinal(at_beg(1):cs_at(1),:)
               el2=afinal(at_beg(2):cs_at(2),:)
           case '3'
               el1=afinal(at_beg(1):cs_at(1),:)
               el2=afinal(at_beg(2):cs_at(2),:)
               el3=afinal(at_beg(3):cs_at(3),:)
           case '4'
               el1=afinal(at_beg(1):cs_at(1),:)
               el2=afinal(at_beg(2):cs_at(2),:)
               el3=afinal(at_beg(3):cs_at(3),:)
               el4=afinal(at_beg(4):cs_at(4),:)
           case '5'
               el1=afinal(at_beg(1):cs_at(1),:)
               el2=afinal(at_beg(2):cs_at(2),:)
               el3=afinal(at_beg(3):cs_at(3),:)
               el4=afinal(at_beg(4):cs_at(4),:)
               el5=afinal(at_beg(5):cs_at(5),:)
           case '6'
               el1=afinal(at_beg(1):cs_at(1),:)
               el2=afinal(at_beg(2):cs_at(2),:)
               el3=afinal(at_beg(3):cs_at(3),:)
               el4=afinal(at_beg(4):cs_at(4),:)
               el5=afinal(at_beg(5):cs_at(5),:)
               el6=afinal(at_beg(6):cs_at(6),:)
           otherwise
               disp('Error. Too many atom types. Please create new case in
switch lat_st.')
       end

%% tiling in x y z
switch resize_option
    case 'none'
    case 'tile'
        pt=prod(tiling);
        num_perattype_tiling=num_attypes.*pt
        at_sort=nan(laf,1);
        for k=1:lat
            ind1=at_beg(k);
            ind2=cs_at(k);
            at_sort(ind1:ind2)=k;
        end

        ax=repmat(afinal,tiling(1),1);
        for k=1:tiling(1)
            ind1t=(k-1).*laf+1;
            ind2t=k.*laf;
            ax(ind1t:ind2t,1)=ax(ind1t:ind2t,1)+k-1;
        end
        lax=size(ax,1);
        axy=repmat(ax,tiling(2),1);
        for k=1:tiling(2)
            ind1t=(k-1).*lax+1;
            ind2t=k.*lax;
            axy(ind1t:ind2t,2)=axy(ind1t:ind2t,2)+k-1;
        end
```

```
        laxy=size(axy,1);
        axyz=repmat(axy,tiling(3),1);
         for k=1:tiling(3)
            ind1t=(k-1).*laxy+1;
            ind2t=k.*laxy;
            axyz(ind1t:ind2t,3)=axyz(ind1t:ind2t,3)+k-1;
        end
        laxyz=size(axyz,1);

        tile_rep=repmat(tiling,laxyz,1);
        axyz_rel=axyz./tile_rep;
        axyz_rel=double(axyz_rel);

        depths=unique(axyz_rel(:,3))
        number_of_depths=numel(depths)

        cell_size_tiling=diff_a.*tiling %in Angstroems

        asx=repmat(at_sort,tiling(1),1);
        asxy=repmat(asx,tiling(2),1);
        asxyz=repmat(asxy,tiling(3),1);

        disp('Relative coordinates of atoms of tiled unit cell soted by
atom types; Element1 = elt1; Element2 = elt2...')
        lat_st=num2str(lat);
      switch lat_st
          case '1'
              el1t=axyz_rel
          case '2'
              el1t=axyz_rel(asxyz==1,:)
              el2t=axyz_rel(asxyz==2,:)
          case '3'
              el1t=axyz_rel(asxyz==1,:)
              el2t=axyz_rel(asxyz==2,:)
              el3t=axyz_rel(asxyz==3,:)
          case '4'
              el1t=axyz_rel(asxyz==1,:)
              el2t=axyz_rel(asxyz==2,:)
              el3t=axyz_rel(asxyz==3,:)
              el4t=axyz_rel(asxyz==4,:)
          case '5'
              el1t=axyz_rel(asxyz==1,:)
              el2t=axyz_rel(asxyz==2,:)
              el3t=axyz_rel(asxyz==3,:)
              el4t=axyz_rel(asxyz==4,:)
              el5t=axyz_rel(asxyz==5,:)
          case '6'
              el1t=axyz_rel(asxyz==1,:)
              el2t=axyz_rel(asxyz==2,:)
              el3t=axyz_rel(asxyz==3,:)
              el4t=axyz_rel(asxyz==4,:)
              el5t=axyz_rel(asxyz==5,:)
              el6t=axyz_rel(asxyz==6,:)
          otherwise
              disp('Error. Too many atom types. Please create new case in
switch lat_st.')
      end

end
```

```
disp('To exchange atoms copy atom coordinates from one atom type to another
in the crystal file.')
disp('To create vacancies delete atoms in the crystal file.')
disp('To create interstitial atoms, add coordinates of that atom to the
crystal file.')

% 1)Copy the values of the positions of the atoms into the crystal file.
% Make sure you assign them to the correct atom type. The sequence is the
% same as in the input file.
% 2)to check your unit cell: check whether final composition is the
materials
% composition. If the unit cell is defined wrong the code will probably
% crash at "num_primcell". So if code crashes there: check your unit
% cell!!! It's probably not a unit cell.
```

17.4 Matlab Code – The Effective Z

```
%calculates an effective Z for AlMgScZr at different conditions and
%thicknesses
%angelina orthacker
%30.06.2014

%Assumptions:
% particle is complete and perfectly spherical
% matrix is pure (no Sc, no Zr) ...otherwise change Sc_m and Zr_m;
% particle has a composition of Al3ScxZr(1-x) with x<1
% Z_eff is calculated for the one particle with a specific diameter for
% different distances from the centre of the particle
% all the Mg is equally dissolved in the Matrix - can be changed by
% changing Mg

clear all
close all

%Sc to Zr ratio in particle
Sc2Zr=15;
ratioScZr_core=11.31;
ratioScZr_shell=9.25;
dp=50; %diameter of particle
dstep=0.25;
powZ=2;

%Composition in at%:
Al=0.9548;
Mg=0.04;
Sc=0.004;
Zr=0.0012;

%matrix pure
Al_m=Al/(Al+Mg);
Mg_m=Mg/(Al+Mg);
Sc_m=0;
Zr_m=0;


%f...atomic fraction
Z=[12;13;21;40]; % Z of Mg, Al, Sc, Zr

%% % strictly for Al3Sc
```

```
fpSc=[0;3;1;0]; % particle with Sc only - no Zr
f=fpSc;
f=(f./sum(f)).';
fpSc=f;

Zeff=@(Z,f)(f*Z.^powZ).^(1/powZ);
%Zeff=@(Z,f)(f*Z.^1.3)./((f*Z.^0.3));

%% for any Sc/Zr ratio

ratioScZr=Sc2Zr;
fSc=ratioScZr/(ratioScZr+1);
fZr=1/(ratioScZr+1);

f=[0;3;fSc;fZr];
f=(f./sum(f)).';
f_rat=f;

Zc=Zeff(Z,f)


%% core shell
%ratio core
ratioScZr=ratioScZr_core;
fSc=ratioScZr/(ratioScZr+1);
fZr=1/(ratioScZr+1);

f=[0;3;fSc;fZr];
f=(f./sum(f)).';

Zc=Zeff(Z,f)

%ratio shell
ratioScZr=ratioScZr_shell;
fSc=ratioScZr/(ratioScZr+1);
fZr=1/(ratioScZr+1);

f=[0;3;fSc;fZr];
f=(f./sum(f)).';

Zs=Zeff(Z,f)

%difference core shell
diff_cs_abs=Zc-Zs;
diff_cs_rel=(Zc-Zs)/Zc;

%% with matrix
fp=f_rat;
fm=[Mg_m,Al_m,Sc_m,Zr_m];

rp=dp./2;
r_vec=[0:dstep:rp];
d_vec=2.*sqrt(rp.^2-r_vec.^2);
t_final=[];
%t_final2=t_final;
Z_final=[];
Z_final2=Z_final;
max_t=200; %in nm
step=10; %in nm ...for t
```

```
for n=1:numel(d_vec)
d=d_vec(n);
min_t=dp; %in nm
t=[min_t:step:max_t].'; %thickness in nm

[fmfm,tt]=meshgrid(fm,t);
dd=d.*ones(size(tt));
fpfp=repmat(fp,length(t),1);
f=(fpfp.*dd+fmfm.*(tt-d))./tt; %right size...;
Z_pinm=Zeff(Z,f);

%t_final2=[t_final2,t]
Z_final2=[Z_final2,Z_pinm]
t_final=[t_final;t];
Z_final=[Z_final;Z_pinm];
end

% Z_finalb=Z_final2.';
% Z_finalb2=Z_finalb(:);
% r_vec2=repmat(r_vec',1,numel(t)););
% r_vecb2=r_vec2(:);

figure
plot(t_final,Z_final,'.')
xlabel('thickness in nm')
ylabel('Z_e_f_f')
title(['Al_3Sc_xZr_1_-_x with a Sc/Zr ratio of ',num2str(Sc2Zr),' in an
AlMg matrix'])


%sort for 2nd plot
Z_finalb=Z_final2.';
Z_finalb2=Z_finalb(:);
r_vec2=repmat(r_vec',1,numel(t));
r_vecb2=r_vec2(:);
%xlim([0,200]);
%ylim([12,20])

figure(2)
plot(r_vecb2,Z_finalb2,'.')
xlabel('distance from centre of particle in nm')
ylabel('Z_e_f_f')
title(['Al_3Sc_xZr_1_-_x with a Sc/Zr ratio of ',num2str(Sc2Zr),' in an
AlMg matrix','; particle size: ',num2str(dp),'nm'])
%xlim([0,200]);
%ylim([12,20])
```

17.5 Matlab Code – SIs from Masks Including Subshells

```
%SI from mask
%Angelina
%27.02.2015

clear all
close all
```

```
mask_name='E:\Projects\AlMgScZr\2014-04-14 s2_2\gatan-haadf_merged-s2_2-
ali_good_newrec_TVmin_mu2h5-labels.tif';
spectral_volume=Dataset.load('E:\Projects\AlMgScZr\2014-04-14 s2_2\EDS SI
SIRT_rec_lambda0p2_new.h5');

%%
outputFilename1='E:\Projects\AlMgScZr\2014-04-14 s2_2\fromMasks_new\gatan-
haadf_merged-s2_2-ali_good_newrec_TVmin_mu2h5-labels_SI_1_core_2.mrc';
outputFilename2='E:\Projects\AlMgScZr\2014-04-14 s2_2\fromMasks_new\gatan-
haadf_merged-s2_2-ali_good_newrec_TVmin_mu2h5-labels_SI_2_shell_2.mrc';
outputFilename3='E:\Projects\AlMgScZr\2014-04-14 s2_2\fromMasks_new\gatan-
haadf_merged-s2_2-ali_good_newrec_TVmin_mu2h5-labels_SI_3_prec2_2.mrc';
outputFilename4='E:\Projects\AlMgScZr\2014-04-14 s2_2\fromMasks_new\gatan-
haadf_merged-s2_2-ali_good_newrec_TVmin_mu2h5-labels_SI_4_matrix_2.mrc';
%%
[mask0, mask1, mask2, mask3, mask4] = getMasksFromTif(mask_name);

%%
this=spectral_volume;
SI_1 = writeSIUsingMask_test4(this, mask1);
SI_1.writeToMrcSISeries(outputFilename1)

%%

SI_2 = writeSIUsingMask_test4(this, mask2);
SI_2.writeToMrcSISeries(outputFilename2)

SI_3 = writeSIUsingMask_test4(this, mask3);
SI_3.writeToMrcSISeries(outputFilename3)

SI_4 = writeSIUsingMask_test4(this, mask4);
SI_4.writeToMrcSISeries(outputFilename4)

disp('done')

%%




%SI from mask
%Angelina
%27.02.2015
%altered to get subshells 13-24

%mask_name='E:\Projects\AlMgScZr\2014-10-03 EBW72a500 anal\amira\FEI-HAADF-
aligned-TVmin_mu2h3_rec_noPM-labels.tif';
%spectral_volume=Dataset.load('E:\Projects\AlMgScZr\2014-10-03 EBW72a500
anal\amira\EDS SI SIRT_rec_lambda0p1.h5');
mask_name='E:\Projects\AlMgScZr\2014-04-14 s2_2\gatan-haadf_merged-s2_2-
ali_good_newrec_TVmin_mu2h5-labels.tif';
spectral_volume=Dataset.load('E:\Projects\AlMgScZr\2014-04-14 s2_2\EDS SI
SIRT_rec_lambda0p2_new.h5');

corevalue=1;%3;
shellvalue=2;%1;

%%
```

```
% outputFilename1='E:\Projects\AlMgScZr\2014-10-03 EBW72a500 anal\amira\EDS
SI SIRT_rec_lambda0p1 FEI-HAADF-aligned-TVmin_mu2h3_rec_noPM-
labels_SI_1.mrc';
% outputFilename2='E:\Projects\AlMgScZr\2014-10-03 EBW72a500 anal\amira\EDS
SI SIRT_rec_lambda0p1 FEI-HAADF-aligned-TVmin_mu2h3_rec_noPM-
labels_SI_2.mrc';
% outputFilename3='E:\Projects\AlMgScZr\2014-10-03 EBW72a500 anal\amira\EDS
SI SIRT_rec_lambda0p1 FEI-HAADF-aligned-TVmin_mu2h3_rec_noPM-
labels_SI_3.mrc';
%
% outputFilenameS1='E:\Projects\AlMgScZr\2014-04-14 s2_2\EDS SI
SIRT_rec_lambda0p2_new_SI_S1.mrc';
% outputFilenameS2='E:\Projects\AlMgScZr\2014-04-14 s2_2\EDS SI
SIRT_rec_lambda0p2_new_SI_S2.mrc';
% outputFilenameS3='E:\Projects\AlMgScZr\2014-04-14 s2_2\EDS SI
SIRT_rec_lambda0p2_new_SI_S3.mrc';
% outputFilenameS4='E:\Projects\AlMgScZr\2014-04-14 s2_2\EDS SI
SIRT_rec_lambda0p2_new_SI_S4.mrc';
% outputFilenameS5='E:\Projects\AlMgScZr\2014-04-14 s2_2\EDS SI
SIRT_rec_lambda0p2_new_SI_S5.mrc';
% outputFilenameS6='E:\Projects\AlMgScZr\2014-04-14 s2_2\EDS SI
SIRT_rec_lambda0p2_new_SI_S6.mrc';
% outputFilenameS7='E:\Projects\AlMgScZr\2014-04-14 s2_2\EDS SI
SIRT_rec_lambda0p2_new_SI_S7.mrc';
% outputFilenameS8='E:\Projects\AlMgScZr\2014-04-14 s2_2\s2_2 subshells
correct\EDS SI SIRT_rec_lambda0p2_new_SI_S8.mrc';
% outputFilenameS9='E:\Projects\AlMgScZr\2014-04-14 s2_2\EDS SI
SIRT_rec_lambda0p2_new_SI_S9.mrc';
% outputFilenameS10='E:\Projects\AlMgScZr\2014-04-14 s2_2\EDS SI
SIRT_rec_lambda0p2_new_SI_S10.mrc';
% outputFilenameS11='E:\Projects\AlMgScZr\2014-04-14 s2_2\EDS SI
SIRT_rec_lambda0p2_new_SI_S11.mrc';
% outputFilenameS12='E:\Projects\AlMgScZr\2014-04-14 s2_2\EDS SI
SIRT_rec_lambda0p2_new_SI_S12.mrc';

% BEGIN use these filenames  for getting subshells 13-24. uncomment other
filenames above and also uncomment part (is described/marked in function)
in "getmultishellMasksFromTif"
outputFilenameS1='E:\Projects\AlMgScZr\2014-04-14 s2_2\EDS SI
SIRT_rec_lambda0p2_new_SI_S13.mrc';
outputFilenameS2='E:\Projects\AlMgScZr\2014-04-14 s2_2\EDS SI
SIRT_rec_lambda0p2_new_SI_S14.mrc';
outputFilenameS3='E:\Projects\AlMgScZr\2014-04-14 s2_2\EDS SI
SIRT_rec_lambda0p2_new_SI_S15.mrc';
outputFilenameS4='E:\Projects\AlMgScZr\2014-04-14 s2_2\EDS SI
SIRT_rec_lambda0p2_new_SI_S16.mrc';
outputFilenameS5='E:\Projects\AlMgScZr\2014-04-14 s2_2\EDS SI
SIRT_rec_lambda0p2_new_SI_S17.mrc';
outputFilenameS6='E:\Projects\AlMgScZr\2014-04-14 s2_2\EDS SI
SIRT_rec_lambda0p2_new_SI_S18.mrc';
outputFilenameS7='E:\Projects\AlMgScZr\2014-04-14 s2_2\EDS SI
SIRT_rec_lambda0p2_new_SI_S19.mrc';
outputFilenameS8='E:\Projects\AlMgScZr\2014-04-14 s2_2\EDS SI
SIRT_rec_lambda0p2_new_SI_S20.mrc';
outputFilenameS9='E:\Projects\AlMgScZr\2014-04-14 s2_2\EDS SI
SIRT_rec_lambda0p2_new_SI_S21.mrc';
outputFilenameS10='E:\Projects\AlMgScZr\2014-04-14 s2_2\EDS SI
SIRT_rec_lambda0p2_new_SI_S22.mrc';
outputFilenameS11='E:\Projects\AlMgScZr\2014-04-14 s2_2\EDS SI
SIRT_rec_lambda0p2_new_SI_S23.mrc';
outputFilenameS12='E:\Projects\AlMgScZr\2014-04-14 s2_2\EDS SI
SIRT_rec_lambda0p2_new_SI_S24.mrc';
```

```
% END use these filenames  for getting subshells 13-24.
%%
%[mask0, mask1, mask2, mask3] = getMasksFromTif(mask_name);
[mask0, mask1, mask2, mask3, shell1, shell2, shell3, shell4, shell5,
shell6, shell7, shell8, shell9, shell10, shell11, shell12] =
getmultishellMasksFromTif(mask_name, corevalue, shellvalue, 1, 12);

%%
this=spectral_volume;
% SI_1 = writeSIUsingMask_test2(this, mask1);
% SI_1.writeToMrcSISeries(outputFilename1);
%
% % SI_2 = writeSIUsingMask_test2(this, mask2);
% % SI_2.writeToMrcSISeries(outputFilename2);
%
% SI_3 = writeSIUsingMask_test2(this, mask3);
% SI_3.writeToMrcSISeries(outputFilename3);


SI_S1 = writeSIUsingMask_test2(this, shell1);
SI_S1.writeToMrcSISeries(outputFilenameS1)


SI_S2 = writeSIUsingMask_test2(this, shell2);
SI_S2.writeToMrcSISeries(outputFilenameS2)

SI_S3 = writeSIUsingMask_test2(this, shell3);
SI_S3.writeToMrcSISeries(outputFilenameS3)

SI_S4 = writeSIUsingMask_test2(this, shell4);
SI_S4.writeToMrcSISeries(outputFilenameS4)

SI_S5 = writeSIUsingMask_test2(this, shell5);
SI_S5.writeToMrcSISeries(outputFilenameS5)

SI_S6 = writeSIUsingMask_test2(this, shell6);
SI_S6.writeToMrcSISeries(outputFilenameS6)

SI_S7 = writeSIUsingMask_test2(this, shell7);
SI_S7.writeToMrcSISeries(outputFilenameS7)

SI_S8 = writeSIUsingMask_test2(this, shell8);
SI_S8.writeToMrcSISeries(outputFilenameS8)

SI_S9 = writeSIUsingMask_test2(this, shell9);
SI_S9.writeToMrcSISeries(outputFilenameS9)

SI_S10 = writeSIUsingMask_test2(this, shell10);
SI_S10.writeToMrcSISeries(outputFilenameS10)

SI_S11 = writeSIUsingMask_test2(this, shell11);
SI_S11.writeToMrcSISeries(outputFilenameS11)

SI_S12 = writeSIUsingMask_test2(this, shell12);
SI_S12.writeToMrcSISeries(outputFilenameS12)

% SI_2 = writeSIUsingMask_test2(this, mask2);
% SI_2.writeToMrcSISeries(outputFilename2);
```

```
disp('done')

%%
%SI_1.writeToMrcSISeries(outputFilename1)
%SI_2.writeToMrcSISeries(outputFilename2)
%SI_3.writeToMrcSISeries(outputFilename3)
```

17.6 Matlab Codes - 2D Diffusion Simulation

```
%Diffusion Simulation 2D
%Angelina Orthacker
%23.02.2016

%This program calculates the diffusion in a precipitate-matrix system in
%2D via Fick's second law.
%The chemical potential is calulated as the derivative of the Gibbs energy
%of the system .
%Originally an Al3(Al,Sc,Zr)precipitate and Al as matrix material.

clear all
close all

%parameters to set
ncx=25; %number of cells
ncy=ncx;
dx=4.101*10^(-10); %cell_size in nm
dy=dx;
Tc=500; %temperature in °C
T=Tc+273.15; %temperature in K
c_crit=0.25;%critical (Sc+Zr)concentration for diffusion via 6-jump cyles
n_timesteps=6000000;%number of timesteps
dt=3*10^(-9); %timestep
x=dx.*(1:ncx);
y=dy.*(1:ncy); %distance from centre of precipitate
A=0.1; %parameter for Gibbs Energy
B=-A./(2*log(1/3)); %parameter for Gibbs Energy - chosen so that the Gibbs
energy has a minimum for Al3(Sc,Zr)
perc10=n_timesteps/100; %10 percent of timesteps for showing progress in
loop
Cmin=1e-5; % minimum concentration (of Sc or Zr) in matrix - because of
problems with the chemical potential for c=0
dc_max=0.4;
c_Schranke=1e-5;
t_now=0;
dt_max=1;
r=11;
cSc_prec=0.159;
cZr_prec=0.0001;
cSc_matrix=0.001;
cZr_matrix=0.001;
t_final_max=1000;

% diffusivity - constants
EaScAl=1.79; %activation energy for diffusion of Sc in matrix
EaZrAl=2.51; %activation energy for diffusion of Zr in matrix
EaScL12_a=6.34; %activation energy for diffusion of Sc in L12 alpha-type
vacancies
EaScL12_b=5.62; %activation energy for diffusion of Sc in L12 beta-type
vacancies
```

```
EaZrL12_a=5.51; %activation energy for diffusion of Zr in L12 alpha-type
vacancies
EaZrL12_b=5.26; %activation energy for diffusion of Zr in L12 beta-type
vacancies
D0Sc=5.31*10^(-4); % diffusion constant Sc in Al
D0Zr=728*10^(-4); % diffusion constant Zr in Al

kB=8.617332478*10^(-5); %in eV/K
R=8.314; % gas constant

%predefinition
dt_final=nan(1,n_timesteps);

EaSc=ones(ncy,ncx)*EaScAl;
EaZr=ones(ncy,ncx)*EaZrAl;

cZr=zeros(ncy,ncx)+Cmin+0.01;
cSc=zeros(ncy,ncx)+Cmin+0.05;
mu=zeros(ncy,ncx);

JxZr=zeros(size(cZr,1),size(cZr,2)+1);
JxSc=JxZr;
JyZr=zeros(size(cZr,1)+1,size(cZr,2));
JySc=JyZr;

% initial concentrations
cZr(1:end,1:end)=cZr_matrix;%.*rand(1,nc/2);
cSc(1:end,1:end)=cSc_matrix;%.*rand(1,nc/2);randomisation for more realstic
initial conditions



rx_max=round((ncx-1)./2);
mx1=[-rx_max:rx_max];
ry_max=(ncy-1)./2;
my1=[-ry_max:ry_max];
[mx_mesh,my_mesh]=meshgrid(mx1,my1);
mask_in=(mx_mesh.^2+my_mesh.^2)<=r.^2;
cSc(mask_in)=cSc_prec;
cZr(mask_in)=cZr_prec;

cSc_initial=cSc; %for figure
cZr_initial=cZr; %for figure


c_min_in=cSc_initial+cZr_initial;

figure(3)
surf(c_min_in)



%% calculation of Gibbs free energy for system
n_perc=101;
n_steps=200;

g_mix=zeros(n_steps+1,n_perc);
g_sep=g_mix;
g_diff=g_mix;
```

```
for k=1:n_perc
pZr=(k-1)*100/(n_perc-1);

[G_Zr_plus_Sc_a,G_matrix_and_prec_a]=main_routine(pZr,n_steps);

g_mix(:,k)=G_Zr_plus_Sc_a;
g_sep(:,k)=G_matrix_and_prec_a;

diff_G=G_matrix_and_prec_a-G_Zr_plus_Sc_a;
g_diff(:,k)=diff_G;

G_Zr_plus_Sc_a_eV=G_Zr_plus_Sc_a./1000; %in eV
G_matrix_and_prec_a_eV=G_matrix_and_prec_a./1000; %in eV

end

max_sum=1;
dc=max_sum./n_steps;
dZr=1/n_perc;
[mu_g, dummy]=numdiff1_xy(g_mix,dc,dZr);


%%
figure(1)
%for iter=1:10
for t=1:n_timesteps


    cmin=cZr+cSc; %concentration of Sc + Zr


    %finding correct activation energy depending on concentration
    %choosing type of vacancy randomly in case of L12 structure
    if rand(1)<0.5, EaScL12=EaScL12_a; else EaScL12=EaScL12_b; end
    if rand(1)<0.5, EaZrL12=EaZrL12_a; else EaZrL12=EaZrL12_b; end

    EaSc(cmin>=c_crit)=EaScL12;
    EaSc(cmin<=c_crit)=EaScAl;
    EaZr(cmin>=c_crit)=EaZrL12;
    EaZr(cmin<=c_crit)=EaZrAl;

    %diffusion coefficient
    DSc=D0Sc*exp(-EaSc./(kB*T));
    DZr=D0Zr*exp(-EaZr./(kB*T));


    %determination of flux
    [DSc_avx,DSc_avy]=average(DSc);
    [DZr_avx,DZr_avy]=average(DZr);

    [cSc_avx,cSc_avy]=average(cSc);
    [cZr_avx,cZr_avy]=average(cZr);

    cmin2=cmin;
    cmin2(cmin2>=0.25)=0.25;
    cZr2=cZr;
    cZr2(cZr2>=cmin)=cmin(cZr2>=cmin);
```

```
    i_mu_sum=round(cmin2.*(n_steps-1)./0.25+1);
    i_mu_sum(i_mu_sum>=n_steps+1)=n_steps+1;
    i_mu_sum(i_mu_sum<1)=1;
    i_mu_zr=round(cZr2./cmin.*(n_perc)+1);
    i_mu_zr(i_mu_zr>=n_perc-1)=n_perc-1;
    i_mu_zr(i_mu_zr<1)=1;
    for l=1:ncx
        for m=1:ncy
    mu(l,m)=mu_g(i_mu_sum(l,m),i_mu_zr(l,m));

        end
    end
   [mu1diffx,mu1diffy]=numdiff1_xy(mu,dx,dy);


            JScx_calc=-1./(R.*T).*DSc_avx.*cSc_avx.*mu1diffx;
            JZrx_calc=-1./(R.*T).*DZr_avx.*cZr_avx.*mu1diffx;
            JxSc(:,2:end-1)=JScx_calc;
            JxZr(:,2:end-1)=JZrx_calc;

            JScy_calc=-1./(R.*T).*DSc_avy.*cSc_avy.*mu1diffy;
            JZry_calc=-1./(R.*T).*DZr_avy.*cZr_avy.*mu1diffy;
            JySc(2:end-1,:)=JScy_calc;
            JyZr(2:end-1,:)=JZry_calc;


%% making sure there are no negative concentrations by making sure no
material can flow out of cells, if the concentration of the respective
element is below a critical concentration (c_Schranke)
            clSc=cSc<c_Schranke;

            cx_posSc=[zeros(ncy,1),clSc];
            cx_negSc=[clSc,zeros(ncy,1)];
            Jx_negSc=JxSc<0;
            Jx_posSc=JxSc>0;
            maskJx_posSc=1-cx_posSc.*Jx_posSc;
            maskJx_negSc=1-cx_negSc.*Jx_negSc;
            JxSc=JxSc.*maskJx_posSc.*maskJx_negSc;


            cy_posSc=[zeros(1,ncx);clSc];
            cy_negSc=[clSc;zeros(1,ncx)];
            Jy_negSc=JySc<0;
            Jy_posSc=JySc>0;
            maskJy_posSc=1-cy_posSc.*Jy_posSc;
            maskJy_negSc=1-cy_negSc.*Jy_negSc;
            JySc=JySc.*maskJy_posSc.*maskJy_negSc;


            clZr=cZr<c_Schranke;

            cx_posZr=[zeros(ncy,1),clZr];
            cx_negZr=[clZr,zeros(ncy,1)];
            Jx_negZr=JxZr<0;
            Jx_posZr=JxZr>0;
            maskJx_posZr=1-cx_posZr.*Jx_posZr;
            maskJx_negZr=1-cx_negZr.*Jx_negZr;
            JxZr=JxZr.*maskJx_posZr.*maskJx_negZr;
```

```
            cy_posZr=[zeros(1,ncx);clZr];
            cy_negZr=[clZr;zeros(1,ncx)];
            Jy_negZr=JyZr<0;
            Jy_posZr=JyZr>0;
            maskJy_posZr=1-cy_posZr.*Jy_posZr;
            maskJy_negZr=1-cy_negZr.*Jy_negZr;
            JyZr=JyZr.*maskJy_posZr.*maskJy_negZr;

            %% finding an ideal timestep dt

            [JxSc1diffx,JxSc1diffy]=numdiff1_xy(JxSc,dx,dy);
            [JxZr1diffx,JxZr1diffy]=numdiff1_xy(JxZr,dx,dy);

            [JySc1diffx,JySc1diffy]=numdiff1_xy(JySc,dx,dy);
            [JyZr1diffx,JyZr1diffy]=numdiff1_xy(JyZr,dx,dy);



            dcdtSc=JxSc1diffx+JySc1diffy;
            dcdtZr=JxZr1diffx+JyZr1diffy;

            critSc_mat=dcdtSc./cSc;
            critZr_mat=dcdtZr./cZr;

            critSc=max(max(abs(critSc_mat)));
            critZr=max(max(abs(critZr_mat)));
            crit=max([critSc,critZr]);

            dt_test=dc_max/crit;

            if dt_test>dt_max, dt_test=dt_max; end


%calculating the new concentrations for "after the timestep"
            cSc_tplus1=cSc-dt_test.*dcdtSc;
            cZr_tplus1=cZr-dt_test.*dcdtZr;

            cSc=cSc_tplus1;
            cZr=cZr_tplus1;

    cmin=cSc+cZr;
    t_now=t_now+dt_test;
    %disp(t_now);
    % for showing progress in the loop
    if mod(t,perc10)==0, disp(t); disp(t_now); end
    if mod(t,perc10)==0, surf(cmin); drawnow; end
   % if mod(t,perc10)==0, surf(cSc); drawnow; end
   dt_final(t)=dt_test;

   if t_now>=t_final_max, t=n_timesteps; end

end

%t_final=cumsum(dt_final);


%display results in figures
```

```
figure(2)
plot(1:n_timesteps,dt_final)

cSc_r=real(cSc);
cZr_r=real(cZr);

t_final=cumsum(dt_final);
%%
figure(4)
imagesc(cmin,[0 0.25]);
hold on
colorbar;
axis equal tight
title(['t = ',num2str(t_now);])
hold off


figure(5)
imagesc(c_min_in,[0 0.25]);
colorbar;
axis equal tight
title('t = 0')
```

This diffusion simulation makes use of several subroutines, which are not standard Matlab functions but were written by people involved in the project - either me, or Bernhard Sonderegger. To allow the reader to completely follow this simulation all of the subroutines will be part of the attachment, not only the ones I was an author of. I will clearly state if certain routines were not written by me. Thus, if not further commented, the routine or function was written by myself. However, even if written by myself I must mention, that I enjoyed great support and guidance by Bernhard Sonderegger through the whole process of setting up the diffusion simulation.

The chemical potential was calculated from the derivative of the Gibbs free energy of the system, which was calculated from a function written by Bernhard Sonderegger called “main_routine.m” This function, however was not only used as a subroutine for the diffusion simulation, but was also used to calculate the Gibbs energy of the system. It was an essential routine, as it revealed the negative curvature of the Gibbs energy of the $Al_3(Al,Sc,Zr)$ system, and thus represented the theoretical confirmation of the spinodal behavior suspected from STEM investigations.

```
function
[H_Zr_plus_Sc,H_matrix_and_prec,S_Zr_plus_Sc,G_Zr_plus_Sc,G_matrix_and_prec
]=main_routine(pZr, n_steps);

T=773; % Temperature in K
[eps_1,eps_2]=initialise_energies(T); % accesses list of 1st and 2nd nearest
neighbour energies

 % predefinitions of variables
H_Zr_plus_Sc=zeros(n_steps+1,1);
S_Zr_plus_Sc=zeros(n_steps+1,1);
G_Zr_plus_Sc=zeros(n_steps+1,1);
G_matrix_and_prec=zeros(n_steps+1,1);

% Example: Zr:Sc is 1:10, together: 15-25at%
% Rest is aluminium

% fractions
```

```
% this section was altered by Angelina
% pZr=50; % percentage Zr of Sc+Zr
frZr=pZr/100; % fraction Zr of Sc+Zr
frSc=1-frZr;
%end alterations Angelina

% this loop calculates the enthalpy, entropy and Gibbs energy of
Al3(Al,Sc,Zr)for different concentrations
for n=1:n_steps+1
    Zr_plus_Sc=(n-1)./n_steps.*100; % in at%
    c_Zr=Zr_plus_Sc/100.*frZr;
    c_Sc=Zr_plus_Sc/100.*frSc;
    c_Va=0;
    [x_SL1,x_SL2,x_SL3]=fill_2SL_anyAl(c_Zr,c_Sc,c_Va); %occupies the
sublattices
    H=calc_enthalpy_3SL(x_SL1,x_SL2,x_SL3,eps_1,eps_2); %calculates the
according enthalpy
    H_Zr_plus_Sc(n)=H;
    S=angie_entropy(x_SL1,x_SL2,x_SL3);
    S_Zr_plus_Sc(n)=S;
    G=H-T*S;
    G_Zr_plus_Sc(n)=G;

end

% comparison to Al-channels
% same loop as above, but now a separation of Al and Al3(Sc,Zr)

H_matrix_and_prec=zeros(26,1);

H_matrix=H_Zr_plus_Sc(1);
G_matrix=G_Zr_plus_Sc(1);
H_prec=H_Zr_plus_Sc(n_steps+1);
G_prec=G_Zr_plus_Sc(n_steps+1);
for n=1:n_steps+1
    Zr_plus_Sc=(n-1)./n_steps.*25;; % in at%
    c_Al=1-Zr_plus_Sc/100;
    f_matrix=4*c_Al-3;
    f_prec=1-f_matrix;
    H_matrix_and_prec(n)=f_matrix*H_matrix+f_prec*H_prec;
    G_matrix_and_prec(n)=f_matrix*G_matrix+f_prec*G_prec;
end

end
```

The main routine also uses several subroutines/ functions:
One of them is the following: “initialialise_energies”, which was also written by Bernhard Sonderegger. This function basically is a list of energies (first and second nearest neighbour energies) retrieved from literature, which can be called up by the main-routine.

```
function [eps_1,eps_2]=initialise_energies(T);

% defining interaction energies according to
% Clouet et al, Nature Materials 5 (2006) 482-488
% Energies taken from "Supplementary Information" page 26, Table S3

% eps_1 are interaction energies of 1st nearest neigbours
% eps_2 are interaction energies of 2nd nearest neigbours
```

```
% index/Code for elements:
% Al: 1
% Zr: 2
% Sc: 3
% Va: 4 (Paper says "V" but means Vacancy, so I use "Va")

% Unit for energy for now) is eV
% Unit for temperature is Kelvin


eps_1=zeros(4,4);
eps_2=zeros(4,4);

eps_1(1,1)=-560;              %Al-Al
eps_1(1,2)=-979+0.244*T;      %Al-Zr
eps_1(1,3)=-759+0.21*T;       %Al-Sc
eps_1(1,4)=-222;              %Al-Va
eps_1(2,2)=-1045;             %Zr-Zr
eps_1(2,3)=-611;              %Zr-Sc
eps_1(2,4)=-350;              %Zr-Va
eps_1(3,3)=-650;              %Sc-Sc
eps_1(3,4)=-757;              %Sc-Va
eps_1(4,4)=0;                 %Va-Va

eps_1(2,1)=eps_1(1,2);        %matrix is symmetric
eps_1(3,1)=eps_1(1,3);
eps_1(3,2)=eps_1(2,3);
eps_1(4,1)=eps_1(1,4);
eps_1(4,2)=eps_1(2,4);
eps_1(4,3)=eps_1(3,4);

eps_2(1,1)=0;                 %Al-Al
eps_2(1,2)=101-0.0233*T;      %Al-Zr
eps_2(1,3)=113-0.0334*T;      %Al-Sc
eps_2(1,4)=0;                 %Al-Va
eps_2(2,2)=0;                 %Zr-Zr
eps_2(2,3)=-2.77;             %Zr-Sc
eps_2(2,4)=0;                 %Zr-Va
eps_2(3,3)=0;                 %Sc-Sc
eps_2(3,4)=0;                 %Sc-Va
eps_2(4,4)=0;                 %Va-Va

eps_2(2,1)=eps_2(1,2);
eps_2(3,1)=eps_2(1,3);
eps_2(3,2)=eps_2(2,3);
eps_2(4,1)=eps_2(1,4);
eps_2(4,2)=eps_2(2,4);
eps_2(4,3)=eps_2(3,4);

end
```

Another subroutine used by „main_routine“ is “fill_2SL_anyAl”, which was written by Bernhard Sonderregger and me. Bernhard Sondereger wrote the routine “fill_2L”, which would fill the sublattices, but was more restrictive, e.g. only allowing Al-concentration higher than 75%. As the diffusion simulation needs to allow any Al-concentration the routine was adapted to allow and cope with any desired concentrations and in this version was renamed to “fill_2SL_anyAl”. This was realized via a switch, treating both cases (Al-concentrations above and below 75 at.%) separately.

```
function [x_SL1,x_SL2,x_SL3]=fill_2SL_anyAl(c_Zr,c_Sc,c_Va);

% now we do NOT assume c_Al>=75%
% Al: 1
% Zr: 2
% Sc: 3
% Va: 4 (Paper says "V" but means Vacancy, so I use "Va")


% fills the 3 sublattices according to the given chemical composition
% chemical composition is in at% (total)
% c denotes the concentrations in at% in the system
% x denotes the probability of an atom within a sublattice
% concentration of Aluminium is calculated so that the sum of all c is 1
% vacancies are not considered yet

%c_Va=0; %Angelina: now c_Va is part of the variables
c_Al=1-c_Zr-c_Sc-c_Va;
if c_Al>=0.75, sat=0; else sat=1; end %sat switches between the two cases
% The system consists of 3 sublattices:
% SL1: Al (now we do NOT assume c_Al>=75%)
% SL2: (Zr,Sc,Al)
% SL3: (Sc,Al) % Zr content is very small so we keep it in the 2nd SL only.

x_SL1=zeros(4,1);
x_SL2=zeros(4,1);
x_SL3=zeros(4,1);

switch sat
    case 0

x_SL1(1)=1; % completely filled with Al

% the rest of the Al is now evenly distributed on SL2 and SL3
c_Al_Rest=c_Al-0.75;
x_SL2(1)=c_Al_Rest/2*8;
x_SL3(1)=c_Al_Rest/2*8;

x_SL2(2)=c_Zr.*4;
x_SL3(2)=c_Zr.*4;

x_SL2(3)=c_Sc.*4;
x_SL3(3)=c_Sc.*4;

    case 1

c_rest=0.75-c_Al;
x_SL1(1)=c_Al./0.75; % filled with all the Al
x_SL1(2)=c_Zr.*c_rest./(0.25+c_rest)./0.75;
x_SL1(3)=c_Sc.*c_rest./(0.25+c_rest)./0.75;


x_SL2(1)=0;
x_SL3(1)=0;

x_SL2(2)=((c_Zr-x_SL1(2))./2)./0.25;
x_SL3(2)=((c_Zr-x_SL1(2))./2)./0.25;
```

```
x_SL2(3)=((c_Sc-x_SL1(3))./2)./0.25;
x_SL3(3)=((c_Sc-x_SL1(3))./2)./0.25;


end

end
```

"calc_enthalpy_3SL" was another subroutine of the "main_routine" for the calculation of the Gibbs energy. It calculates the Enthalpy and was written by Bernhard Sonderegger.

```
function H=calc_enthalpy_3SL(x_SL1,x_SL2,x_SL3,eps_1,eps_2)

% Predefinition of variables for initialising the relevant average bond
energies
eps_AA1=0;
eps_AA2=0;
eps_AB1=0;
eps_AC1=0;
eps_BC2=0;

% calculation of bond energies
for element1=1:4
    for element2=1:4

eps_AA1=eps_AA1+x_SL1(element1)*x_SL1(element2)*eps_1(element1,element2);

eps_AA2=eps_AA2+x_SL1(element1)*x_SL1(element2)*eps_2(element1,element2);

eps_AB1=eps_AB1+x_SL1(element1)*x_SL2(element2)*eps_1(element1,element2);

eps_AC1=eps_AC1+x_SL1(element1)*x_SL3(element2)*eps_1(element1,element2);

eps_BC2=eps_BC2+x_SL2(element1)*x_SL3(element2)*eps_2(element1,element2);
    end
end

% calculation of enthalpy from bond energies
H=12*eps_AA1+9*eps_AA2+3*eps_AB1+3*eps_AC1+3/2*eps_BC2;


End
```

"angie_entropy" calculates the entropy of the system, it was written in cooperation with Bernhard Sonderegger.

```
function S=angie_entropy(x_SL1,x_SL2,x_SL3)
% Entropy Angelina

kB=8.6173324e-5; %in eV
S=0;
S_UG1=0;
S_UG2=0;
S_UG3=0;

N_UG1=3;
N_UG2=0.5;
N_UG3=0.5;
```

```
for element=1:4
    x=x_SL1(element);
    if x>0
        S_UG1=S_UG1-kB*N_UG1*(x*log(x));
    end

    x=x_SL2(element);
    if x>0
        S_UG2=S_UG2-kB*N_UG2*(x*log(x));
    end

    x=x_SL3(element);
    if x>0
        S_UG3=S_UG3-kB*N_UG3*(x*log(x));
    end
end

S=S_UG1+S_UG2+S_UG3;
S=S*1000;                % Einheit: meV

end
```

At this point all the subroutines of the "main_routine" calculating the Gibbs energy have been covered. We can now continue with other subroutines accessed by the 2D diffusion simulation.
Another function used by the diffusion simulation, is a routine for numerical differentiation, called numdiff1_xy. It was written by me.

```
function [mx1diff,my1diff]=numdiff1_xy(m,dx,dy)

% Gives numerical first and second derivative in x and y of a function of
which the
% values f(x) given in the matrix
% Input parameters:
%   m... ...values f(x) of function f
%   dx... ...step size in x for derivation (delta x)
%   dy... ...step size in y for derivation (delta y)
% Output parameters:
%   mx1diff... ...first derivative of m via x
%   my1diff... ...first derivative of m via y



    mx_1=m(:,1:end-1);
    mx1=m(:,2:end);

    mx1diff=(mx1-mx_1)./dx;


    my_1=m(1:end-1,:);
    my1=m(2:end,:);

    my1diff=(my1-my_1)./dy;
```

The diffusion simulation also accesses a function called “average”, which calculates the average between two matrix elements in x- and y-direction. This function is e.g. necessary for the flux-calculation, as they have to be done at the interface between two cells.

```
function [avx, avy]=average(m);
%calculates the average between 2 neighbouring matrix elements of a 2D
%array. avx averages in x direction. avy averages in y direction.

mx1=m(:,1:end-1);
mx2=m(:,2:end);
avx=(mx1+mx2)./2;

my1=m(1:end-1,:);
my2=m(2:end,:);
avy=(my1+my2)./2;
```

```
Diffsim paper

%Diffusion Simulation 2D
%Angelina Orthacker
%23.02.2016

%This program calculates the diffusion in a precipitate-matrix system in
%2D via Fick's second law.
%The chemical potential is calulated as the derivative of the Gibbs endergy
%of the system .
%Originally Al3(Sc,Zr)-Al

clear all
close all

%parameters to set
ncx=25; %number of cells
ncy=ncx;
dx=4.101*10^(-10); %cell_size in nm
dy=dx;
Tc=500; %temperature in °C
T=Tc+273.15; %temperature in K
c_crit=0.25;%critical (Sc+Zr)concentration for diffusion via 6-jump cyles
n_timesteps=60000000;%number of timesteps
dt=3*10^(-9); %timestep
x=dx.*(1:ncx);
y=dy.*(1:ncy); %distance from centre of precipitate
A=0.1; %Parameter for Gibbs Energy
B=-A./(2*log(1/3)); %Parameter for Gibbs Energy - chosen so that the Gibbs
energy has a minimum for Al3(Sc,Zr)
perc10=n_timesteps/100; %10 percent of timesteps for showing progress in
loop
Cmin=1e-5; % minimum concentration (of Sc or Zr) in matrix - because of
problems with the chemical potential for c=0
dc_max=0.6;
c_Schranke=1e-5;
t_now=0;
dt_max=1;
r=11;
cSc_prec=0.12;
```

```
cZr_prec=0.04;
cSc_matrix=0.001;
cZr_matrix=0.0012;
t_final_max=300;
c_mat_def=0.01;
a_rand=0.0018;

% diffusivity - constants
EaScAl=1.79; %activation energy for diffusion of Sc in matrix
EaZrAl=2.51; %activation energy for diffusion of Zr in matrix
EaScL12_a=6.34; %activation energy for diffusion of Sc in L12 alpha-type
vacancies
EaScL12_b=5.62; %activation energy for diffusion of Sc in L12 beta-type
vacancies
EaZrL12_a=5.51; %activation energy for diffusion of Zr in L12 alpha-type
vacancies
EaZrL12_b=5.26; %activation energy for diffusion of Zr in L12 beta-type
vacancies
D0Sc=5.31*10^(-4); % diffusion constant Sc in Al
D0Zr=728*10^(-4); % diffusion constant Zr in Al

kB=8.617332478*10^(-5); %in eV/K
R=8.314; % gas constant

%predefinition
dt_final=nan(1,n_timesteps);

EaSc=ones(ncy,ncx)*EaScAl;
EaZr=ones(ncy,ncx)*EaZrAl;

cZr=zeros(ncy,ncx)+Cmin+0.01;
cSc=zeros(ncy,ncx)+Cmin+0.05;
mu=zeros(ncy,ncx);

JxZr=zeros(size(cZr,1),size(cZr,2)+1);
JxSc=JxZr;
JyZr=zeros(size(cZr,1)+1,size(cZr,2));
JySc=JyZr;

% initial concentrations
cZr(1:end,1:end)=cZr_matrix;%+(rand(size(cZr))-0.5).*a_rand;
cSc(1:end,1:end)=cSc_matrix;%+(rand(size(cSc))-0.5).*a_rand;

% prec_beginning=4;
% prec_end=17;
% prec_beginning2=6;
% prec_end2=15;
%
cZr(prec_beginning:prec_end,prec_beginning:prec_end)=0.04;%.*rand(1,nc/2);
%
cSc(prec_beginning:prec_end,prec_beginning:prec_end)=0.14;%.*rand(1,nc/2);
% cZr(prec_beginning2:prec_end2,prec_beginning2:prec_end2)=0.00;
% cSc(prec_beginning2:prec_end2,prec_beginning2:prec_end2)=0.18;
% cSc_initial=cSc; %for figure
% cZr_initial=cZr; %for figure

% prec_beginning=4;
% prec_end=17;
% % prec_beginning2=6;
% % prec_end2=15;
```

```
%
cZr(prec_beginning:prec_end,prec_beginning:prec_end)=0.02;%.*rand(1,nc/2);
%
cSc(prec_beginning:prec_end,prec_beginning:prec_end)=0.13;%.*rand(1,nc/2);
% % cZr(prec_beginning2:prec_end2,prec_beginning2:prec_end2)=0.00;
% % cSc(prec_beginning2:prec_end2,prec_beginning2:prec_end2)=0.18;
% cSc_initial=cSc; %for figure
% cZr_initial=cZr; %for figure

rx_max=round((ncx-1)./2);
mx1=[-rx_max:rx_max];
ry_max=(ncy-1)./2;
my1=[-ry_max:ry_max];
[mx_mesh,my_mesh]=meshgrid(mx1,my1);
mask_in=(mx_mesh.^2+my_mesh.^2)<=r.^2;
cSc(mask_in)=cSc_prec;
cZr(mask_in)=cZr_prec;

cSc=cSc+(rand(size(cSc))-0.5).*a_rand;
cZr=cZr+(rand(size(cZr))-0.5).*a_rand;

cSc_initial=cSc; %for figure
cZr_initial=cZr; %for figure


c_min_in=cSc_initial+cZr_initial;

figure(3)
surf(c_min_in)



%% calculation of gibbs free energy for system
n_perc=101;
n_steps=200;

g_mix=zeros(n_steps+1,n_perc);
g_sep=g_mix;
g_diff=g_mix;

for k=1:n_perc
pZr=(k-1)*100/(n_perc-1);

[G_Zr_plus_Sc_a,G_matrix_and_prec_a]=main_routine(pZr,n_steps);

g_mix(:,k)=G_Zr_plus_Sc_a;
g_sep(:,k)=G_matrix_and_prec_a;

diff_G=G_matrix_and_prec_a-G_Zr_plus_Sc_a;
g_diff(:,k)=diff_G;

G_Zr_plus_Sc_a_eV=G_Zr_plus_Sc_a./1000; %in eV
G_matrix_and_prec_a_eV=G_matrix_and_prec_a./1000; %in eV

end

max_sum=1;
dc=max_sum./n_steps;
dZr=1/n_perc;
```

```
[mu_g, dummy]=numdiff1_xy(g_mix,dc,dZr);


%%
figure(1)
%for iter=1:10
for t=1:n_timesteps


    cmin=cZr+cSc; %concentration of Sc + Zr


    %finding correct activation energy depending on concentration
    %choosing type of vacancy randomly in case of L12 structure
    if rand(1)<0.5, EaScL12=EaScL12_a; else EaScL12=EaScL12_b; end
    if rand(1)<0.5, EaZrL12=EaZrL12_a; else EaZrL12=EaZrL12_b; end

    EaSc(cmin>=c_crit)=EaScL12;
    EaSc(cmin<=c_crit)=EaScAl;
    EaZr(cmin>=c_crit)=EaZrL12;
    EaZr(cmin<=c_crit)=EaZrAl;

    %diffusion coefficient
    DSc=D0Sc*exp(-EaSc./(kB*T));
    DZr=D0Zr*exp(-EaZr./(kB*T));

    [DSc_avx,DSc_avy]=average(DSc);
    [DZr_avx,DZr_avy]=average(DZr);

    [cSc_avx,cSc_avy]=average(cSc);
    [cZr_avx,cZr_avy]=average(cZr);

    cmin2=cmin;
    cmin2(cmin2>=0.25)=0.25;
    cZr2=cZr;
    cZr2(cZr2>=cmin)=cmin(cZr2>=cmin);


    i_mu_sum=round(cmin2.*(n_steps-1)./0.25+1);
    i_mu_sum(i_mu_sum>=n_steps+1)=n_steps+1;
    i_mu_sum(i_mu_sum<1)=1;
    i_mu_zr=round(cZr2./cmin.*(n_perc)+1);
    i_mu_zr(i_mu_zr>=n_perc-1)=n_perc-1;
    i_mu_zr(i_mu_zr<1)=1;
    for l=1:ncx
        for m=1:ncy
    mu(l,m)=mu_g(i_mu_sum(l,m),i_mu_zr(l,m));

        end
    end
   [mu1diffx,mu1diffy]=numdiff1_xy(mu,dx,dy);
    %      mu=chem_pot(A,B,cmin); %chemical potential
%       [mu1diffx,mu1diffy]=numdiff1_xy(mu,dx,dy);


            JScx_calc=-1./(R.*T).*DSc_avx.*cSc_avx.*mu1diffx;
            JZrx_calc=-1./(R.*T).*DZr_avx.*cZr_avx.*mu1diffx;
            JxSc(:,2:end-1)=JScx_calc;
            JxZr(:,2:end-1)=JZrx_calc;
```

```
JScy_calc=-1./(R.*T).*DSc_avy.*cSc_avy.*mu1diffy;
JZry_calc=-1./(R.*T).*DZr_avy.*cZr_avy.*mu1diffy;
JySc(2:end-1,:)=JScy_calc;
JyZr(2:end-1,:)=JZry_calc;

%               for x=1:ncx
%                   for y=1:ncy
%                       if cZr(y,x)<c_Schranke
%                           if JxZr(y,x)<0,     JxZr(y,x)=0;    end
%                           if JxZr(y,x+1)>0,   JxZr(y+1,x)=0;  end
%                       end
%                       if cSc(y,x)<c_Schranke
%                           if JxSc(y,x)<0,     JxSc(y,x)=0;    end
%                           if JxSc(y,x+1)>0,   JxSc(y,x+1)=0;  end
%                       end
%
%                       if cZr(y,x)<c_Schranke
%                           if JyZr(y,x)<0,     JyZr(y,x)=0;    end
%                           if JyZr(y+1,x)>0,   JyZr(y+1,x)=0;  end
%                       end
%                       if cSc(y,x)<c_Schranke
%                           if JySc(y,x)<0,     JySc(y,x)=0;    end
%                           if JySc(y+1,x)>0,   JySc(y+1,x)=0;  end
%                       end
%                   end
%               end
%
%
%
%%
clSc=cSc<c_Schranke;

cx_posSc=[zeros(ncy,1),clSc];
cx_negSc=[clSc,zeros(ncy,1)];
Jx_negSc=JxSc<0;
Jx_posSc=JxSc>0;
maskJx_posSc=1-cx_posSc.*Jx_posSc;
maskJx_negSc=1-cx_negSc.*Jx_negSc;
JxSc=JxSc.*maskJx_posSc.*maskJx_negSc;


cy_posSc=[zeros(1,ncx);clSc];
cy_negSc=[clSc;zeros(1,ncx)];
Jy_negSc=JySc<0;
Jy_posSc=JySc>0;
maskJy_posSc=1-cy_posSc.*Jy_posSc;
maskJy_negSc=1-cy_negSc.*Jy_negSc;
JySc=JySc.*maskJy_posSc.*maskJy_negSc;


clZr=cZr<c_Schranke;

cx_posZr=[zeros(ncy,1),clZr];
cx_negZr=[clZr,zeros(ncy,1)];
Jx_negZr=JxZr<0;
Jx_posZr=JxZr>0;
maskJx_posZr=1-cx_posZr.*Jx_posZr;
maskJx_negZr=1-cx_negZr.*Jx_negZr;
JxZr=JxZr.*maskJx_posZr.*maskJx_negZr;
```

```
            cy_posZr=[zeros(1,ncx);clZr];
            cy_negZr=[clZr;zeros(1,ncx)];
            Jy_negZr=JyZr<0;
            Jy_posZr=JyZr>0;
            maskJy_posZr=1-cy_posZr.*Jy_posZr;
            maskJy_negZr=1-cy_negZr.*Jy_negZr;
            JyZr=JyZr.*maskJy_posZr.*maskJy_negZr;

            %%

            [JxSc1diffx,JxSc1diffy]=numdiff1_xy(JxSc,dx,dy);
            [JxZr1diffx,JxZr1diffy]=numdiff1_xy(JxZr,dx,dy);

            [JySc1diffx,JySc1diffy]=numdiff1_xy(JySc,dx,dy);
            [JyZr1diffx,JyZr1diffy]=numdiff1_xy(JyZr,dx,dy);



            dcdtSc=JxSc1diffx+JySc1diffy;
            dcdtZr=JxZr1diffx+JyZr1diffy;

            critSc_mat=dcdtSc./cSc;
            critZr_mat=dcdtZr./cZr;

            critSc=max(max(abs(critSc_mat)));
            critZr=max(max(abs(critZr_mat)));
            crit=max([critSc,critZr]);

            dt_test=dc_max/crit;

            if dt_test>dt_max, dt_test=dt_max; end
            %dt_test=1;

            cSc_tplus1=cSc-dt_test.*dcdtSc;
            cZr_tplus1=cZr-dt_test.*dcdtZr;

            cSc=cSc_tplus1;
            cZr=cZr_tplus1;

    cmin=cSc+cZr;
    t_now=t_now+dt_test;
    %disp(t_now);
    % for showing progress in the loop
    if mod(t,perc10)==0, disp(t); disp(t_now); end
    if mod(t,perc10)==0, surf(cmin); drawnow; end
   % if mod(t,perc10)==0, surf(cSc); drawnow; end
   dt_final(t)=dt_test;

   if t_now>=t_final_max, break; end

end

%t_final=cumsum(dt_final);

figure(2)
plot(1:n_timesteps,dt_final)
```

```
cSc_r=real(cSc);
cZr_r=real(cZr);

t_final=cumsum(dt_final);
%%
figure(4)
imagesc(cmin,[0 0.25]);
hold on
colorbar;
axis equal tight
title(['t = ',num2str(t_now);])
hold off


figure(5)
imagesc(c_min_in,[0 0.25]);
colorbar;
axis equal tight
title('t = 0')

N_channels=sum(sum((cmin<=c_mat_def)))-sum(sum((c_min_in<=c_mat_def)));
perc_channels=N_channels/sum(sum((c_min_in>=c_mat_def)))
%%

prec=cmin(mask_in);
figure(6)
hist(prec,25)

% %%
% figure(26)
% plot(1:nc,cSc,'r')
% hold on
% plot(1:nc,cSc_initial,'*')
% plot(1:nc,cZr,'g')
% plot(1:nc,cZr_initial,'x')
% hold off
%end
```

```
function list_of_dt=main_routine;

% we now set up the input data of our simulation:

size=10;        %size of the cube: there are going to be 4*size^3 atoms.
c_Al=0.75;
c_Zr=0.02;
c_Sc=0.23;      % sum of c_Al, c_Sc and c_Zr is 1. c_Va is extra.
c_Va=0.001;
T=774;          % Temperature in Kelvin
```

```
[lattice,first_NN,second_NN,list_of_Va,c_Al_real,c_Sc_real,c_Zr_real,c_Va_r
eal]=set_up_and_fill_lattice_SL4(size,c_Al,c_Sc,c_Zr,c_Va);

[e_jump,f_jump,eps_1,eps_2]=initialise_energies(T);
list_of_dt=zeros(100,1);

for timestep=1:100


[lattice,list_of_Va,dt]=diffusion_timestep(lattice,size,first_NN,second_NN,
list_of_Va,e_jump,f_jump,eps_1,eps_2,T);
    test_vacancy_positions(lattice,list_of_Va);
    list_of_dt(timestep,1)=dt;

end

end
```

The main routine also uses several subroutines/ functions:
One of them is the following: “set_up_and_fill_lattice_SL4”, which was also written by Bernhard Sonderegger.

```
function
[lattice,first_NN,second_NN,list_of_Va,c_Al_real,c_Sc_real,c_Zr_real,c_Va_r
eal]=set_up_and_fill_lattice_SL4(size,c_Al,c_Sc,c_Zr,c_Va);

% this routine is going to be similar to the general SL fill routine
% difference is that SLs1-3 are automatically filled with Al
% and SL4 with Sc and Zr
% However, vacancies are put randomly all over the place.

% this function sets up a cubis lattic of Al3(Al,Sc,Zr) structure
% at this stage, the elements are placed in random order
% the lattice is divided into 4 sublattices: Al-Al-Al-(Al,Sc,Zr)
% in addition, vacancies are put into the lattice
% the concentration of lattices is not taken into account for the general
% chemical composition
% all compositions are in atomic fracture, a number between 0 and 1
% there is going to be a random number generator involved, so there might
% be a small discrepancy between numinal and actual concentrations

% index/Code for elements:
% Al: 1
% Zr: 2
% Sc: 3
% Va: 4 (Paper says "V" but means Vacancy, so I use "Va")

% in addition, we set up a list of 1st and second nearest neighbors,
% which is going to help us calculating energies (global and local)
% and also helps us calculating potential diffusion

% structure of the matrix "lattice"
% lattice(SL_nr,x,y,z)

%structure of the lattice "first_NN" and "second_NN" see below
```

```
nr_of_Va=0;
nr_of_Al=0;
nr_of_Zr=0;
nr_of_Sc=0;


c_Al_SL4=(c_Al-0.75)*4;
c_Zr_SL4=c_Zr*4;
c_Sc_SL4=c_Sc*4;



list_of_Va=zeros(1,4);

lattice=zeros(4,size,size,size);
for SL=1:3
    for x=1:size
        for y=1:size
            for z=1:size
                if rand<c_Va
                    lattice(SL,x,y,z)=4; %we have generated a vacancy
                    nr_of_Va=nr_of_Va+1;
                    list_of_Va(nr_of_Va,:)=[SL,x,y,z];
                else

                    lattice(SL,x,y,z)=1;
                    nr_of_Al=nr_of_Al+1;

                end
            end
        end
    end
end

SL=4;
for x=1:size
    for y=1:size
        for z=1:size
            if rand<c_Va
                lattice(SL,x,y,z)=4; %we have generated a vacancy
                nr_of_Va=nr_of_Va+1;
                list_of_Va(nr_of_Va,:)=[SL,x,y,z];
            else
                r=rand;
                if r<c_Al_SL4 %we take this first since the probability is
highest
                    lattice(SL,x,y,z)=1;
                    nr_of_Al=nr_of_Al+1;
                else
                    r=r-c_Al_SL4;
                    if r<c_Zr_SL4
                        lattice(SL,x,y,z)=2;
                        nr_of_Zr=nr_of_Zr+1;
                    else
                        lattice(SL,x,y,z)=3;
                        nr_of_Sc=nr_of_Sc+1;
                    end
                end
            end
        end
```

```
    end
end

c_Va_real=nr_of_Va/(4*size^3);
c_Al_real=nr_of_Al/(nr_of_Al+nr_of_Zr+nr_of_Sc);
c_Zr_real=nr_of_Zr/(nr_of_Al+nr_of_Zr+nr_of_Sc);
c_Sc_real=nr_of_Sc/(nr_of_Al+nr_of_Zr+nr_of_Sc);

% the lattice has now been set. We now define the nearest neigbor matrices
% Format:
% first_NN(Nr(1..48),parameters(1..5))
    %Nr: number of entry
    %parameters:
        % column 1: SL of investigated atom
        % column 2: SL of neigboring atom
        % column 3-5: relative position of neigboring, using indezzes

first_NN=zeros(48,5);
first_NN(1,:)=[1,2,0,0,0];
first_NN(2,:)=[1,2,0,0,-1];
first_NN(3,:)=[1,2,0,1,0];
first_NN(4,:)=[1,2,0,1,-1];

first_NN(5,:)=[1,3,0,0,0];
first_NN(6,:)=[1,3,0,0,-1];
first_NN(7,:)=[1,3,1,0,0];
first_NN(8,:)=[1,3,1,0,-1];

first_NN(9,:)=[1,4,0,0,0];
first_NN(10,:)=[1,4,1,0,0];
first_NN(11,:)=[1,4,0,1,0];
first_NN(12,:)=[1,4,1,1,0];


first_NN(13,:)=[2,1,0,0,0];
first_NN(14,:)=[2,1,0,-1,0];
first_NN(15,:)=[2,1,0,0,1];
first_NN(16,:)=[2,1,0,-1,1];

first_NN(17,:)=[2,3,0,0,0];
first_NN(18,:)=[2,3,1,0,0];
first_NN(19,:)=[2,3,0,-1,0];
first_NN(20,:)=[2,3,1,-1,0];

first_NN(21,:)=[2,4,0,0,0];
first_NN(22,:)=[2,4,1,0,0];
first_NN(23,:)=[2,4,0,0,1];
first_NN(24,:)=[2,4,1,0,1];


first_NN(25,:)=[3,1,0,0,0];
first_NN(26,:)=[3,1,-1,0,0];
first_NN(27,:)=[3,1,0,0,1];
first_NN(28,:)=[3,1,-1,0,1];

first_NN(29,:)=[3,2,0,0,0];
first_NN(30,:)=[3,2,0,1,0];
first_NN(31,:)=[3,2,-1,0,0];
first_NN(32,:)=[3,2,-1,1,0];
```

```
first_NN(33,:)=[3,4,0,0,0];
first_NN(34,:)=[3,4,0,1,0];
first_NN(35,:)=[3,4,0,0,1];
first_NN(36,:)=[3,4,0,1,1];


first_NN(37,:)=[4,1,0,0,0];
first_NN(38,:)=[4,1,0,-1,0];
first_NN(39,:)=[4,1,-1,0,0];
first_NN(40,:)=[4,1,-1,-1,0];

first_NN(41,:)=[4,2,0,0,0];
first_NN(42,:)=[4,2,0,0,-1];
first_NN(43,:)=[4,2,-1,0,0];
first_NN(44,:)=[4,2,-1,0,-1];

first_NN(45,:)=[4,3,0,0,0];
first_NN(46,:)=[4,3,0,-1,0];
first_NN(47,:)=[4,3,0,0,-1];
first_NN(48,:)=[4,3,0,-1,-1];

second_NN=zeros(24,5);

second_NN(1,:)=[1,1,1,0,0];
second_NN(2,:)=[1,1,-1,0,0];
second_NN(3,:)=[1,1,0,1,0];
second_NN(4,:)=[1,1,0,-1,0];
second_NN(5,:)=[1,1,0,0,1];
second_NN(6,:)=[1,1,0,0,-1];

second_NN(7,:)=[2,2,1,0,0];
second_NN(8,:)=[2,2,-1,0,0];
second_NN(9,:)=[2,2,0,1,0];
second_NN(10,:)=[2,2,0,-1,0];
second_NN(11,:)=[2,2,0,0,1];
second_NN(12,:)=[2,2,0,0,-1];

second_NN(13,:)=[3,3,1,0,0];
second_NN(14,:)=[3,3,-1,0,0];
second_NN(15,:)=[3,3,0,1,0];
second_NN(16,:)=[3,3,0,-1,0];
second_NN(17,:)=[3,3,0,0,1];
second_NN(18,:)=[3,3,0,0,-1];

second_NN(19,:)=[4,4,1,0,0];
second_NN(20,:)=[4,4,-1,0,0];
second_NN(21,:)=[4,4,0,1,0];
second_NN(22,:)=[4,4,0,-1,0];
second_NN(23,:)=[4,4,0,0,1];
second_NN(24,:)=[4,4,0,0,-1];

end
```

Another one of the subroutines used by the “main_routine” is the function “initialialise_energies”, again written by Bernhard Sonderegger. This function basically is a list of energies (first and second

nearest neighbour energies and jump energies) retrieved from literature, which can be called up by the main-routine.

```
function [e_jump,f_jump,eps_1,eps_2]=initialise_energies(T);

% defining interaction energies according to
% Clouet et al, Nature Materials 5 (2006) 482-488
% Energies taken from "Supplementary Information" page 26, Table S3
% jump energies are taken from table S4, page 27
% jump frequencies are taken from table S4, page 27

% eps_1 are interaction energies of 1st nearest neigbours
% eps_2 are interaction energies of 2nd nearest neigbours
% e_jump are the contributions from the jumping atom to the saddle point
% f_jump are the jump frequencies

% index/Code for elements:
% Al: 1
% Zr: 2
% Sc: 3
% Va: 4 (Paper says "V" but means Vacancy, so I use "Va")

% Unit for energy for is meV
% Unit for temperature is Kelvin

e_jump=zeros(4,1);
f_jump=zeros(4,1);

%e_jump(1,1)=-8219;          % Al (meV)
%e_jump(2,1)=-11464;         % Zr (meV) from literature - does not seem
correct
%e_jump(3,1)=-9434;          % Sc (meV) from literature - does not seem
correct %e_jump(4,1)=0;

e_jump(1,1)=-8219;          % Al (meV)
e_jump(2,1)=-10464;         % Zr (meV) improved values
e_jump(3,1)=-8434;          % Sc (meV) improved values
e_jump(4,1)=0;



f_jump(1,1)=1.36e14;        % Al (1/s)
f_jump(2,1)=9e16;           % Zr (1/s)
f_jump(3,1)=4e15;           % Sc (1/s)
f_jump(4,1)=1;

eps_1=zeros(4,4);
eps_2=zeros(4,4);

eps_1(1,1)=-560;            %Al-Al
eps_1(1,2)=-979+0.244*T;    %Al-Zr
eps_1(1,3)=-759+0.21*T;     %Al-Sc
eps_1(1,4)=-222;            %Al-Va
eps_1(2,2)=-1045;           %Zr-Zr
eps_1(2,3)=-611;            %Zr-Sc
eps_1(2,4)=-350;            %Zr-Va
eps_1(3,3)=-650;            %Sc-Sc
```

```
%eps_1(3,4)=-757;            %Sc-Va
eps_1(3,4)=-141;             %Sc-Va new value (Angelina: Clouet et al.
mentioned/suggested as alternative value in text in supplements - not in
table - ab inito value; more meaningful than other value)
eps_1(4,4)=0;                %Va-Va

eps_1(2,1)=eps_1(1,2);       %matrix is symmetric
eps_1(3,1)=eps_1(1,3);
eps_1(3,2)=eps_1(2,3);
eps_1(4,1)=eps_1(1,4);
eps_1(4,2)=eps_1(2,4);
eps_1(4,3)=eps_1(3,4);

eps_2(1,1)=0;                %Al-Al
eps_2(1,2)=101-0.0233*T;     %Al-Zr
eps_2(1,3)=113-0.0334*T;     %Al-Sc
eps_2(1,4)=0;                %Al-Va
eps_2(2,2)=0;                %Zr-Zr
eps_2(2,3)=-2.77;            %Zr-Sc
eps_2(2,4)=0;                %Zr-Va
eps_2(3,3)=0;                %Sc-Sc
eps_2(3,4)=0;                %Sc-Va
eps_2(4,4)=0;                %Va-Va

eps_2(2,1)=eps_2(1,2);
eps_2(3,1)=eps_2(1,3);
eps_2(3,2)=eps_2(2,3);
eps_2(4,1)=eps_2(1,4);
eps_2(4,2)=eps_2(2,4);
eps_2(4,3)=eps_2(3,4);

end
```

Another sub-function of the main_routine is "diffusion_timestep", also written by Bernhard Sonderegger:

```
function
[lattice,list_of_Va,dt]=diffusion_timestep(lattice,size_of_lattice,first_NN
,second_NN,list_of_Va,e_jump,f_jump,eps_1,eps_2,T);

% this routine includes everything that is to happen within one timestep
% for diffusion.

% Now comes a timestep:

[list_of_probabilities,most_probable_jumps]=probability_of_vacancy_jumps(la
ttice,size_of_lattice,first_NN,second_NN,list_of_Va,e_jump,f_jump,eps_1,eps
_2,T);

[list_of_jumps,nr_of_jumps,dt]=define_vacancy_jumps(size_of_lattice,lattice
,list_of_Va,most_probable_jumps,list_of_probabilities,first_NN);

% Now the jumps are acutally perfoermed:

for va_jump=1:nr_of_jumps

    Va=list_of_jumps(va_jump,1);
    jump=list_of_jumps(va_jump,2);
```

```
    SL1=list_of_Va(Va,1);
    jump=jump+(SL1-1)*12;

    x1=list_of_Va(Va,2);
    y1=list_of_Va(Va,3);
    z1=list_of_Va(Va,4);

    SL2=first_NN(jump,2);

    x2=x1+first_NN(jump,3);
    y2=y1+first_NN(jump,4);
    z2=z1+first_NN(jump,5);

    if x2>size_of_lattice
        x2=x2-size_of_lattice;
    end
    if y2>size_of_lattice
        y2=y2-size_of_lattice;
    end
    if z2>size_of_lattice
        z2=z2-size_of_lattice;
    end
    if x2<1
        x2=x2+size_of_lattice;
    end
    if y2<1
        y2=y2+size_of_lattice;
    end
    if z2<1
        z2=z2+size_of_lattice;
    end


    % structure of the matrix "lattice"
    % lattice(SL_nr,x,y,z)

    atom1=lattice(SL1,x1,y1,z1);
    atom2=lattice(SL2,x2,y2,z2);

    if atom2~=4

        lattice(SL1,x1,y1,z1)=atom2;
        lattice(SL2,x2,y2,z2)=atom1;

        list_of_Va(Va,1)=SL2;
        list_of_Va(Va,2)=x2;
        list_of_Va(Va,3)=y2;
        list_of_Va(Va,4)=z2;
    end

end

end
```

17.7 Matlab Code - Error Analysis Voxel Spectroscopy

```
% error analysis voxel spec
% Angelina Orthacker
```

```
% vectors contain errors for each element; sqrt(counts) or as delivered
from software e.g. digital micrograph
v1=[2.2,109.4,36.7,6.2];
v3=[5.2,273.3,89.7,2.2];
vec=[2.5,135.3,45.3,1.1];
%vec=v1+v3+vec;
veck=[1,1,1.2,6.8];

v=zeros(3,4);
v(1,:)=vec;
v(2,:)=vec;
v(3,:)=vec;
v(2,1)=vec(3);
v(2,3)=vec(1);
v(3,1)=vec(4);
v(3,4)=vec(1);

vk=zeros(3,4);
vk(1,:)=veck;
vk(2,:)=veck;
vk(3,:)=veck;
vk(2,1)=veck(3);
vk(2,3)=veck(1);
vk(3,1)=veck(4);
vk(3,4)=veck(1);

for n=2:3
vn=v(n,:);
vkn=vk(n,:);

ia=vn(1);
ib=vn(2);
ic=vn(3);
id=vn(4);

Dia=sqrt(ia);
Dib=sqrt(ib);
Dic=sqrt(ic);
Did=sqrt(id);

fria=Dia/ia;
%frib=Dib/ib
%fric=Dic/ic
%frid=Did/id

ka=vkn(1);
kb=vkn(2);
kc=vkn(3);
kd=vkn(4);

kab=ka/kb;
kcb=kc/kb;
kdb=kd/kb;

Dkab=ka/kb*0.1;
Dkcb=kc/kb*0.1;
Dkdb=kd/kb*0.1;

par=(ia+ib*kab+ic*kab/kcb+id*kab/kdb);
```

```
ca2=ia/par

dia=ia/par^2;
dib=-ia*kab/par^2;
dic=-ia*kab/kcb/par^2;
did=-ia*kab/kdb/par^2;
dkab=-ia*(ib+ic/kcb+id/kdb)/par^2;
dkcb=ia*ic*kab/(ic*kab+(ia+ib*kab+id*kab/kdb)*kcb)^2;
dkdb=ia*id*kab/(id*kab+(ia+ib*kab+ic*kab/kcb)*kdb)^2;

dcak=dia*Dia+abs(dib)*Dib+abs(dic)*Dic+abs(did)*Did+abs(dkab)*Dkab+abs(dkcb
)*Dkcb+abs(dkdb)*Dkdb;
dca=dia*Dia+abs(dib)*Dib+abs(dic)*Dic+abs(did)*Did;
dcas=sqrt(dia^2*Dia^2+abs(dib)^2*Dib^2+abs(dic)^2*Dic^2+abs(did)^2*Did^2);%
+abs(dkab)*Dkab+abs(dkcb)*Dkcb+abs(dkdb)*Dkdb;
dca2=dca/0.25;%*ca2;
dcas2=dcas/0.25;%*ca2;
f2=fria*ca2/0.25;

out=[dcak, dca, dcas, dca2,dcas2, f2]
end

disp('end')
```

18 Publications and Award

18.1 Award

2015 - M&M Presidential Scholar Award (Microscopy and Microanalysis Society of America)

18.2 Peer Review Publications

Diffusion Defining Atomic-Scale Spinodal Decomposition within Nanoprecipitates
A. Orthacker, G. Haberfehlner, J. Taendl, M. C. Poletti, B. Sonderegger G. Kothleitner
Nature Materials 17 (2018) 1101-1107

Chemical degradation and morphological instabilities during focused ion beam prototyping of polymers
A. Orthacker, R. Schmied, B. Chernev, J. E. Fröch, R. Winkler, J. Hobisch, G. Trimmel, H. Plank
Phys. Chem. Chem. Phys. (2014) 16 (4), 1658.

Tunable 3D Nanoresonators for Gas-Sensing Applications
G. Arnold, R. Winkler, M. Stermitz, A. Orthacker, J. H. Noh, J. Fowlkes, G. Kothleitner, M. Huth, P. D. Rack, H. Plank
Advanced Functional Materials (2018) DOI: 10.1002/adfm.201707387

Influence of the degree of scandium supersaturation on the precipitation kinetics of rapidly solidified Al-Mg-Sc-Zr alloys
J. Taendl , A. Orthacker, H. Amenitsch, G. Kothleitner, C. Poletti
Acta Materialia 117 (2016) 43-50

In-situ observation of recrystallization in an AlMgScZr alloy using confocal laser scanning microscopy
J. Taendl , S. Nambu, A. Orthacker, G. Kothleitner, J. Inoue, T. Koseki, C. Poletti
Materials Characterization (2015) 108, 137.

Nanoscale voxel spectroscopy by simultaneous EELS and EDS tomography
G. Haberfehlner, A.Orthacker, M. Albu, J. L. and G. Kothleitner
Nanoscale (2014) 6 (23), 14563.

A combined approach to predict spatial temperature evolution and its consequences during FIB processing of soft matter
R. Schmied, J.E. Fröch, A. Orthacker, J. Hobisch, G. Trimmel, H. Plank
Phys. Chem. Chem. Phys. (2014) 16 (13), 6153.

Fundamental resolution limitations during electron induced direct write synthesis
G. Arnold, R. Timilsina, J. Fowlkes, A. Orthacker, G. Kothleitner, P. D. Rack, H. Plank
Applied Materials and Interfaces (2014) DOI: 10.1021/am5008003

18.3 Conference Talks

Analytical Electron Tomographic Investigations Revealing Self Stabilization of Core-Shell Precipitates through Opposing Diffusion Processes
A. Orthacker, G. Haberfehlner, J. Tändl, M.C. Poletti, B. Sonderegger, G. Kothleitner
Advanced Materials Day in Graz , Austria, September 2016

Analytical Electron Tomographic Investigations Revealing Self Stabilization of Core-Shell Precipitates through Opposing Diffusion Processes
A. Orthacker, G. Haberfehlner, J. Tändl, M.C. Poletti, B. Sonderegger, G. Kothleitner
European Microscopy Congress in Lyon , France, August 2016

Analytical Electron Tomography of Aluminum Alloys with Nano-Precipitates and its Physical Challenges
A. Orthacker, G. Haberfehlner, J. Tändl, M.C. Poletti, G. Kothleitner
Materials Day 2015 in Graz , Austria, September 2015

Physical and Practical Challenges in Analytical Electron Tomography of Aluminum Alloys
A. Orthacker, G. Haberfehlner, J. Tändl, M.C. Poletti, L. J. Allen, G. Kothleitner
Microscopy and Microanalysis 2015 Meeting in Portland, Oregon, USA, August 2015

Analytical Electron Tomographic Investigation of Aluminium Alloys with Nano-Precipitates
A. Orthacker, G. Haberfehlner, J. Tändl, M.C. Poletti, G. Kothleitner
18. Tagung Festkörperanalytik in Vienna, Austria, June 2015

Analytical Electron Tomographic Investigation of an Aluminium Alloy with Nano-Precipitates
A. Orthacker, G. Haberfehlner , J. Tändl , M.C. Poletti, G. Kothleitner
ASEM Workshop in Graz, Austria, May 2015

Tomography in Analytical Transmission Electron Microscopy of Nanomaterials
A. Orthacker, G. Haberfehlner, J. Tändl, M.C. Poletti, G. Kothleitner
Materials Day 2014 in Graz , Austria, October 2014

Experimental and Computational Aspects of Analytical Electron Tomography and its Application to Nanomaterials
A. Orthacker, G. Haberfehlner, J. Tändl, M.C. Poletti, G. Kothleitner
64. Jahrestagung der Österreichischen Physikalischen Gesellschaft in Pöllau , Austria, September 2014

Tomography in Analytical Transmission Electron Microscopy of Nanomaterials
A. Orthacker, G. Haberfehlner , J. Tändl , M.C. Poletti, G. Kothleitner
ASEM Workshop in Vienna, Austria, May 2014

Improved Morphological and Chemical Stability during FIB Soft Matter Processing
A. Orthacker, R. Schmied, B. Chernev, G. Trimmel, H. Plank
E-MRS Spring Meeting in Strasbourg, France, May 2013

Improved Morphological and Chemical Stability during FIB Soft Matter Processing
A. Orthacker, R. Schmied, B. Chernev, G. Trimmel, H. Plank
ASEM Workshop in Vienna, Austria, April 2013

Advanced Soft Matter Processing via Focussed Ion Beams
A. Orthacker, R. Schmied, B. Chernev, G. Trimmel, H. Plank
ICPS in Utrecht, The Netherlands, August 2012

18.4 Conference Posters

Investigation of the non-equilibrium formation of stoichiometric precipitates in multi-component aluminium alloys
A. Orthacker, G. Haberfehlner, J. Tändl, C. Poletti, B. Sonderegger and G. Kothleitner
ASEM Workshop 2017 in Vienna, Austria, April 2017

Tomography in Analytical Transmission Electron Microscopy of Nanomaterials
A. Orthacker, G. Haberfehlner, J. Tändl , M.C. Poletti, G. Kothleitner
International Microscopy Congress in Prague, The Czech Republic, September 2014

Tomography in Analytical Transmission Electron Microscopy of Nanomaterials
A. Orthacker, G. Haberfehlner, J. Tändl, M.C. Poletti, G. Kothleitner
European Workshop on Spatially-Resolved Electron Spectroscopy in Graz, Austria, April 2014

Chemical Degradation and Morphological Instabilities during Focused Ion Beam Prototyping of Polymers: a Problem and a Solution
A. Orthacker, R. Schmied, B. Chernev, G. Trimmel, H. Plank
Materials Day 2013 in Graz, Austria, October 2013

Improved Morphological and Chemical Stability during FIB Soft Matter Processing
A. Orthacker, R. Schmied, B. Chernev, G. Trimmel, H. Plank
EMAT Workshop in Antwerp, Belgium, June 2013

Improved Morphological and Chemical Stability during FIB Soft Matter Processing
A. Orthacker, R. Schmied, B. Chernev, G. Trimmel, H. Plank
Nano and Photonics in Mauterndorf, Austria, March 2013